Lipid topography and lytic peptides:

A lipocentric model for pore-forming antimicrobial agents

By

David James Paterson, BSc, MRes.

January 2015

Submitted in fulfilment of the requirements for the degree of

Doctor of Philosophy

School of Biomedical Engineering

College of Engineering

University of Glasgow

Abstract

Linear cationic antimicrobial peptides are a diverse family of membrane-active peptides, linked by physiochemical characteristics that induce membrane disruptive effects, including the formation of membrane spanning pores. They offer potential development as novel antimicrobial therapeutics, due to their high potency and evidenced resistance to bacterial drug resistance mechanisms. Complex lipid-peptide interactions are believed to govern their pore formation activity, and their mechanism of selectivity between prokaryotic and eukaryotic cells. Some peptides (e.g. magainin) show a high degree of selectivity for bacterial cells, while some (e.g. melittin) target bacterial and mammalian cells indiscriminately. Within this report, high-throughput microfluidics is used to investigate the pore formation capabilities, of selective and non-selective antimicrobial peptides, within biomimetic vesicles representing both bacterial and mammalian cells. Microfluidics offers precise control over the exposure of lipid membranes to antimicrobial peptides, allowing the pore-formation process to be elucidated in greater detail than conventional techniques. A new model for their mechanism of action is proposed, where lipid topography and lipid-peptide steric interactions exert influence over both pore formation and the selectivity mechanism. The model has potential to inform the rational drug design of future antimicrobial agents, using linear cationic antimicrobial peptides as a template.

Contents

Abbreviations 8

Table list 10

Figure list 11

Equation list 15

Acknowledgements 16

1. Introduction 17

1.1 Bacterial drug-resistance 17

1.1.1 Antibiotics 17

1.1.2. Causes of bacterial drug-resistance 18

1.2. Drug targets for conventional antibiotics 18

1.2.1. Bacterial cell-wall synthesis 18

1.2.2. Bacterial protein synthesis 19

1.2.3. Bacterial DNA replication and repair 19

1.3. Mechanisms of acquired bacterial drug-resistance 20

1.3.1. Destruction of antibiotic warhead 20

1.3.2. Drug efflux pumps 20

1.3.3. Modification of drug target 21

1.4. Horizontal gene transfer (HGT) 21

1.5. Multidrug resistant strains 21

1.6. Combating drug-resistance 22

1.7. Future of antimicrobial chemotherapy 22

1.8. Lipid membranes 22

1.8.1. Physiochemical structure and properties of lipids 23

1.8.2. Lipid topology and the geometrical membrane model 24

1.8.3. The lipid bilayer 27

1.8.4. Lipid domains and phases 28

1.8.5. Prokaryotic versus eukaryotic membranes 30

1.9. Linear cationic antimicrobial peptides (LCAMPs) 32

1.9.1. LCAMP activity 33

1.9.2. Physiochemical properties 33

1.9.3. Biological target of LCAMPS 33

1.9.4. Mechanisms of action of LCAMPs 34

1.9.5. Experimental investigation of LCAMP activity 38
1.9.6. LCAMPs and drug-resistance 38
1.9.7. Comparison of two prototypical LCAMPs 39
1.9.8. Structure-function relationships of LCAMPs 40
1.9.9. Factors underpinning prokaryotic and eukaryotic selectivity 42
1.9.10. Magainin and melittin pores 43
1.9.11. LCAMP homology with other proteins 44
1.10. Lipid-peptide interactions 44
1.10.1. Lipid clustering around membrane-bound LCAMPs 45
1.10.2. Lipid interactions and LCAMP activity 45
1.10.3. Lipid interactions inducing pore formation 47
2. Materials and methods 49
2.1. Design of microfluidic device 49
2.2. Device microfabrication 50
2.3. GUV electroformation 52
2.3.1. Off-chip electroformation protocol 53
2.3.2. On-chip electroformation protocol 55
2.4. Dye-leakage protocol 56
2.5. Data processing 56
2.5.1. Background and photobleaching correction 57
2.5.2. Time correction 57
2.5.3. Kinetic grouping behaviour 57
2.5.4. Multiple leakage phase analysis 58
3. Peptide-induced effect (PIEs) profiling 61
3.1. PIEs 61
3.1.1. No effect 61
3.1.2. Bursting 62
3.1.3. Pore-mediated leakage 62
3.1.4. Carpet mechanism 62
3.1.5. Micellisation 62
3.2. Membrane systems 62
3.3. PIE-profiles 63
3.4. PIEs of melittin 63
3.4.1. Binary lipid systems 63
3.4.2. Ternary lipid systems 65

3.4.3. Peptide concentration and PIE-profiles 68
3.5. PIEs of magainin 70
3.5.1. Ternary lipid systems....70
3.6. Quaternary system PIEs 72
3.7. Fatty acid unsaturation geometry and PIEs 74
3.8. All-or-none versus graded leakage....76
3.9. PIE average initiation times....76
3.9.1. Burst initiation times (red circles) 78
3.9.2. Pore-mediate leakage initiation times (blue circles)....78
3.9.3. Carpet mechanism initiation times (turquoise circles) 79
3.9.4. Micelle initiation times (pink circles) 79
3.10. PIE summary....80
4. Pore-mediated leakage in zwitterionic membranes 82
4.1. Melittin dye-efflux kinetics 82
4.1.1. DOPC membrane system 82
4.1.2. DOPC:DPPC membrane system....87
4.1.3. DOPC:DOPE membrane system 94
4.2. Zwitterionic leakage kinetics summary....101
5. Pore-mediated leakage in anionic membranes 103
5.1. DOPC:DOPE:DOPG membrane system....103
5.2. DOPC:DOPE:DPPG membrane system 105
5.3. DOPC:DOPE:LPG membrane system....111
5.4. DOPC:DOPE:POPG membrane system....114
5.5. DOPC:DPPC:DOPG membrane system....115
5.6. DOPC:DPPC:DPPG membrane system....116
5.7. mGUV membrane system 123
5.8. DOPC:DOPE:DOPG:DPPG membrane system 135
5.9. Summary 140
6. Discussion 142
6.1. The free energy of lipid-LCAMP interactions 142
6.1.1. Membrane partitioning....143
6.1.2. Secondary structure formation....144
6.1.3. Electrostatic interactions 144
6.1.4. Protein conformation....144
6.1.5. Peptide immobilisation 145

6.1.6. Lipid perturbation 145
6.2. Membrane free volume and packing frustration 146
6.3. LCAMP behaviour during pore-formation 146
6.4. Energy of the membrane-inserted monomer 147
6.5. Energy of the lipid-LCAMP raft 150
6.6. Membrane penetration of LCAMP monomers 151
6.7. Helical steric asymmetry and membrane tension 152
6.8. Key residues – Tryptophan and Phenylalanine 155
6.9. Reshaping the toroidal pore 158
6.10. Pore formation in peptide-free membrane 160
6.11. Energy of the pore structure 162
6.12. Global versus local membrane tension 163
6.13. LCAMP modulation of bulk membrane tension 167
6.14. Selectivity mechanism 167
6.15. Charge distribution 168
6.16. Model predictions 169
6.16.1. Prediction 1 - Lipid-AMP raft energetics 170
6.16.2. Prediction 2 - Pore energetics 170
6.16.3. Prediction 3 - Stochastic behaviour 170
6.16.4. Prediction 4 - Pore behaviour 170
6.16.5. Prediction 5 - Pore size and quantisation 171
6.16.6. Prediction 6 - Pore number 171
6.17. Application of model to experimental data 171
6.17.1. Pore-mediated leakage data 172
6.17.2. PIE data 178
6.18. Bacterial biomimetic membranes and melittin 178
6.18.1. Activity 179
6.18.2. Bursting 180
6.18.3. Pore-mediated leakage 180
6.18.4. Carpet mechanism 181
6.18.5. Micellisation 181
6.19. Bacterial biomimetic membranes and magainin 181
6.19.1. Activity 182
6.19.2. Bursting 183
6.19.3. Pore-mediate leakage 184

6.19.4. Carpet mechanism 184
6.19.5. Micellisation 185
6.20. Mammalian biomimetic membranes and LCAMPs 185
6.20.1. Melittin and mGUV membranes 186
6.20.2. Magainin and mGUV membranes 187
6.21. Application to *in-vivo* membranes 187
6.22. Application to the literature 188
6.22.1. Intracellular target mechanism 188
6.22.2. Biphasic leakage 189
6.22.3. Graded versus all-or-none leakage 189
7. References 190

Abbreviations

A	Alanine
AIDS	Acquired immune deficiency syndrome
AMP	Antimicrobial peptide
bGUV	Bacterial giant unilamellar vesicle
CDC	Centre for Disease control
DEPG	Dielaidoylphosphoglycerol
DOPC	Dioleoylphosphatidylcholine
DOPE	Dioleoylphosphatidylethanolamine
DOPG	Dioleoylphosphatidylglycerol
DNA	Deoxyribonucleic acid
DPPC	Dipalmitoylphosphatidylcholine
DPPG	Dipalmitoylphosphoglycerol
HIV	Human immunodeficiency virus
HGT	Horizontal gene transfer
G	Glycine
F	Phenylalanine
K	Lysine
LCAMP	Linear cationic antimicrobial peptide
L_d	Liquid disordered
L_o	Liquid ordered
LPG	Lyso-phosphoglycerol
M2a	Magainin II amide
mGUV	Mammalian giant unilamellar vesicle
MIC	Minimum inhibitory concentration
PA	Phosphoric acid
PC	Phosphatidylcholine

PE	Phosphatidylethanolamine
PG	Phosphoglycerol
PI	Phosphatidylinositol
PIE	Peptide-induced effect
POPG	1-palmitoyl-2-oleoylphosphoglycerol
POPS	1-palmitoyl-2-oleoylphosphatidylserine
PS	Phosphatidylserine
REES	Red-edge excitation shift
W	Tryptophan

Table list

Table 1: List of lipid mixtures.....53

Table 2: Electroformation pulse sequence.....54

Table 3: PIE timings for melittin.....77

Table 4: PIE timings for magainin.....77

Figure list

Figure 1.1: Space-filling lipid diagram……..23

Figure 1.2: Lipid topographies; conical, inverse-conical and cylindrical……..24

Figure 1.3: Conical lipid packing structures……26

Figure 1.4: Inverse-conical lipid packing structures……26

Figure 1.5: Cylindrical lipid packing structures……27

Figure 1.6: Bilayer cross section……28

Figure 1.7: Liquid-disordered lipid membrane……29

Figure 1.8: Gel-phase lipid membrane……29

Figure 1.9: Liquid-ordered lipid membrane……29

Figure 1.10: Lipid-protein raft……30

Figure 1.11: Shai-Matsuzaki-Huang model for LCAMP action……35

Figure 1.12: Ordered and disordered toroidal pore structures……37

Figure 1.13: Polar angle and membrane insertion depth……40

Figure 1.14: Peptide-free pore formation……48

Figure 2.1: Microfluidic device schematic……49

Figure 2.2: Photolithography process……51

Figure 2.3: SEM pictures of device……52

Figure 2.4: AFM image of deposited lipid film……54

Figure 2.5: Assembled microfluidic device……55

Figure 2.6: Biomimetic dye-filled vesicles within the microfluidic device……56

Figure 2.7: Background and photobleaching correction……57

Figure 2.8: Kinetic grouping of leakage traces……58

Figure 2.9: Averaged leakage kinetics……59

Figure 2.10: Multiphase leakage trace……59

Figure 2.11: Comparison of individual leakage phases……60

Figure 3.1: Classification of peptide-induced effects……61

Figure 3.2: PIE-profile for DOPC:X binary membranes with 1 µM melittin……64

Figure 3.3: PIE-profiles for DOPC:DOPE:X membranes with 1 μM melittin……65

Figure 3.4: PIE-profiles for DOPC:DPPC:X membranes with 1 μM melittin……67

Figure 3.5: Peptide concentration and the PIE-profiles of melittin in binary systems……68

Figure 3.6: Peptide concentration and the PIE-profiles of melittin in ternary systems……69

Figure 3.7: PIE-profiles for DOPC:DOPE:X membranes with 1 μM magainin……71

Figure 3.8: PIE-profiles for DOPC:DPPC:X membranes with 1 μM magainin……72

Figure 3.9: PIE-profile for DOPC:DOPE:DOPG:DPPG membrane with 1 μM melittin……73

Figure 3.10: PIE-profile for DOPC:DOPE:DOPG:DPPG membrane with 1 μM magainin……74

Figure 3.11: PIE-profile for DOPC:DOPE:DEPG membrane with 1 μM melittin……75

Figure 3.12: PIE-profile for DOPC:DOPE:DEPG membrane with 1 μM magainin……76

Figure 4.1: Dye-leakage kinetics for DOPC vesicles with 1 μM melittin……83

Figure 4.2: Multiphase leakage traces from 1 μM melittin - DOPC system……84

Figure 4.3: Single phase dye-leakage kinetics for DOPC vesicles with 5 μM melittin……85

Figure 4.4: Multiphase dye-leakage kinetics for DOPC vesicles with 5 μM melittin……86

Figure 4.5: DOPC with 1 and 5 μM melittin……87

Figure 4.6: Leakage traces from 1 μM melittin – DOPC:DPPC system……88

Figure 4.7: Multiphase leakage traces from 1 μM melittin – DOPC:DPPC system……89

Figure 4.8: Long time-scale leakage from 1 μM melittin – DOPC:DPPC system……90

Figure 4.9: Leakage traces from 5 μM melittin – DOPC:DPPC system……91

Figure 4.10: Multiphase leakage traces from 5 μM melittin – DOPC:DPPC system……92

Figure 4.11: DOPC:DPPC with 1 and 5 μM melittin……93

Figure 4.12: Overlay of DOPC and DOPC:DPPC 1 μM melittin data……94

Figure 4.13: Leakage traces from 1 μM melittin – DOPC:DOPE system……95

Figure 4.14: Multiphase leakage traces from 1 μM melittin – DOPC:DOPE system……96

Figure 4.15: Leakage traces from 5 μM melittin – DOPC:DOPE system……97

Figure 4.16: Multiphase leakage traces from 5 μM melittin – DOPC:DOPE system……98

Figure 4.17: DOPC:DOPE with 1 and 5 μM melittin……99

Figure 4.18: Overlay of DOPC and DOPC:DOPE 1 μM melittin data……100

Figure 4.19: Overlay of DOPC:DPPC and DOPC:DOPE 1 μM melittin data……..101

Figure 5.1: Leakage traces from 1 μM melittin – DOPC:DOPE:DOPG system……..104

Figure 5.2: Multiphase leakage traces from 1 μM melittin – DOPC:DOPE:DOPG system……105

Figure 5.3: Leakage traces from 1 μM melittin – DOPC:DOPE:DPPG system……106

Figure 5.4: Leakage traces from 1 μM magainin – DOPC:DOPE:DPPG system……107

Figure 5.5: Multiphase leakage traces from 1 μM magainin – DOPC:DOPE:DPPG system……108

Figure 5.6: Leakage traces from 5 μM magainin – DOPC:DOPE:DPPG system……109

Figure 5.7: Long time-scale leakage from 5 μM magainin – DOPC:DOPE:DPPG system……110

Figure 5.8: Multiphase leakage traces from 5 μM magainin – DOPC:DOPE:DPPG system……111

Figure 5.9: Leakage traces from 1 μM melittin – DOPC:DOPE:LPG system……112

Figure 5.10: Multiphase leakage traces from 1 μM melittin – DOPC:DOPE:LPG system……113

Figure 5.11: Leakage traces from 1 μM magainin – DOPC:DOPE:LPG system……114

Figure 5.12: Leakage traces from 1 μM melittin – DOPC:DPPC:DOPG system……115

Figure 5.13: Leakage traces from 1 μM melittin – DOPC:DPPC:DPPG system……117

Figure 5.14: Multiphase leakage traces from 1 μM melittin – DOPC:DPPC:DPPG system……118

Figure 5.15: Leakage traces from 1 μM magainin – DOPC:DPPC:DPPG system……119

Figure 5.16: Multiphase leakage traces from 1 μM magainin – DOPC:DPPC:DPPG system……120

Figure 5.17: Multiphase leakage traces from 1 μM magainin – DOPC:DPPC:DPPG system……121

Figure 5.18: Overlay of DOPC:DPPC:DPPG 1 μM melittin and magainin data……122

Figure 5.19: PIE-profiles for DOPC:DPPC:DPPG with 1 μM melittin and magainin data……123

Figure 5.20: Leakage traces from 1 μM melittin – mGUV system……124

Figure 5.21: Multiphase leakage traces from 1 μM melittin – mGUV system……125

Figure 5.22: Leakage traces from 5 μM melittin – mGUV system……126

Figure 5.23: Multiphase leakage traces from 5 μM melittin – mGUV system……127

Figure 5.24: Overlay of mGUV 1 and 5 μM melittin data……128

Figure 5.25: Leakage traces from 1 μM magainin – mGUV system……129

Figure 5.26: Multiphase leakage traces from 1 μM magainin – mGUV system……130

Figure 5.27: Leakage traces from 5 μM magainin – mGUV system……131

Figure 5.28: Multiphase leakage traces from 1 μM magainin – mGUV system……..132

Figure 5.29: Overlay of mGUV 1 and 5 μM magainin data……133

Figure 5.30: Overlay of mGUV 5 μM magainin and melittin data……134

Figure 5.31: Leakage traces from 1 μM melittin – quaternary system……136

Figure 5.32: Multiphase leakage traces from 1 μM melittin – quaternary system……137

Figure 5.33: Leakage traces from 1 μM magainin – quaternary system……..138

Figure 5.34: Multiphase leakage traces from 1 μM magainin – quaternary system……..139

Figure 5.35: Overlay of quaternary 1 μM magainin and melittin data……..140

Figure 6.1: Influence of lipid topography on LCAMP membrane disruption……148

Figure 6.2: Lipid clustering around a LCAMP helix……..149

Figure 6.3: Influence of lipid-peptide clustering of raft energetics……..151

Figure 6.4: Steric asymmetry of a membrane-bound magainin helix……154

Figure 6.5: Tryptophan and phenylalanine as interfacial space fillers……..156

Figure 6.6: Tryptophan and phenylalanine stabilised pore structure……159

Figure 6.7: Lipid geometry based induction of pore structures……..161

Figure 6.8: Pre-pore collection of lipid-peptide rafts into raft aggregates……164

Figure 6.9: Pore-formation and negative feedback within the membrane tension……..166

Figure 6.10: Charge distribution along melittin and magainin helices……..169

Figure 6.11: Grouping of dye efflux kinetics……..173

Figure 6.12: Pore opening/closing cycle induced by negative feedback loop……..174

Figure 6.13: Leakage kinetic similarity between melittin and magainin……176

Figure 6.14: Differently sized pores open within a single membrane……177

Figure 6.15: Individual lipids controlling the bacterial PIE-profiles of melittin……..179

Figure 6.16: Individual lipids controlling the bacterial PIE-profiles of magainin……182

Figure 6.17: Comparison of the mGUV PIE-profiles of magainin and melittin……..185

Equation list

Equation 1: Lipid packing parameter……..25

Equation 2: Contributions to the energetics of LCAMP membrane binding……142

Equation 3: Energetics of membrane stretching……..145

Equation 4: Energetics of membrane bending……..145

Equation 5: Energy of a pore structure……..162

Equation 6: Pore energy contributions of local and global effects from LCAMPs……..178

Acknowledgements

I would like to express my heartfelt gratitude to my PhD supervisor, Professor Jon Cooper, for his guidance, encouragement and especially patience throughout the course of my PhD research. Special acknowledgement and appreciation to Dr. Julien Reboud for his enthusiastic assistance in my research, and to Dr. Rab Wilson for generous help with the microfabrication process.

I would like to express my appreciation to my family for their continual support during the last four years, especially my father, Robert Paterson, and brother, Iain Paterson.

I wish to acknowledge the Doctoral Training Centre, together with the European Physical Science Research Council and the Biotechnology and Biological Sciences Research Council, for the financial support to this research.

Writing a thesis would be much harder without the help of many people who have been generous with their time, enthusiasm and knowledge. Merely saying “thank you” seems an inadequate acknowledgement of their contributions.

1. Introduction

1.1 Bacterial drug-resistance

Drug-resistant bacterial strains are one of the emerging challenges to developed world medicine in the 21st century[1]; in many countries, drug-resistant bacterial infections are the leading cause of death from infectious agents. The CDC statistics for 2013 show that there were over 2 million new cases of bacterial infections that failed to respond to conventional treatments, with over 23,000 deaths.[2] The CDC figures for the same year for HIV infection show less than 50,000 new incidences of the disease, with over 15,000 deaths attributed to AIDS. Coming less than 50 years after the famous quote often attributed to the United States Surgeon General (1965 – 1969) Dr. William H. Stewart – "It is time to close the book on infectious diseases, and declare the war against pestilence won.", these statistics are an alarming indication that progress made in treating infectious pathogens in the preceding decades may be becoming undone.

Driven by societal and technological progress, deaths from infectious agents have been greatly reduced in the last few centuries. Better nutrition and housing lead to decreased host susceptibility, while curtailing disease transmission though improved housing and safer food and water, led to huge reductions in the prevalence of death due to infectious agents.[1] From the discovery of bacteria as infectious agents in the late 19th century, it was almost fifty years before the production of the first effective treatment for a bacterial infection; the sulphonamides introduced in 1937.[3] Bacterial acquired drug-resistance operates via a quick timeline, with the average time for appearance of drug resistant strains being less than two years.[4][5] For example, the first sulphonamide-resistant strain was reported in the late 1930's.[3]

Widespread introduction of antimicrobial agents in the mid-twentieth century was a major factor in the decline of deaths from infectious diseases,[1] and is rightly credited as one of the greatest advances of modern medicine. Thanks to the upsurge in drug-resistance within bacterial populations, this trend looks to be reversing, as the prevalence of drug-resistant strains increases world-wide.[1][2] Infection with a drug-resistant bacterial strain greatly reduces treatment efficacy, and increases the risk of complications and mortality rates,[6] and the ongoing pandemic of drug-resistant bacteria in first-world hospitals threatens a return to the preantibiotic era.

1.1.1 Antibiotics

Antibiotics are chemotherapeutic agents that are selectively toxic for bacterial cells over host cells, and can be classed as either bactericidal, where the action of the antibiotic kills the target bacteria, or bacteriostatic, where the antibiotic inhibits the growth of the pathogen.

1.1.2. Causes of bacterial drug-resistance

There are three major factors underpinning the development drug-resistant bacterial strains, namely the increased selective pressure from over prescription of antimicrobials;[1][7][8] the decreased production of novel antibiotic agents[1] and the huge population and high mutation rate of bacteria.[5] The rampant prescription of antibiotics is perhaps the leading cause of drug-resistance, in the sixty years since their introduction, many millions of tons of antibiotics have entered circulation.[3][6] and worldwide between 100 – 200 thousand tons of antibiotic materials are produced annually.[9] A large proportion of antibiotics are consumed by the meat and dairy industries, up to 70% of total production in the US.[10] Agricultural animals are therefore an important reservoir for the emergence of drug-resistant pathogens. The current paradigm of producing new or modified antibiotics to combat the emergence of bacterial strains resistant to older antibiotics is failing, due to the low drug-pipeline delivery of novel antimicrobial agents.[1][11][12] Medical history demonstrates the adaptive nature of bacterial populations, with perhaps the most pertinent the story of methicillin, the first designer "anti-resistance" antibiotic. From the introduction of methicillin, it was less than three years before widespread emergence of resistant bacteria emerged.[3] The huge populations and high mutation rates of bacteria mean that it is a question of when, not if, the necessary mutations will occur that confer drug-resistance.

1.2. Drug targets for conventional antibiotics

There are three proven targets for the main antimicrobial therapeutics; bacterial cell wall synthesis, bacterial protein synthesis and bacterial DNA replication and repair. The following sections provide a brief outline of these drug targets, giving specific examples in each case for antimicrobial agents affecting these targets.

1.2.1. Bacterial cell-wall synthesis

The bacterial cell is a sophisticated and complex multi-layered structure, contributing significant mechanical strength and resistance to osmotic shock.[5][13] Bacteria can be divided into classes, gram-positive, gram-negative and gram-variable, based on their retention of the gram stain.[13][14] Common within all classes is the presence of peptidoglycan, a highly covalently interlinked mesh of peptides and glycans.[5][13][15] Peptidoglycan forms a rigid exoskeleton, providing much of the mechanical strength and resistance to osmolysis present in bacteria, with the degree of cross-linking within the network directly correlated to the structural integrity of the bacteria.[5][15] Cross-linking in the peptidoglycan layer is modulated by two enzyme families; transpeptidases, linking adjacent peptide strands with amide bridges and transglycosylases, lengthening the peptideoglycan strands.[5][15] Disruption of bacterial cell-

wall synthesis is an established antibiotic target,[11] and several classes of antibiotics exploit the biochemistry of peptidoglycan synthesis to exert their bactericidal or bacteriostatic effects.

The ß-lactam antibiotic family, which includes penicillins and cephalosporins, contain a four carbon lactam ring. The sterically strained ring is the antibiotic warhead, targeting both transpeptidase and transglycosylase enzymes, acting as a psuedosubstrate peptidoglycan biosynthesis intermediate.[5] The antibiotic attacks the enzyme, opening the lactam ring to covalently bind to the enzymes active site. The enzyme is unable to hydrolyse this bond, and the active site is blocked, removing the enzyme from participation in peptidoglycan biosynthesis reactions.[15] The antibiotic vancomycin also targets peptidoglycan synthesis, but unlike the ß-lactam family of antibiotics, it sequesters the peptide substrate rather than a direct attack on the enzyme.[16] Both penicillins and vancomycin prevent the crosslinking of peptidoglycan chains, reducing its mechanical strength, and leaving the bacteria vulnerable to osmotically-induced lysis.[5][15]

1.2.2. Bacterial protein synthesis

Bacterial protein synthesis is an attractive drug target, as prokaryotic RNA and ribosomal machinery are distinct enough from the host cells protein synthesis machinery, that bacterial protein synthesis can be targeted without interrupting eukaryotic cellular protein synthesis.[5] The complex biosynthesis pathways offer many interdiction points for antibiotic chemotherapy, during the initiation, elongation and termination phases of protein synthesis, creating a multifaceted target for new antibiotics.[15] Tetracyclines were the first antibiotics to be described as broad-spectrum antimicrobial agents, i.e. possessing activity against a wide range of gram-positive and gram-negative bacteria. They exert their antimicrobial activity through blocking access of aminoacyl-tRNAs to the 30S bacterial ribosomal subunit, preventing the synthesis of new proteins.[15][17] Aminoglycosides also bind to prokaryotic ribosomal subunit 30S, but are unique amongst antibiotics targeted at protein synthesis pathways, in that they are bactericidal rather than bacteriostatic.

1.2.3. Bacterial DNA replication and repair

The fluoroquinolones are a synthetic class of antimicrobial agents, specifically designed to target members of the DNA gyrase enzymes (specifically topoisomerases II and IV), which are responsible for uncoiling double-stranded bacterial DNA after replication.[15] Drug-bound topoisomerases and cleaved DNA form a stable complex, arresting the DNA replication process at the cleavage stage, leading to immediate bacteriostasis and eventual cell death.

1.3. Mechanisms of acquired bacterial drug-resistance

The mechanism of action of antimicrobial agents, and the development of acquired resistance are intimately linked,[18] for a complete discussion of the emergence of drug-resistance in bacterial populations, it is necessary to explore the molecular mechanisms underpinning the acquisition of resistance. Bacterial populations utilise a number of mechanisms to achieve resistance to antibiotics. To illustrate this point different mechanisms of resistance will be provided, for each of the drug targets mentioned in the previous section. Note however, that process of acquiring drug-resistance is extremely adaptable, and multiple mechanisms of resistance for each antibiotic are typically reported,[5][12][17] with >20,000 potential resistance genes reported in bacteria.[3]

1.3.1. Destruction of antibiotic warhead

The classic example of bacterial resistance is the acquisition of penicillin-resistance, via a single nucleotide polymorphism that creates ß-lactamase enzymes, which target the ß-lactam ring of penicillin.[19][20] Over 1,000 resistance related lactamase enzymes have been identified,[3] acting via hydrolysis of the sterically strained lactam ring that characterises penicillin-derived antibiotics.[19][20] Bacterial strains have been isolated that are resistant to the latest generation of penicillin derived antibiotics, through the expression of the New Delhi metallo-ß-lactamase enzyme.[21]

1.3.2. Drug efflux pumps

Effective treatment requires administered antibiotics to reach their target site, and accumulate to therapeutic levels. For example, tetracycline antibiotics which impair bacterial protein synthesis must first penetrate the outer membrane (in gram-negative bacteria), cross the periplasmic space and permeate the inner cytoplasmic membrane before reaching their target – the bacterial ribosome. Both gram-negative and gram-positive bacteria have been observed to overproduce membrane proteins that act as drug efflux pumps, transporting antibiotics back against the desirable concentration gradient.[5][22][23] The acquisition of drug-resistance via the production of drug efflux pumps is simplified, due to strains of bacteria producing natural antibiotic compounds, in order to supress neighbouring bacterial populations. To render those compounds ineffective in themselves, many of these antibiotic producing species utilise drug efflux pumps to remove the compound from within their membrane compartments, and rendering it therapeutically ineffective.[22] As many antibiotics are derived from bacterial compounds, it requires relatively little changes in the bacterial genome to acquire a plasmid containing a drug efflux pump, and overexpress the protein. Drug efflux pumps typically display low substrate selectivity, meaning that whole classes of antimicrobial agents can be rendered ineffective by the overexpression of one drug efflux pump.[22][23]

1.3.3. Modification of drug target

Another path to bacterial drug-resistance is through modification of the drug target structure, typically a protein within a biosynthesis pathway, rendering the antibiotic vulnerable to bacterial genome mutations which change the target proteins sequence. There are many examples of extremely rapid resistance development, when antimicrobials are targeted at a specific protein, which can be easily mutated. To illustrate this point, consider the emergence of *M. tuberculosis* strains which are resistant to the first-line indicated treatment with fluoroquinone antibiotics. Fluoroquinones act by forming a stable complex with DNA gyrase enzymes, interrupting bacterial cell replication, leading to cell death. Piton and co-workers (2010) report a clear relationship between amino acid mutation and the *M. tuberculosis* resistance phenotype. Fluoroquinolones bind to the gyrase-DNA complex at the quinolone binding pocket, which is comprised of both amino acid and DNA residues.[24][25] Mutations to amino acids within this pocket confer varying levels of fluoroquinolone resistance, with three residues demonstrated to play particularly key roles.[24]

1.4. Horizontal gene transfer (HGT)

HGT is a form of genetic exchange between bacteria, that can occur via uptake of extracellular DNA released by other bacteria (transformation), or by phage-mediated transfer from phage-infected donor cells (transduction) or via plasmid exchange during bacterial conjugation.[26] These processes have played a considerable role in the emergence of resistance to the ß-lactam antibiotics.[3] Numerous resistance genes can be gathering in single plasmids,[4][27] enabling efficient transfer of multidrug resistance between bacterial populations.

1.5. Multidrug resistant strains

Commonly described by the term “superbugs”, these pathogens demonstrate increased morbidity and mortality, due to the acquisition of multiple mutations bestowing enhanced resistance to the antimicrobials commonly prescribed for their treatment. Commonly known as multidrug-resistant bacteria, the most notorious strain is multidrug-resistant *Staphylococcus aureus* (MRSA), which attained its infamy mainly through intensive press coverage in the mid to late 1990’s. For example MDR *Vibrio cholera* is a far more virulent pathogen, far exceeding MRSA in infection, both in numbers and deleterious consequences.[3] A frightening new phenomenon is the emergence of totally drug-resistant strains of *M. tuberculosis*,[28] which are highly resistant to all the first- and second-line therapeutics indicated for tuberculosis treatment. Although the resistant strains of *Vibrio* cholera and *M.* tuberculosis are (so far) restricted to Asia and South America leading to low press coverage, and hence given low

priority by the medical research complex, these pathogens mark a return to preantibiotic era levels of treatment.

1.6. Combating drug-resistance

Several strategies have been proposed to overcome bacteria drug-resistance, including coadministration of antibiotics with agents that block common resistance mechanisms;[3] dual antibiotic therapy;[3][28] and the chemical evolution of the therapeutic warhead. Certain antimicrobial agents are withheld from general prescription, to reserve for the treatment of problematic drug-resistant bacterial infections. Vancomycin is one of these, but even these "last resort therapeutics" are becoming ineffective,[8] with vancomycin-resistant enterococcus now at pandemic levels in US hospitals.[29] It is never-the-less clear from the statistics that the war against infectious disease is far from won, and new strategies are desperately required, in the battle to stay ahead of the ever changing front lines of the single-celled enemy.

1.7. Future of antimicrobial chemotherapy

The cycle of rapid bacterial acquisition of drug-resistance to novel antibiotics must be broken, with the optimal strategy being the development of new antibiotics immune to the mechanisms of drug resistance. The three main drug targets for conventional antimicrobials, i.e. bacterial cell-wall and protein synthesis together with DNA replication and repair, are all vulnerable to the acquisition of resistance through small changes in the genome of the target organism. New antibiotics with low specificity targets would involve a much more complicated, and thus less commonly occurring, resistance mechanism; one such possible target is the bacterial cell membrane.

1.8. Lipid membranes

In-vivo lipid membranes are complex, heterogeneous mixtures of a large variety of constituent lipids.[30][31] The complexity of membranes suggests their function is not to merely separate cellular compartments and delineate the boundaries of the cell, and indeed many roles in biological processes have been attributed to lipids.[30][32] Cellular functions fulfilled by membrane lipids included serving as membrane protein anchoring sites;[32] cell-to-cell signalling[33][34] and vesicle trafficking.[35] Synthesised in the endoplasmic reticulum,[30] lipids are then redistributed to the desired membrane via a complex vesicle trafficking network.[33] Cells carefully modulate their membrane lipid composition as part of cellular homeostasis, and typical membrane composition is characterised by the presence of a large variety of lipids. The total eukaryotic lipidome possesses over 1000 members,[30] and human

erythrocytes alone are estimated to have over 200 different lipid species.[31] The large variety of lipid species is reflected in the genome, with around 5% of genes dedicated to the production and maintenance of a diverse portfolio of cellular lipids.[30] These factors suggest it is advantageous to maintain large and varied lipid stocks within the membrane.

1.8.1. Physiochemical structure and properties of lipids

The properties of phospholipids, the most numerous class of eukaryotic membrane lipids,[30] are primarily a result of their physiochemical characteristics. Their strong amphipathic character, results in a "love-hate" relationship with water and defines their behaviour, including their self-assembly into supramolecular structures and their lipid-lipid and lipid-peptide interactions. The chemical components of a phospholipid can be split into three parts, the polar headgroup moiety; the polar glycerol backbone and two non-polar hydrophobic fatty acid tailgroups, depicted in figure 1.1.

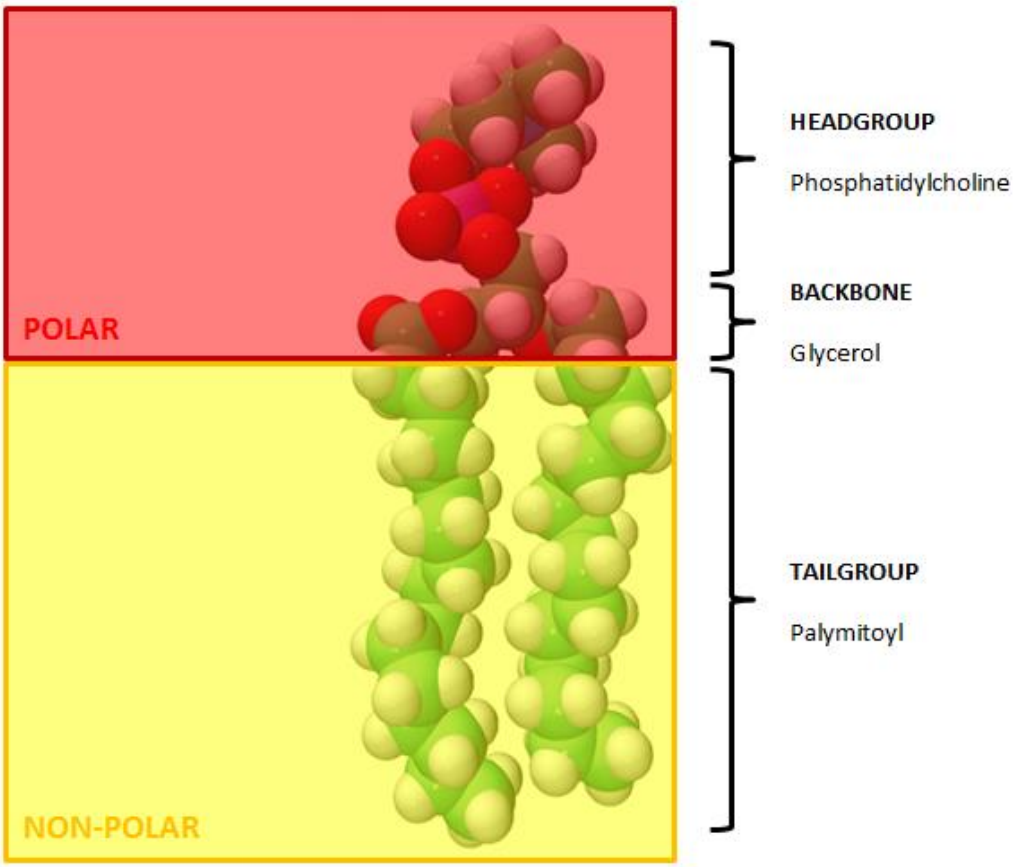

Figure 1.1: Space-filling diagram of DPPC, a phospholipid with two palmitoyl (16:0) fatty acid tailgroups, with carbon atoms are shown as green spheres; hydrogen as white spheres; oxygen as red spheres; phosphor as purple spheres and nitrogen as blue spheres. The red overlay depicts the polar headgroup region of the amphipathic lipid structure, containing the oxygen, nitrogen and phosphor atoms of the glycerol backbone and Phosphatidylcholine headgroup. The yellow overlay covers the non-polar tailgroup region, containing the hydrophobic acyl chains.

Aggregation is a characteristic phenomenon of amphipathic materials in polar solvents;[36] the high energy cost of exposing the hydrophobic fatty acid chains to the surrounding aqueous solution, is the primary force driving the formation of supramolecular structures.[31]

1.8.2. Lipid topology and the geometrical membrane model

The role of lipid topography in the organisation of biological membranes has been the subject of recent research activity, as with many biological process, lipid *structure* and lipid *function* are interdependent. Lipids possess varying topographies, dependent on their headgroup and tailgroup components, that can be described as conical, inverse-conical and cylindrical (figure 1.2).

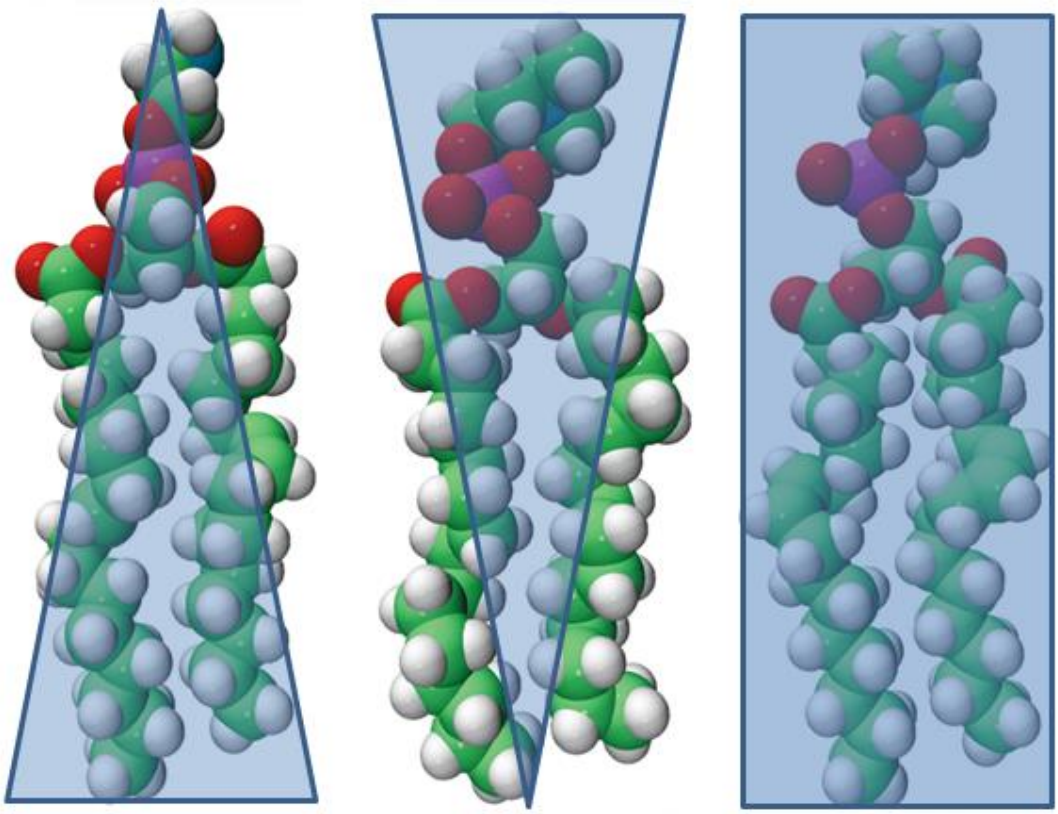

Figure 1.2: Space-filling models of the phospholipids DOPE (left), DPPC (middle) and DOPC (right), with the blue overlay depicting their topographic character. Carbon atoms are shown in green; hydrogen in white; oxygen in red; phosphor in purple and nitrogen in blue. DOPE possesses two oleic fatty acid chains, with a 9z unsaturated bond adding a kink to the 18C chain, increasing the hydrophobic volume. Together with its small PE headgroup, this lends the lipid a conical geometry, and a packing parameter > 1. DPPC has a larger PC headgroup coupled with lower volume palmitoyl fatty acid chains, which are 16C long and saturated, giving the lipid inverted cone geometry and a packing parameter < 1. DOPC possesses cylindrical geometry, due to its large headgroup, and high volume fatty acid chains (18:1, 9z), and a packing parameter ~ 1.

The form of the supramolecular structure adopted by lipids in aqueous solution is controlled by their topography. A useful metric for assessing the shape of a lipid molecule within a membrane is the packing parameter (S), introduced by Israelachvili and colleagues,[37] which is defined as the ratio between the lipid headgroup area to the lipid tailgroup volume (equation 1).

$$S = \frac{V}{al}$$

Where V = volume of the hydrocarbon tailgroup; a = headgroup area and l = length of the hydrocarbon chain. The packing parameter describes the ratio of the areas occupied, in the plane of the water-lipid interface, by the headgroup and tailgroup components of the lipid. Lipids with small headgroup areas and large fatty acid chains possess conical geometry, especially if the chains contain unsaturated bonds, increasing the volume occupied by the hydrocarbons. Inverse-conical geometry lipids are characterised by having larger headgroup than tailgroups areas, i.e. a large headgroup like Phosphatidylcholine (PC) and/or low volume short and fully saturated fatty acids. If the areas occupied by the head and tailgroups are roughly equal, the lipid topography can be described as cylindrical. The consideration of membrane lipids as geometrical shapes interacting within a liquid-crystalline lattice, has been the major impact of Helfrichs seminal 1976 paper,[38] and will see much application within this thesis.

Lipids in aqueous solution will form supramolecular packing arrangements, to minimise unfavourable interactions between their hydrophobic tailgroups, and the surrounding water molecules. Each packing conformation represents an energy minimum for that lipid,[39] and the particular conformation chosen can be predicted based on the lipids packing parameter. Lipids with large headgroups and small hydrocarbon volumes, will possess packing parameters < ½, and prefer to form structures like micelles and hexagonal phase (figure 1.3).

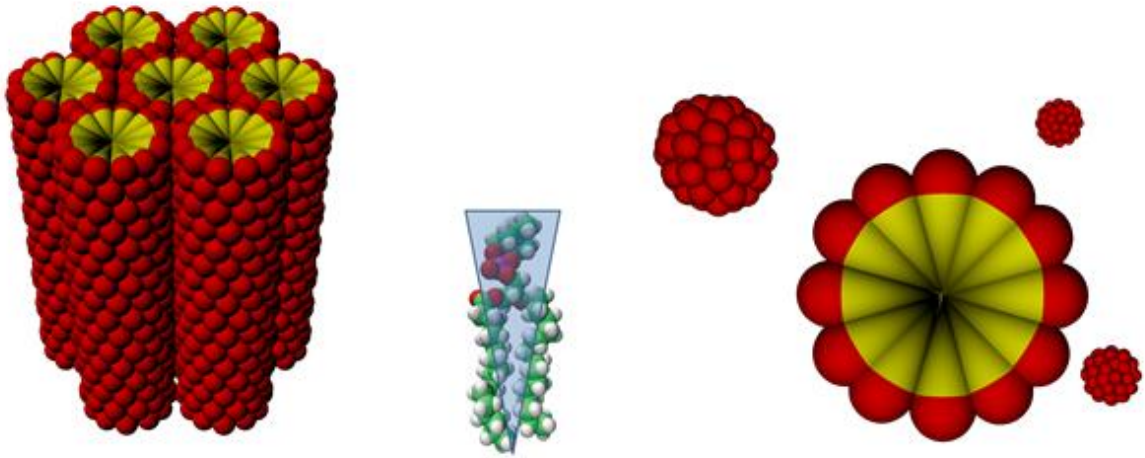

Figure 1.3: Lipid supramolecular structures self-assembled by inverted conical topography lipids when in aqueous solution, with the lipid headgroups depicted in red and the lipid tailgroups shown in yellow. (Right) hexagonal phase consists of compact tubular structures, with the polar headgroups facing outward, assembled to protect the non-polar acyl chain tailgroups from unfavourable interactions with the surrounding water. Typical packing parameter values for lipids which prefer to arrange in this manner are between 1/3 and ½. The tubular structures will often aggregate, resulting in a hexagonal array, from which the phase takes its name. (Left) micellular structures are another possibility for inverted conical lipids, with a packing parameters < 1/3, where the lipids arrange themselves into spherical structures, again to protect their hydrophobic cores from interactions with the surrounding water.

Lipids with small headgroups and large hydrocarbon volumes will form inverse-hexagonal phase, typically constructed by lipids with packing parameters > 1 (figure 1.4). Lastly, lipids with packing parameters between ½ and 1 have roughly cylindrical geometry, caused by similarity in their headgroup and tailgroup areas, and will prefer to adopt bilayer structures (figure 1.5).

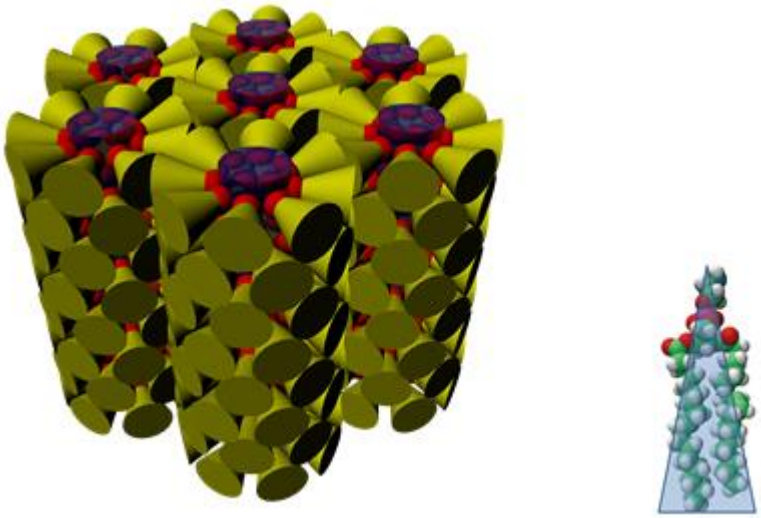

Figure 1.4: Lipids with packing parameters > 1 can form inverse hexagonal phase, where the lipids are arranged in a cylindrical structure around a water column, with the polar headgroups facing the water. The tubes pack together into a hexagonal array, protecting the non-polar acyl chains from interactions with water.

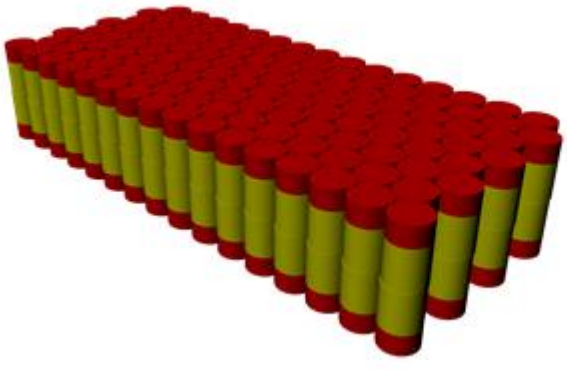

Figure 1.5: Lipids with packing parameters between ½ and 1 will prefer to form bilayer structures in aqueous solution. The similar lipid headgroup and tailgroup areas ensuring that the flat structure of the bilayer represents the lowest energy conformation for that particular lipid.

Lipids can be separated into two broad classes based on topographical character; bilayer lipids which prefer to form flat bilayers, and non-bilayer lipids which form more highly curved structures. Moreover, in heterogeneous lipid systems, the packing parameter is additive;[40] i.e. the average bulk structure will be based on the average packing parameter of the lipid mixture. A collection of lipids with an average packing parameter of < ½ forms supramolecular structures with associated positive curvature, those with packing parameters around 1 form flat non-curved structures, and those with packing parameters > 1 adopt negatively-curved structures. Other phases than those pictured are possible, like saddle and cubic phases, with more complex geometrical arrangements of lipids and associated curvatures. Note that due to packing parameter additivity, bilayer structures can be formed which contain non-bilayer lipids, and indeed completely from non-bilayer lipids.[40] Aggregation of non-bilayer lipids has been connected to cellular processes, including cell fusion;[41] cell budding and fission;[30][42][43] membrane protein function[32][33] and protein translocation across membranes.[44][45]

1.8.3. The lipid bilayer

Prokaryotic and eukaryotic cellular membranes are bilayer structures, and the target of LCAMPs. The physical structure of a lipid bilayer consists of two opposing lipid monolayer (figure 1.6), with the hydrophobic acyl chains sequestered together from thermodynamically unfavourable interactions with the surrounding water molecules.[30]

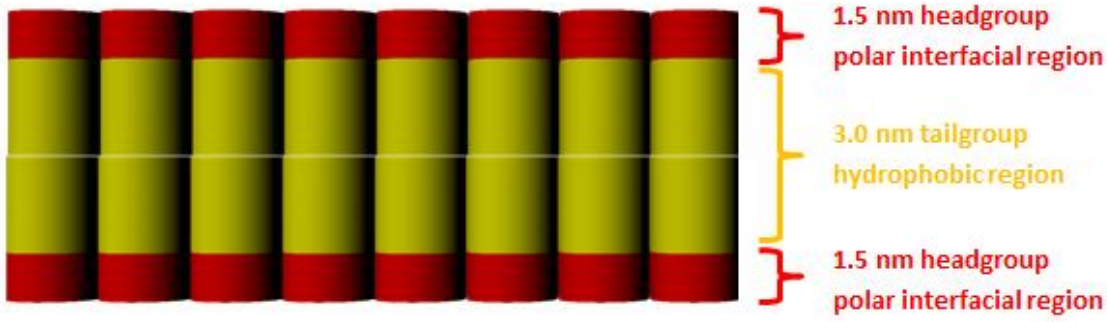

Figure 1.6: Side-view of a bilayer using Helfrichs geometrical packing model, constructed from cylindrical topography lipids, with lipid headgroups depicted in red and tailgroups shown in yellow. The acyl chains of the two opposing monolayer form a non-polar hydrocarbon core to the bilayer, about 3 nm thick, while the polar headgroups and associated water molecules form a 1 nm thick interfacial layer, between the hydrophobic bilayer core and the surrounding water molecules.

The two layers of interacting acyl chains form the membranes hydrocarbon core, about 3 nm thick, surrounded by the headgroup interfacial region, protecting the core form the water. The interfacial region is ~ 1.5 nm thick, when the accompanying hydrating water molecules are included, meaning the thickness of a fully hydrated lipid bilayer is comprised of approximately equal parts hydrophobic and hydrophilic components. The bilayer is strengthened by hydrogen and electrostatic bonds between the lipid headgroups in the interfacial region, and Van der Waals interactions between the lipid fatty acids chains in the membranes core.

1.8.4. Lipid domains and phases

The forces and interactions experienced by lipids within a membrane structure are not equal, different lipid components show selective interaction preferences with each other, leading to a non-uniform structure at the molecular level.[46] Lipid domains never reach equilibrium, they are strictly dynamic structures; Almeida and co-workers[46] calculated that a nanodomain of 150 lipid molecules would dissipate in less than 10 µs, given the fast lateral diffusion characteristic of fluid-phase lipid membranes. Three lamellar lipid phases are worth further consideration here; the liquid-disordered (L_d) phase; the liquid-ordered (L_o) phase and the solid gel-phase. The L_d phase is the most biological relevant, with many membrane proteins in the fluid phase.[30][47] The fluid phase is characterised by faster lateral diffusion, and low order within the acyl chain region,[30][33] and is composed primarily of lipids featuring unsaturated fatty acids (figure 1.7).

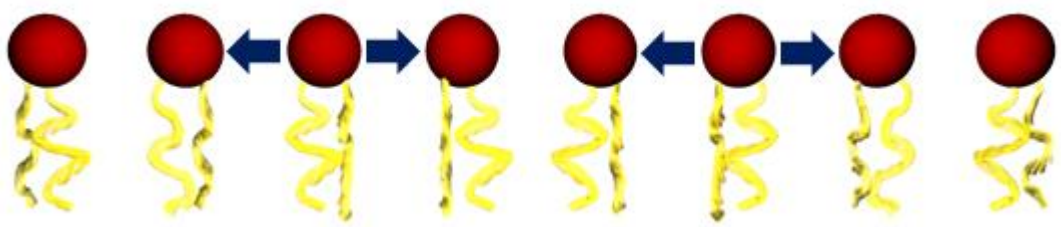

Figure 1.7: Diagram of a lipid membrane in the liquid-disordered phase, with lipid headgroups depicted in red, and fatty acid tailgroups in yellow. Large blue arrows indicate the fast lateral diffusion that is characteristic of fluid lipid membranes.

In contrast the gel-phase contains lipids with acyl chain compositions dominated by long, saturated fatty acids (figure 1.8). Gel-phase lipids demonstrate a slower rate of lateral diffusion than in the fluid-phase, and the order parameter of the acyl chains is markedly higher.[30]

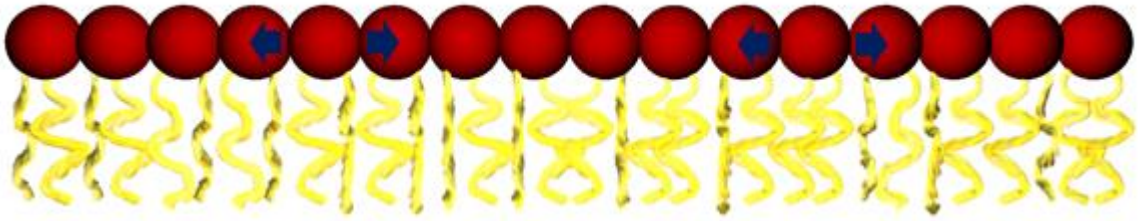

Figure 1.8: Diagram of a lipid membrane in the gel phase, with lipid headgroups depicted in red and fatty acid tailgroups in yellow. Small blue arrows indicate the slower lateral diffusion characteristic of gel lipid membranes. The closer packing of the lipids is a result of the increased interactions between the acyl chains, generating order in the hydrocarbon core.

L_o phase possesses characteristics of both fluid and gel-phases, and is uniquely found within eukaryotic cells.[48] L_o phases are composed of bilayer lipids and cholesterol, demonstrating the fast lateral diffusion of an L_d membrane, together with the ordered acyl chains of the gel-phase (figure 1.9).

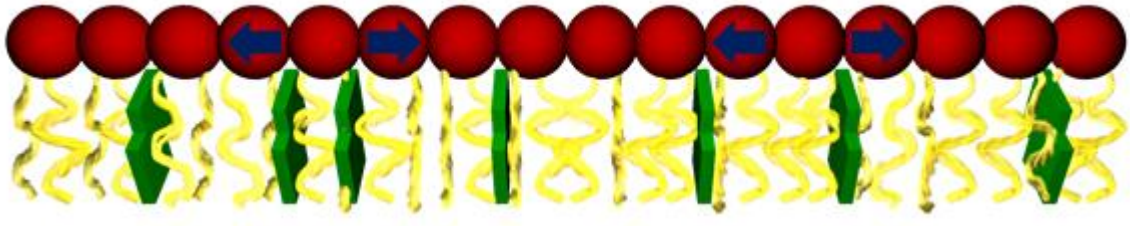

Figure 1.9: Diagram of a lipid membrane in the liquid-ordered phase, with polar lipid headgroups depicted in red, the non-polar fatty acid tailgroups in yellow and cholesterol molecules in green. The cholesterol intercalates with the lipid acyl chains, where it both condenses and fluidises the hydrocarbon region. Large blue arrows indicate the faster lateral diffusion encountered in liquid-ordered membranes. The closer packing of the lipids is a result of the increased interactions between the acyl chains and cholesterol, generating order in the hydrocarbon core.

It is worth noting that the leaflet phase behaviours of a bilayer are coupled together, with phase formation in one leaflet reported to induce phase formation of the opposite leaflet.[30] Artificial lipid systems mimicking eukaryotic plasma membranes display well understood phase behaviours, with large micron-scale L_o and L_d phase coexistence; however *in-vivo* behaviour is more complex. The *In-vivo* evidence of phase coexistence suggests much smaller lipidic domains (< 300 nm), which cannot be visualised by conventional fluorescent microscopy, as domain diameter smaller than wavelength of excitation light.[30] It is speculated that large-scale phase discrimination does not occur *in-vivo*, due to the confinement of lipid lateral diffusion by abundant membrane proteins. Membrane properties can change abruptly at phase boundaries (figure 1.10), showing large variations in headgroup charge and composition; acyl chain saturation and length; overall membrane thickness and membrane protein composition between different membrane phases.[33]

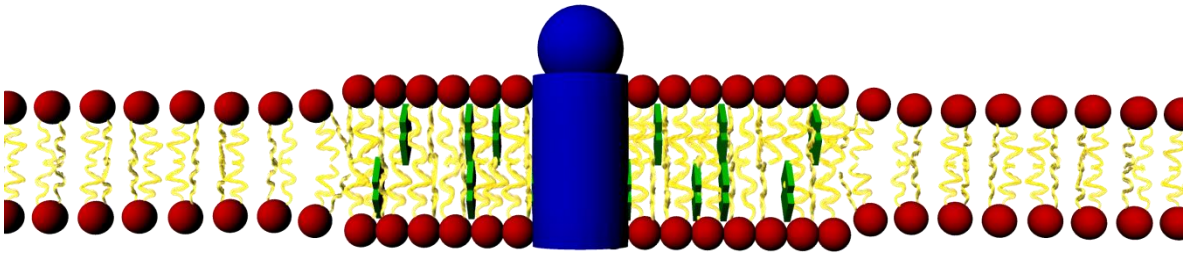

Figure 1.10: Diagram showing a liquid-ordered raft contained within a liquid-disordered membrane, with lipid headgroups depicted in red, tailgroups in yellow, cholesterol in green and membrane proteins in blue. The condensing effect of cholesterol contained within the liquid-ordered raft increases the hydrophobic core thickness, resulting in an increase in membrane thickness compared to the surrounding fluid phase. Many membrane proteins show a distinct phase preference, and are often found contained within lipid rafts with similar compositions.

The rate of lipid transfer between membrane leaflets, or lipid "flip-flop" varies significantly depending on the lipid charge and topography, resulting in a range of membrane half-lives from hours or even days for lipids with large and/or charged headgroups like PG, to seconds for sterols,[30][33] however the rate of lateral diffusion is always several orders of magnitude faster.

1.8.5. Prokaryotic versus eukaryotic membranes

The plasma membranes of prokaryotes and eukaryotes exhibit significant variation in physiochemical properties like headgroup composition and charge, as well as differences in fatty acid composition. It is these fundamental differences that render bacterial membranes an attractive target for novel antimicrobial therapeutics.

1.8.5.1. Eukaryotic membranes

The largest class of eukaryotic lipids is the glycerophospholipid family, comprising of PC/PE/PS/PI and PA species, with PC typically representing about 50% of the total lipid content of a eukaryotic membrane.[30][33] Phosphatidylcholine lipids feature large zwitterionic headgroups, and typically contain one *cis*-unsaturated fatty acid, these properties result in the majority of PCs being in fluid phase at room temperature. The large headgroup results in packing parameters around 1, and as a result most PC lipids are bilayer forming in aqueous solution. Spingolipids are the next most represented class of eukaryotic membrane lipids,[30] split between the sphingomyelin and glycosphingolipids classes, both typically containing saturated or *trans*-unsaturated acyl chains. The fatty acid composition of sphingomyelin and glycosphingolipids result in taller, narrower inverted conical topographies, and many lipids of these classes are gel-phase at room temperature, and can be fluidised by sterols to form liquid-ordered domains. Phosphatidylserine is the main anionic lipid component of eukaryotic membranes, and is sequestered within in the inner membrane leaflet,[49] resulting in a large charge asymmetry across the membrane leaflets of eukaryotic cells. Several other lipid classes are asymmetrically distributed across the membrane leaflets, including PE and PI, which are also largely sequestered to the inner membrane leaflets. As a result of this preferential lipid segregation between leaflets most eukaryotic membranes display considerable lipid composition asymmetry, e.g. human erythrocytes contain SM and PC in the outer leaflet, and virtually no PS, while the inner leaflet contains PS, PE and PI.[50] The interleaflet lipid gradients are maintained by a network of ATP-dependent lipid transporters, called flippases, floppases and scramblases. Flippases transport lipids from the outer extracellular leaflet into the cytoplasmic leaflet, whereas floppases perform the opposite function, transporting lipids from the inner to the outer membrane leaflet. Scramblases are directionally non-specific, capable of redistributing lipids across either membrane leaflet.[50] In summary, eukaryotic membrane leaflets are highly asymmetric, with PS, PE and PE sequestered to the inner leaflet. This renders the outer membrane composed mainly of lipids like PC and SM, i.e. electrically neutral and with packing parameters typically between ½ and 1, i.e. bilayer lipids. Extracts of eukaryotic cellular membranes typically display large spontaneous curvatures, for example DOPC displays radii of curvature of -11 nm, and DPPC has radii of curvature of +14.7 nm.[51] Of all the component lipids of eukaryotic membranes, only cholesterol displays considerable negative curvature, with radii of curvature of 2 nm.[51]

1.8.5.2. Prokaryotic membranes

The membranes of prokaryotic cells display several contrasting features to eukaryotic cell membranes. The primary difference is the overall negative charge of the outer membrane leaflet of prokaryotes, due to the inclusion of anionic lipids like CL and PG.[52][53] Bacterial membranes also display more subtle topographical differences in their outer leaflets, namely the inclusion of large amounts of

high packing parameter lipids, i.e. lipids with small headgroups and/or large hydrophobic volumes like PE. These differences in membrane lipid topography lead to prokaryotic membranes showing intrinsic curvatures much greater than eukaryotic membranes, for example Osterberg and colleagues[54] report that total lipid extracts from *Acholeplasma laidlawii* form inverted hexagonal phases with diameters between 5.8 – 7.5 nm, i.e. spontaneous radii of curvature of ~-3.3 nm on average. Moreover, the bacteria maintain this curvature profile when grown in conditions containing either palmitic or oleic acid, despite the large differences in hydrophobic volume induced by inclusion of these fatty acids into the membrane, via modulation of the membrane headgroup composition. Kollmitzer and co-workers[51] present the typical radii of curvatures for many of the lipids found prokaryotic membranes, they reported that DOPE membranes display a radii of curvature of -2.5 nm, and POPE -3.2 nm. Literature values for the radius of curvature of inverted hexagonal phase structures show good agreement with these values, for example the -3.5 nm radius of curvature for POPE membranes in Siegel and Epand.[54]

Although comparison of curvature values between papers is complicated by the dependence of the value on the precise experimental conditions, like salt content, temperature, variable inclusion of short chain hydrocarbons and pH,[52][54] it is never-the-less clear that bacteria maintain the curvature of their membranes within a narrow band, keeping their membrane much close to the lamellar to non-lamellar phase boundaries than mammalian cells. The large amount of cellular resources bacteria devote to plasma membrane topographical homeostasis has been suggested to indicate that membrane curvature is a functionally important membrane parameter carefully regulated by the organism.[55] To summarise membrane composition differences between prokaryotic and eukaryotic membranes, it is necessary to place emphasis on two factors; first, that the outer leaflet of bacterial cells contains a high net amount of anionic lipids, while mammalian cells have zwitterionic outer leaflets; second, that the topography of bacterial membranes high negative curvature, while the curvature of mammalian membranes is neutral.

1.9. Linear cationic antimicrobial peptides (LCAMPs)

The urgent need for novel antimicrobials has driven a resurgence of interest in naturally occurring antibiotic molecules, with LCAMPs appearing among the most promising for future development as antibacterial chemotherapies. LCAMPs are part of the innate immune system, responsible for first-line quick response to bacterial invasion of the host.[56][57] Almost ubiquitously expressed within nature, LCAMPs are found in taxonomically diverse groups such as insects;[58][59] amphibians[60] and mammals.[61] Such widespread expression suggests that LCAMPs are evolutionarily ancient components of host defence against invading pathogens, and have remained remarkably effective as the front line host defence against invading pathogens.[18] The LCAMP family is remarkably diverse, with over 1000 members listed to date.[63]

1.9.1. LCAMP activity

LCAMPs generally exhibit broadband antimicrobial activity,[56][63] with many peptides displaying secondary viricidal and tumouricidal activities.[63] They are highly potent, with most peptides bactericidal at low micromolar concentrations,[64][65] with some operating at even lower levels.[18] LCAMP potency compares well to conventional antibiotics; to demonstrate this we can compare the activities of two widely studied LCAMPs, magainin and melittin, to two widely prescribed antibiotics, amoxicillin and azithromycin, against the bacteria *S.pneumoniae*. Amoxicillin is an orally taken beta-lactam antibiotic, and displays MICs against multiple strains of *S.pneumoniae* of between 43.8 nM and 15.3 μM.[66] Azithromycin is a macrolide antibiotic, possessing MICs against *S.pneumoniae* of between 80.1 nM and 341.8 μM.[67] The LCAMP magainin II amide returns MICs against a similar variety of *S.pneumoniae* strains of 1.6 μM to 51.6 μM, while melittin returned a MIC of 2.2 μM.[68] Some LCAMPs are highly selective between prokaryotic and eukaryotic cells, e.g. magainin,[60] and the peptides as a class show remarkable immunities to the development of acquired bacterial drug-resistance. The combination of high potency, selectivity and immunity from bacterial drug-resistance render LCAMPs into promising candidates for development as antibiotics.[58][65]

1.9.2. Physiochemical properties

Unusually for a protein family, it is shared physiochemical and structural properties, rather than sequence homology, which characterises the LCAMP protein superfamily.[64] The primary marker for an LCAMP is a pronounced amphipathic helix when bound to a lipid membrane, with the polar and charged amino acid residues distributed along one face of the helix, and the opposite face composed of non-polar residues.[58][62] The amphipathic helix facilitates the interaction of the helical peptide with other amphipathic structures, like phospholipid membranes, and indeed many LCAMPs only adopt amphipathic helical conformation upon binding to lipid membranes or when aggregated together.[62][63] Another feature of LCAMP amino acid sequence is the high proportion of the cationic residues lysine, arginine and histidine, giving the peptides their characteristic positive charge.

1.9.3. Biological target of LCAMPS

There are many excellent reviews in the literature of the antimicrobial activity exerted by LCAMPs,[57][58] with the consensus that their mode of action involves membrane disruption and pore formation within the cellular membranes of bacteria, although some evidence of intracellular targets exists. Strong evidence for this comes from the observation that LCAMPs with inverted sequences, or composed from all D-isomers of amino acids, possess identical antibiotic and pore-forming properties to their parent peptides.[57][62] This indicates that the antimicrobial effect of LCAMPS is not exerted through

interactions with specific chiral proteins targets, and instead LCAMPs are widely reported to target the cellular membrane itself, disrupting membrane integrity. This results to the dissipation of transmembrane ionic gradients, increased water flow across the membrane and leakage of intracellular contents.[58][62] Bacterial membranes are underutilised targets for antibiotic therapy, with significant differences existing between prokaryotic and eukaryotic membranes.[64]

1.9.4. Mechanisms of action of LCAMPs

The LCAMP family has been widely studied, but controversy still exists over their exact mechanism of action. Several general models have been proposed to explain their membrane disruption and antimicrobial activity, with perhaps the most widely accepted being the Shai-Matsuzaki-Huang (SMH) model.[64] It has been suggested that no single model is capable of adequately describing the activity of this diverse peptide family,[18][63] and that LCAMPs may act through a variety of different mechanisms.[69][70] Strong evidence for multiple leakage mechanisms is the contrast in the size-dependence of LCAMP-induced leakage from model membrane systems, with studies reporting both size-dependent leakage[69] and size-independent leakage.[71]

1.9.4.1. Shai-Matsuzaki-Huang model

The SMH model begins with the spontaneous binding of the peptide, from aqueous solution to the outer leaflet of the target membrane. The peptide initially inserts in helical form, parallel to the plane of the bilayer, often referred to as the S-state.[58][60][63] Peptide insertion is accompanied by membrane thinning,[62][63] reported to be non-uniform across the bilayer, but instead concentrated around the inserted peptide.[72] Once a threshold concentration of membrane-bound peptide has been achieved, the peptide helix begins to insert parallel to the membrane normal plane, referred to as the I-state. The critical concentration required to induce the change from S-state to the I-state, varies with both peptide and lipid compositions.[63] The change of orientation is associated with the initiation of membrane disruption,[63][73] although the exact mechanism of LCAMPs membrane permeation is unknown, with several models proposed in the literature, including pore formation, carpet and detergent-like mechanisms, depicted in figure 1.11.

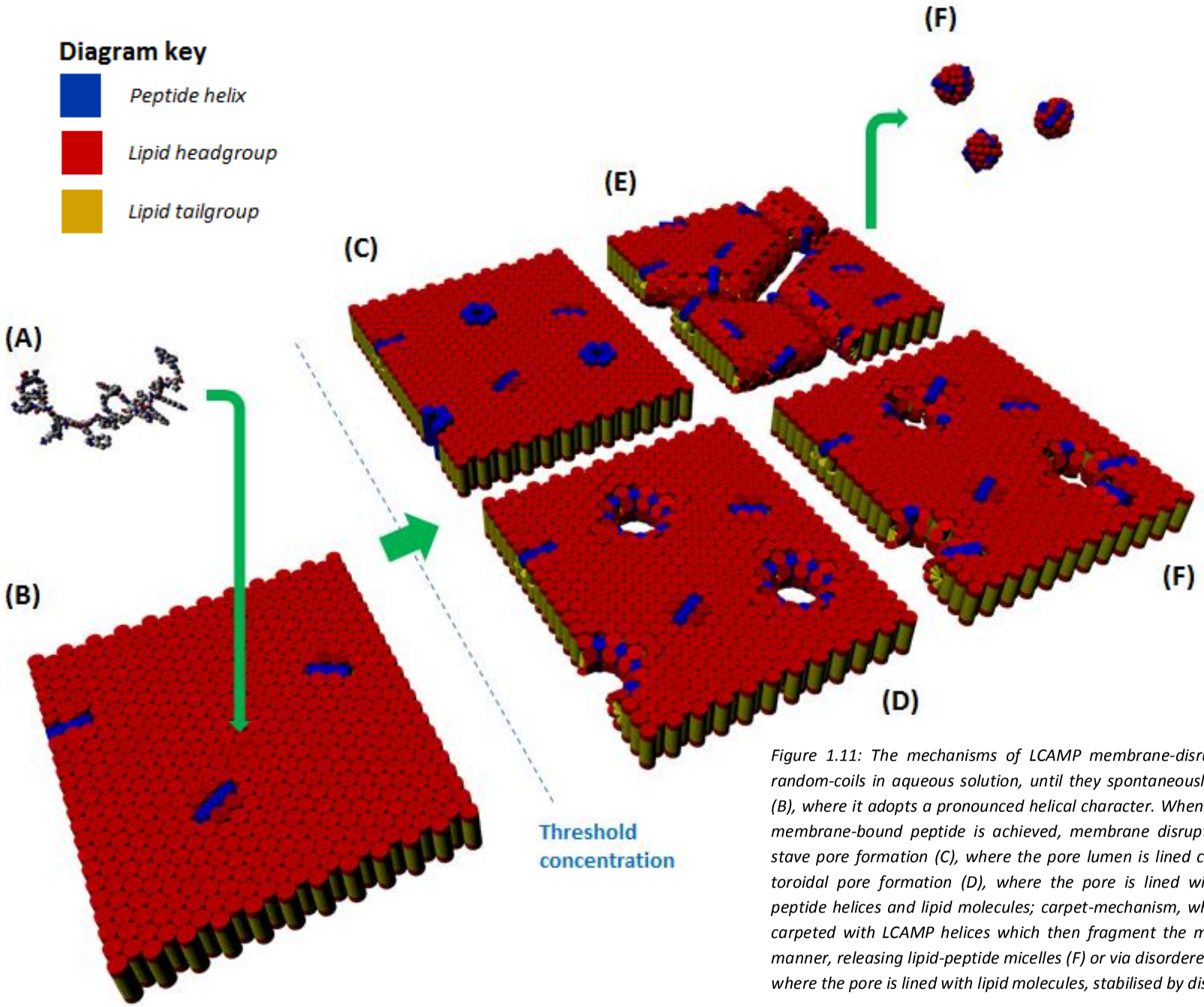

Figure 1.11: The mechanisms of LCAMP membrane-disruption. (A) LCAMPs exist as random-coils in aqueous solution, until they spontaneously binds to a lipid membrane (B), where it adopts a pronounced helical character. When a threshold concentration of membrane-bound peptide is achieved, membrane disruption occurs by either barrel-stave pore formation (C), where the pore lumen is lined completely by LCAMP helices; toroidal pore formation (D), where the pore is lined with both regularly-orientated peptide helices and lipid molecules; carpet-mechanism, where the membrane becomes carpeted with LCAMP helices which then fragment the membrane in a detergent-like manner, releasing lipid-peptide micelles (F) or via disordered toroidal pore formation (F), where the pore is lined with lipid molecules, stabilised by disordered LCAMP helices.

1.9.4.2. Barrel-stave pore mechanism

Barrel-stave transmembrane pores are composed of bundles of individual peptides, with a central pore lumen, with alamethicin a well-studied example of a peptide operating via the barrel-stave model.[62][63] Barrel-stave pores can contain varying amounts of peptide helices, which line the pore lumen with their polar and charged residues pointing inwards, forming a water filled central channel. Crucial to this model is the ability of membrane-bound peptide monomers to recognise and aggregate with each other, at low surface concentrations, as it is extremely energetically unfavourable for a single helix to transverse the membrane, due to unfavourable interactions between the polar/charged residues of the peptide, and the hydrophobic core of the bilayer.[57] The barrel-stave model for LCAMP action has become disfavoured for several reasons, primarily because the structural parameters of the pores do not match those expected for barrel-stave pores. Firstly, peptides forming barrel-stave pores form walls around 1.1 nm thick,[73] approximately the same diameter as an alamethicin helix, while LCAMP pores display channel walls with a diameter of ~2.0 nm, significantly wider than a peptide helix. Secondly, most LCAMP helices are not long enough to fully span the bilayer.[73] Other reasons why the barrel-stave mechanism is disfavoured include the repulsive Columbic energy, which would prohibit association of the cationic LCAMPs; alamethicin is zwitterionic, allowing the peptide helices to exist in close proximity. Fluorescent energy transfer studies also indicate that LCAMP monomers are not closely associated when in its membrane-bound S-state.[74] The size of the pores formed by LCAMPs also rule out the barrel-stave mechanism, being typically 3 – 4 nm in diameter, which if of barrel-stave construction would require > 10 peptide helices to fully line the pore lumen, and likely be unstable to shape deformation.[73]

1.9.4.3. Toroidal pore mechanism

Proposed by Matsuzaki and colleagues[75] the toroidal pore mechanism also proposes that peptide-induced membrane permeability is caused by transmembrane pore structures. Unlike the barrel-stave model however, the pore lumen is lined with both lipid and peptide molecules.[62][63][75] Idealised toroidal pore structures require considerable curvature induction of the membrane lipids, both negative curvature to form the pore lumen, and positive curvature to bend the two membrane leaflets in the bilayer normal plane, until the two leaflets merge[73] – the leaflet fold structure. When forming a toroidal pore, the polar/charged face of the amphipathic peptide helix interacts with the polar/charged headgroup region of the lipids, and the non-polar hydrophobic face interacts with the non-polar hydrophobic lipid acyl tailgroups.[63][73] The pores formed within the membrane have been reported as both transient and stable within the literature,[58][76] and cooperative inter-helix behaviour has been implicated in the formation of the pores.[76][77] Peptides thought to at least partially operate via toroidal pore mechanisms include magainin and melittin.[58][63][65] Several experimental observations support

toroidal pores as the mechanism of membrane permeability employed by LCAMPs, including the rapid flip-flop of both lipids and peptide induced by LCAMP pore formation;[75][76] visualisation of pores induced by structurally similar peptides, e.g. x-ray diffraction images for Bax toroidal pores;[78] the high variability of LCAMP electrophysiology results, unlike alamethicin-like barrel-stave pores, which produce consistent electrophysiology traces;[73] and pore ion selectivity, which can be modulated via the charge of the target membrane, suggesting a role for lipid molecules in the pore structure.[79] Sengupta and co-workers[80] suggest a less well defined toroidal pore structure, where the majority of the pore is lined with lipid molecules, and only one or two LCAMPs insert into the membrane for each pore, with the remainder binding to the pore edge. Figure 1.12 depicts a comparison between ordered and disordered toroidal pore structures.

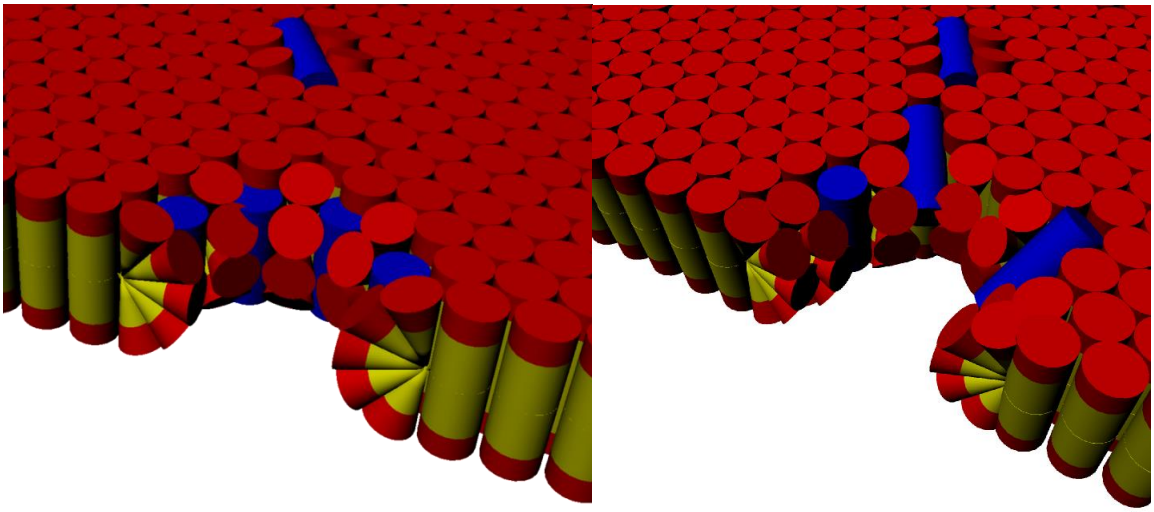

Figure 1.12: Comparison of ordered and disordered toroidal pore structures, with lipids represented by cylindrical and inverted-cone geometrical shapes. Lipid headgroups are depicted in red, and the lipid tailgroups in yellow, with peptide helices in blue. (Left) Diagram of an idealised toroidal pore, with regular arrangement of helices within the structure, and tight positive curvature within the leaflet fold structure. The pore lumen requires negative curvature generation, where lipid tailgroups occupy more volume than headgroups. (Right) Diagram of a disordered toroidal pore, showing only one peptide helix that has fully inserted into the membrane, with the remainder of pore-associated peptides binding to the pore edge.

1.9.4.4. Carpet mechanism

Peptides that disrupt lipid membranes via the carpet mechanism self-associate within a membrane, forming an extensive peptide "carpet" on the surface of the membrane leaflet.[57][62][63] The model is based upon intercalation of the LCAMP helix into the bilayer, followed by cooperative binding between the peptides. After a critical threshold of membrane-bound peptide is reached, membrane solubilisation occurs in a detergent-like manner, with the loss of mixed peptide-lipid micelles into the surrounding solution.[62][82] The presence of anionic lipids facilitates the self-association of the typically cationic peptides, by reducing the electrostatic repulsion present for peptides in close proximity,[62] and appears to facilitate leakage via carpet mechanism.[70] Contrary to the barrel-stave and toroidal pore

mechanisms, it is not necessary for the peptide helices to fully penetrate into the hydrophobic bilayer core, nor assemble with their hydrophilic residues facing each other.[57] Prior to membrane collapse, transient holes may appear in the membrane, enabling passage of low-molecular weight compounds across the membrane, which maybe toroidal in nature.[57] Factors counting against the carpet mechanism as the sole cause of LCAMP-induced membrane disruption include the low concentration of peptide required to generate membrane permeability, in both dye leakage and electrophysiology experiments.[58][79] The carpet mechanism requires a very dense accumulation of peptide,[65] and several papers link the disruption of membranes via the carpet mechanism to the intrinsic curvature of the target membrane.[62][63]

1.9.4.5. Intracellular target mechanism

Membrane disruption has long been implicated as the primary bactericidal mechanism of LCAMPs, but there are some indications that some LCAMPS may interact with intracellular targets. Brogden[63] reports LCAMPs can induce the activation of phospholipases and autolysins within cells.

1.9.5. Experimental investigation of LCAMP activity

As membrane disruption is the crucial bactericidal activity of LCAMPs, a popular experimental technique is to study the release of enclosed fluorescent molecules from within biological or artificial model membrane systems, through the LCAMP-induced pores.[69][76][82] Incorporation of differently sized fluorescent markers within the membrane systems can provide information on pore sizes.[69]

1.9.6. LCAMPs and drug-resistance

Compared to conventional antimicrobial therapies which encounter rapid development of drug-resistance in bacterial populations, LCAMPs are extraordinary evolutionary success stories. Unlike antibiotics like penicillin, which bacteria easily circumvent through the mechanisms of acquired drug-resistance, bacteria display a surprising lack of resistance to AMPs.[56][64] Repeated attempts to generate drug-resistance to pexiganan through exposure of > 3000 clinical isolates to subinhibitory levels of peptide were unsuccessful.[56] In contrast to conventional antibiotics, which attack specific high-affinity targets, LCAMPs have maintained effectiveness over millions of years by targeting a low-specificity target – the bacterial plasma membrane. Nature has ensured that bacteria cannot easily develop resistance by slight changes to their genome, which would rapidly occur due to their high mutation rate. Because the drug target is the bacterial membrane, to acquire resistance a bacteria must substantially redesign its membrane structure, incurring a fitness cost and requiring a more complex resistance

acquisition process, i.e. requiring a large raft of simultaneous mutations.[64] Some strains of bacteria have nevertheless displayed resistance to AMPs through a variety of mechanisms, demonstrated by the following two examples of the acquired resistance to LCAMPS. Strains of *S. aureus* achieved resistance by transporting D-alanine from the cytoplasm to the outer leaflet membrane surface, reducing the net negative charge by the esterification of the anionic phosphate groups of the teichoic acid polymers found in the outer membrane, with basic amino groups.[18] Bacteria can also acquire resistance through expression of proteolytic enzymes which target the LCAMPs,[64] a strain of *S.aureus* can cleave LL37 using a metalloprotease called aureolysin.[83] However resistance acquired via proteolytic degradation is an inefficient mechanism, as LCAMPs in general lack unique amino acid sequence motifs to serve as binding sites for selective proteolytic destruction. Despite these reported examples of resistance, bacteria as a whole remain remarkable susceptible to the action of these potentially therapeutically useful peptides, with the wide range of bacterial susceptibilities to LCAMP action remaining unexplained.[64] Peschel and Sahl[18] suggest that bacterial resistance to LCAMPs has coevolved over evolutionary timescales, leading to a delicate balance between host defence and pathogen susceptibility.

1.9.7. Comparison of two prototypical LCAMPs

Two of the most well studied LCAMPs are magainin and melittin, with several excellent reviews in the literature.[58][59][60] The next section will present brief reviews of the sources, physiochemical properties and key points for both these peptides.

1.9.7.1. Melittin

Melittin is the principle component (~50% of the dry weight) of the venom of the European honey bee *Apis mellifera*. It is comprised of 26 amino acid residues, which can assemble into an amphipathic helix. Its amino-terminal is primarily comprised of hydrophobic residues, and its carboxy-terminal contains a KRKR motif.[58] Its sequence is GIGAVLKVLTTGLPALISWIKRKRQQ-$CONH_2$, and possesses a +6 charge at physiological pH, composed of its amino-terminal, K7 and the KRKR motif at the carboxy-terminal. In aqueous solution it adopts a random-coil conformation, and is typically found as a monomer, although it is capable of forming an aqueous helical tetrameric aggregate at high peptide and salt concentrations. The terminals of melittin, i.e. GIG and KRKRQQ, are thought to not participate in the assembled helix in the membrane-bound peptide.[58] The P14 residue interrupts the assembled helix, as well as adding a kink to the assembled helix, with the angle between the two helical segments estimated at 140 – 160°. Melittin is non-selective between mammalian and bacterial cells, displaying high levels of haemolytic activity; melittin is capable of lysing erythrocytes at sub-micromolar concentrations. Melittin-induced leakage reported to be biphasic, with fast and slow components.[58][77] Degrado and

colleagues[77] report that 40% of haemoglobin release from erythrocytes occurs quickly, with a rapid decrease in cell number, with the remainder of the leakage occurring over longer timescales.

1.9.7.2 Magainin II

Magainin is a 23 residue LCAMP isolated from the skin of the African clawed frog *Xenopus laevis*, and has the sequence GIGLFKHSAKKFGKAFVGQIMNS. Like melittin, it carries a significant positive charge of +4 at physiological pH, forms membrane-bound helices, and is believed to exert its antimicrobial effects through membrane disruption. Unlike melittin, it displays a high level of selectivity between prokaryotic and eukaryotic cells.[75]

1.9.8. Structure-function relationships of LCAMPs

It is understood that an LCAMPs amphipathic structure and physiochemical properties exert the majority of its membrane disruptive effects,[57][58] This section examines the structure-function relationships of LCAMPs, to determine their effect on peptide activity, with a particular focus on factors effecting prokaryotic and eukaryotic selectivity.

1.9.8.1. Amphipathic helix charge distribution

Both the angle subtended by polar residues on the helical face, and positive charge distribution along the helix are important. Shai[57] reports that peptides with their positive charge concentrated at the terminal ends of the membrane-bound helix (e.g. melittin) are more lytic to eukaryotic cells, than peptides with a large positive charge distributed along the backbone (e.g. magainin).

1.9.8.2. Polar angle subtended on helical face

Membrane binding involves penetration of the hydrophobic face of the peptide into the hydrophobic core of the bilayer, while the hydrophilic face remains in contact with the polar interfacial/headgroup area, or with the aqueous solution.[65] It is therefore a reasonable assumption, that the depth of LCAMP membrane penetration will therefore depend on the arrangement of the hydrophobic/hydrophilic amino acid residues around the assembled peptide helix, i.e. the angle subtended by the polar and charged residues around the assembled helical face (figure 1.13).

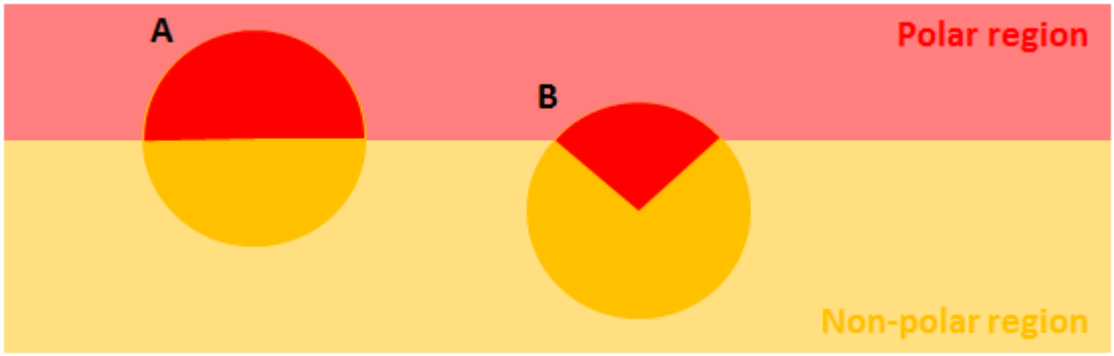

Figure 1.13: Diagram of the effect of the angle subtended by the polar/charged residues on the peptide helical face, on the membrane penetration of two LCAMPs. Polar areas of the bilayer and peptide are coloured red, and non-polar regions coloured in yellow. (A) A peptide with large polar angles can only insert a limited portion of its helical volume into the hydrophobic bilayer core. (B) Peptides with small polar angles can insert a greater volume of helix into the membrane core.

Peptides with narrow angles subtended by polar residues on helical face (i.e. melittin) penetrate deeper into bilayers,[58][84] and generate negative curvature strain within the membrane, by increasing the volume of the hydrocarbon bilayer core to a greater extent than the interfacial headgroup region. Conversely, peptides with wide subtended angles (i.e. magainin) lead to shallower penetration, and positive curvature induction.[65][84] The membrane disruption of LCAMPs is found to decrease with increasing polar angle, although the reasons are as yet unclear, although it can be explained by less peptide volume inserted within the lipid bilayer, as well as increased electrostatic repulsion between the peptides due to more charged residues.[65]

1.9.8.3. Key residues of magainin and melittin

Despite the lack of sequence homology between LCAMP family members, and the widely held position that it is the physiochemical structure of LCAMPs that are responsible for the bactericidal activity of the peptides, key residues have been identified for the membrane disruption induced by these LCAMPs. In this section we will dissect the key residues of the prototypical LCAMP melittin. The single tryptophan residue of melittin (W19) has been identified as a particularly crucial amino acid residue, although its actual position in the helix was found to be relatively unimportant.[58] Melittin substitution analogues with a single tryptophan residue displayed haemolytic activity in the order of potencies W17 > W19 = W11 > W9,[85] and variation of the W position effected the aggregation behaviour of melittin in solution. Tryptophan prefers residing in the complex interfacial environment of the membrane leaflet, as the π-electronic structure of its aromatic ring and flat rigid shape prevents

entry into hydrophobic bilayer core,[57][86] and phenylalanine may also show a preference for the interfacial headgroup area of the membrane leaflet.

Structure-function studies of melittin indicate that removal of P14 eliminates the helix-breaking kink in membrane-bound melittin, increasing the helical content of the LCAMP, and longer amphipathic helices are associated with higher haemolytic ability for many LCAMPs,[58] for example P14A substitution increases the haemolytic activity of melittin twofold. However P14A melittin displays less stable electrophysiology behaviour, indicating that channel formation may not dominate its haemolytic behaviour, unlike the native peptide.[87] This implies that selective peptides can be rendered into non-selective peptides by substituting the proline residue, and thus increasing the helical content.[65]

Alteration of the KRKR carboxy-terminal motif has been reported to decrease its haemolytic activity.[58] Several of the residues in the hydrophobic face of melittin have also been reported to modulate peptide activity, in particular the leucine residues. Leucine is an ideal residue for penetration into membrane bilayers, due to its low steric activity and high hydrophobicity.[88] Magainin, a shallow membrane penetrator, contains only 2 leucine and isoleucine residues, while melittin, a deep penetrator, contains seven of these amino acids. Substitution of the leucine residues in melittin (especially L9) leads to reduced haemolytic activity compared to native peptide,[85] and in parallel, replacement of W19 with leucine lowers haemolytic activity.[89] LCAMP activity appears to be controlled by a complex network of interdependent factors, and key to these residues modulation of LCAMP activity has not yet been elucidated within the literature.

1.9.8.4. Aggregation of melittin within membranes

No consensus exists within the literature about the aggregation state of melittin contained within membranes, with several conflicting papers published.[58] However, the SMH model proposes that melittin exists as a membrane-bound monomer at low peptides concentrations and low ionic strength, although kinetic studies strongly suggest that melittin aggregation within the membrane acts as a precursor of pore formation in at least some cases.[77] Takei and co-workers[90] demonstrate that formation of a melittin dimer is the rate-limiting step in the kinetics of pore formation, indicating that peptide aggregation is likely under specific conditions.

1.9.9. Factors underpinning prokaryotic and eukaryotic selectivity

Melittin and magainin possess similar pore-forming activity,[73][75][76] yet display very different selectivity between prokaryotic and eukaryotic cells. Degrado and co-workers[77] report rapid haemolysis induced by melittin at sub-micromolar concentrations, while magainin is almost inactive against

erythrocytes at considerably higher concentrations.[91] Both peptides possess a high net positive charge at physiological pH, and can be expected to interact more strongly with anionic membranes. Both magainin and melittin show a preference for bacterial membranes, whose outer membrane leaflet contains anionic lipids, in preference to mammalian membranes, which feature zwitterionic outer membrane leaflets.[57] In addition, the outer surface of gram-negative bacteria contains anionic lipopolysaccharide, which can increase bacterial resistance to LCAMPs, through binding and sequestering the cationic peptides, preventing their access to the bacterial membrane.[57] Selective LCAMPs, such as magainin II, tend to be accommodated within the interfacial region of the bilayer, while non-selective LCAMPs like melittin, tend to penetrate deeper into the hydrophobic core of the membrane leaflet.[57] Magainin with its increased polar angle, possesses less hydrophobic residues available for insertion into the hydrophobic membrane core. As a result magainin displays decreased affinity for zwitterionic membranes, and a greater preference for anionic bacterial membranes than melittin.[65] Unfortunately however, there appears to be no simple relationship between peptide charge and antimicrobial activity.[65] Cholesterol is found within eukaryotic membranes, yet is totally absent from bacterial membranes, and induces tighter lipid packing and increases the bilayer bending energy. It has been reported to reduces both binding and membrane penetration depth of LCAMPs, and it renders model membrane systems resistant to LCAMP-induced membrane disruption.[58][91] The presence of liquid-ordered cholesterol containing rafts seems to exert influence on membrane-disruption by LCAMPs, with HcHenry and colleagues[92] reporting that cholesterol exerts a substantial inhibitory effect in non-raft containing membranes, but the effect disappears in raft containing membrane systems.

1.9.10. Magainin and melittin pores

Magainin and melittin are generally accepted to be toroidal pore forming peptides.[58][73] Both peptides form pores of similar sizes; magainin forms pores with diameters of 3 to 5 nm, comprising of 4 to 7 magainin monomers and around 90 lipid molecules,[59][60] while melittin forms pores 2.5 to 5.0 nm in diameter.[69][73] The diameter of the pores induced by melittin, increases with increasing peptide concentration,[76] with Katsu and co-workers[93] reporting a pore radius of 1.3 nm at a peptide concentration of 0.2 µM, and a radius of 2.4 nm at a peptide concentration of 0.8 µM. Melittin pore lifetime was reported as <10 ms,[76] but again the lifetime appears to vary with peptide concentration and lipid composition.[58][76][94] There is no consensus within the literature of the leakage kinetics of LCAMP-induced pores from artificial model membranes, with two major mechanism noted; “all-or-none” leakage, where an individual vesicle will either display 100% leakage or remain unaffected; graded leakage, where vesicles will display partial leakage of contents.[71] However both magainin and melittin have been reported to operate via both mechanisms in the literature; magainin 2 reported to

operate via graded mechanism[95] and via all-or-none;[96][97] melittin reported as operating via all-or-none[98] and by graded release.[99]

1.9.11. LCAMP homology with other proteins

Helical amphipathicity is a characteristic of many membrane proteins, and putative transmembrane segments of membrane proteins.[58] For example, the two LCAMPs that are the primary focus of this thesis, magainin and melittin, possess structural or sequence homology with numerous proteins and peptides with significant current research interest. The proapoptotic proteins of the Bcl-2 family that control the release of apoptogenic factors from mitochondria share many structural features with LCAMPs, and are thought to operate via the formation of toroidal pores in the mitochondrial outer membrane.[100] The structural and mechanistic homology seen between LCAMPs and certain amyloid proteins are even more striking, and Last and Miranker[101] demonstrate that magainin 2 and the islet amyloid polypeptide possess incredible synergy at bacterial membrane disruption. Mixtures of the two peptides show activities two orders of magnitude greater than the simple sums of the activities of the individual peptides. The LCAMP family also shares sequence and structural homology with viral coat peptides linked to membrane disruption and fusion, for example the Nef1 – 25 HIV1 virulence factor,[102] and the tobacco mosaic virus coat protein.[58] Research into the membrane disruptive effects of LCAMPs has therefore a broader scope than just investigation of antimicrobial activity, and magainin and melittin are ideal for investigation of the mechanisms underpinning the action of all these peptides.

1.10. Lipid-peptide interactions

The heterogeneous lipid composition of cellular membranes leads to a complex set of interactions with proteins embedded within the membrane. These interactions create a free energy landscape for the lipid-peptide system, with local minima representing the interaction of proteins with lipids that lower the free energy of the system, and maxima that occur when interacting with lipids that raise the free energy.[103] It is reasonable to assume the formation of dynamic lipid-peptide rafts around membrane-bound proteins, based on these free energy considerations, and indeed Almeida and co-workers[46] suggest that the most probable cause of nanodomain rafts within the membrane is dynamic lipid aggregates centred around individual proteins. Jacobsen and colleagues[104] suggests three length scales for lipid domains, with the smallest being nanoclusters, consisting of sub 10 nm dynamic associations of lipids, or the immediate surroundings of membrane-bound proteins, that can have properties different from the larger scale structures, i.e. significant fluctuations of local energies, lipid densities and composition. Expanding the length scale, we next encounter nanodomains, 10 to 100 nm domains possessing slower dynamics and lower fluctuations than nanoclusters. Microdomains are the

largest in scale, representing clusters of lipids and lipid-peptides > 1 μm in scale, possessing the slowest dynamics and lowest fluctuations.

Membrane proteins show distinct phase preferences, with the fluid L_d phase generally preferred,[105] although gel-phase partitioning can occur if there is precise hydrophobic matching between the peptide and surrounding lipids.[30][33] Cholesterol binding domains confer upon the protein a preference for L_o phases,[48] although it is unclear as to whether the protein binds to existing cholesterol-rich lipid phases, or initiates the assembly of a L_o phase around itself. Formation of protein-induced dynamic lipid rafts is well understood within the literature, with many proteins requiring the presence of select lipids in order to function.[106][107] Membrane protein function is modulated by a wide variety of lipid bilayer properties,[31] including fluidity; lateral pressure; intrinsic curvature; lipid packing and hydrophobic mismatch. Lazaridis[108] provides computational support for the effects of membrane properties on protein conformation and orientation, and concludes that membrane physiochemical properties can drive protein aggregation within membranes.

1.10.1. Lipid clustering around membrane-bound LCAMPs

As noted above, membrane protein function has been reported to be influenced by the properties of the surrounding lipids, however when considering the interaction of lipids with LCAMPs, it is necessary to consider the reciprocal of this arrangement, that peptides embedded within the membrane can affect the membranes properties. Evidence for this assertion can be found both experimentally and computationally. Dibble and Feigenson[109] determined that helical peptides can induce the formation of non-bilayer phases at a concentration of a few mol%, and lipid domain formation can be initiated by interactions with membrane-bound peptides.[110] When inserted into a membrane, magainin disrupts the lipid packing for an estimated 5 nm radius around the membrane-bound LCAMP,[111][112] creating a membrane “hotspot” of increased free energy, i.e. a local maxima in the membranes energy landscape. Factors identified as controlling the clustering around membrane-bound LCAMP helices include electrostatics,[113][114] fatty acid unsaturation[58][115] and curvature.[60]

1.10.2. Lipid interactions and LCAMP activity

If the mechanism of action of LCAMPs depends on selective aggregation with membrane lipids, then the lipid composition of the target membrane should have pronounced effects on the membrane-disruptive effects of LCAMPs. This is found to be the case, with distinct differences in activity and selectivity induced by varying the membrane composition of the target membrane.[65] The electrostatic properties of the target membrane have been shown to exert a powerful effect on the activity of

LCAMPs.[57][58][65] The influence of lipid charge appears to go beyond the increased affinity of the cationic peptide for membranes containing anionic lipids; e.g. although the affinity of the LCAMP melittin for anionic lipid membranes is a hundred fold higher than for neutral lipid membranes,[116] > 98 % of M2a binds to zwitterionic POPC membranes within a short time frame.[65] This indicates that the increased rate of binding due to the electrostatic interaction between cationic peptide and anionic lipid, cannot solely account for the increased activity of the peptide within the anionic membranes, as the total amount of bound peptide is almost identical between the differently charged membrane systems.

The intrinsic curvature of the membrane lipids has also been shown to effect LCAMP activity,[58][84] for example, M2a is more active in POPG membranes than in POPS membranes.[60] Both lipids have the same charge and acyl chains, but the PS headgroup is considerably smaller than the PG headgroup, rendering POPG a cylindrical geometry lipid, and POPS a conical geometry lipid. Further evidence for the preference of magainin for positive curvature lipids comes from the NMR work of Strandberg and colleagues,[117] who found that M2a does not insert within membranes (i.e. does not achieve the I-state) containing negative curvature lipids. In contrast, within membranes containing positive curvature lipids, magainin quickly transitioned from S-state to I-state. The data unequivocally shows that the surface-associated helical form of magainin is stabilised by negative curvature lipids. Lipid unsaturation has been demonstrated to affect the penetration depth and secondary structure of LCAMPs. Raghuraman and Chattopadhyay[115] use REES and W19 fluorescent lifetime studies to demonstrate that a greater degree of lipid unsaturation leads to shallower penetration of LCAMP helices. The reduced helical content within membranes containing multiple unsaturated lipids, detected by OCD, indicates melittin has trouble penetrating the hydrophobic core as a helix, when the membrane contains multiply unsaturated acyl chains.

The presence of cholesterol has been found to generally reduce LCAMP activity in a concentration dependant manner.[118][119] Cholesterol is totally absent from bacterial membranes, but is present in high proportions within eukaryotic membranes.[119] The sterol has been reported to both reduce LCAMP binding to cholesterol containing membranes,[65][119] as well as reducing the penetration of melittin into the bilayer.[119] By using fluorescent quenching experiments, Raghuraman and Chattopadhyay[119] detected decreased penetration of W19 of melittin of ~0.8 nm in membranes containing 40 % cholesterol, compared to cholesterol-free membranes. The factors influencing lipid clustering around membrane-bound LCAP helices, are the same factors that exert an effect on the peptides activity, with this consilience forming a key link between lipid clustering and the mechanism of action of these peptides. Lateral segregation of lipids into dynamic lipid-peptide nanoclusters may therefore be of crucial importance to the mechanism of action of LCAMPs,[62][120] by forming lipid domains with significantly different local properties to the bulk membrane phase.

1.10.3. Lipid interactions inducing pore formation

One of the key points of this thesis is that lipid-LCAMP interactions can induce the formation of toroidal pores, through manipulation of local membrane properties, via selective aggregation with preferred lipids. Even in peptide-free membranes, it has been demonstrated that selective aggregation of lipids can induce the formation of pores,[121] with the inclusion of lipids with extreme inverse-conical geometry (DHPC) forming micron-scale pores within DPPC GUVs. Interestingly, above the phase transition temperature of DPPC, the GUVs display spherical non-porated forms. Upon decreasing the temperature below the phase transition of DPPC, the formation of solid-phase DPPC domains occurs, forming fluid domains enriched with the positive curvature DHPC. Large micron-scale pores would then form within the vesicle membrane. This can be explained using the Helfrich geometrical model of lipid interactions, to consider the changes in the vesicle membrane during the phase transition from homogeneous DHPC:DPPC fluid-phase to DPPC solid-phase and DPPC:DHPC fluid-phase coexistence. As the solid-phase domains form the surrounding bulk membrane becomes increasing enriched with the non-bilayer lipid DHPC, which forms spherical micelles in aqueous solution, with an associated increase in membrane packing frustration. The increase in the bilayer free energy eventually overcomes the energy required for the lipid remodelling into a pore, with the inverse-conical lipids forming a tightly curved cap at the pore rim. The phase transition and supramolecular reorganisation process is depicted in figure 1.14.

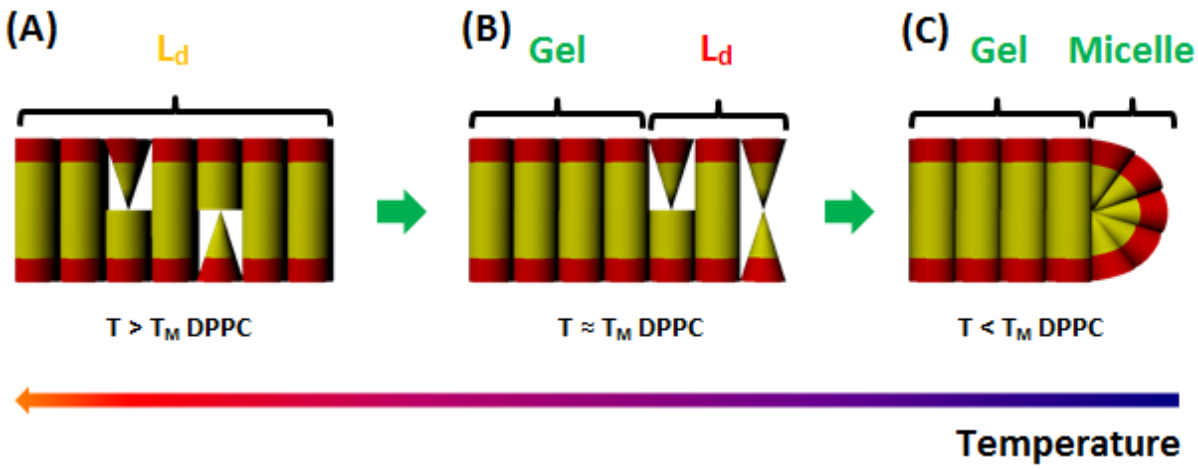

Figure 1.14: Diagram of a DPPC:DHPC membrane in the membrane normal plane, depicting the phase transition and supramolecular reorganisation reported within Sakuma and coworkers (2010), upon the cooling of a DPPC:DHPC membrane, from above the phase transition temperature (T_M) of DPPC (40.1 °C) to below the phase transition temperature. The bilayer lipid DPPC is shown as a cylinder, and micelle-preferring DHPC lipids as inverse cones. (A) Above the T_M the DPPC:DHPC system exists as a bilayer, with the DHPC dispersed throughout the bulk DPPC lipids, creating a homogeneous liquid-disordered (L_d) phase. The presence of non-bilayer lipids in the bulk phase induces packing frustration, raising the energy of the bilayer compared to pure DPPC, indicated by the amber shading of the L_d label. (B) As temperature approaches T_M the DPPC begins to coalesce into a gel-phase, excluding the DHPC and increasing its concentration within the surrounding L_d-phase. This creates a lower energy DPPC-rich phase, indicated by the green shading of the gel label, and a higher energy DHPC-rich phase, indicated by the red shading to the L_d label. (C) Below T_M the DPPC-rich domains grow and the surrounding L_d-phase continues to increase in energy, until supramolecular organisation of the L_d phase bilayer is less energetically favourable than reorganisation of the DHPC-rich phase, into a leaflet fold structure capping the edges of a pore. This results in the DPPC lipids occupying their preferred bilayer organisation, and the DHPC lipids existing as micelle-like structures, reducing internal packing frustration and minimising the free energy of the system.

This conformation minimises the free energy of the system, with the pore rim minimising the DHPC free energy, and the surrounding DPPC phase achieving a packing parameter ~ 1. Sakuma and co-workers[121] provides an elegant example of the lipid-lipid interactions of large microdomains inducing large (~5 µm) pore formation, while lipid-LCAMP interactions work at the nanocluster levels, able to exploit the higher fluctuations in the free energy landscape at the nanoscale.

2. Materials and methods

2.1. Design of microfluidic device

Several considerations were taken into account during the design process, including generating a low back pressure microfluidic device, and the requirement for high throughput capability. The design chosen is presented in figure 2.1, and allows for integrated on-chip GUV production; washing; trapping and precise control over vesicle exposure to LCAMPs.[122]

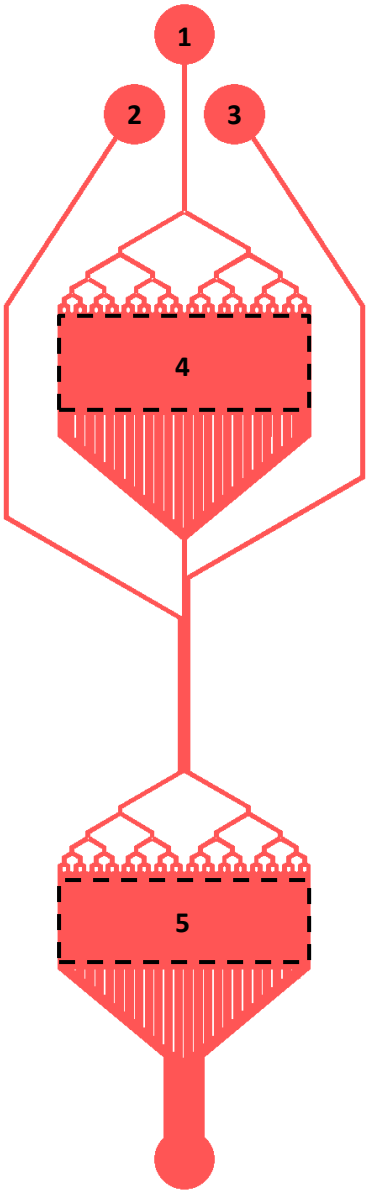

Figure 2.1: Schematic for the microfluidic device, for the high-throughput manufacture, trapping and analysis of artificial biomimetic GUVs. Labelled as follows: (1) Microfluidic channel for moving the GUVs into the microfabricated trap arrays; (2) Channel for the introduction of the LCAMP solution to the entrapped vesicles; (3) Washing channel to remove peptide and extraneous dye from the entrapped GUVs; (4) Electroformation chamber for the on-chip production of biomimetic GUVs; (5) Chamber containing the high density microtrap array, for the entrapment of GUVs, using microfluidic flow to pin vesicles within PDMS pillar traps.

The device features a chamber for the electroformation of GUVs, then utilises the precise control over fluid flow offered by microfluidics to manoeuver the vesicles into nanofabricated PDMS traps. The traps are manufactured in dense arrays, allowing multiple trapped GUVs to be analysed within one experiment, increasing the throughput of the device. The design incorporates two separate channels for the introduction of solutions to the entrapped vesicles, allowing washing steps to be easily integrated

into the experimental protocol, and for LCAMPs to be introduced. Microfabricated pillars within the microfluidic channels, as well as the trap geometry, act as size filters allowing only GUVs with diameters between 10 and 40 μm to be trapped.

2.2. Device microfabrication

A PDMS device was manufactured by constructing a master mould of SU8 on a silicon wafer, using standard photolithography techniques as depicted in figure 2.2. The negative photoresist SU8-3050 (Microchem Corporation, USA) was applied onto a four inch silicon wafer (University Wafer, USA), using a spin-coater (Headway Research Inc., USA) at 3000 rpm, to produce a 50 μm layer. The wafer was then given a pre-exposure bake, at 95 °C for 15 minutes on a hot plate, to remove the solvent. After cooling back to room temperature, an MA6 mask aligner system (Suss Micro Tec AG, Germany) was used to pattern the device design onto the SU8 layer, using an exposure time of 42 seconds. The wafer was then post-baked for 1 minute on a hot plate, at a temperature of 65 °C, before being transferred to a 95 °C hotplate for a further 4 minutes. The wafer was allowed to cool to room temperature, before being developed in Microposit 2-methoxy-1-methylethyl acetate EC solvent (Shipley European Ltd., UK). The development was performed in an ultrasonicator, to ensure complete removal of SU8 photoresist from the fine details of the design. After the non-exposed photoresist was removed, the mould was carefully rinsed with isopropyl alcohol (Sigma-Aldrich, UK), and dried under a stream of nitrogen. The mould was then hard baked at 180 °C for two hours, to harden the resist, and increase the number of pulls from the finished master mould. To confirm depth of resist, a Dektak 6M depth profiler (Veeco Europe, Germany) was used to confirm the height of the channels as 50 μm. The wafer was then coated in silane (XXX), to ease the removal of the PDMS chips from the mould, by gas-phase deposition under vacuum for 45 minutes. The completed wafer was then mounted into a glass petri dish, and secured in position with 1 cm of Sylgard 184 PDMS (Dow Corning, Massachusetts, USA), mixed as a 5:1 ratio of monomer to curing agent. A section of PDMS was excised, leaving a margin of 1 cm around the device, and PDMS chips could then be cast from the finished mould, using a 10:1 ratio of monomer to curing agent to cast a chip with depth ~3 mm. A chip was visualised using a Hitachi S-4700 scanning electron microscope (Hitachi High-Tech Co., Japan), to check the microtrap array geometry (figure 2.3), and then further chips cast.

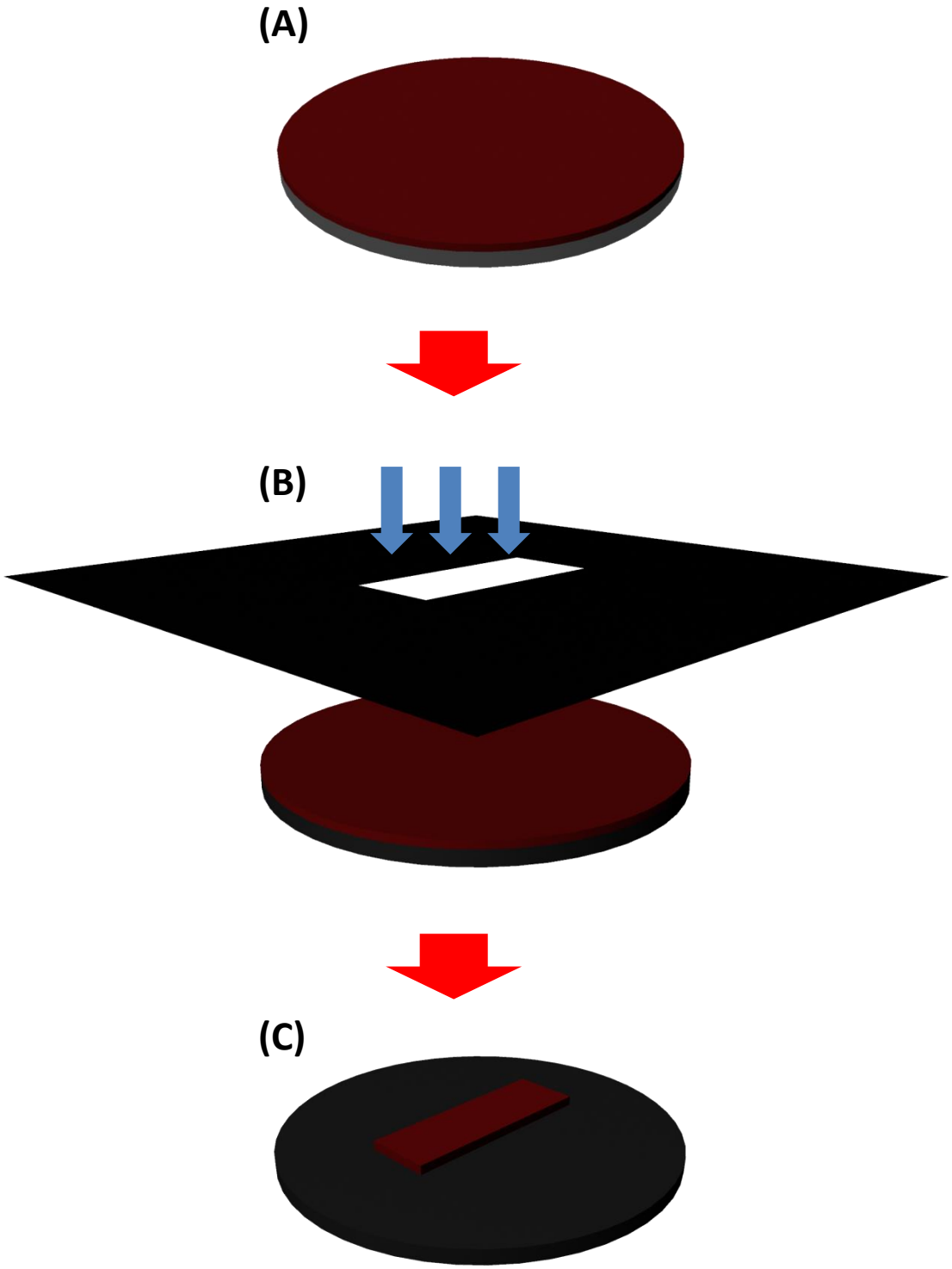

Figure 2.2: Diagram depicting the photolithography process, to create the silicon master mould for the GUV microtrap array device. (A) Four inch silicon wafer (grey), with a 50 µm layer of SU8-3050 negative photoresist (red), applied via spin-coating at 3000 rpm. (B) After a pre-exposure bake at 95 °C for 15 minutes, the photoresist was exposed to UV light (blue arrows) through a negative photomask. The wafer is then given a post-exposure bake at 95 °C for 4 minutes, then developed in Microposit EC solvent, to remove the non-exposed photoresist. (C) The wafer is then hard baked at 180 °C for 2 hours, to produce the final negative master-mould.

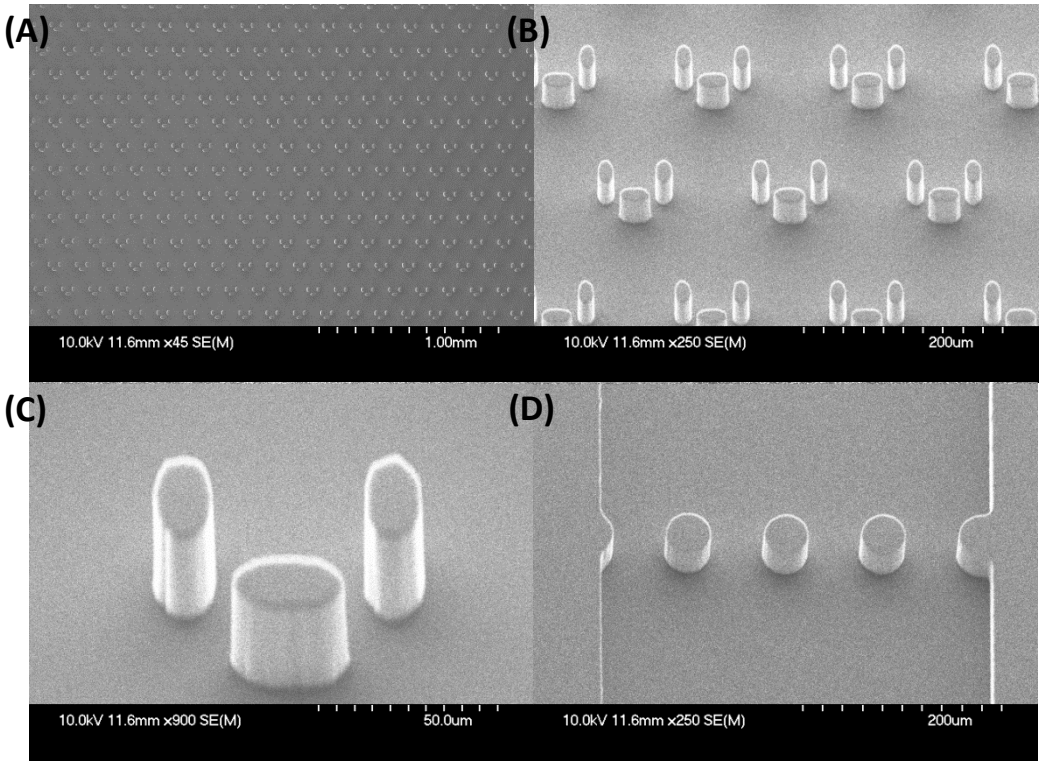

Figure 2.3: Scanning electron microscopy pictures of the device geometry, with the scales as depicted on each image: (A) Low magnification image (x45), demonstrating the high density of the microtrap array, enabling high-throughput analysis. (B) Higher magnification image taken at an angle of 45°, depicting the trap geometry. (C) Close up image of a single GUV trap, taken at a magnification of x900 and an angle of 45°. (D) View of the PDMS pillars within the microfluidic channel, between the electroformation chamber and the microtrap array, designed to act as a size filter, allowing only GUVs with a diameter between 10 and 40 µm to pass.

Once cast, the electroformation chamber was excised using a scalpel, taking care to not block the microfluidic channels. Holes were punched into the PDMS to allow the entry and exit of the solutions into the channels, and the chip was plasma bonded to a clean glass microscope slide. The slides were immediately transferred into a solution of 100 mM glucose containing 0.1 % BSA, and sonicated to fill the microfluidic channels, with care taken to completely remove air from the microtrap array chamber. The BSA coated the inside of the PDMS device, presenting a more hydrophilic surface to the vesicles, to increase their stability within the device when pinned to the PDMS microtrap pillars. The chips were kept within the glucose and BSA solution until needed, then flushed with 100 mM glucose solution.

2.3. GUV electroformation

The production of GUVs via electroformation relies on passing an alternating electric field across hydrating lipid layers, causing the lipids to reorganise into lamellar vesicular structures. The microfluidic device was designed to be compatible with both on- and off-chip electroformation of GUVs, and the protocols for both are presented below. The selected lipid compositions are presented below in table 1, and represent a varied mix of lipid topography, with large variations in headgroup, fatty acid composition and unsaturation and charge. All lipids were ordered from Avanti Polar Lipids (Alabaster, USA), and used without further purification.

LIPID MIX*	Molar percentage
DOPC	100
DOPC:DPPC	80:20
DOPC:DOPE	80:20
DOPC:DOPE:DOPG	60:20:20
DOPC:DOPE:DPPG	60:20:20
DOPC:DPPC:DOPG	60:20:20
DOPC:DPPC:DPPG	60:20:20
DOPC:DOPE:LPG	60:20:20
DOPC:DOPE:DEPG	60:20:20
DOPC:DOPE:POPG	60:20:20
DOPC:DOPE:DOPG:DPPG	60:20:10:10
DOPC:DPPC:cholesterol	35:35:30

*Table 1: List of the lipid compositions used in the dye-leakage experiments, showing the lipids within each mic and their molar percentage compositions. The selected lipids present binding LCAMPs to a wide variety of lipid topographies, featuring varying lipid headgroups, fatty acid composition and charge. DOPC as a cylindrical geometry bilayer lipid was used as a base membrane. *for fluorescence visualisation 0.05 mol% of DHPE-Rhodamine was added to each lipid mixture.*

2.3.1. Off-chip electroformation protocol

The desired lipids were made up to a final concentration of 3.75 mg/ml, in a solution of 95:5 % chloroform:acetonitrile, and sonicated for 30 minutes to ensure even dispersal of the lipids within the solution. An electrical connection was made with an ITO-coated slide, with approximate dimensions 30 x 30 mm, using either copper conductive tape or a copper wire secured with conductive paint. The conductivity for the slide was obtained using a multimeter to measure the resistance, between the ends of the wire and the centre of the ITO slide, and only those slides with < 40 Ω were used. The lipid solution was then spin-coated onto the conductive surface of the ITO-coated slide, at 300 rpm, to give a uniform coating of lipids across the entire slide. The thickness of the lipid film was assessed by AFM (XXX), and the results presented in figure 2.4. After spin-coating, the slides were dried under vacuum for two hours, to ensure the removal of all solvent traces from the lipid film. The coated slide was then separated from the conductive surface of another ITO-coated slide by a 1.5 mm spacer, either a rubber o-ring or a PDMS block with an excised centre, and sealed with vacuum grease. The electroformation process requires two solutions; an interior electroformation buffer consisting of 100mM sucrose, 5 mM HEPES (pH adjusted to 7.4 using 25% KOH) with 10 µM 3kDa dextran-AlexaFluor488 and 15 µM dextran-AlexaFluor647; and an exterior washing buffer consisting of 100mM glucose, 5 mM HEPES (pH adjusted to 7.4 using 25% KOH).

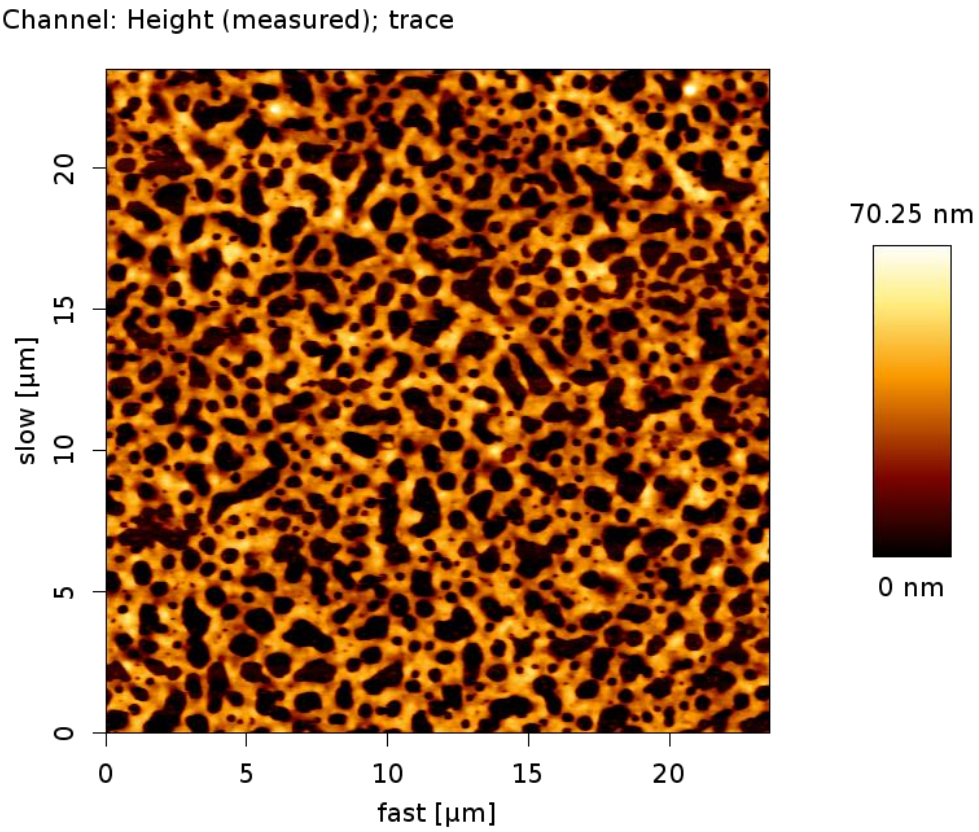

Figure 2.4: Scanning AFM picture of the lipid film on an ITO-coated glass slide, after spin-coating with a 3.75 mg/ml solution of the lipid DOPC in a 95:5 % chloroform:acetonitrile solution. Although appearing uniform at a macro-scale, the micro-scale structure displays a "holes and rims" topography, of dried lipid layers surrounding flat areas, assumed to be the basement glass slide. The average depth of the lipid layers is approximately 40 – 50 nm.

The space between the ITO slides was filled with electroformation solution, and an AC field electric pulse sequence was applied between the slides, with the parameters listed in table 2.

Time (minutes)	Frequency (Hz)	Voltage (Vpp)	Pulse shape
0 -20	10	0.5	Sine wave
20 – 40	10	1.0	Sine wave
40 – 60	10	1.5	Sine wave
60 – 120	10	2.0	Sine wave
120-180	4	2.5	Square wave

Table 2: Electroformation pulse parameters, listing the length of time each sequence is applied for, the frequency in Hertz, the field strength in Vpp and the field shape. The field strength is ramped up to 2.0 Vpp over 60 minutes, allowing small vesicular structures to form, then maintained at 2.0 Vpp for a further 60 minutes, where the small structures merge into larger vesicles. After 120 minutes, the frequency is adjusted to 4 Hz, the strength changed to 2.5 Vpp and the field shape changed to a square wave. This aids in detaching the formed GUVs from the ITO slide.

After electroformation, the GUVs are carefully transferred into the excised chamber in the PDMS chip, and the chamber filled with washing solution. The density gradient between the sucrose buffer within the vesicles, and the surrounding glucose solution, causes the GUVs to quickly settle to the bottom of the chamber, aiding both visualisation and transfer into the microfluidic device. The chip was sealed with a custom glass microscope slide, machined to include entry and exit ports for the PDMS device, forming a glass-PDMS-glass sandwich structure. The device was then sealed using a bespoke metal clamp, and the entry and exit ports fitted with tubing connected to syringe pumps, as pictured in figure 2.5. The tubes were sealed to the ports using silicon sealant to ensure a watertight seal.

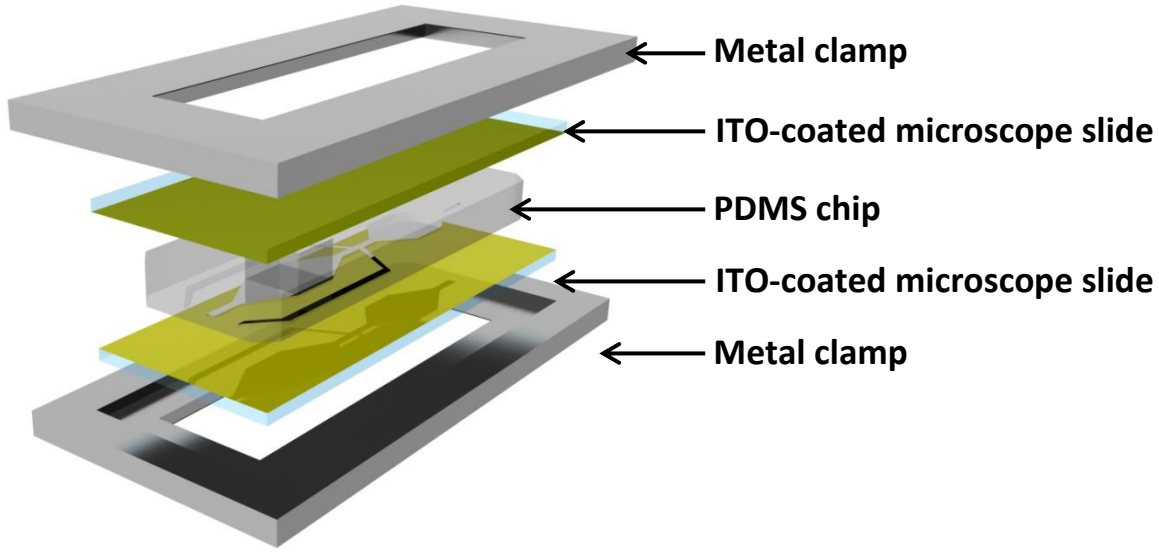

.

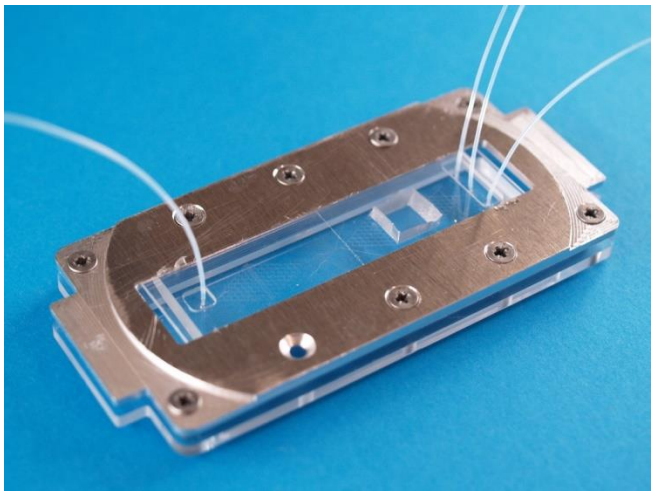

Figure 2.5: (Top) Exploded schematic of the finished device, showing the glass-PDMS-glass sandwich construction. The version depicted is the on-chip electroformation, with the PDMS chips positioned between two ITO-coated microscope slides, with the bespoke metal clamp acting to seal the device (Bottom) Picture of the assembled device. Showing the entry and exit ports of the microfluidic device are plumbed with tubing, connected to syringe pumps

2.3.2. On-chip electroformation protocol

On-chip electroformation uses the same pulse sequence as the off-chip procedure, but instead of the electroformation being carried out in a separate device, it is carried out within the excised chamber in the PDMS device. On-chip electroformation requires casting a thinner chip (~1.5 mm), in order to maintain the same electric field strength, and that the chip is bonded to an ITO-coated microscope slide, before being coated with the glucose/BSA solution. The lipid layer is spin-coated onto a ITO-coated

microscope slide, custom machined to allow access to the entry and exit ports of the PDMS chip, and electrical contact points made on the two ITO-coated slides. The device is assembled as shown previously, with the excised chamber being filled with the electroformation solution, and the pulse sequence in table 2 is applied.

2.4. Dye-leakage protocol

Once the GUVs are contained within the chamber, either through on- or off-chip electroformation as shown in figure 2.6, wash solution is used to flow the vesicles into the microtrap array

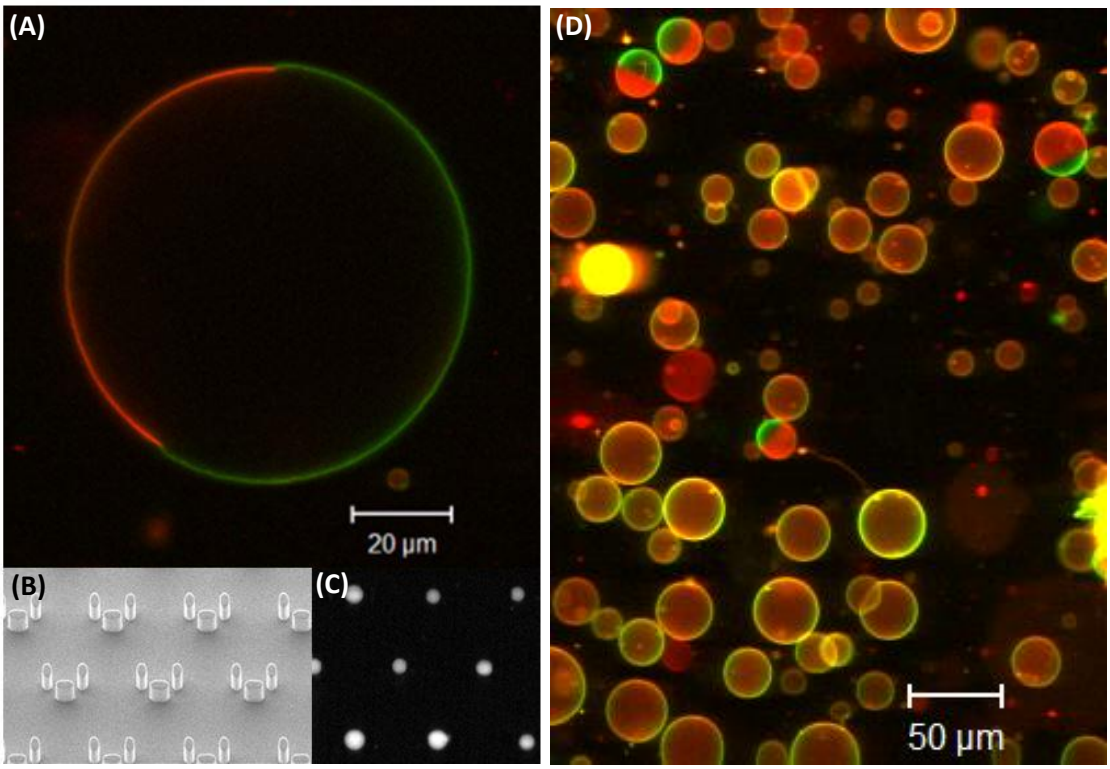

Figure 2.6: (A) Equatorial cross-section of a biomimetic mGUV, composed of DOPC:DPPC:cholesterol (35:35:30 mol%), obtained via confocal microscopy. The membrane contains 0.05 mol% of the fluid-phase marker DHPE-rhodamine lissamine B, visualised in red, and 0.1 mol% of the gel-phase marker cholesterol-BODIPY, visualised in green. (B) SEM picture of the PDMS microtrap array, taken at an angle of 45°, showing the high trap density. (C) Fluorescence microscopy picture of mGUVs within the PDMS microtrap array, visualising the 3 kDa dextran-AlexaFluor fluorescence. (D) mGUVs within the electroformation chamber, showing the high yield possible using electroformation.

To establish a negative control set, a total 292 GUVs were trapped within the microtrap array, and left under microfluidic flow for three hours in peptide-free conditions.

2.5. Data processing

The selection of PIEs that produced pore-mediated leakage events were data processed to remove artefacts like fluorescence background, photobleaching and the variation in initiation timings. The data processing allowed easy comparison of the leakage data from different GUVs.

2.5.1. Background and photobleaching correction

The raw leakage traces were background and photobleaching corrected, using the data from the peptide-free vesicles to construct photobleaching curves, as depicted in figure 2.7. The data was then normalised, to ease comparison between GUVs of varying diameters.

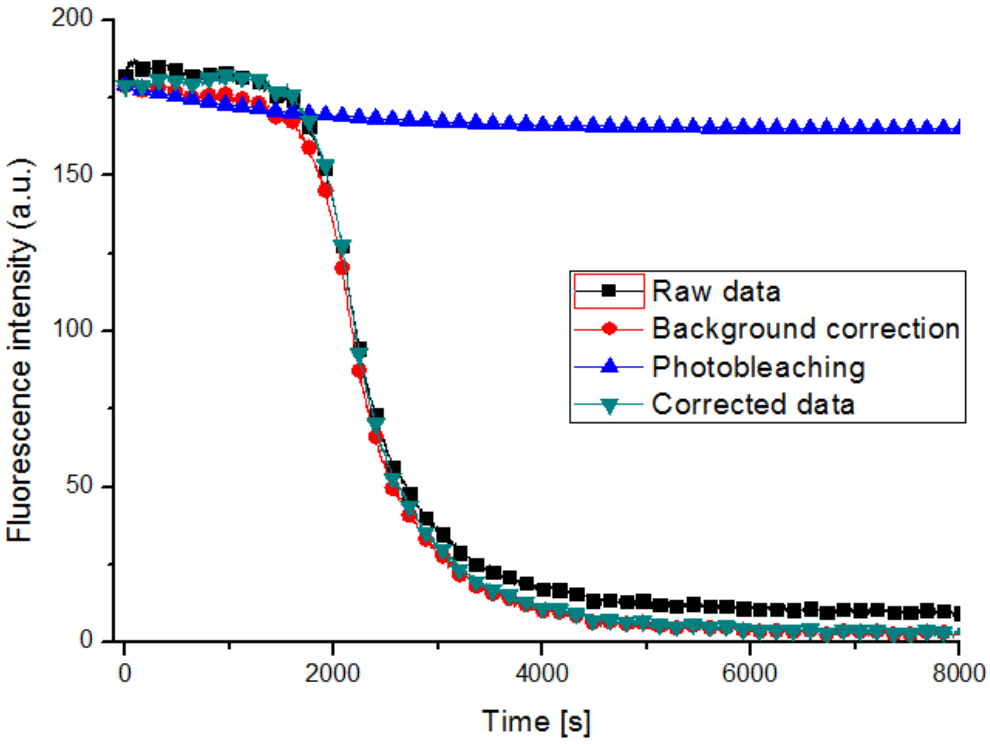

Figure 2.7: Graph demonstrating the data processing required to generate the final data, using a 10 kDa dextran leakage trace from a DOPC:DOPE:DPPG vesicle, exposed to 5 μM of the LCAMP magainin. The raw data (black squares) was adjusted for background fluorescence, which was typically <10 %, to create the background corrected trace (red diamonds). The photobleaching curves established using data from peptide-free control experiments (blue triangles), was then used to correct the leakage data for photobleaching, and create the final leakage trace (turquoise triangles).

2.5.2. Time correction

To correct for the variation in initiation of the pore-mediated leakage events, the leakage traces were truncated to remove the part of the trace before the initiation of the leak. This allows easy comparison of the dye-efflux kinetics from the individual GUVs.

2.5.3. Kinetic grouping behaviour

After data correction the leakage traces were compared to one another, and were found to organise into distinct kinetic groups, where individual GUVs show similar leakage kinetics, with an example shown in figure 2.8.

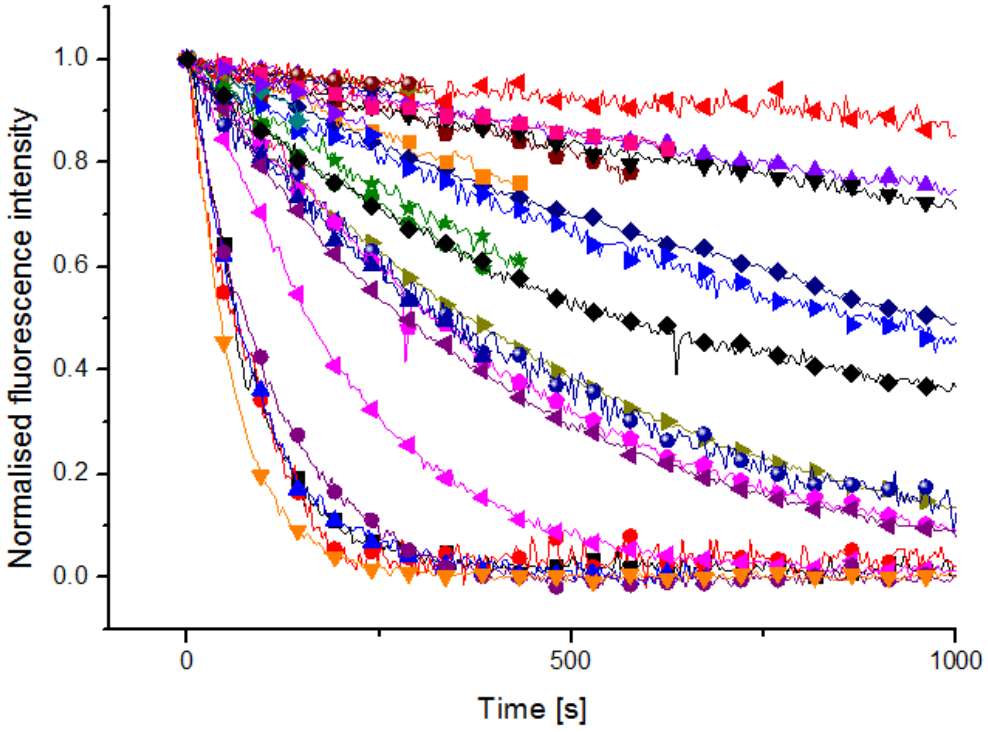

Figure 2.8: Compiled leakage traces for the 3 kDa dextran marker from a total of 29 DOPC:DPPC:DPPG vesicles, exposed to 1 µM of the LCAMP magainin. The kinetics organise into distinct groups, with each GUV within a group demonstrating similar leakage kinetics over considerable time periods (>1000 s). The group showing the fastest kinetics operates via the carpet mechanism, not pore-mediated leakage, and is included for comparison only.

The leakage traces can be compiled into average traces for each group, as shown in figure 2.9, which displays the averaged data from figure 2.8.

2.5.4. Multiple leakage phase analysis

Numerous leakage traces displayed distinct changes in kinetics during the time-course of an experiment, with abrupt increases or decreases in kinetics, pictured in figure 2.10.

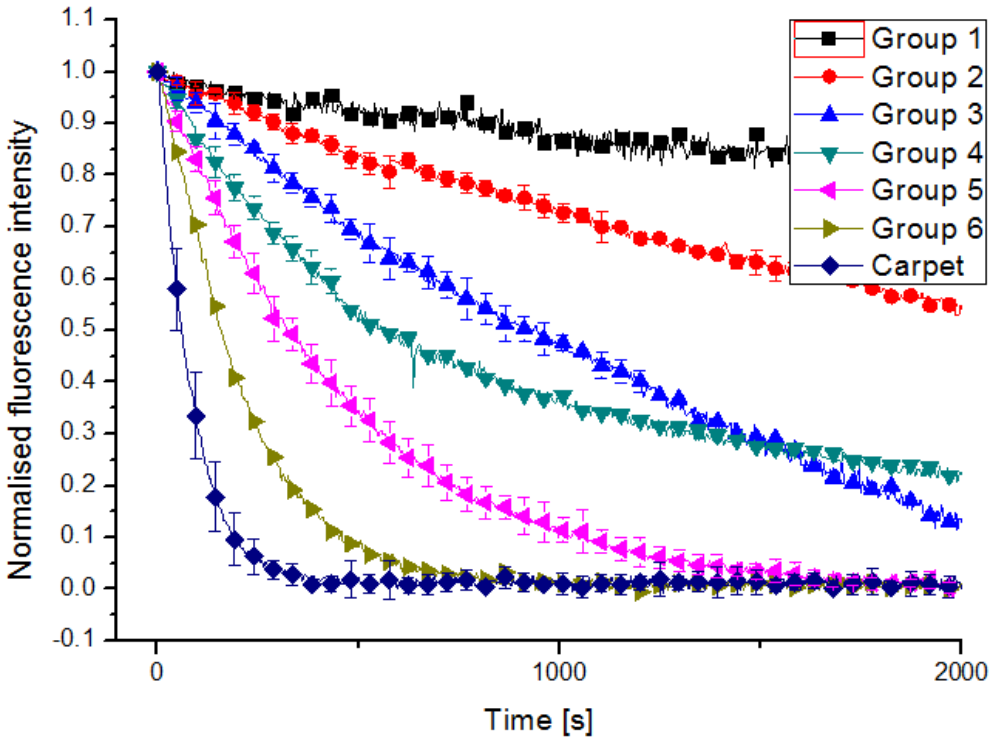

Figure 2.9: Averaged leakage traces for the DOPC:DPPC:DPPG membrane system, for a total of 29 vesicles exposed to 1 µM magainin, with the groups identified as in the figure legend. A total of six groups can be identified within the leakage data, with the error bars representing the standard deviation of the individual leakage traces within each group.

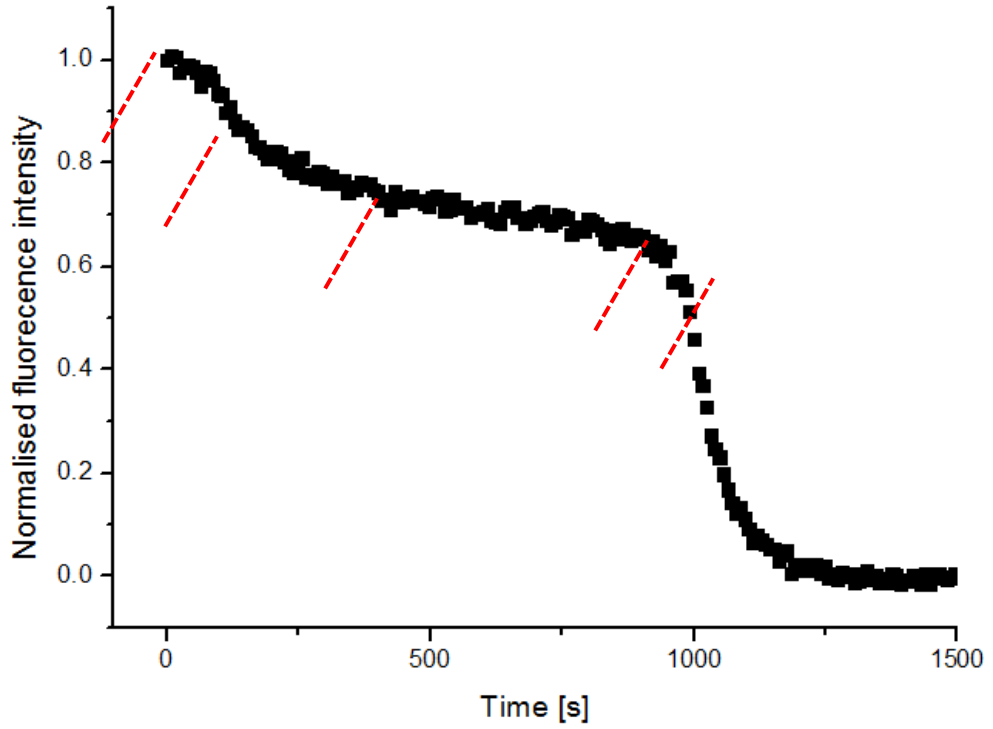

Figure 2.10: Graph presenting a trace displaying distinct and abrupt changes in the dye-efflux kinetics from a single DOPC GUV, expose to 5 µM of the LCAMP melittin. The changes in kinetics are indicated by the dashed red lines, with each individual phase lasting between 68 and 474 seconds.

To investigate this phenomenon, the individual leakage phase were separated out and renormalized, treating each change in the leakage kinetics as the initiation of a new leak. Figure 2.11 presents the same leakage data seen in figure 2.10, after renormalisation, and allows each individual phase to be compared.

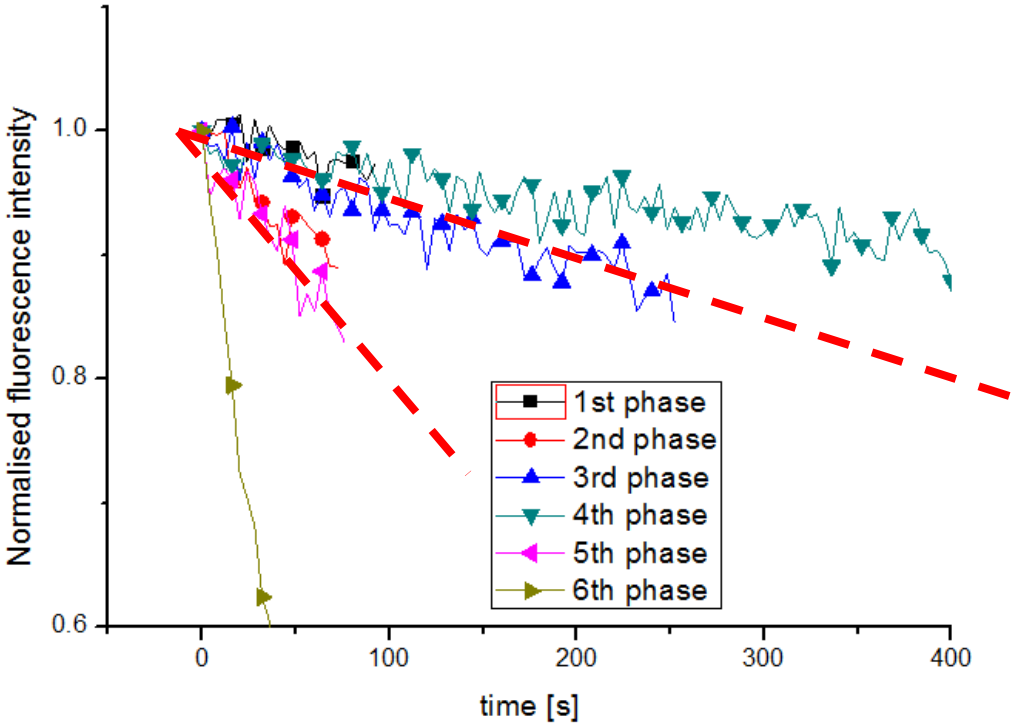

Figure 2.11: Graph presenting the individual phases of a multiphase leakage trace, after each phase has been renormalised. The individual leakage phase kinetics organise into groups, and switch between the different rates of dye-efflux. The red lines indicate the average kinetics of each group, and are intended as a guide to the eyes only.

3. Peptide-induced effect (PIEs) profiling

3.1. PIEs

The high-throughput dye leakage experiments revealed a complex regime of outcomes to the lipid-LCAMP interactions of the GUVs caught within the microfluidic device. These set of outcomes have been collectively termed peptide-induced effects (PIEs), and are presented below in figure 3.1. The definitions of each PIE are presented below, listing the criteria used to classify the results of the interactions of the LCAMPs magainin and melittin with GUVs.

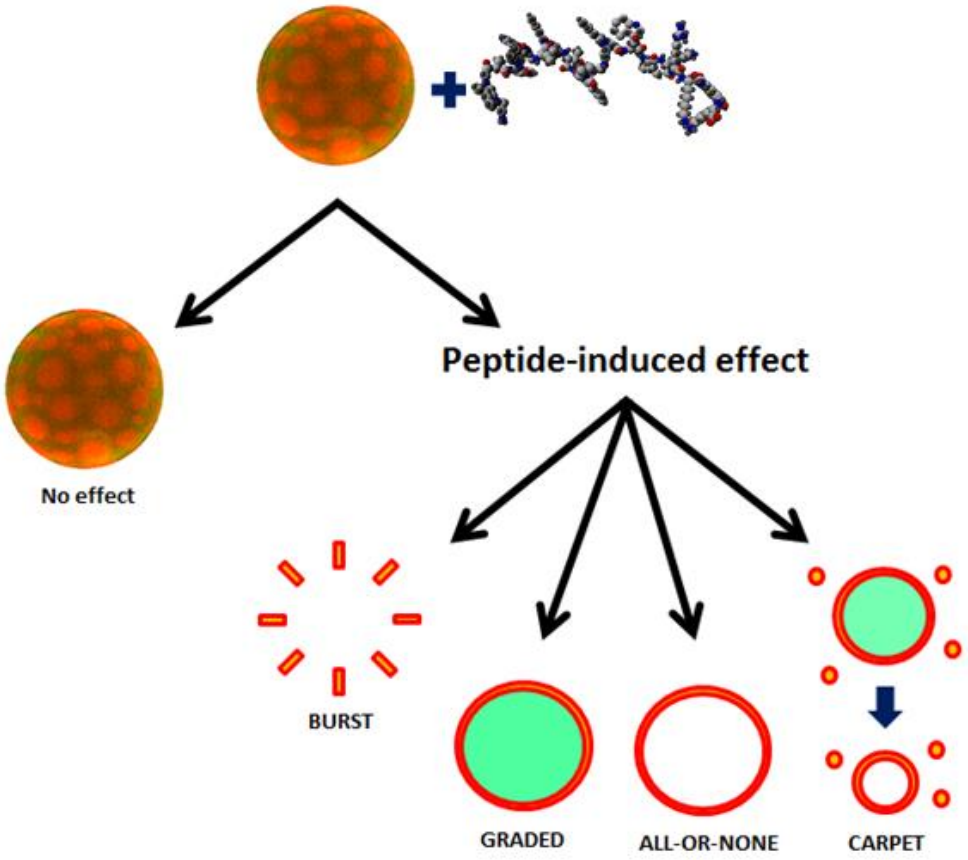

Figure 3.1: Diagram depicting the PIEs induced by the microfluidic exposure of GUVs, to the LCAMPs magainin and melittin. Some vesicles survived to the end of the experimental timecourse (120 min) with no visible escape of content (no effect); some vesicles suffered rapid and total membrane failure (burst); some GUVs had lost a portion of their contents, with no membrane alteration (graded); some vesicles had lost all their contents, with no membrane alteration (all-or-none) and some vesicles both lost their contents and displayed micellisation of their membranes (carpet).

3.1.1. No effect

GUVs surviving to the end of the experimental timecourse, with no escape of vesicle contents, or reduction in membrane volume, result in the LCAMP being declared inactive within GUV. Melittin was typically more active than magainin within the systems tested, with a notable exception; the inclusion of DPPG within membrane systems resulted in magainin displaying comparable activity to melittin.

3.1.2. Bursting

Some vesicles suffered complete membrane failure upon exposure to the peptide, and received the burst PIE classification.

3.1.3. Pore-mediated leakage

Vesicles exposed to LCAMPs which displayed loss of contents, with no accompanying loss of membrane volume, were classed as leaking via pore-mediated leakage.

3.1.4. Carpet mechanism

Some GUVs lost their contents after exposure to LCAMPs, with accompanying loss of membrane volume, and were classified as leaking via carpet mechanism. A typical carpet mechanism leak involved very fast loss of vesicle contents, with a continuous steady reduction in GUV diameter, as lipid-peptide micelles were lost to the surrounding solution.

3.1.5. Micellisation

A small fraction of the entrapped vesicles displayed an instantaneous reduction of vesicle diameter, unlike the carpet mechanism, where the loss of membrane volume was continuous and steady. This vesicle population was classified as displaying micelle behaviour.

3.2. Membrane systems

A large proportion of the research done on the membrane disrupting activity of LCAMPs has been performed in one component homogeneous systems,[98][112][115] with the remainder being carried out within two component binary systems.[113][119] There have been few papers published featuring the interaction of LCAMPs with complex membranes featuring heterogeneous lipid topography. The studies carried out are understandably skewed towards popular and cheaper lipids, that are easy to work with at room temperature, and can easily be manipulated into bilayers. To fully understand the interaction of LCAMPs, with the extremely heterogeneous and complex *in-vivo* lipid membranes, a rigorous examination of the lipid-peptide interactions within more complex model membrane systems is needed. The membrane systems tested (table 1) are built around DOPC as a base membrane, selected as suitable due to its neutral charge, cylindrical geometry (S = 1.08) and ease of electroformation. Binary, tertiary and quaternary lipid systems were created, by doping the base membrane with other lipids carefully selected to span the desired range of physiochemical properties. The chosen membrane systems present a membrane set with variation in several key physiochemical properties known to affect LCAMP activity; charge; fatty acid length and unsaturation and intrinsic curvature. The quaternary system DOPC:DOPE:DOPG:DPPG (60:20:10:10 mol%) was also selected, and was the most complex membrane model tested

3.3. PIE-profiles

The varying PIEs produced can be compiled into PIE-profiles, which are characteristic for each of the membrane system tested. The profiles show that significant changes in peptide mechanism can be induced via the alteration of membrane composition.

3.4. PIEs of melittin

The PIE-profile data collected for the LCAMP melittin presented a wide range of activities and variation in the PIEs, dependent on the target membrane composition.

3.4.1. Binary lipid systems

Doping a DOPC base membrane with 20 mol% of lipids with varying physiochemical properties, resulting in GUVs with a binary composition, produced the PIE-profiles shown in figure 3.2. The control group consisting of 192 DOPC GUVs (average diameter 19.0 +/- 8.3 μm) trapped within the microfluidic microarray trap, under identical flow conditions but with no exposure to peptide, produced a 90.5 % inactive profile. The control GUVs displayed low amounts of both bursting (3.2 %) and leaking (6.3 %), but carpet and micelle effects were completely absent. Exposure of DOPC GUVs to 1 μM melittin produced a profile demonstrating 100 % peptide activity (29 vesicles with an average diameter of 23.2 +/- 6.8 μm), containing mainly bursting (33.3 %) and pore-mediated leaking (50 %) effects. The carpet PIE accounted for 6.7 % of activity, and the micelle PIE was completely absent. Inclusion of 20 mol% DPPC, a lipid which possesses two 16C saturated fatty acid tails and displays positive intrinsic curvature (S = 0.74), deactivated melittin activity compared to pure DOPC membranes (total of 160 GUVs with an average diameter of 17.9 +/- 7.8 μm) The DOPC:DPPC membrane displayed an activity of 73.1 %, with pore-mediated leakage accounting for 35 % of the total PIEs. The remainder of the PIEs were split between bursting (14.4 %), micelle (13.1 %) and carpet (10.6 %). Addition of the conical non-bilayer lipid DOPE, with its small headgroup and large volume unsaturated fatty acid tailgroups (S = 1.41), produced a more significant shift of PIE-profile from pure DOPC than addition of DPPC (from a total of 227 GUVs with an average diameter of 16.2 +/- 6.5 μm). 90.7 % of vesicles displayed a PIE, with the highest pore-mediated leakage percentage recorded for all of the binary vesicles exposed to 1 μM melittin (53.1 %). Unlike pure DOPC and DOPC:DPPC membranes, where the carpet mechanism, was the lowest frequency PIE recorded, in DOPC:DOPE membranes GUVs leaking via the carpet mechanism were the second most frequent PIE at 19.8 %. Bursting accounted for 12.5 % of PIEs, while micelle made up only 5.3 %.

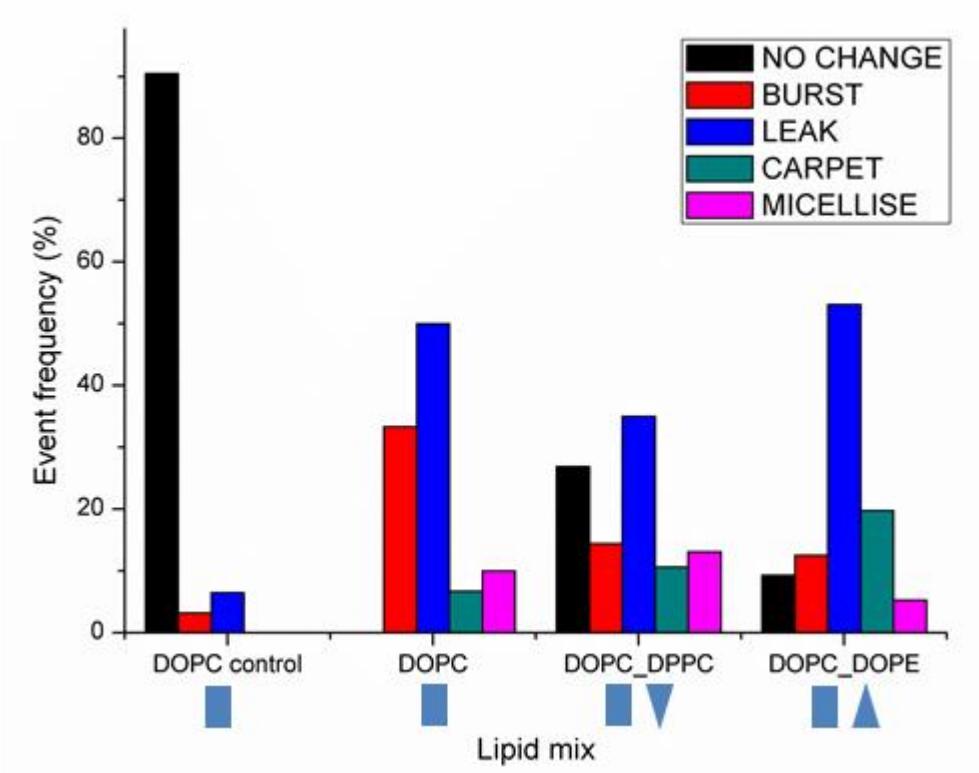

Figure 3.2: PIE profiles produce, by the variation of lipid topography within binary lipid mixtures, from GUVs exposed to 1 µM melittin. Membrane topography is indicated by the blue geometrical shapes below the lipid mixes, and a peptide-free DOPC membrane control (192 GUVs) is included as the left most PIE profile, with > 90 % of the control vesicles surviving unchanged to the end of the experiment. Melittin is highly active within cylindrical DOPC membranes, with 100 % of the 29 GUVs displaying a PIE, profile is dominated by bursting and pore-mediated leakage events, with a small proportion (~15 %) of carpet and micellisation events. Melittin is significantly less active within DOPC:DPPC membranes, the addition of the inverse-conical geometry lipid DPPC lowers the peptide activity by > 30 %, and produces a PIE profile dominated by pore-mediated leakage. Addition of the conical geometry lipid DOPE to DOPC membranes increases both activity and carpet mechanism PIEs compared to DOPC:DPPC membranes, but the profile remains dominated by pore-mediated leakage.

In summary, the binary membrane systems exposed to 1 µM melittin produced differing PIE-profiles, and doping the cylindrical DOPC membrane with the conical DOPE lipid produced a larger shift than DPPC doping. Pore-mediated leakage remained the PIE with the highest population for the binary systems, but doping with conical lipids like DOPE appears to favour the carpet mechanism. It is interesting to note that inclusion of different topography lipids within the neutral topography DOPC membrane appears to significantly reduce the frequency of the bursting PIE for both cases; doping with the inverted conical DPPC lipid reduced bursting to 14.4 % compared to 33.3 % recorded in the base DOPC system, and doping with DOPE reduced it to 12.5 %. Melittin is a negative curvature inducing LCAMP, and when targeting membranes containing lipids with the opposite curvature lipids, like DPPC, it produces low activity levels. When attacking membranes containing lipids possessing negative curvature, like DOPE, the carpet mechanism becomes favoured.

3.4.2. Ternary lipid systems

Increasing the complexity of the membrane, by the addition of a third lipid with differing topographical properties to a base DOPC:DOPE membrane to create a ternary system, produced the PIE-profiles shown in figure 3.3.

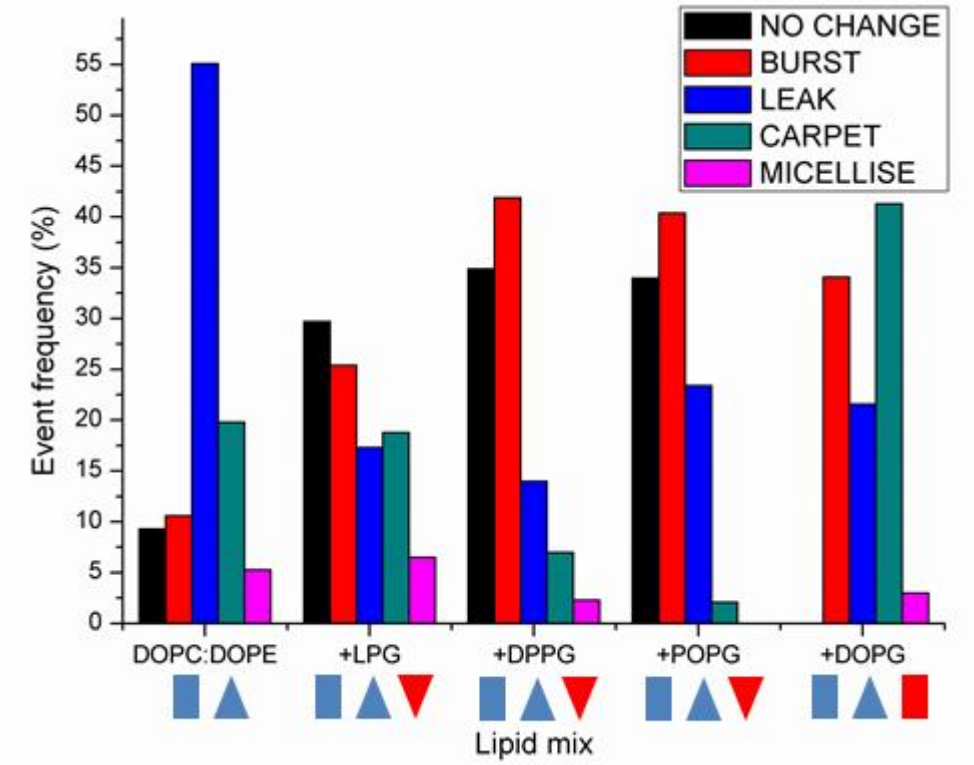

Figure 3.3: PIE profiles produced by the variation of anionic lipid topography, within the DOPC:DOPE:X lipid mixtures, from GUVs exposed to 1 µM melittin. Base DOPC:DOPE membrane (227 GUVs) included on the left for reference, with the lipid(s) doped into the base DOPC membrane listed below each profile. Membrane topography is indicated by the geometrical shapes below the lipid mixes, with blue shapes indicating neutral lipids and red indicating anionic lipids. Inclusion of the highly positively curved anionic lipid LPG within the DOPC:DOPE membrane (138 GUVs) produces a large PIE-profile shift, deactivating melittin activity by 20 %, and reducing pore-mediated leakage and increasing bursting. Doping of the DOPC:DOPE membrane with the positive curvature anionic lipid DPPG (44 GUVs) produces a similar PIE-profile shift, displaying reduced activity with increased bursting and less pore-mediated leaking. Addition of the positively curved lipid POPG (47 GUVs) also produces similar profile shifts from the DOPC:DOPE membrane as the addition of LPG and DPPG. Doping with the cylindrical geometry anionic lipid DOPG (167 GUVs) produces a contrasting PIE-profile shift, displaying increased melittin activity, and a profile that is dominated by carpet leakage, with reduced pore activity.

Melittin introduced to the DOPC:DOPE:LPG membrane system was significantly less active (-20.4 %) than within the DOPC:DOPE membrane, from 138 GUVs with an average diameter of 17.1 +/-7.0 µm. The extreme inverse-conical geometry of LPG produced a significant profile shift compared to the DOPC:DOPE membrane; bursting increased 19.1 % and pore-mediated leakage was reduced by 37.6 %. Carpet and micelle PIEs remained constant compared to the DOPC:DOPE membrane, at 18.8 and 6.5 % respectively, suggesting these PIEs result from lipid-peptide interactions that do not include LPG. Inclusion of DPPG, an anionic lipid with two 16:0 unsaturated fatty acids and possessing positive curvature, again produced less activity than the base DOPC:DOPE membrane when exposed to 1 µM melittin, with 34.9 % of vesicles surviving unchanged to the end of the experiment (44 GUVs with an average diameter of 11.9 +/- 4.8 µm). The profile was similar to the DOPC:DOPE:LPG membrane system,

except for a 16.5 % increase in bursting, compensated by an 11.8 % decrease in the carpet mechanism PIE. Addition of POPG rather than DPPG to the DOPC:DOPE membrane (47 GUVs with an average diameter of 11.8 +/- 6.5 μm), decreases the positive curvature of the anionic lipid, by increasing the hydrocarbon volume through replacement of one 16:0 acyl chain with an 18:1 (9z) chain. This change of hydrocarbon volume increases the amount of pore-mediated leakage by 9.4 % compared to the DPPG containing membrane system, coupled to a reduction in both the carpet mechanism (-4.9 %) and the micelle PIE (-2.3 %).The final ternary system of DOPC:DOPE:DOPG displayed the largest shift in PIE-profile, and produced the most active DOPC:DOPE:X system, displaying 100 % activity from 167 GUVs with an average diameter of 18.9 +/- 7.7 μm. The profile produced similar levels of bursting and pore-mediated leakage as the DOPC:DOPE:POPG system, but a substantial 39.2 % increase in the carpet mechanism PIE.

The three inverse-conical anionic lipids with positive curvatures, all display lower melittin activity than the base DOPC:DOPE membrane system, while the cylindrical anionic DOPG displays increased melittin activity, indicating that curvature additivity plays a role in the PIE produced. The clustering of positive curvature-inducing anionic lipids around the cationic negative curvature-inducing LCAMP melittin reduces peptide activity, via reduction of the packing strain induced in the membrane by the LCAMP. Arranging the anionic adulterant lipids into increasing packing parameters, i.e. decreasing positive curvature, gives the order LPG>DPPG>POPG>DOPG, moving from LPG a lipid possessing only one 16:0 fatty acid chain and very low hydrocarbon volume to DOPG, which has two 18:1 carbon acyl chains. The positive curvature anionic lipids (LPG/DPPG/POPG) within the series all return similar profiles, all featuring high levels of bursting as the primary PIE, and across the LPG, DPPG and POPG series the frequency of the carpet mechanism decreases. The jump in PIE-profile shift when moving from the positively curved anionic lipids (LPG/DPPG/POPG) to the cylindrical neutral curvature anionic DOPC is pronounced, with a 39.2 % increase in carpet mechanism, and overall 34 % increase in activity compared to the POPG containing membrane system. This large change in melittin activity and PIE-profile, is produced from the replacement of one 16:0 fatty acid with its 18:1 (9z) equivalent, demonstrating a large change in peptide function produced by a small alteration of the target membrane.

The second set of ternary membranes were of the form DOPC:DPPC:X, before including 20 mol% of anionic lipids possessing different topographical properties, produced the PIE-profiles shown below in figure 3.4. Compared to the DOPC:DPPC base membrane system, the inclusion of the positively curved DPPG produced a higher frequency of pore-mediated leakage (+18.5 %) from a total of 71 GUVs with an average diameter of 17.4 +/- 5.6 μm. The overall PIE-profile was similar to the base membrane, with the increase in pore-mediated leakage compensated by a slightly higher activity (+4.4%) and a reduction in the micelle PIE (-10.3 %). Inclusion of DOPG within the base membrane again produced the largest PIE-profile shift, and the most active membrane system (total of 86 GUVs with an average diameter of 18.7 +/- 6.0 μm). Pore-mediated leakage is the highest frequency event at 56.9 %, the highest level for any membrane system at this melittin concentration. The carpet PIE also displays a significant increase from the DOPC:DPPC base membrane of 20.8 %, with bursting (-10.9 %) and micelle (-9.6 %) both reduced.

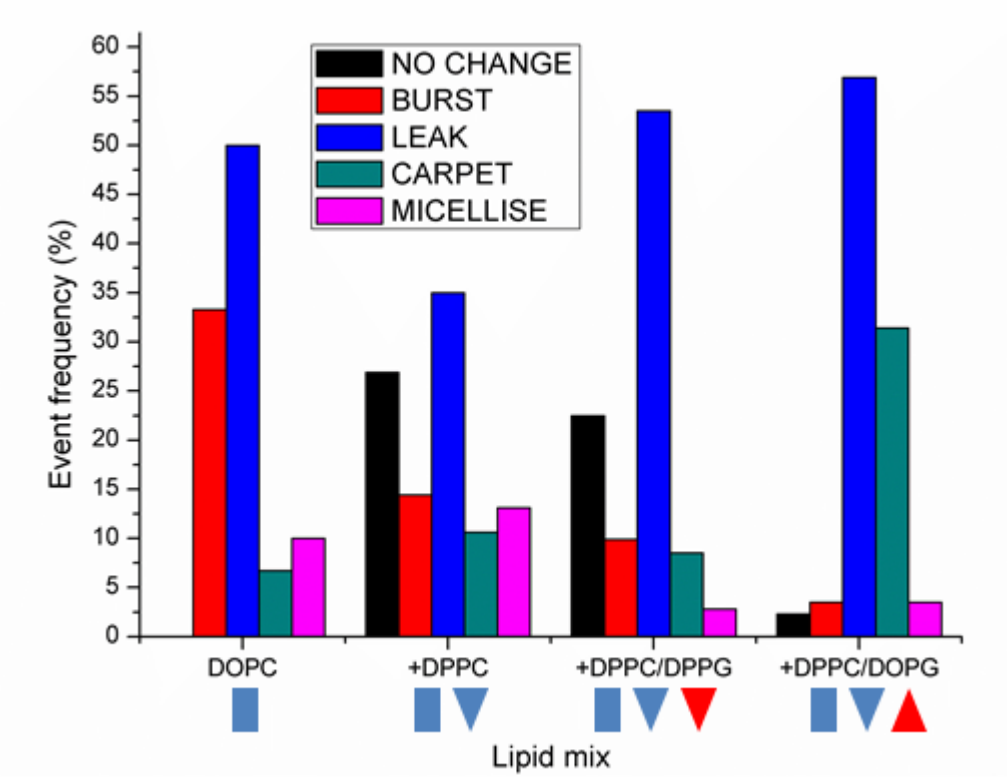

Figure 3.4: Graph of the PIE profiles produced, by the variation of lipid topography within tertiary DOPC:DPPC containing lipid mixtures, from GUVs exposed to 1 μM melittin. Pure DOPC membrane (29 GUVs), and DOPC:DPPC membranes (160 GUVs) included for reference, with the lipid(s) doped into the base DOPC membrane listed below each profile. Membrane topography is indicated by the geometrical shapes below the lipid mixes, with blue shapes indicating neutral lipids and red indicating anionic lipids. Inclusion of the positively curved anionic lipid DPPG into the DOPC:DPPC membrane (71 GUVs) increases the pore-mediated leakage, and reduces the micellisation effect, compared to DOPC:DPPC membranes. Doping of the DOPC:DPPC membrane with the negative curvature anionic lipid DOPG (132 GUVs) produces a significant PIE-profile shift, compared to addition of DPPG to the same membrane. Peptide activity is increased by ~20 %, and the profile is now dominated by pore-mediated leakage (56.9 %) and carpet leakage (31.4 %).

The DOPC:DPPC:X membranes generally display higher activity levels than their DOPC:DOPE:X counterparts, and produce significantly higher levels of pore-mediated leakage events than either the binary lipid systems or the DOPC:DOPE:X ternary lipid systems. To demonstrate this point we can compare melittin activity and pore formation within the DOPC:DOPE:DPPG and DOPC:DPPC:DPPG membranes systems, which produce activities of 65.1 and 75.5 % respectively, and pore-mediated leakage frequencies of 14 and 53.5 % respectively. This indicates that the inclusion of lipids with the physiochemical properties of DPPC, i.e. zwitterionic, positive curvature and saturated acyl tailgroups, favour both the overall activity and the pore-mediated leakage mechanism of melittin. In both the DOPC:DOPE:X and DOPC:DPPC:X membrane systems, inclusion of the anionic DOPG lipid increased the carpet effect frequency compared to their respective base membrane systems. Addition of DOPG also activates melittin within the DOPC:DPPC:X system, compared to the DPPG containing system it is 20.3 % more active.

3.4.3. Peptide concentration and PIE-profiles

To examine the effect of LCAMP concentration on the PIE-profiles produced by melittin, the lipid systems DOPC, DOPC:DPPC and DOPC:DOPE were exposed to 5 µM of melittin under identical flow conditions, and the profiles compared to the 1 µM results. A total of 72 DOPC GUVs with an average diameter of 21.3 +/- 7.7 µm, were exposed to 5 µM melittin, and produced the PIE-profile shown in figure 3.5. Both the 1 and 5 µM DOPC vesicles produced similar profiles, dominated by pore-mediated leakage events, but the higher melittin concentration of melittin was 30.6 % less active. The DOPC:DPPC membrane system also returned comparable profiles across the concentrations, both being dominated by pore-mediated leakage from a total of 75 DOPC:DPPC GUVs with an average diameter of 17.5 +/- 6.3 µm. The higher melittin concentration was 21.6 % more active than the lower concentration, with the increased activity evident in the 31.7 % higher frequency of pore-mediated leakage. The DOPC:DOPE system again returned similar profiles across both melittin concentrations, but in contrast to the DOPC:DPPC system, the addition of negative rather than positive topography zwitterionic lipids produced a shift from pore-mediated leakage to carpet mechanism, rather than the increased pore formation of the DOPC:DPPC membrane system.

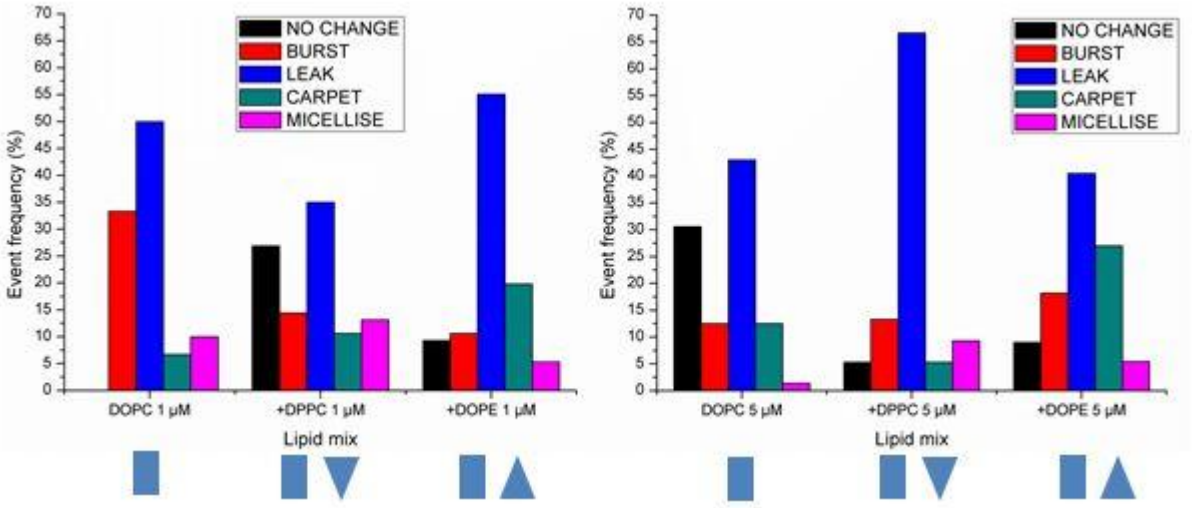

Figure 3.5: Comparison of the PIE-profiles obtained at differing melittin concentrations, 1 (left) and 5 (right) µM, for binary mixtures of a base DOPC membrane doped with lipids of varying topography, indicated by the blue block shapes under each lipid mix. The base DOPC membrane displays reduced activity, mainly explained by a decrease in bursting, when exposed to the higher concentration of melittin, but the profile remains dominated by pore-mediated leakage. Doping the base membrane with the positive curvature lipid DPPC, produces higher peptide activity at higher melittin concentrations, with the increased activity almost completely represented by the increase in pore-mediated leakage. Conversely, the membrane doped with the conical topography lipid DOPE displays similar activities at both melittin concentrations, but a PIE-profile shift from pore-mediated leakage to carpet mechanism and increased bursting.

The systems tested in figure 3.5 all produced PIE-profiles broadly comparable across the two different melittin concentrations, with all the profiles maintaining their primary PIE across the two concentrations; all the zwitterionic binary membrane systems are dominated by pore-mediated leaking events, despite varying lipid topography. It is interesting to note however, that the DOPC membrane doped with the inverse-conical geometry lipid DPPC produced higher pore leakage at the 5 µM concentration, while the inclusion of the opposite conical geometry lipid DOPE, produced a significant switch from pore-mediated leaking (-14.6 %) to the carpet mechanism (+7.2 %), although pore-mediated

leaking remained the primary PIE. Testing the effect of melittin concentration of the more complicated ternary anionic lipid systems produced the PIE-profiles shown in figure 3.6.

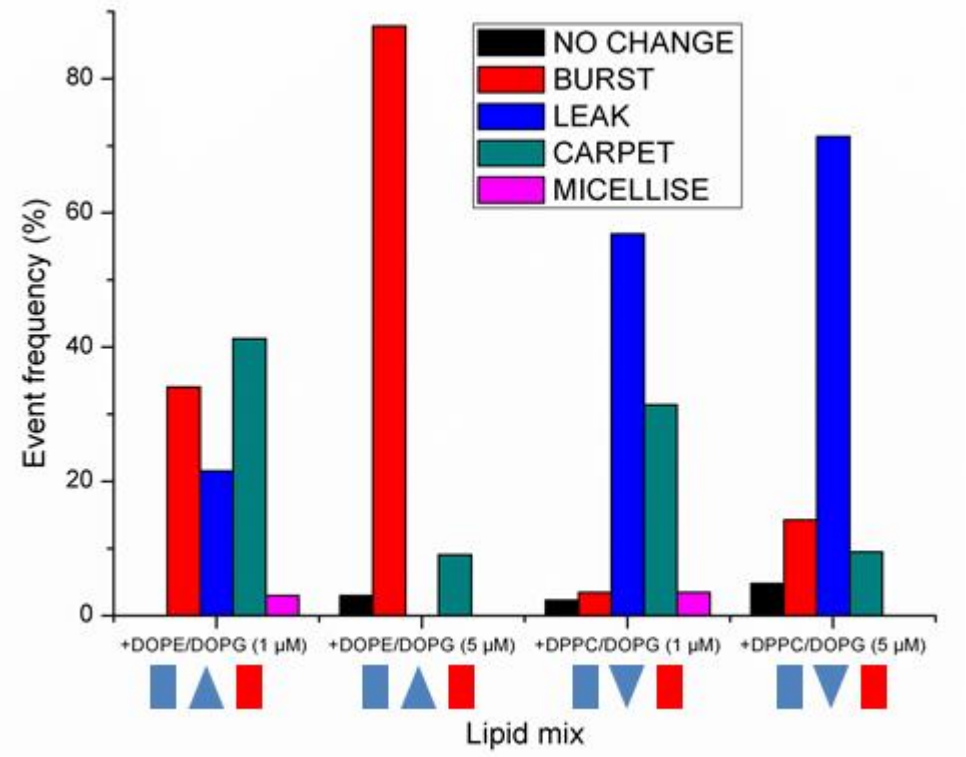

Figure 3.6: Comparison of the PIE-profiles obtained at differing melittin concentrations, 1 and 5 µM, for base DOPC membranes doped with the lipids indicated below each profile, forming ternary lipid systems with contrasting zwitterionic and anionic lipid properties. The lipid geometries are indicated by the block shapes underneath each profile, with zwitterionic geometry indicated in blue, and anionic topography depicted in blue. The DOPC:DOPE:DOPG membrane system undergoes a marked profile shift on exposure to higher levels of melittin, with the profile becoming dominated by bursting events. The replacement of the negative curvature inducing lipid DOPE with the positive curvature lipid DPPC, produced comparable PIE-profiles across both concentrations of melittin, with both profiles dominated by pore-mediated leakage events. The increase in concentration of LCAMP also produced a decrease in the carpet PIE of -21.9 %.

A total of 67 DOPC:DOPE:DOPG GUVs, with an average diameter of 25.5 +/- 6.5 µm, were exposed to the higher 5 µM concentration of melittin, and demonstrated a significant PIE-profile change, moving from a profile containing approximately equal levels of bursting and carpet mechanism, to one composed almost entirely of bursting (> 85 %). Inclusion of the opposite topography DPPC lipid within an otherwise identical lipid mix, produced comparable profiles across the two concentrations, for the total of 18 GUVs tested (average diameter of 16.5 +/- 6.9 µm), with a similar shift to that seen in the zwitterionic binary lipid DOPC:DPPC system; an increase in pore-mediate leakage couple to a decrease in carpet mechanism, again suggesting that the positive curvature lipid DPPC favours pore formation and disfavours the carpet mechanism. The 5 µM DOPC:DPPC:DOPG membrane produced the highest level of pore-mediated leakage for any membrane system tested (71.4 %). The large difference in PIE-profiles obtained, between the 1 and the 5 µM melittin DOPC:DOPE:DOPG membrane systems, is likely to be produced by the increased rate of peptide binding to the membrane at the higher concentration. Rapid binding of the negative curvature LCAMP melittin, to heterogeneous anionic membranes containing negative curvature zwitterionic lipids like DOPE, destabilises the membrane and causes complete membrane failure. This effect was not observed within the DOPC:DOPE membrane, indicating that the

electrostatic interactions between the anionic DOPG and the cationic LCAMP, play an important role in the bursting process. The quicker binding in the DOPC:DPPC:DOPG membrane system causes a shift in the PIE-profile, decreasing the amount of bursting relative to pore-mediated leakage events. Unlike the DOPC:DOPE:DOPG and DOPC:DOPE membrane systems, comparison of the DOPC:DPPC:DOPG membrane to its DOPC:DPPC counterpart, displays that increasing the melittin concentration has the same effect in this membrane pairing. This suggests the zwitterionic positive curvature lipid DPPC reduces the bursting frequency, as when exposed to 5 μM melittin, the DPPC containing membrane displays 73.6 % reduced frequency of the bursting PIE, compared to the otherwise identical membrane containing DOPE.

3.5. PIEs of magainin

The LCAMP M2a was considerably less active than melittin in the majority of the membrane systems tested, although the peptide displayed high levels of activity within certain membranes.

3.5.1. Ternary lipid systems

The addition of 1 μM M2a to ternary lipid systems, containing DOPC:DOPE doped with a series of anionic PG lipids, with varying degrees of intrinsic curvature, fatty acid unsaturation and hydrocarbon volume, produced the PIE-profile shown in figure 3.7. A total of 35 DOPC:DOPE:LPG GUVs with an average diameter of 20.0 +/- 7.5 μm were exposed to the LCAMP, displaying magainin activity of 49 %. The PIE-profile produced was dominated by bursting, with the bursting frequency more than twofold the frequencies of the pore-mediated leakage and carpet PIEs. Inclusion of DPPG within the DOPC:DOPE membrane system (total of 55 GUVs with an average diameter of 13.6 +/- 5.7 μm) resulted in higher M2a activity compared to the LPG containing system, presenting a peptide activity of 70.9 %, the highest magainin activity of any membrane system tested at this peptide concentration. The profile also displayed slightly increased carpet activity (+5.0 %) and reduced bursting frequency (-13.0 %), compared to that obtained for the DOPC:DOPE:LPG. Both of the membrane systems DOPC:DOPE:POPG and DOPC:DOPE:DOPG displayed low magainin activity, with the POPG membrane producing low amounts of bursting (4.3 %) and carpet mechanism (6.5%). The DOPG containing system was effectively inactive, displaying activity of < 6 %. Only one membrane system for the DOPC:DOPE:X series displayed peptide activity greater than 50 % - the DPPG system, which returned > 22 % higher activity than the second most active LPG containing system, although both these systems demonstrated significantly greater magainin activity than the POPG and DOPG containing membrane systems. This indicated that the positive curvature of the anionic lipids mediates magainin activity, suggesting a role for the electrostatic interactions between the anionic PG lipid headgroups and the cationic LCAMP amino acid residues in magainin, in activating the peptide within the target membrane.

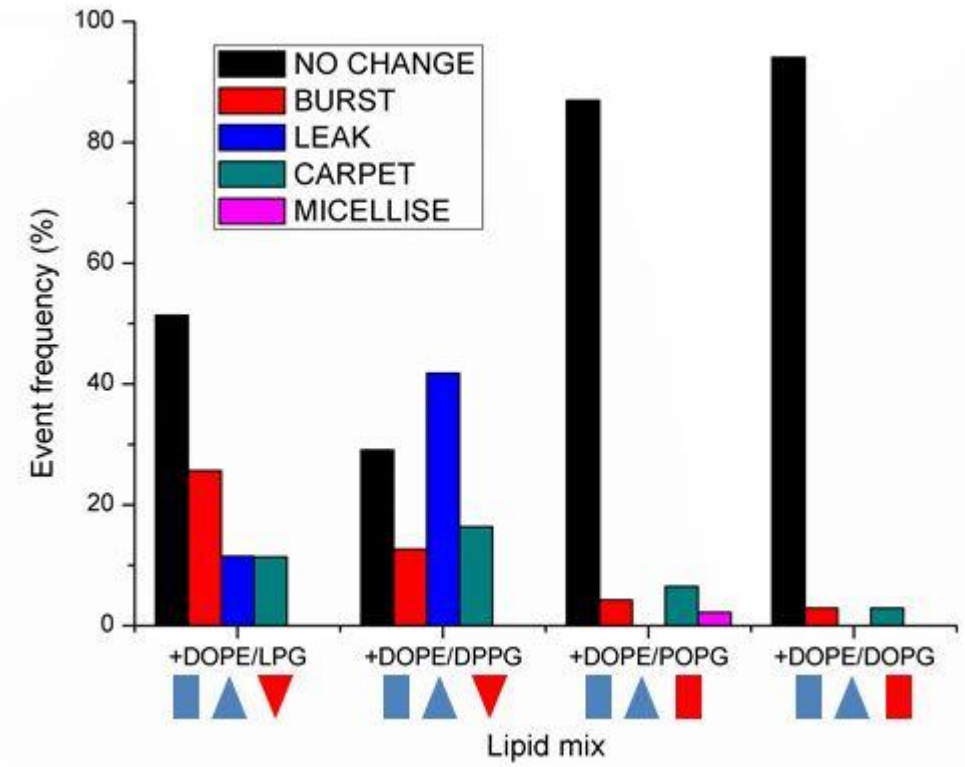

Figure 3.7: PIE-profiles for DOPC membranes doped with the adulterant lipids noted beneath the profile, after exposure to 1 µM M2a, with the lipid topographies of each membrane displayed as geometric shapes beneath the relevant profile. Inclusion of LPG within a DOPC:DOPE membrane produces a profile dominated by bursting, with lesser amounts of pore-mediated leakage and carpet mechanism. The DOPC:DOPE membrane doped with DPPG produces the highest M2a activity of all the lipid systems tested, with the PIE-profile comprised mainly of pore-mediated leakage. M2a is almost inactive within both the POPG and DOPG containing membrane systems, with activity < 15 %.

The positive curvature inducing LCAMP magainin is activated in membranes with similar (i.e. positive) topography anionic lipids, like DPPG (S = 0.78), and deactivated in membranes with containing lipids possessing packing parameters closer to one, like DOPG. The PIE-profiles obtained for the DOPC:DOPE:LPG membrane system are remarkable consistent for both 1 µM melittin and magainin, with both peptides displaying moderate activity of 71 and 49 % respectively. The profiles highest frequency PIE is bursting, and both show identical amounts of the pore-mediated leakage and carpet events. Addition of the extreme topography lipid LPG produces PIE-profiles that are almost identical for both of the LCAMPs, suggesting that the activity of the peptide within LPG containing membrane systems may primarily be due to its interactions with the lyso-lipid. Interestingly, the DOPC:DOPE:DOPG membrane system exposed to M2a was in fact more stable than a peptide-free system under identical flow conditions, with 94.1 % of vesicles surviving to the end of the experimental timecourse, compared to 90.5 % for the peptide-free system. Replacement of the DOPE to create the DOPC:DPPC:X systems, produced the PIE-profiles shown in figure 3.8, after exposure to 1 µM M2a. The first member of the DOPC:DPPC:x system contains the anionic lipid DOPG, with unsaturated fatty acids and deactivates M2a, with less than 12 % of the 76 GUVs (average diameter of 19.4 +/- 7.7 µm) producing a PIE. The second member of the DOPC:DPPC:X membrane system contains the anionic lipid DPPG, and is almost fourfold more active than the DOPG containing membrane (45.8 % active), producing a PIE-profile containing absolutely no bursting events, the only membrane system for either melittin or magainin to demonstrate no absolute membrane failure events.

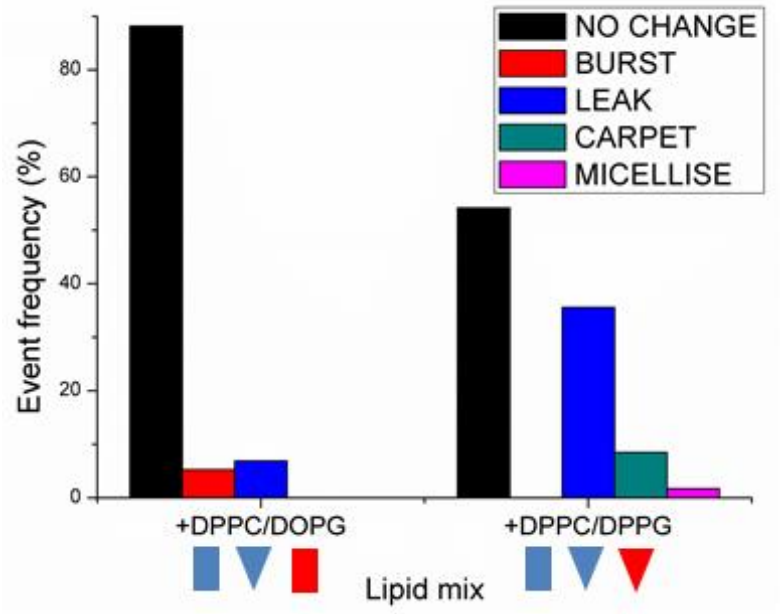

Figure 3.8: Graphs displaying the PIE-profiles for DOPC membranes doped with the lipids indicated, after exposure to 1 µM M2a, with the lipid geometries indicated by the block shapes under the profiles. Inclusion of DPPC and DOPG within the membrane deactivates magainin, with < 15 % activity. Replacing the DOPG with DPPG significantly increases peptide activity to ~ 50 %, with the PIE-profile dominated by pore-mediated leakage.

The PIE-profiles for the DOPC:DPPC containing membrane systems again demonstrate the ability of the anionic lipid DOPG to deactivate M2a, where the charge clustering of anionic lipids with opposite membrane curvature to the LCAMP almost completely removes the ability of the peptide to disrupt the target membrane. Positive curvature anionic lipids have the opposite effect, with the three most active membranes also containing the three anionic lipids with lowest packing parameters; DOPC:DOPE:DPPG (70.9 % active); DOPC:DOPE:LPG (48.6 % active) and DOPC:DPPC:DPPG (45.8 % active). This pattern suggests that the topographic qualities of the anionic lipids clustering around a membrane-bound magainin helix are the key to the peptides activity.

3.6. Quaternary system PIEs

The quaternary lipid system DOPC:DOPE:DPPG:DOPG features different topography in its anionic lipids, and produced a different PIE-profile from the ternary DOPC:DOPE:DPPG and DOPC:DOPE:DOPG systems when exposed to 1 µM melittin, shown in figure 3.9. Inclusion of opposing topography anionic lipids favours both pore-mediated leakage and micelle events, in a total of 36 GUVs with an average diameter of 19.0 +/- 5.7 µm, resulting in the highest frequency of micelle events of all the membrane systems tested (38.9 %). The ternary lipid systems display the effects of including a single topography anionic lipid, with the positive curvature inducing DPPG producing one of the less active melittin profiles (65.1 % active), with the bursting frequency of 41.9 % threefold higher than the next most frequent event (pore-mediate leakage at 14 %). Inclusion of the anionic DOPG lipid, which possesses significantly higher hydrophobic volume than DPPG favoured different PIEs, still producing a high rate of bursting (34.1 %) but the highest frequency PIE is now the carpet mechanism at 41.3 %.

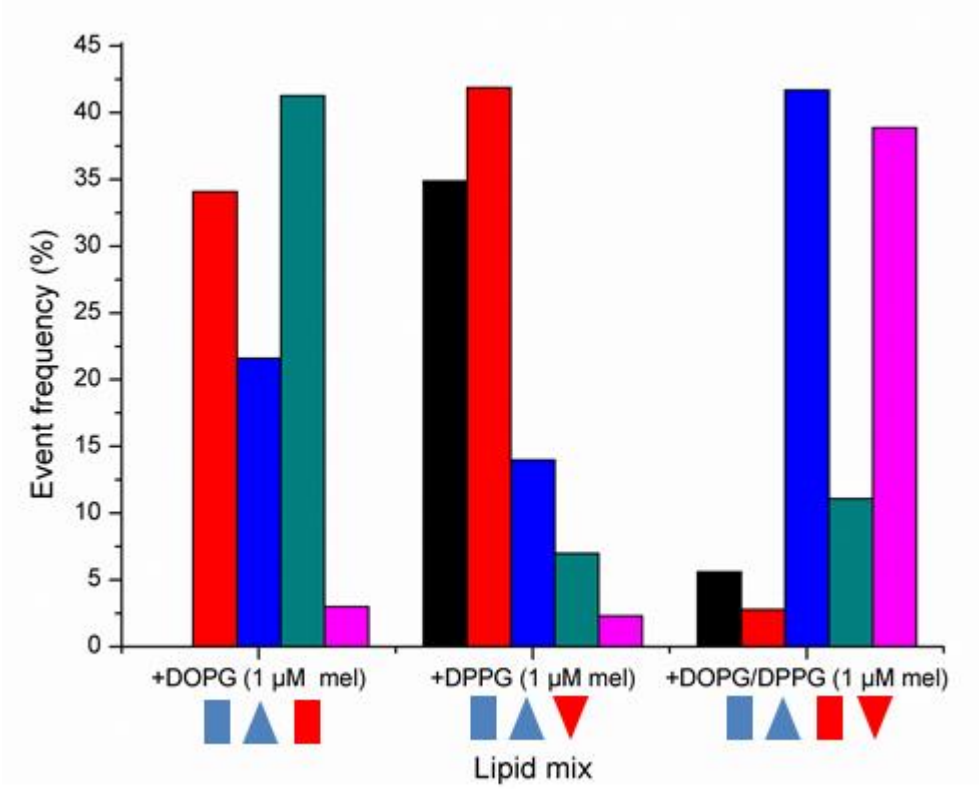

Figure 3.9: PIE-profiles for the lipid mix DOPC:DOPE:DOPG:DPPG, produced after exposure to 1 µM melittin, with the ternary lipid mixes DOPC:DOPE:DOPG and DOPC:DOPE:DPPG included for comparison. Membrane topography depicted by the block shapes below each profile, with zwitterionic lipid topography shown in blue, and anionic lipid topography shown as red. Inclusion of multiple anionic topographies produces a large shift in PIE-profile compared to the monotopographic anionic membranes, which themselves produce significantly different profiles. The quaternary mix is dominated by pore-mediated leakage and micelle events, with bursting events occurring at much lower frequency than in the ternary lipid systems. Compared to the DOPG containing lipid mix, bursting and carpet mechanisms are reduced in the quaternary system, and pore-mediated and micelle events occur much more frequently. Compared to the DPPG containing system, the quaternary is much more active, with less bursting events, and a much higher frequency of pore-mediated and micelle events.

A membrane containing multiple anionic topographies produces a significantly different PIE-profile from either of the membranes containing homogeneous anionic topographies, and indeed, different from any other lipid mix tested. Analysis of the PIEs of the quaternary lipid system after exposure to 1 µM magainin produced the PIE-profile shown in figure 3.10, from a total of 75 GUVs with an average diameter of 16.5 +/- 7.3 µm. Unlike the melittin profile, exposure to magainin produced a profile displaying event frequencies in between those produced in the companion ternary lipid mixes, featuring single topography anionic lipids. Activity was 46.7 % in the DOPC:DOPE:DOPG:DPPG membrane system, compared to 70.9 and 5.9 % in the DOPC:DOPE:DPPG and DOPC:DOPE:DOPG systems respectively. This midway trend continued for all the PIEs recorded for the quaternary lipid system; bursting was 9.3 % compared to 12.7 and 2.9 % in the ternary systems (average 7.8 %); pore-mediated leaking was 18.7 % compared to the 20.0 % ternary average; carpet mechanism was 13.3 % compared to 16.4 and 2.9 % (average 9.65 %).

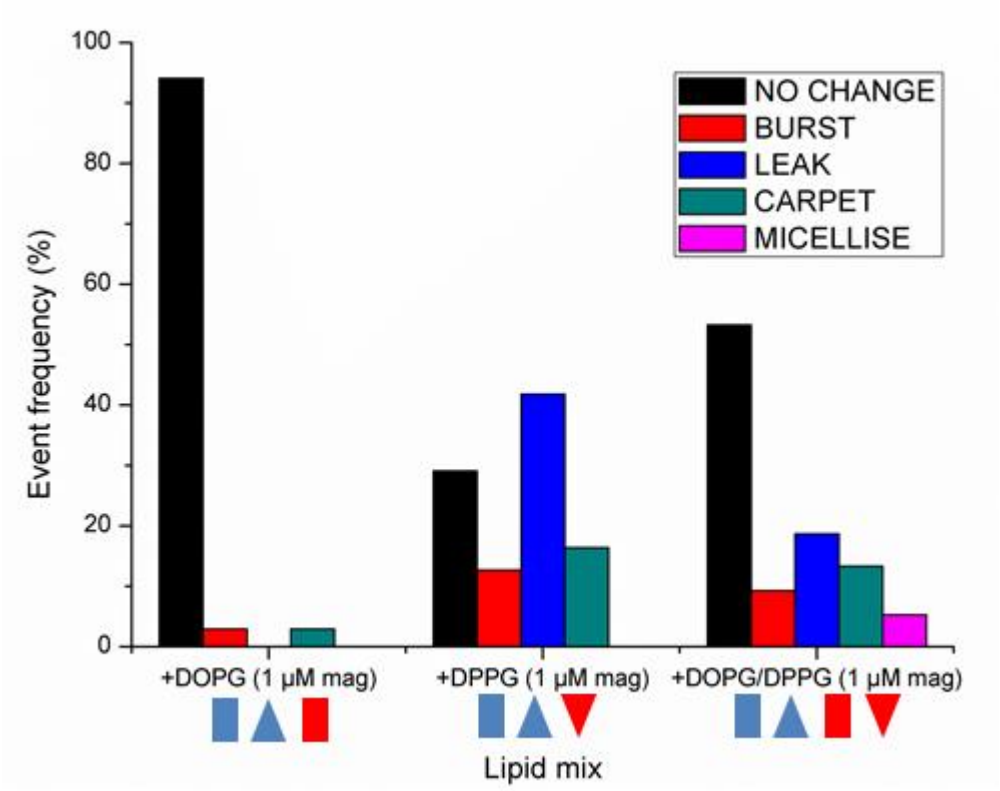

Figure 3.10: PIE-profiles for the quaternary lipid mix DOPC:DOPE:DOPG:DPPG, produced after exposure to 1 µM M2a, with the ternary lipid mixes DOPC:DOPE:DOPG and DOPC:DOPE:DPPG included for comparison. The lipid topography for each membrane is depicted by the block shapes below each profile, with zwitterionic lipid topography shown in blue, and anionic lipid topography shown as red. Inclusion of multiple anionic topographies produces a PIE-profile between those produced by membranes containing single anionic lipid topography, which themselves produce significantly different profiles. The quaternary mix is not dominated by any single PIE, with pore-mediated leakage being the favoured PIE event at 18.7 %, compared to 13.3 % for carpet and 9.3 % for bursting events. The peptide activity lies between the two ternary lipid systems at 46.7 %, compared to 70.9 and 5.9 % for the three component lipid vesicles.

3.7. Fatty acid unsaturation geometry and PIEs

The influence of unsaturated bond geometry was demonstrated by the inclusion DEPG within a DOPC:DOPE base membrane. DEPG contains 18:1 (9E) fatty acid chains, where the unsaturated bond takes a *trans* isomeric form, as opposed to the *cis* form found in the rest of the unsaturated lipids tested, i.e. the 9Z fatty acid chains found in DOPE/DOPC/DOPG etc. The *trans* DEPG produces the PIE-profile shown in figure 3.11, after exposure of a total of 31 GUVs with an average diameter of 13.8 +/- 3.7 µm to 1 µM melittin, and displays the highest level of bursting for any lipid mix (87.1 %). The dramatic differences produced by changes in the fatty acid isomerism of the anionic component of the membrane, demonstrates the strong dependence of melittin action on the lipid topography of the target membrane. *Trans* isomerism reduces the hydrophobic volume of the lipid; the *trans* bond reduces the kink introduced in the acyl chain by the unsaturation, limiting lipid splay compared to *cis* unsaturated acyl chains.

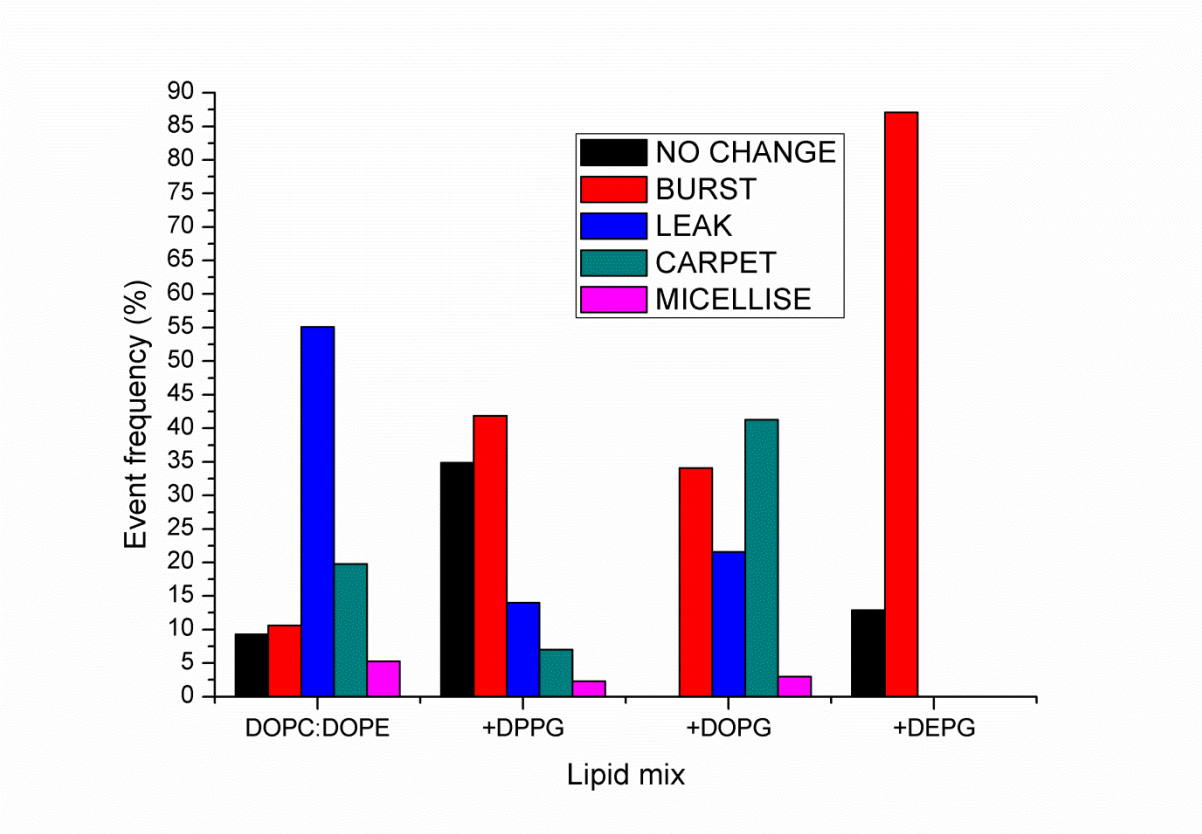

Figure 3.11: Comparison of the PIE-profiles obtained for the inclusion of the 18:1 (9E) fatty acid containing lipid, in a DOPC:DOPE membrane exposed to 1 µM melittin, together with the DOPC:DOPE and DPPG and DOPG doped membranes for comparison. The DEPG containing membrane produces a profile dominated by bursting PIEs, more than twofold higher than either of the other anionic membranes, and the highest recorded for any lipid mix. Bursting is the only PIE recorded for the 9E fatty acid lipid, while the other lipid mixes produce much more varied PIE-profiles.

The isomerism change to the membrane resulted in only bursting PIEs being produced, after exposure to membrane-bound melittin. DEPG membranes exposed to 1 µM magainin display a much less extreme shift to their PIE-profile, shown in figure 3.12, which records the PIEs recorded from a total of 95 GUVs with an average diameter of 17.2 +/- 6.3 µm. Magainin is only mildly active in DEPG membranes, recording an activity of 25.8 %, compared to the activity of 87.1 % recorded for melittin. The much higher activity of melittin in DEPG containing membrane suggests that changes in fatty acid isomerism at the depth in the membrane represented by the ninth carbon, i.e. 9Z or 9E isomerism, produces a much greater effect on the free energy of the lipid-melittin aggregate, than it does on the lipid-magainin aggregate. The complete lack of any other PIEs than bursting in the melittin/DEPG PIE-profile, suggests that the change in fatty acid isomerism totally disfavours all the other PIEs, as no other lipid mix produced a profile so dominated by bursting. The magainin/DEPG profile contained bursting as its highest frequency event, but also low levels of the other three PIEs, i.e. pore-mediated leakage; carpet mechanism and micelle events. This suggests that M2a is much less sensitive to changes in the acyl chain at the depth represented by the ninth carbon in the chain.

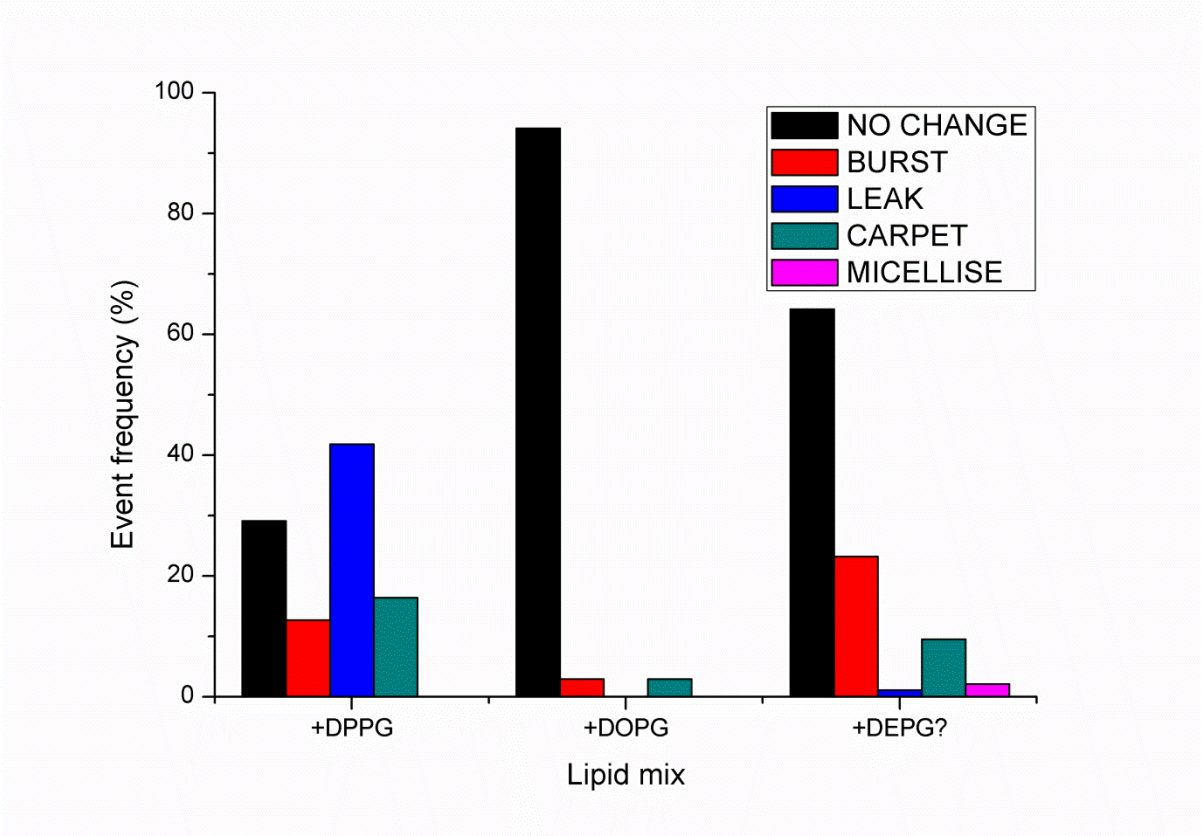

Figure 3.12: Comparison of the PIE-profiles obtained for the inclusion of the 18:1 (9E) fatty acid containing lipid, in a DOPC:DOPE membrane exposed to 1 μM magainin, together with the DOPC:DOPE:DPPG and DOPC:DOPE:DOPG membranes for comparison purposes. The DEPG containing membrane produces activity midway between the two companion membrane systems, displaying 35.8 % activity, compared to 70.9 and 5.9 % activity for the DPPG and DOPG containing membrane systems respectively. Bursting was the highest frequency PIE, but unlike the melittin exposed system, DEPG containing membranes displayed other PIEs, when exposed to the same concentration of magainin.

3.8. All-or-none versus graded leakage

Unlike many reports within the literature, we found no fundamental difference in the pore-mediated leakage from the entrapped vesicles. The all-or-none model proposes that once leakage has been initiated by the peptide, it will continue until all the vesicular contents have escaped, while the graded model proposes that only partial leakage will occur, and then membrane will reseal. Under our more rigorous, robust and repeatable experimental conditions, it is possible to clearly state that both this models are operating via the same mechanism, but merely following different leakage kinetics, as once leakage initiates under constant peptide binding conditions it continues until the vesicles contents are depleted.

3.9. PIE average initiation times

The timings of the PIEs varied considerably between membranes with differing lipid compositions, and the complete timing list for the lipid mixes mentioned in this chapter are presented in the tables 3 and 4, for the LCAMPS magainin and melittin. The three membrane systems demonstrating the fast average occurrence of each PIE were ringed with the following colours, to highlight them for further discussion; fastest bursting membranes (red); fastest leaking (blue); fastest carpet mechanism

(turquoise) and fastest micelle events (pink). Note, only membrane PIE timings with >3 GUVs were included in the fastest rings.

LIPID MIX	(μM)	T_{BURST}	SD_{BURST}	T_{LEAK}	SD_{LEAK}	T_{CARPET}	SD_{CARPET}	$T_{MICELLE}$	$SD_{MICELLE}$
DOPC	1	762.5	1468.3	1961.1	2654.8	3600.0	282.8	158.3	123.3
DOPC	5	2062.5	1433.2	4871.7	1720.7	3169.4	1013.3	2000.0	-
DOPC:DPPC	1	2495.7	2631.3	3623.4	2121.6	2926.6	2181.4	2544.7	1826.7
DOPC:DPPC	5	402.5	453.8	1089.3	717.5	2093.8	1837.2	617.9	466.1
DOPC:DOPE	1	1570.8	1581.0	3273.3	2103.3	1347.6	1730.3	2341.7	2020.8
DOPC:DOPE	5	2015.3	1871.7	3327.3	2103.3	1828.3	2114.7	3583.3	2756.6
DOPC:DPPC:DPPG	1	1417.9	879.0	2541.0	1375.4	2553.6	2921.2	1087.5	1396.5
DOPC:DPPC:DOPG	1	616.7	226.8	450.6	174.7	526.9	328.0	361.7	280.2
DOPC:DPPC:DOPG	5	1366.7	444.6	1333.3	1267.5	812.5	760.1	-	-
DOPC:DOPE:DPPG	1	3736.1	2595.9	4041.7	2574.9	258.3	232.3	425	-
DOPC:DOPE:DOPG	1	1187.3	595.8	1556.8	1216.8	1650.4	1257.7	725	-
DOPE:DOPE:DOPG	5	219.4	163.2	-	-	337.5	283.2	-	-
DOPC:DOPE:DEPG	1	1935.2	937.2	-	-	-	-	-	-
DOPC:DOPE:POPG	1	4367.1	2243.5	4351.4	1672.4	175	-	-	-
DOPC:DOPE:LPG	1	1795.0	2169.9	2222.9	1365.6	1811.5	1851.7	1811.1	2091.2
DOPC:DOPE:DPPG:DOPG	1	550	-	441.7	194.6	1162.5	1181.9	410.7	277.5

Table 3: Table containing the PIE timings for the membrane systems exposed to the LCAMP melittin. Included within the table are the lipid mixes tested, the concentration of melittin the membranes were exposed to in μM, the average timings for the four PIEs (T_{burst}/T_{leak}/T_{carpet}/$T_{micelle}$), and the standard deviations (SD) for each. The ringed timings are the members of the three fastest occurrences that occur within the membrane systems exposed to melittin.

LIPID MIX	(μM)	T_{burst}	SD_{burst}	T_{leak}	SD_{leak}	T_{carpet}	SD_{carpet}	$T_{micelle}$	$SD_{micelle}$
DOPC:DPPC:DPPG	1	-	-	3255.4	1619.7	1770.0	1657.1	5250.0	-
DOPC:DPPC:DOPG	1	1593.8	1939.0	1815.0	1086.9	-	-	-	-
DOPC:DOPE:DPPG	1	4407.1	2037.9	289.5	301.9	1808.3	2183.0	-	-
DOPC:DOPE:DPPG	5	1284.3	1527.1	2577.5	1880.8	1198.1	793.4	1250.0	-
DOPC:DOPE:DOPG	1	1500.0	-	-	-	2000.0	-	-	-
DOPC:DOPE:DEPG	1	4971.6	2385.1	1000.0	-	3636.9	1850.7	3350.0	141.4
DOPC:DOPE:POPG	1	525.0	530.3	-	-	1241.7	1683.4	350.0	-
DOPC:DOPE:LPG	1	1677.8	2438.3	3191.7	3033.2	187.5	59.5	-	-
DOPC:DOPE:DPPG:DOPG	1	3241.7	2607.3	3421.9	1885.5	3602.5	2514.0	1493.8	1169.1

Table 4: Table containing the PIE timings for the membrane systems exposed to the LCAMP magainin. Included within the table are the lipid mixes tested, the concentration of melittin the membranes were exposed to in μM, the average timings for the four PIEs (T_{burst}/T_{leak}/T_{carpet}/$T_{micelle}$), and the standard deviations (SD) for each. The ringed timings are the members of the three fastest occurrences that occur within the membrane systems exposed to melittin.

In conjunction with the PIE frequency, the average initiation time of an effect within a particular membrane provide information on two factors. Firstly, a quick initiation time indicates that the lipid-LCAMP interactions necessary to start the PIE occur quickly, with a slow initiation time indicating the converse situation, where the effect requires considerable binding of the peptide and longer lipid-LCAMP interaction times to initiate. Secondly, the population of each effect demonstrates whether the individual effect is energetically favoured within that membrane. For example, a quick initiation time with a low event population, suggests only a few membrane-bound peptide molecules are necessary to start that effect, but the process is high energy and unflavoured within that membrane system. The converse situation, where a long initiation time is coupled to a high event frequency, suggests the opposite; that the process requires more membrane-bound LCAMP and/or longer timescale lipid-LCAMP interactions to produce the event. The first thing noted about the PIE timings is the high variability of the initiation of the events, reflected in the large standard deviations. Secondly, increasing the concentration of the LCAMP fivefold does not always result in quicker event timings; e.g. DOPC vesicles exposed to 1 μM melittin displays an average bursting time of 762.5 s, compared to 2062.5 s for vesicles exposed to 5 μM melittin. It is interesting to note which membrane systems returned the quickest initiation of each PIE for each peptide, and to comment on the lipid topography and physiochemical properties of each lipid within the vesicle. Generally speaking it is interesting to note that although magainin was typically less active than melittin within all the membrane systems tested, the peptide still returns several fastest initiations of PIEs, suggesting that although magainin may be more selective than melittin, it is nevertheless capable of inducing quick membrane disruption within target membranes, if the lipid composition permits.

3.9.1. Burst initiation times (red circles)

Melittin rapidly induces bursting within DOPC:DPPC and DOPC:DOPE:DOPG membrane systems at a concentration of 5μM, the two quickest timings for any lipid mix tested. For DOPC:DPPC the average bursting time of 402.5 s is displayed by 14.4 % of the vesicles, suggesting that rapid binding of 5 μM melittin pushes a small proportion of the vesicle membranes to complete failure, without triggering any other PIEs. Only those membranes which survive for longer periods go on to experience alternative PIEs, with pore-mediated leakage being the most common (35 %). In the DOPC:DOPE:DOPG membrane system exposed to 5 μM melittin, a contrasting situation occurs with relation to the proportions of GUVs that quickly initiate bursting, with ~88 % displaying the effect at an average time of 219.4, the quickest average bursting time displayed by any membrane-LCAMP system. Three quarters of the remaining 12 % of vesicles go on to exhibit the carpet mechanism PIE (9.3 % total). The third fastest system to initiate bursting is the DOPC:DOPE:POPG membrane system, after exposure to 1 μM magainin; unlike the melittin systems, where the higher peptide concentrations returned the fastest bursting times, a magainin system at the lower concentration displayed the fastest bursting time, indicating that lipid composition is more important for magainin than peptide concentration for initiating the bursting PIE.

3.9.2. Pore-mediate leakage initiation times (blue circles)

The quickest membrane to initiate pore-mediate leakage effects was the DOPE:DOPE:DPPG system exposed to 1 μM magainin, where 41.8 % of GUVs displayed pore formation with an average initiation time of 289.5 s. This time was much quicker than any of the other PIEs observed within this membrane system, indicating that at this peptide concentration, the lipid-LCAMP interactions rapidly form toroidal

pores. The higher 5 μM magainin concentration decreased the initiation times for the other PIEs, but the average initiation time for the formation of pores increased by almost an order of magnitude. This indicates that rapid binding of the LCAMP at the higher peptide concentration deactivates the pore formation process, perhaps via decreasing the time available for peptide diffusion within the membrane. The next two fastest initiations of pore-mediate leakage were both within 1 μM melittin systems, and displayed very similar times; the DOPC:DPPC:DOPG system returned a 56.9 % pore-mediated leaking frequency with an average initiation time of 450.6 s, and the DOPC:DOPE:DPPG:DOPG quaternary system produced 41.7 % pore formation with a time of 441.7 s. Note that all these systems contain lipid displaying opposite topography, i.e. DPPC (packing parameter of 0.78) and DOPG (packing parameter of ~1) in the DOPC:DPPC:DOPG system, and DOPE (packing parameter of 1.41) and DPPG (packing parameter of 0.81) in the DOPC:DOPE:DPPG:DOPG system. Together with the negative curvature induction of the peptide, variation in lipid topography produces rapid pore formation in membrane systems exposed to melittin, although inclusion of two opposing anionic topographies in the quaternary system seems to disfavour pore formation slightly. All three membrane systems that produced rapid pore formation went on to record pore-mediated leakage as their highest frequency PIE, suggesting that when the lipid composition allows pore formation, it is the energetically favoured lipid-peptide interaction.

3.9.3. Carpet mechanism initiation times (turquoise circles)

The DOPC:DOPE:LPG membrane system exposed to 1 μM magainin produced the fastest initiation of carpet mechanism, for all lipid mixes tested, and again the average time of 187.5 s was much smaller than the initiation times for the other PIEs demonstrated by the system. Only 11.4 % of vesicles produced the carpet mechanism PIE, with 48.6 % total activity in that membrane system, with the highest frequency effect being pore-mediated leaking. Melittin at 1 μM in the DOPC:DOPE:DPPG membrane system produced the second fastest average initiation time for carpet mechanism effect, of 258.3 s, with 7 % of vesicles displaying the effect (65.1 % overall activity). With the quick initiation time but low event population, this suggests that although the conditions necessary for initiation of carpet mechanism occur quickly, the process is energetically unflavoured, compared to the other PIEs; i.e. in contrast to the bursting effect, which displayed an average initiation time of > 3700 s but a high population of 41.9 %. These facts suggest that this PIE requires a longer time for initiation, but is much more energetically favoured under identical conditions, than the carpet mechanism within this membrane system. The third fastest average initiation time for the carpet mechanism was recorded in the DOPC:DOPE:DOPG membrane exposed to 1 μM melittin, with 41.3 % of GUVs from a total activity of 100 % producing this effect, making it the highest frequency PIE. Compared to DOPC:DOPE:DPPG system, replacement of the positive curvature DPPG with DOPG, produces both a fast initiation time and a high frequency event. The increased hydrophobic volume of DOPG leads to both quick onset of the conditions for the carpet mechanism, and in contrast to the DPPG containing system, energetically favours the process.

3.9.4. Micelle initiation times (pink circles)

Although the micelle PIE is only present at low levels in most membrane systems, one of the quickest average initiation times of 410.7 s, comes from the quaternary DOPC:DOPE:DPPG:DOPG membrane system, which contains the highest frequency of micelle PIE displayed by any membrane

system (38.9 %). The next two highest frequency of micelle events occurred in the DOPC:DPPC membrane system, with 13.1 and 9.3 % recorded after exposure to 1 and 5 μM melittin respectively. The DOPC:DPPC systems returned initiation times of 2544.7 s for 1 μM melittin, indicating that at the same peptide concentration, the lipid-LCAMP interactions for the micelle event both require less membrane-bound peptide and are much less energetically favoured, than in the DOPC:DOPE:DPPG:DOPG membrane system. Addition of DOPG to the DOPC:DPPC:X system produced the second fastest average initiation time for the micelle PIE, recording a time of 361.7 s when exposed to 1 μM melittin. With just 3.5 % of vesicles producing the effect, the addition of DOPG to the DOPC:DPPC membrane decreases the initiation time of the micelle effect by almost fivefold, compared to the base DOPC:DPPC membrane system. This indicates that the rapid clustering of DOPG around the membrane-bound melittin helix within the bulk DOPC:DPPC membrane rapidly produces the conditions needed for the micelle effect, but also energetically disfavours the process. This suggests that aggregation of melittin with lipids featuring bulky hydrophobic volumes, like DOPG with its two 18:1 (9Z) fatty acid tailgroups, is a vital part of initiating the micelle PIE. This suggestion receives support upon consideration of the membrane with the fastest average initiation times for the micelle event, the one component DOPC system. Within this system the membrane-bound peptide can only interact with 18:1 (9Z) containing lipids, and hence produces the rapid initiation of micelle events, the low population of 10 % of DOPC GUVs showing this effect suggests however that it is still energetically disfavoured.

3.10. PIE summary

Doping a base membrane of cylindrical (i.e. neutral) geometry DOPC lipids with adulterant lipids of varying topography and charge, produces a range of PIE-profiles after exposure to the LCAMPs melittin and magainin, with anionic lipids producing a greater shift from the DOPC profile than zwitterionic lipids for both peptides. The DOPC:DOPE:X and DOPC:DPPC:X membrane systems exposed to melittin separate into two distinct groups of PIE-profiles, based on their anionic lipid topography; one group characterised by lower hydrophobic volume anionic lipids, and the other characterised by higher hydrophobic volume anionic lipids. The overall activity of the lipid-melittin system appears to be controlled by the hydrophobic volume of the fatty acids of the anionic lipids within the system. Those containing anionic lipids with lower hydrophobic volume fatty acids (i.e. positive curvature topography lipids like LPG, DPPG and POPG) are significantly less active than those containing DOPG, a negative curvature topography anionic lipid possessing a large hydrophobic volume, caused by its two 18:1 (9Z) oleic acid chains.

The pore-mediated leakage activity of these membranes exposed to melittin however, shows a dependence on the zwitterionic lipid DPPC, with the DOPC:DPPC:X containing systems returning average pore activity of ~55 %, compared to the relevant DOPC:DOPE:X systems average of ~17 %. It can therefore be stated that pore formation is strongly favoured by the presence of DPPC, a zwitterionic lipid, with a large phosphatidylcholine headgroup and low hydrophobic volume. Comparison of the peptide activity of the DOPC:DOPE:X and DOPC:DPPC:X systems, when exposed to magainin also produces two groupings based on anionic lipid topography, but the topographic characteristics for higher activity are reversed compared to melittin. Within lipid-magainin systems, lipids with lower hydrophobic volumes and inverse conical geometry (i.e. LPG and DPPG) activate the peptide, and the highest anionic hydrophobic volume system (DOPC:DOPE:DOPG) returns the lowest activity for any lipid-peptide system tested, lower in fact than a peptide free system under the same experimental

conditions. Unlike melittin, the pore-mediated leakage activity of magainin appears to be independent of the zwitterionic lipid topography, depending only on the anionic content of the membrane.

Despite the trend of lower activity of magainin, compared to melittin within equivalent membranes, the selective magainin displays quick initiation of both leaks and carpet mechanism within certain membranes. This rapid initiation of PIEs once again appears to depend on the topographic character of the anionic membrane components, requiring the presence of large headgroups and low hydrophobic volumes, i.e. inverse-conical geometry negative lipids. It is notable that only certain PIEs occur quickly, for example magainin within DOPC:DOPE:DPPG membranes initiates pore-mediated leakage after an average of 289.5 s, but the other PIEs displayed by this system, the bursting and carpet mechanisms, occur after 4407.1 and 1808.3 s respectively. This indicates that specific electrostatic/steric interactions between DPPG and the membrane-bound magainin helix enables quick pore formation, suggesting that lipid-AMP interactions of inverse-conical anionic lipids with the magainin helix significantly lower the barrier to pore formation. A similar effect is seen in the DOPC:DOPE:LPG system, where the bursting PIE occurs rapidly (187.5 s), and the bursting and pore-mediated leakage PIEs initiate after considerably longer time periods (1677.8 and 3191.7 s respectively). An opposite trend in anionic topography versus PIE initiation time is noticed for the anionic lipid-melittin systems, where quick initiation of PIEs is generally linked to the large hydrophobic volume DOPG lipid, with six of the fastest seven PIEs induced in the anionic systems containing this specific lipid. This indicates that the large hydrophobic volume generated by the two 18:1 (9Z) oleic acid chains can quickly initiate PIEs when interacting with the melittin helix.

4. Pore-mediated leakage in zwitterionic membranes

4.1. Melittin dye-efflux kinetics

The pore-mediated leakage events of the AMP melittin, induced within zwitterionic lipid membranes containing a variety of lipid topographies, display a complex and interesting set of leakage kinetics. This chapter will present the leakage kinetics for melittin, starting with simple one component lipid systems, and gradually increasing the system complexity to include binary zwitterionic membrane systems, to examine the effect of physiochemical properties like fatty acid unsaturation and lipid geometry on the pore-mediated leakage process. The inclusion of two differentially sized fluorescently tagged dextrans within the entrapped GUVs will allow estimation of the LCAMP-induced pore size.

4.1.1. DOPC membrane system

The base DOPC membrane contains only cylindrical topography lipids, with each fatty acid acyl chain containing a single unsaturated carbon-carbon bond, located at the ninth carbon along from the glycerol backbone; i.e. an 18:1 (9Z) acyl chain. When DOPC GUVs containing both 3 and 10 kDa fluorescently tagged dextrans, are exposed to the AMP melittin at a concentration of 1 μM, the enclosed dextrans escape with the kinetics shown in figure 4.1.The leakage kinetics group together into distinct modes displaying similar leakage kinetics, with figure 4.1 displaying the average leakage traces compiled from the following number of vesicles; group 1 compiled from 3 GUVs; group 2 from 6 GUVs; group 3 from 4 GUVs; group 5 from 5 GUVs and group 6 from 3 GUVs. The averaged carpet traces, included for comparison, is compiled from 3 GUVs. The quantised nature of the leakage kinetics suggests that pore-mediated leakage can only proceed via the formation of pores with tightly restricted size and/or number. The standard deviations for the 10 kDa dextrans are larger than the 3 kDa standard errors, indicating the pore-mediated leakage for the larger dextran is subject to increased variability than the smaller molecule. A DOPC lipid membrane is composed of almost perfectly cylindrical lipids; any curvature induction within the membrane must be generated by the AMP itself. The pore-mediated leakage events that generate multi-component traces can be separated into their individual components, and overlaid with the leakage groups compiled from the single component leakage traces. For the DOPC membrane at a melittin concentration of 1 μM, the multi-component traces overlay with the groupings established by the single component traces, and do not result in the creation of any groupings not visible from the single component leakage traces. An example leakage trace containing three components is presented in figure 4.2.

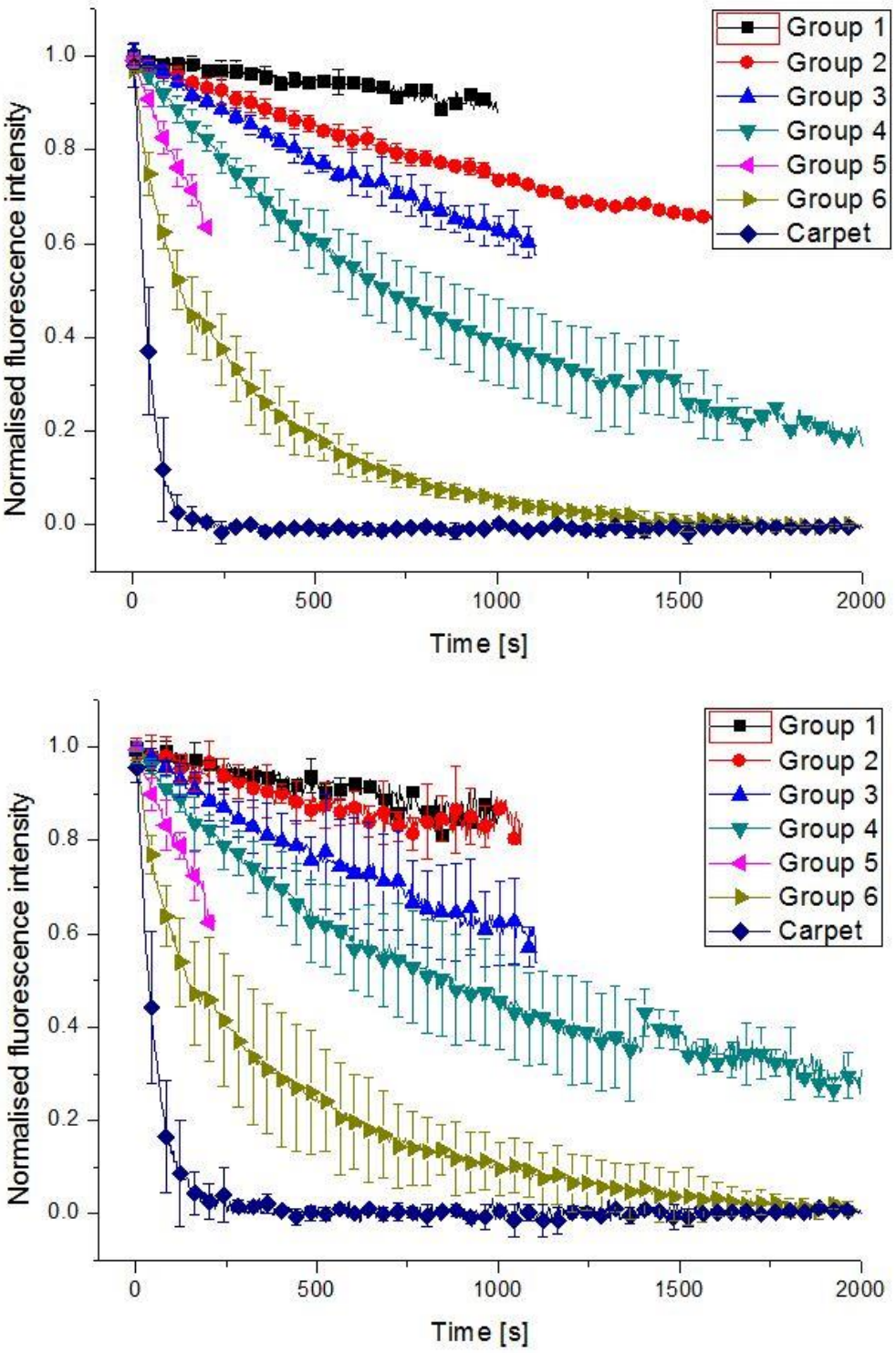

Figure 4.1: Dye leakage kinetics for the dextran-AlexaFluor conjugates contained within DOPC vesicles, after exposure to 1 µM of the AMP melittin, displaying the complete leakage kinetics compiled from the single and multimodal traces. The kinetics for both the 3 kDa (top) and 10 kDa (bottom) traces show distinct grouping into quantised kinetics modes, with the error bars representing the standard deviation for the traces contained within each group. Six pore-mediated leakage groups are visible within the smaller 3 kDa dextrans leakage data, with the carpet mechanism leakage kinetics included for comparative purposes. In contrast to the 3 kDa results, two of the corresponding modes from the larger 10 kDa dextran kinetics follow almost identical kinetics (groups 1 and 2).

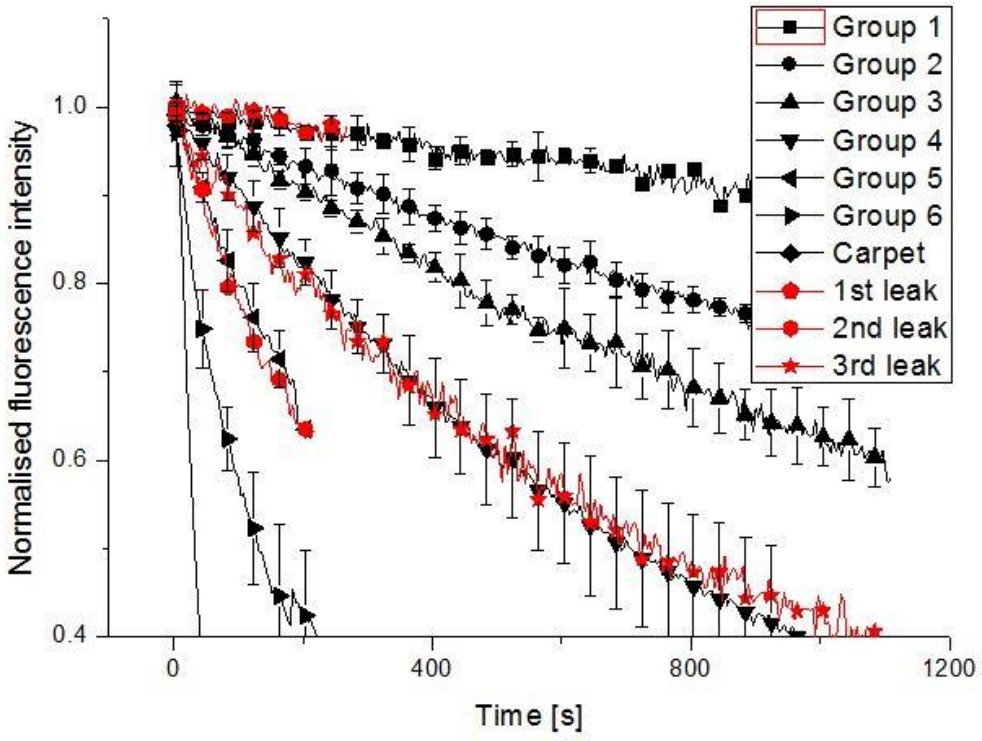

Figure 4.2: Graph demonstrating the overlaying of the individual component leaks from multi-component traces (red), with the kinetic groupings assembled from the single component leakage traces (black). A GUV displaying a three component leaking behaviour was chosen, and demonstrates complex group switching behaviour. The first leakage component (red pentagons) displays leakage kinetics in parallel with group 1, and maintains this behaviour for > 200 s, before switching to match the kinetics of group 5 in its second leakage component (red hexagons). It demonstrates group 5 leakage kinetics for a further 200 s, before beginning its third leakage phase (red stars), where it matches group 4 leakage kinetics until the vesicle contents are completely depleted.

The multi-component leakage traces, where each individual component leak overlays with the leakage kinetic groupings established by averaging the single component leakage traces, provides further evidence for the pore-mediated leakage process occurring via a set of quantised pores. The continual binding of AMP to the lipid membrane during the pore-formation process can alter membrane conditions such that the leakage parameters change from one quantised leakage state to another. When exposed to a melittin concentration of 5 μM melittin, a similar averaged leakage graph for the escape of the enclosed 3 and 10 kDa dextrans can be constructed from the single component leaks, and is depicted in figure 4.3. The number of leakage traces compiled to produce the averaged leakage chart were groups 1 – 3 compiled from 2 GUVs; group 4 from 6 GUVs; group 5 from 3 GUVs and group 6 compiled from 4 GUVs. The carpet group depicted on the chart was produced by averaging the leakage kinetics from 5 vesicles demonstrating the carpet mechanism.

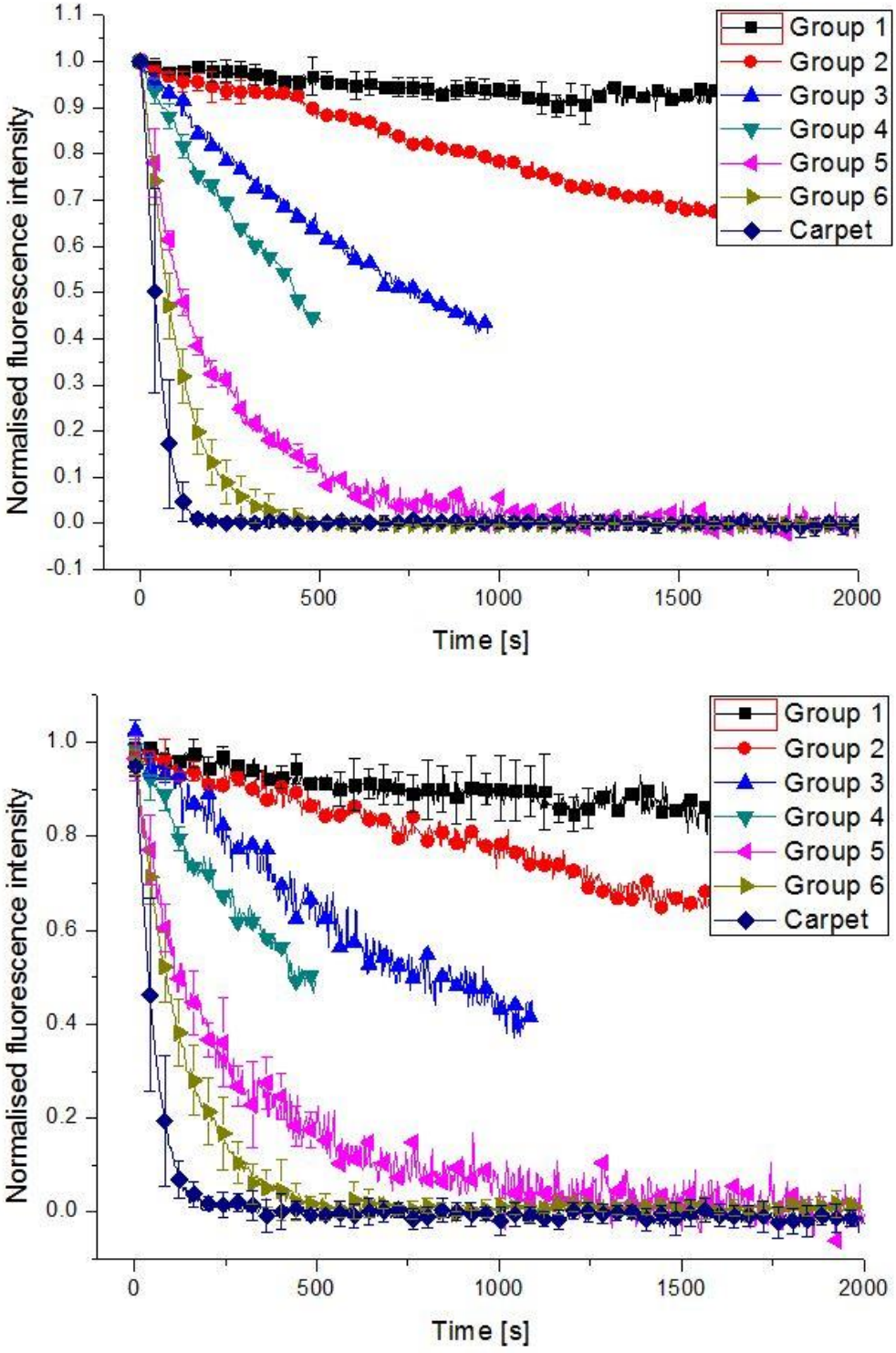

Figure 4.3: Dye leakage kinetics for the pore-mediated leakage process initiated by the exposure of DOPC vesicles to a melittin concentration of 5µM, constructed by averaging the single component leakage traces. The efflux of the 3 kDa (top) and 10 kDa (bottom) dextrans again form distinct groups of similar leakage kinetics.

In contrast to the leakage graphs compiled from the multimodal leakage traces at a melittin concentration of 1 µM, which do not demonstrate the creation of any novel leaking groups, the graphs compiled including the multi-component traces displays a leakage group not found within figure 4.3 (group 3). The novel leakage group follows an individual leakage kinetic in the 3 kDa data, but initially

follows the leakage kinetics of group 4 in the 10 kDa data set, before shifting to slower kinetics after ~450 s.

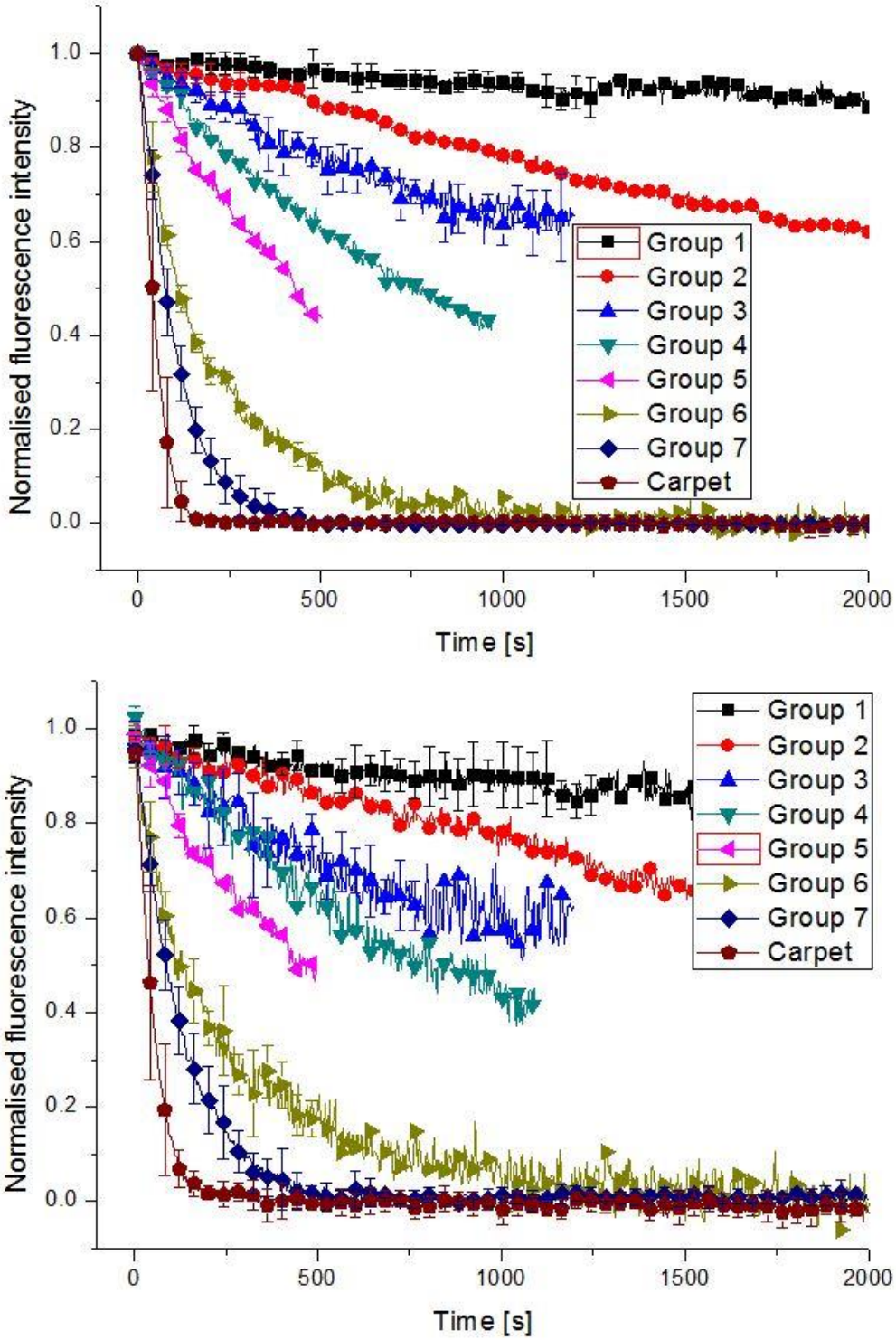

Figure 4.4: Dye leakage kinetics for the pore-mediated leakage process initiated by the exposure of DOPC vesicles to a melittin concentration of 5μM, constructed by averaging the single and multi-component leakage traces. The efflux of the 3 kDa (left) and 10 kDa (right) dextrans again form distinct groups of similar leakage kinetics, with the presence of a new grouping, not present in the graph compiled from the single component leakage traces (group 3).

The graph in figure 4.4 was compiled from the following number of leakage traces; group one from 2 traces; group 2 from 2 traces; group 3 from 8 traces; group 4 from 4 traces; group 5 from 3 traces; group 6 from 8 traces and group 7 from 12 traces. The carpet leakage trace was compiled by averaging 10 leakage traces. To compare the effect of AMP concentration on the dye efflux kinetics induced by melittin from DOPC GUVs, the leakage graphs for both 1 and 5 µM melittin were overlaid, to create the graph shown in figure 44.

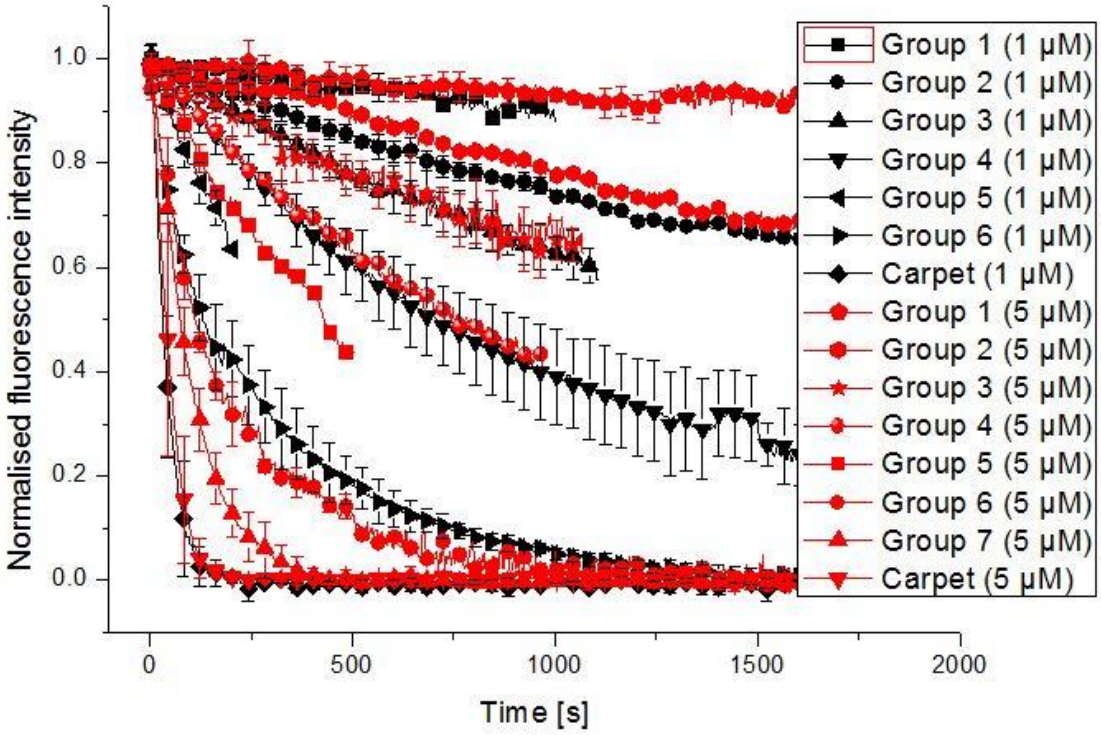

Figure 4.5: Overlaid grouping data for DOPC membrane system, with 1 µM melittin traces shown in black, and 5 µM melittin traces depicted in red. The higher melittin concentration produces traces which almost perfectly overlay with the lower, with the exception of an additional leakage group demonstrating fast leakage kinetics (group 6).

The overlaid data for the two different melittin concentrations match almost perfectly, demonstrating that within mono-topographic membranes, increasing the AMP concentration does not affect the allowed leakage states. Instead the increase of peptide concentration induces faster onset of pore-mediated leakage.

4.1.2. DOPC:DPPC membrane system

Inclusion of DPPC within the DOPC membrane increases topographical variety; DPPC is a lipid possessing positive curvature, induced by its two sixteen carbon saturated fatty acid chains (16:0). Combined with its large choline headgroup, the reduced hydrophobic volume of DPPC compared to DOPC, results in a packing parameter of 0.74 and positive curvature generation within membranes. The leakage data for the DOPC:DPPC (80:20 mol%) membrane system again displayed grouping of the leakage traces into distinct modes, shown in figure 4.6.

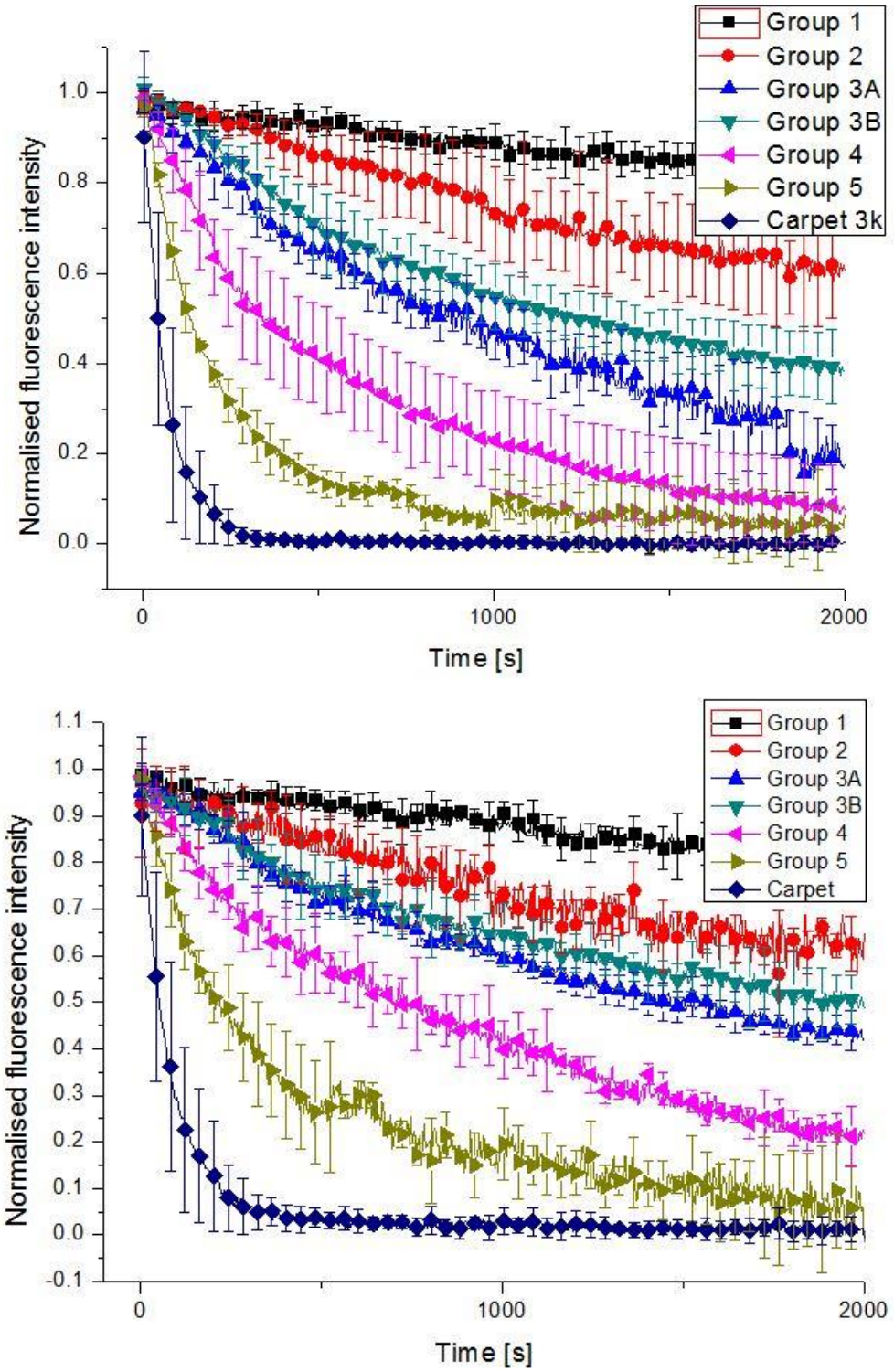

Figure 4.6: Modal dye leakage kinetics for the 3 (top) and 10 (bottom) kDa dextran-Alexafluor markers entrapped within DOPC:DPPC vesicles, exposed to 1 μM melittin, with the error bars representing the standard deviations from the averaged traces within each group. There are seven groupings visible within the leakage kinetics, shown in the diagram key above. Six of the groups represent pore-mediated leakage, with the seventh and fastest leakage group, representing leakage through the carpet mechanism (blue diamonds).

The groupings in figure 4.6 were compiled by averaging 6 traces for group 1; 5 traces for group 2; 10 traces for group 3; 6 traces for group 4; 3 traces for group 5 and 9 traces for the carpet mechanism

group. Similar to the DOPC membrane results, two of the leakage groupings which are clearly separated in the 3 kDa data set, appear to follow almost identical leakage kinetics in the 10 kDa traces (groups 3A and 3B). Multi-component leakage traces can switch between these two groups during the pore-mediated leakage process, as demonstrated in figure 4.7, which splits a 3 kDa leakage trace from a single vesicle into two components which almost perfectly overlay with the two groups. The DOPC:DPPC membrane system produces a similar complex set of leakage groupings to the base DOPC membrane system, featuring six pore-mediated leakage groupings, compared to the six groups seen for the DOPC system.

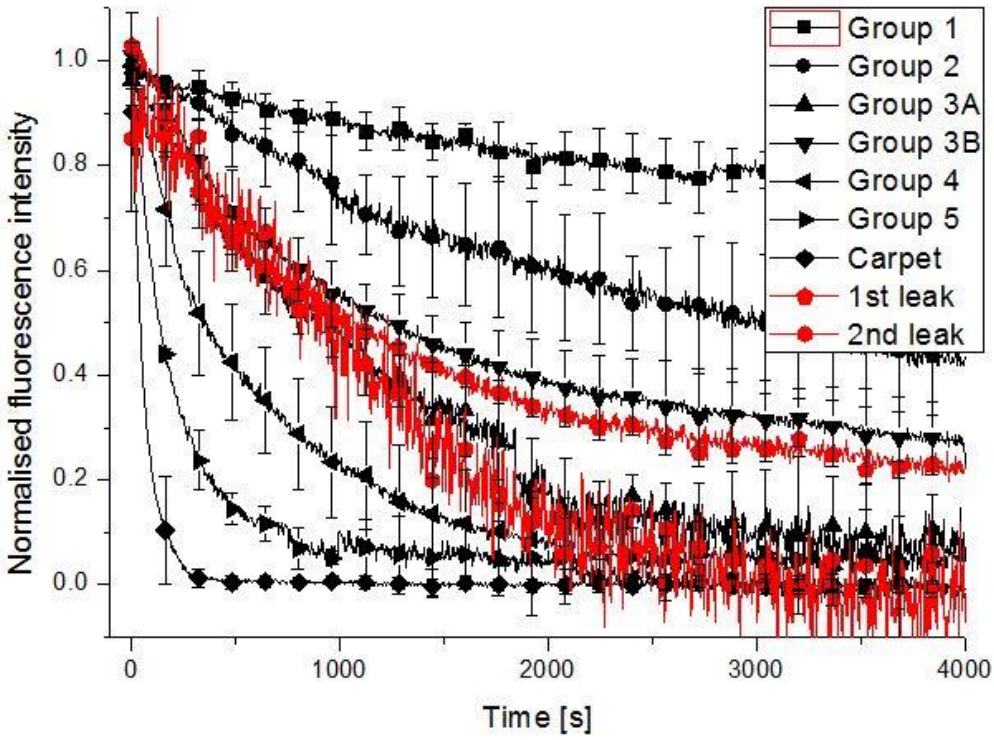

Figure 4.7: Graph displaying the group switching behaviour of the 3 kDa leakage kinetics from a DOPC:DPPC (80:20 mol%) GUV. The trace (red) for the GUV can be separated into two components, and overlaid with the averaged 3 kDa leakage traces (black), demonstrating that conditions in the lipid-peptide systems can change during the pore-mediated leakage process. These changes interrupt the leakage process currently taking place, and force a return to the initial stages of the pore formation process, as demonstrated by the second leak (red hexagons) closely following the kinetics of group 3B (red pentagons) for ~1000 s, before separating to following the faster group 3A kinetics until the vesicle contents are depleted.

The group switching that occurs as depicted in figure 4.7 demonstrates that the pore-mediated leakage process can be interrupted, presumably by continually binding AMPs forcing changes to the lipid-peptide system, and changing the leakage kinetics to another quantised pathway. A further point of interest from the DOPC:DPPC membrane system exposed to 1 µM melittin is that at longer timescales, the leakage kinetics seem to run parallel, indicating that whatever the leakage pattern followed initially by an individual vesicle, the pore-mediated leakage process establishes steady state leakage at longer timescales, shown in figure 4.8.

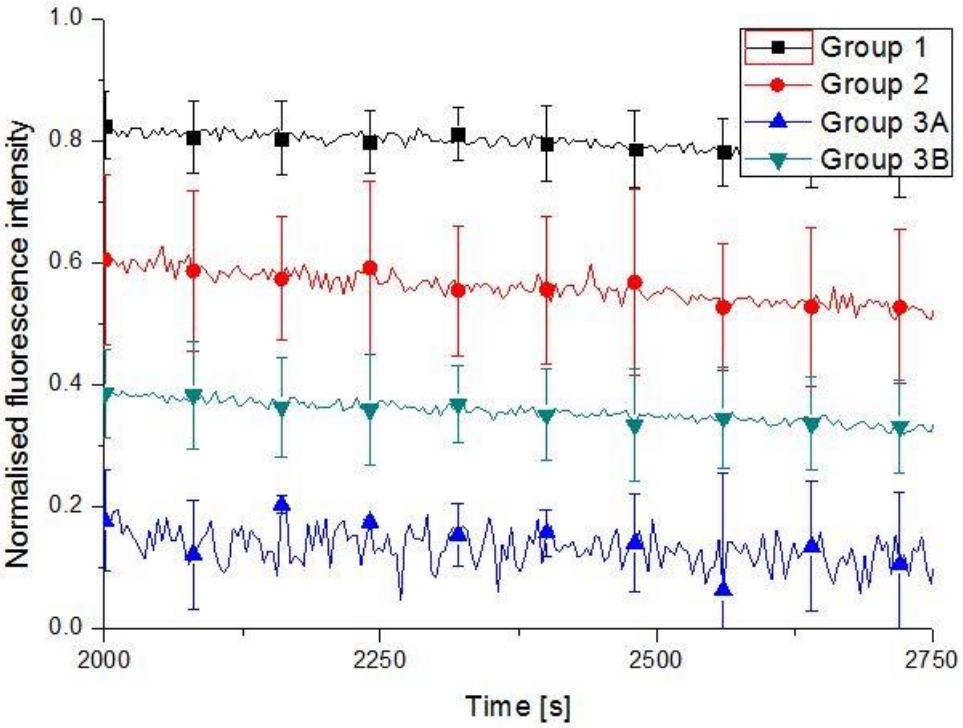

Figure 4.8: Graph demonstrating the parallel nature of the kinetics of the averaged leakage groupings at long timescales, for the DOPC:DPPC membrane system exposed to 1 µM melittin. Linear slope fitting returned values of the slope of group 1 as -4.59 x 10^{-5}, group 2 as -5.07 x 10^{-5}, group 3A as -5.97 x 10^{-5} and group 3B as -4.99 x 10^{-5}. The dye-leakage kinetics of groups 2, 3A and 3B appear to decrease at longer timescales, until they run in parallel with the kinetics of group 1.

The DOPC:DPPC membrane system exposed to 5 µM melittin produces the leakage kinetics displayed in figure 4.9. Clear grouping of the leakage data is again visible within the 3 kDa data set, with the 10 kDa data being less defined. Higher melittin concentration resulted in groups with improved standard errors compared to the lower peptide concentration; i.e. better defined, more distinct groupings of leakage kinetics occurs at a melittin concentration of 5 µM. The merging of two 3 kDa leakage groups into one 10 kDa leakage group is again present, with groups 2 and 3, which follow clearly different kinetics within the 3 kDa data set, follow almost identical kinetics within the 10 kDa data set. The data displayed in figure 4.9 was assembled by the averaging of the following leakage traces for each group; group 1 produced by averaging of 9 traces; group 2 from 3 traces; group 3 from 3 traces; group 4 from 12 traces; group 5 from 4 traces and the carpet mechanism trace from 4 traces. Another feature that reappeared within the 5 µM data set for the DOPC:DPPC membrane system is the matching between the individual multi-component leakage phases, and the leakage groups established by the single-component leakage traces, as demonstrated in figure 4.10.

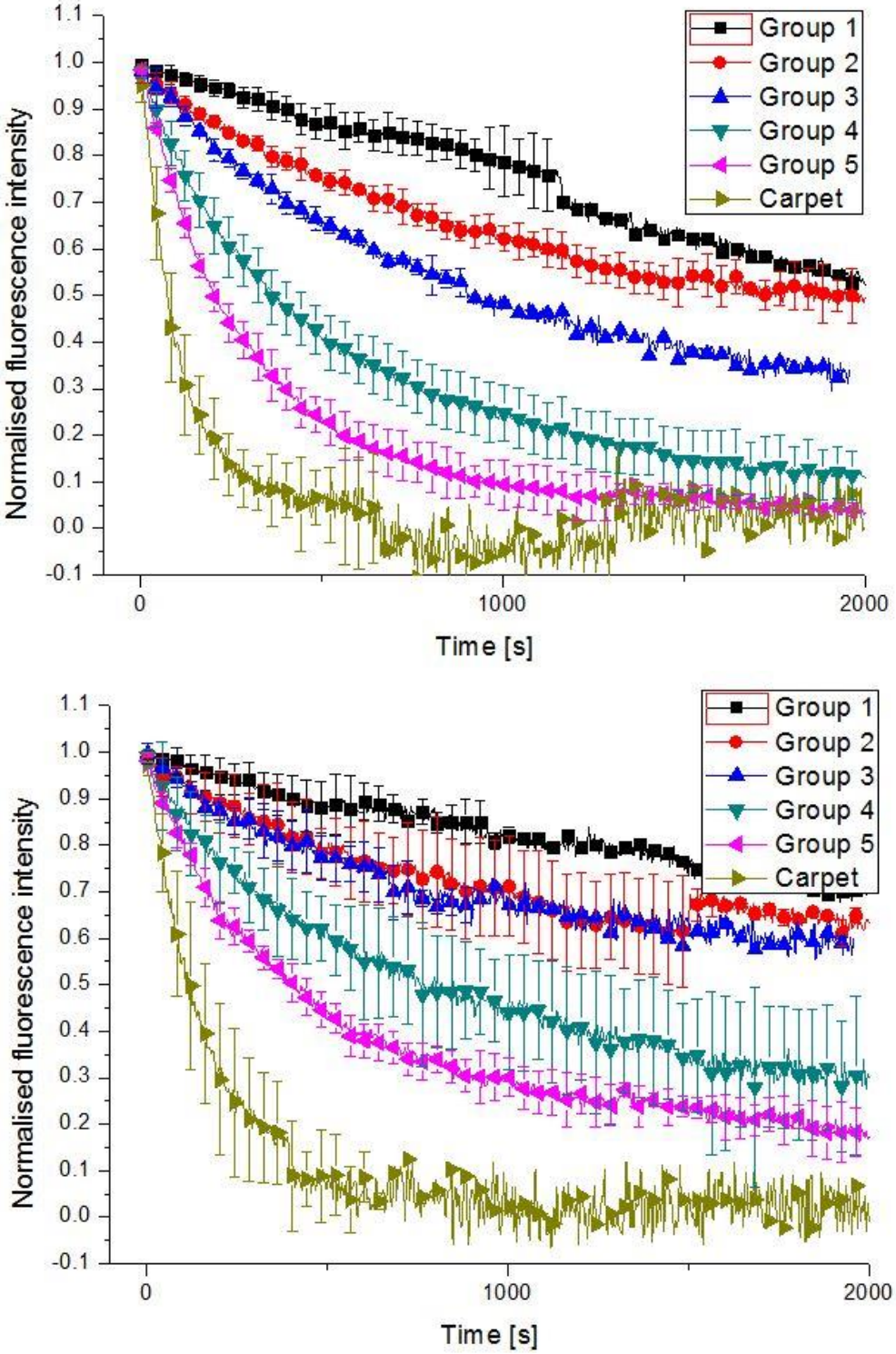

Figure 4.9: Averaged leakage kinetics for the 3 (top) and 10 (bottom) kDa dextrans entrapped within DOPC:DPPC (80:20 mol%) vesicles, exposed to 5 μM melittin. Error bars are the standard deviations from the averaged traces within each group. There are six groupings visible within the leakage kinetics, shown in the diagram key above. Five of the groups represent pore-mediated leakage, with the sixth and fastest leakage group, representing leakage through the carpet mechanism (green triangles).

Figure 4.10 shows a four component leakage trace, which when the individual leakage phases are separated and overlaid with the averaged leakage groups, clearly follow almost identical dye-leakage kinetics to the averaged data. This figure demonstrates that not only can pore-mediated leakage switch

between quantised leakage kinetics during the leakage process, but also that the form of leakage can change, with this vesicle demonstrating a change from pore-mediated to carpet-mediated leakage.

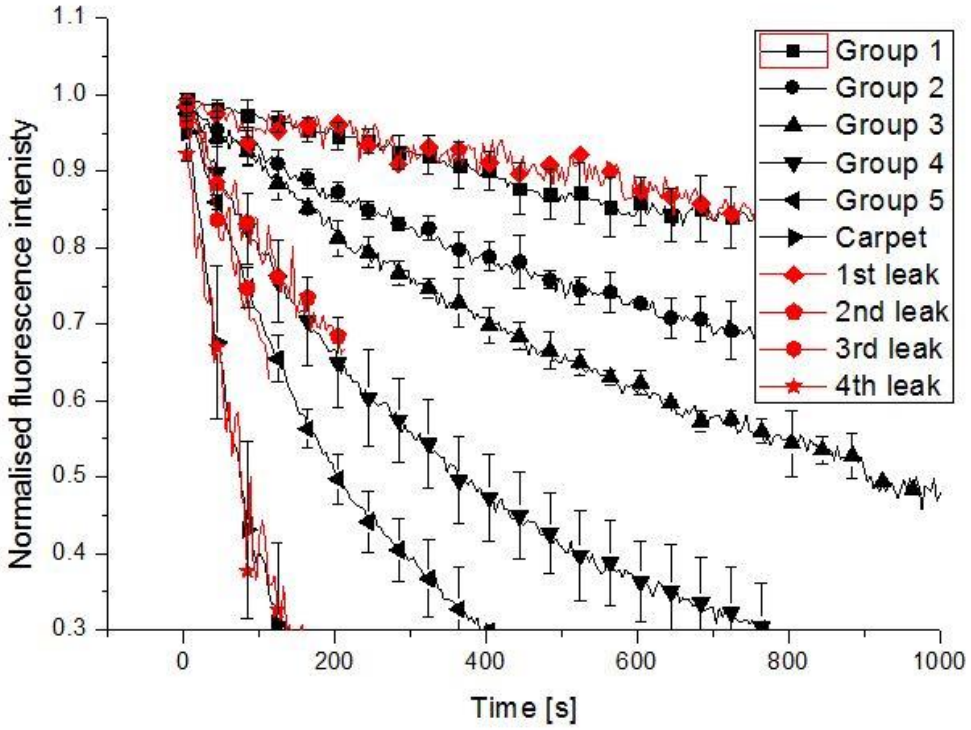

Figure 4.10: Graph demonstrating the group switching capabilities of the pore-mediated leakage process in DOPC:DPPC (80:20 mol%) membranes. The averaged leakage groups are depicted in black, with the individual phases of the multi-component leakage trace shown in red. The initial leak (red diamonds) follows the slowest leakage kinetics of group 1 for ~ 850 s, before the second leak (red pentagons) switched to match the kinetics of the faster group 4 for ~200 s. The third leakage phase (red hexagons) then matches the group 5 kinetics for ~150 s, before the leakage switches groups to match the carpet mechanism.

The overlaying of the 1 and 5 µM data sets for the DOPC:DPPC membrane system produces the graph presented as figure 4.11. Unlike the base DOPC membrane, the overlay of the two melittin concentrations does not show almost perfect matching. Several groups still display almost identical kinetics between the two data sets; groups 2, 3A and 4 of the 1 µM data set display closely matched kinetics with groups 1, 3 and 4 of the 5 µM data set respectively. Interestingly several groups in the 5 µM data set display slower kinetics than their 1 µM counterparts, namely groups 2, 5 and the carpet mechanism.

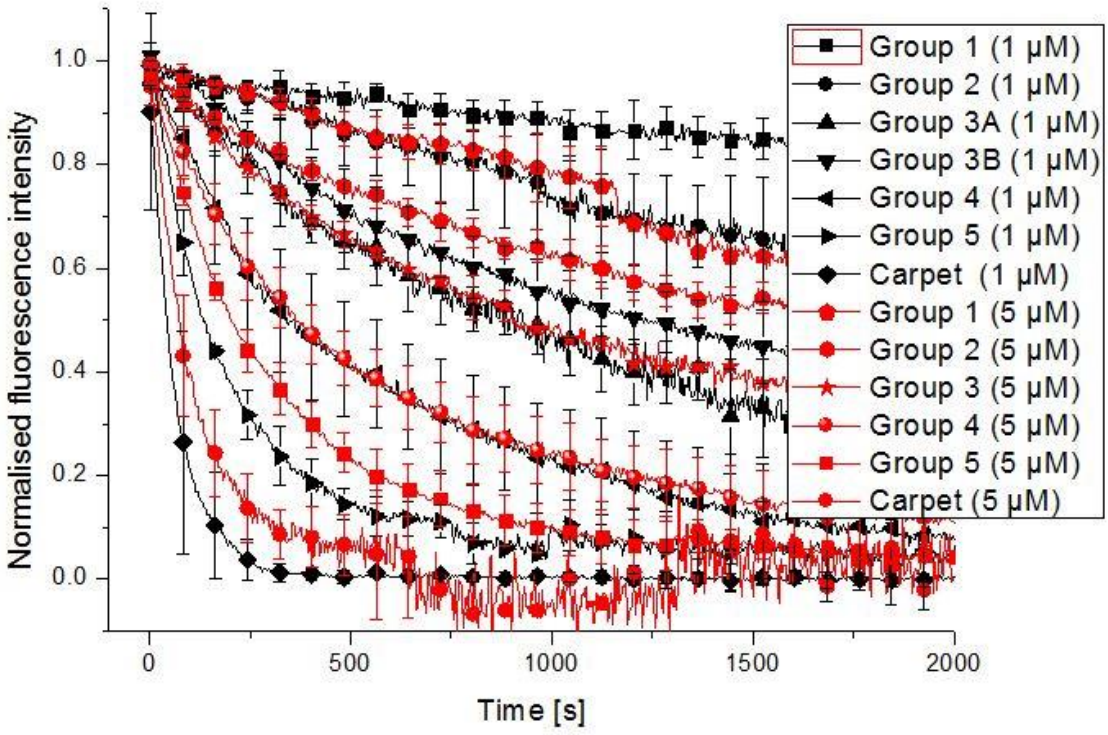

Figure 4.11: Overlaid grouping data for DOPC:DPPC membrane system, with 1 µM melittin traces shown in black, and 5 µM melittin traces depicted in red. Several of the groups show high levels of similarity across the two melittin concentrations, i.e. Groups 2, 3A and 4 of the 1 µM data set closely resemble groups 1, 3 and 4 from the 5 µM data set respectively. The other groups do not follow similar kinetics.

Comparison of the Leakage modes for the DOPC and DOPC:DPPC membrane systems gives the graph presented in figure 4.12 where the averaged leakage groups are overlaid. The overlaid traces are remarkably similar, with both data sets featuring six pore mediated leakage groups, and with four of the six groups displaying closely matched kinetics. From the DOPC data groups 1, 2, 5 and 6 closely match with the corresponding groups from the DOPC:DPPC data set, with group 4 showing a good match at shorter timescales, and only group 3 displaying a poor kinetic match between the two lipid systems. Leakage group 3 from the DOPC membrane system data set demonstrates considerably slower kinetics than group 3 of the DOPC:DPPC data set, which could result from changes in the pore size, number or opening time. The carpet mechanism leakage displays slower kinetics within DOPC:DPPC membranes compared to the base DOPC membrane. The close match between the data sets indicates that doping of the DOPC base membrane with another bilayer lipid, even with a substantially reduced packing parameter (DOPC S = 1.08 and DPPC S = 0.78), produces very little effect in these cases on the pore-mediated leakage kinetics induced by the negative curvature inducing AMP melittin. The primary effect of the inclusion of the positively curved DPPC lipid is seen within the timing of the initiation of the leak. The base DOPC membrane initiates leakage an average of 1961.1 s after exposure to melittin, while the DOPC:DPPC membrane takes substantially longer, returning an average initiation time of 3623.4 s.

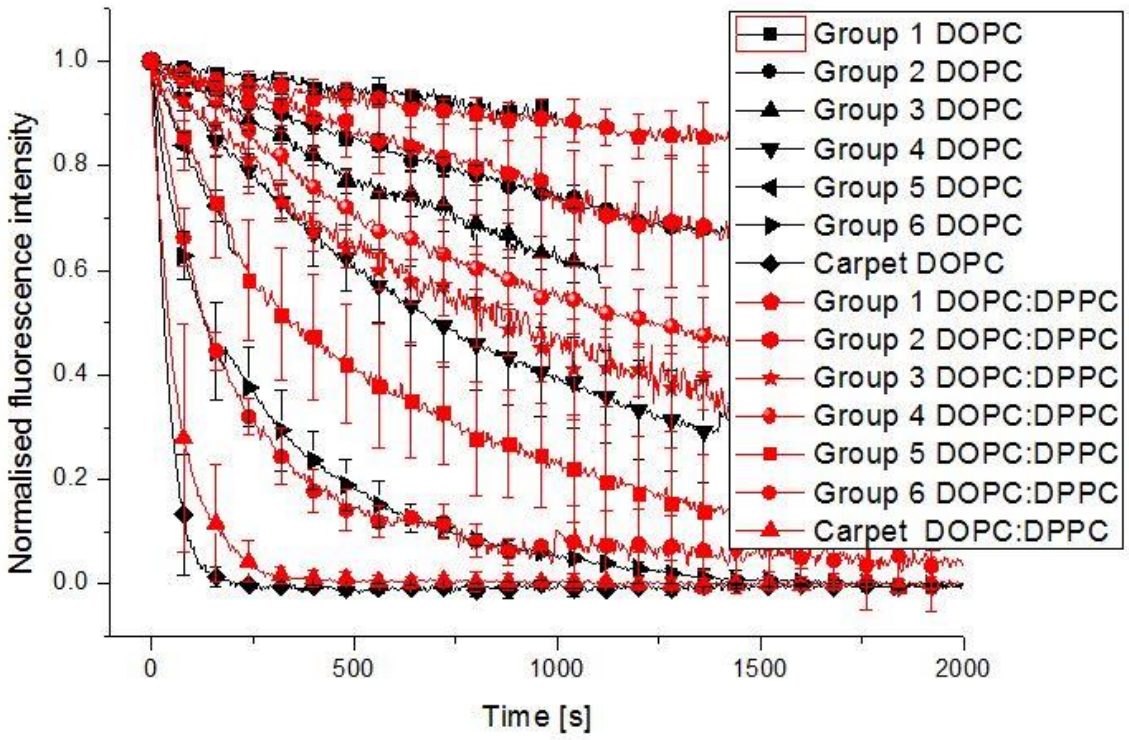

Figure 4.12: Comparison of the dye-leakage groupings from the DOPC and DOPC:DPPC (80:20 mol%) membrane systems, after exposure to 1 µM melittin, with the DOPC data depicted in black and the DOPC:DPPC data shown in red. Many of the groups display very similar kinetics across the two membrane systems; Groups 1, 2, 5 and 6 from the DOPC data set correspond almost exactly with the corresponding groups from the DOPC:DPPC data set. Groups 3 and 4 do not show similar kinetics across the two membrane systems.

The close matches between the efflux kinetics from DOPC and DOPC:DPPC vesicles indicates that the differing lipid compositions of the two membranes exert little influence on the leakage process once leakage has been initiated. Instead the lipids exert their affect prior to pore formation, as evidenced by the differing initiation times for pore-mediated leakage, and the variation in PIE-profiles between the DOPC and DOPC:DPPC membranes.

4.1.3. DOPC:DOPE membrane system

When exposed to 1 µM melittin, DOPC:DOPE (80:20 mol%) GUVs display the dye-leakage kinetics shown in figure 4.13. Similar to the base DOPC and DOPC:DPPC membranes, the 3 kDa leakage data set features clear grouping of the dye-leakage traces into distinct kinetic modes, with the 10 kDa data set featuring less distinct groupings. Compared to DOPC:DPPC membranes, the DOPC:DOPE membrane contains a strong inducer of negative curvature; the smaller headgroup and larger hydrophobic tailgroup volume of DOPE giving the lipid a packing parameter of 1.41.

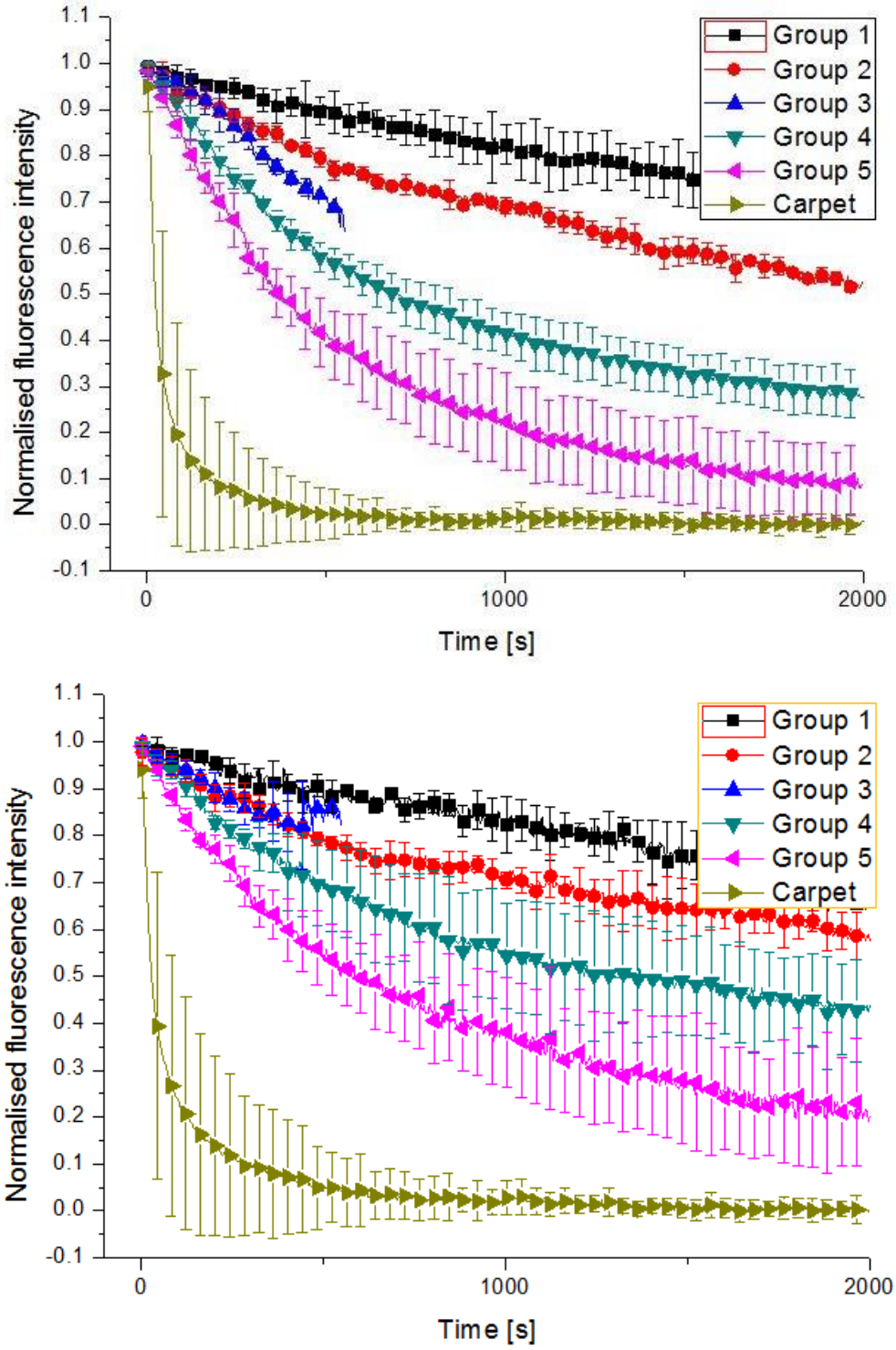

Figure 4.13: Modal dye leakage kinetics for the 3 (top) and 10 (bottom) kDa dextrans entrapped within DOPC:DOPE vesicles, exposed to 1 µM melittin. Error bars are the standard deviations from the averaged traces within each group. There are six groupings visible within the leakage kinetics, shown in the diagram key above. Five of the groups represent pore-mediated leakage, with the sixth and fastest leakage group, representing leakage through the carpet mechanism (green triangles).

The groups displayed in figure 4.13 were averaged from the following number of individual leakage traces; group 1 compiled from 3 traces; group 2 from 7 traces; group 3 from 9 traces; group 4 from 5 traces; group 5 from 9 traces and the carpet grouping is the average of 12 traces. At longer

timescales (>1500 s) the groupings begin to run parallel to the kinetics of group 1, indicating steady state leaking is taking place. Another similarity with the previously reported data sets, is two clearly separated 3 kDa leakage groups demonstrating very similar leakage kinetics within the 10 kDa data set. The DOPC:DPPC and DOPC:DOPE data sets both feature the second and third 3 kDa leakage groups merging into indistinguishable groups in the 10 kDa data set, while within the DOPC data set it is the third and fourth 3 kDa leakage groups which merge. The multi-component leakage traces again demonstrate switching between the leakage groups constructed from the single-component traces, as shown in figure 53. The close match up between the single-component leakage traces and the individual leakage phases of the multi-component traces further demonstrates the quantised nature of the observed dye-leakage data.

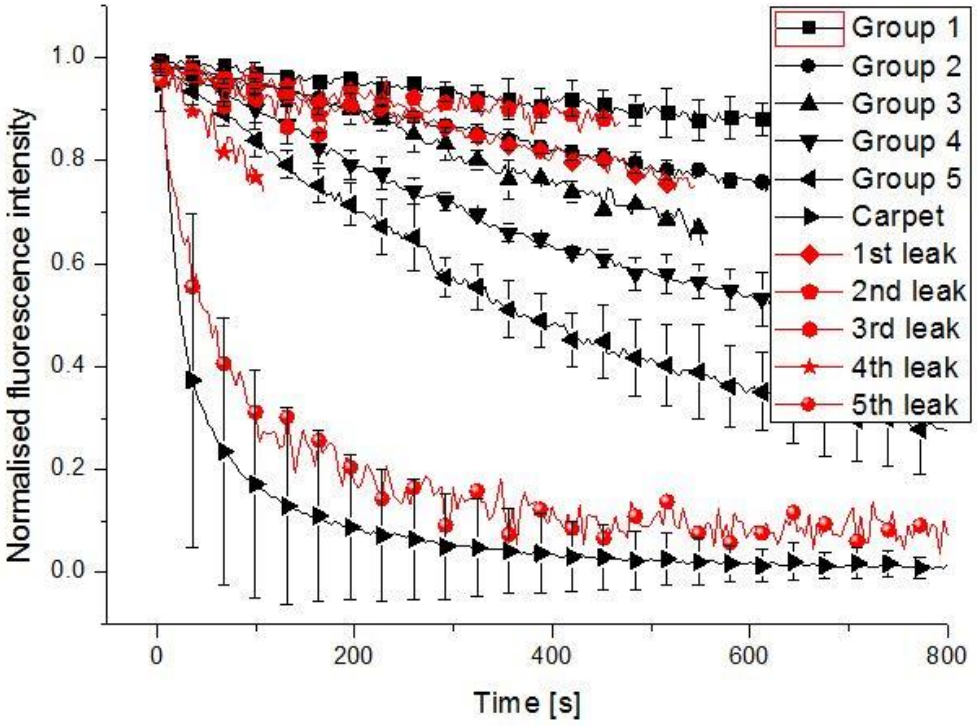

Figure 4.14: Graph displaying the group switching in multi-component leakage traces, demonstrated by a five phase multi-component leakage trace, recorded after exposure of DOPC:DOPE (80:20 mol%) GUVs to 1 µM melittin. The leakage groupings displayed by the single-component traces are depicted in black, with the individual phases of the multi-component traces shown in red. The initial leak (red diamonds) of the multi-component trace runs parallel to the kinetics of group 2 for ~ 500 s, before switching to group 1 kinetics for ~450 s (red pentagons). The third leakage phase (red hexagons) displays almost identical kinetics to group 4, with the fifth leak (red stars) matching group 5 kinetics. The final leak (red circles) follows the kinetics for the carpet mechanism grouping.

When exposed to the higher melittin concentration of 5 µM melittin, the DOPC:DOPE vesicles produced the dye efflux kinetics shown in figure 4.15. Again the common feature of leakage trace grouping was present, but the number of pore-mediated leakage groups was reduced from five to four, compared to the 1 µM melittin DOPC:DOPE data set.

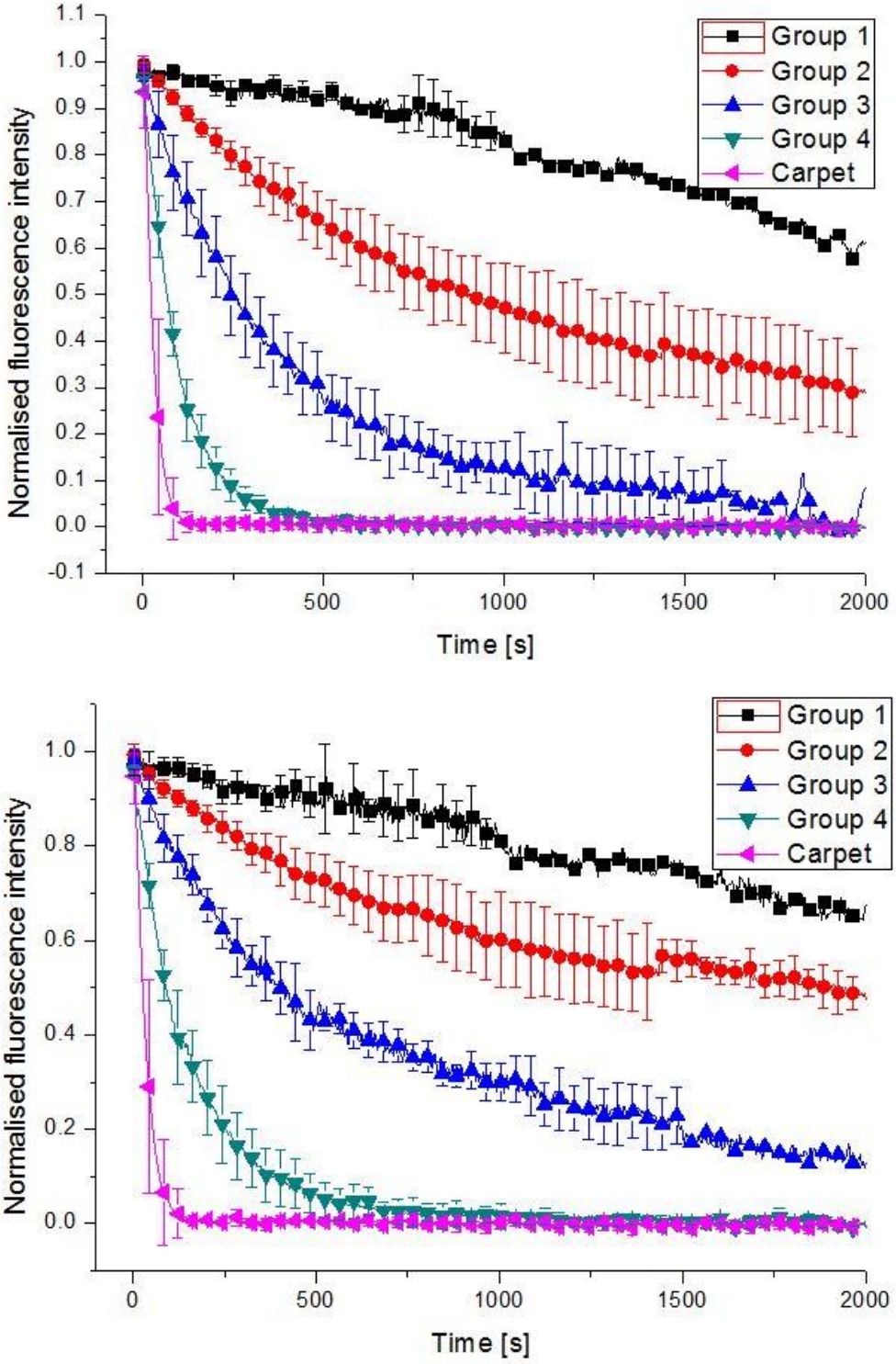

Figure 4.15: Averaged dye leakage kinetics for the 3 (top) and 10 (bottom) kDa dextran-Alexafluor488 entrapped within DOPC:DOPE vesicles, exposed to 5 μM melittin, with the error bars are the standard deviations from the averaged traces within each group. There are five groupings visible within the leakage kinetics, shown in the diagram key above. Four of the groups represent pore-mediated leakage, with the fifth and fastest leakage group, representing leakage through the carpet mechanism (pink triangles).

The averaged leakage traces for the DOPC:DOPE membrane system exposed to 5 μM of melittin were compiled from a total of 32 vesicles, with the distribution between the individual groups as

follows: Group 1 compiled from 6 traces; group 2 from 7 traces; group 3 from 7 traces; group 4 from 5 traces and the carpet mechanism group from 7 traces. Both peptide concentrations in the DOPC:DOPE membrane system produce less complex dye-efflux kinetics than either then DOPC or DOPC:DPPC systems, returning lower numbers of groupings in the leakage data. The DOPC:DOPE data set does not present the merging of separate 3 kDa leakage groups into similar 10 kDa leakage groups that was a common feature of all the data sets previously reported. The data set retains the group switching of multi-component leakage traces demonstrated by the previous data sets, with an example presented in figure 4.16.

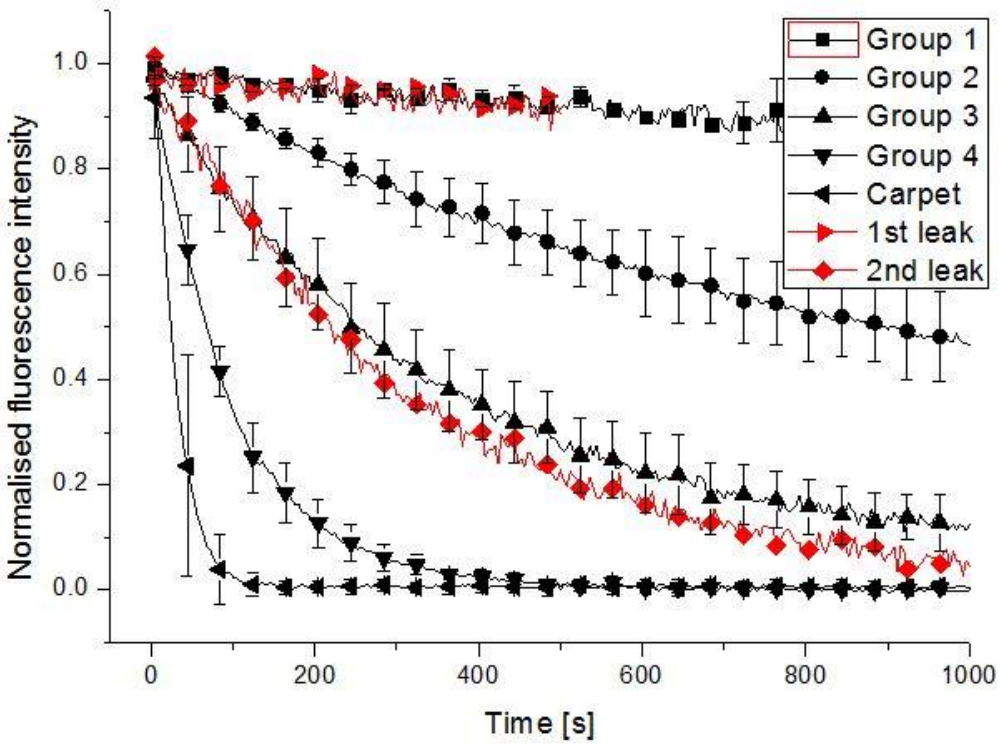

Figure 4.16: Graph of the multi-component group switch determined for the DOPC:DOPE (80:20 mol%) membrane system exposed to 5 µM melittin. The averaged single-component leakage groups are depicted in black, with the individual leakage phases recovered from the multi-component traces shown in red. The first leak (red triangles) matches kinetics with group 1 of the averaged leakage groups for ~450 s, before the second phase (red diamonds) switches groups, matching dye-efflux kinetics with group 3 until the vesicles contents are completely depleted.

Comparison of the 1 and 5 µM DOPC:DOPE data sets produces the graph presented in figure 4.17. In contrast with the DOPC and DOPC:DPPC data sets, inclusion of the negative curvature lipid DOPE results in larger differences between the two peptide concentrations. Only one of the higher melittin concentrations leakage groups present a close match with the lower concentrations groups, with group 1 for both concentrations displaying very similar kinetics. All other 5 µM leakage groups showed no good match with groups from the lower AMP concentration data set, with the groups showing a marked tendency for faster leakage kinetics, with group 4 the fastest pore-mediated leakage kinetics from any data set.

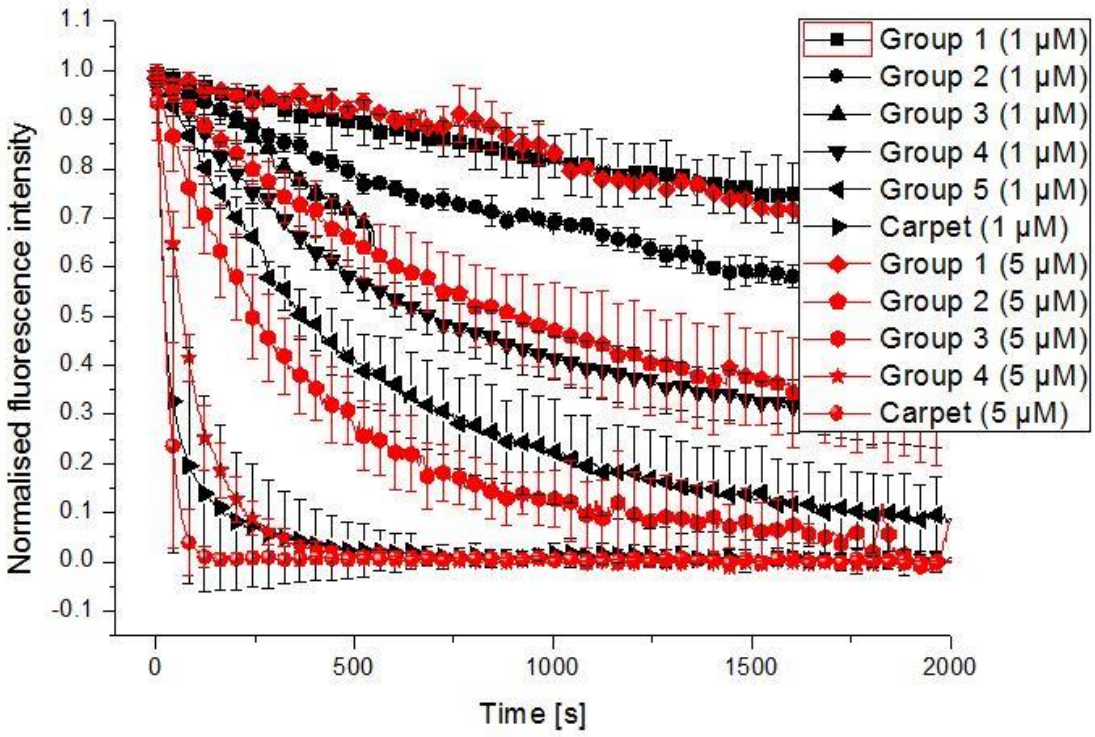

Figure 4.17: Overlaid grouping data for DOPC:DOPE (80:20 mol%) membrane system, with 1 µM melittin traces shown in black, and 5 µM melittin traces depicted in red. The first group for both peptide concentrations demonstrate closely matched kinetics, but subsequent groups do not display similar kinetic matches. Compared to the 1 µM leakage groupings, the groups from the 5 µM data set rapidly progress to faster leakage kinetics, with group 4 demonstrating especially fast pore-mediated leakage, almost comparable to the carpet mechanism kinetics.

To examine the effect of the inclusion of the negatively curved DOPE lipid within the neutral curvature (i.e. cylindrical geometry) DOPC membrane, on the pore formation activity of the AMP melittin, the averaged group kinetics for the DOPC:DOPE membrane system were overlaid with the DOPC system kinetics and presented in figure 4.18. The close match between groups 3, 4 and 5 of the DOPC data and groups 2, 4 and 5 of the DOPC:DOPE data indicate that the negatively curved lipid DOPE exerts little influence on the properties of the pores that produces these kinetically similar leakage groups; e.g. Size and opening times. The average initiation time for pore-mediated leakage in the DOPC:DOPE membrane system is 3273.3 s, compared to the 3623.4 s in the DOPC:DPPC membrane, but both are considerably slower in initiation of pore-mediated leaking than DOPC vesicles (1961.1 s).

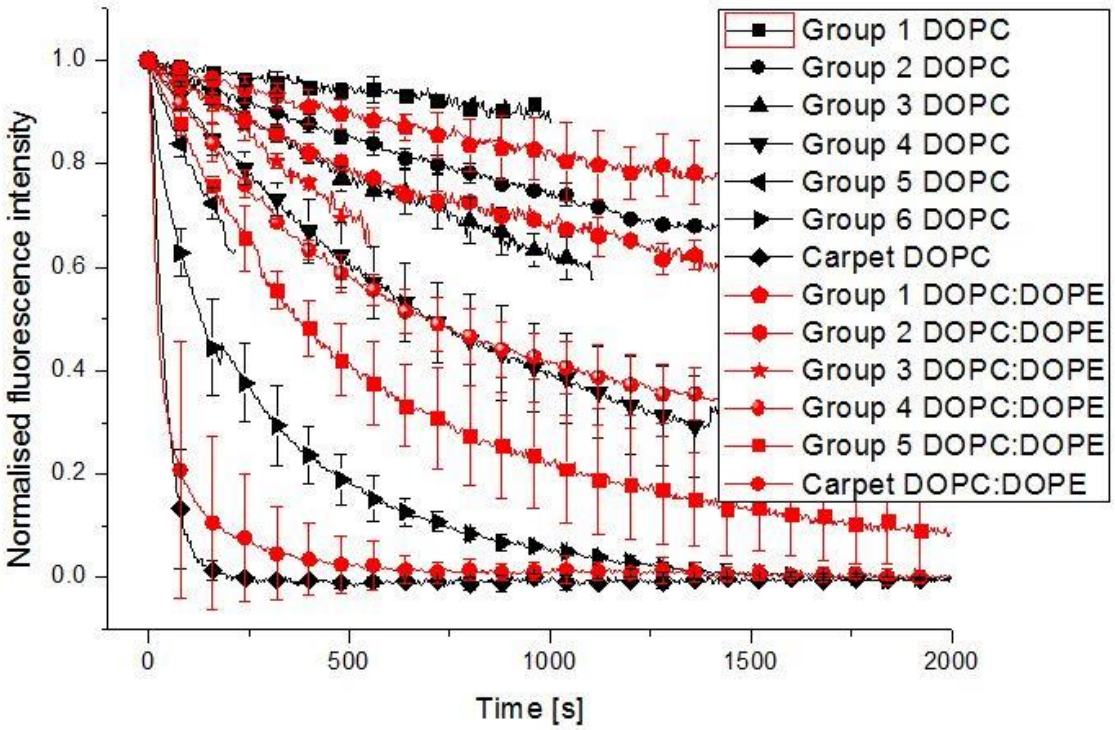

Figure 4.18: Comparison of the cylindrical DOPC base membrane (black) dye-efflux kinetics with the DOPC:DOPE membrane (red), which contains a strongly negative curvature inducing lipid. Groups 4 and 5 of the DOPC data demonstrate closely related kinetics with groups 4 and 5 of the DOPC:DOPE data respectively, and group 2 of the DOPC:DOPE data shows a close similarity to group 3 of the DOPC kinetics at short timescales (< 500 s). The remainder of the pore-mediated leakage groups display no close relationships between the kinetics of the two different membrane systems, exposed to 1 μM melittin.

An overlay of the dye-efflux kinetics data for the DOPC:DPPC and DOPC:DOPE membrane systems is presented in figure 4.19, to demonstrate the influence of the inclusion of opposite topography lipids, within a geometrically neutral DOPC membrane. The inclusion of 20 mol% of the negatively curved DOPE within the base DOPC membrane, produces a greater shift of the dye-efflux kinetic groups from the DOPC kinetics, than the inclusion of identical levels of the positively curved DPPC lipid.

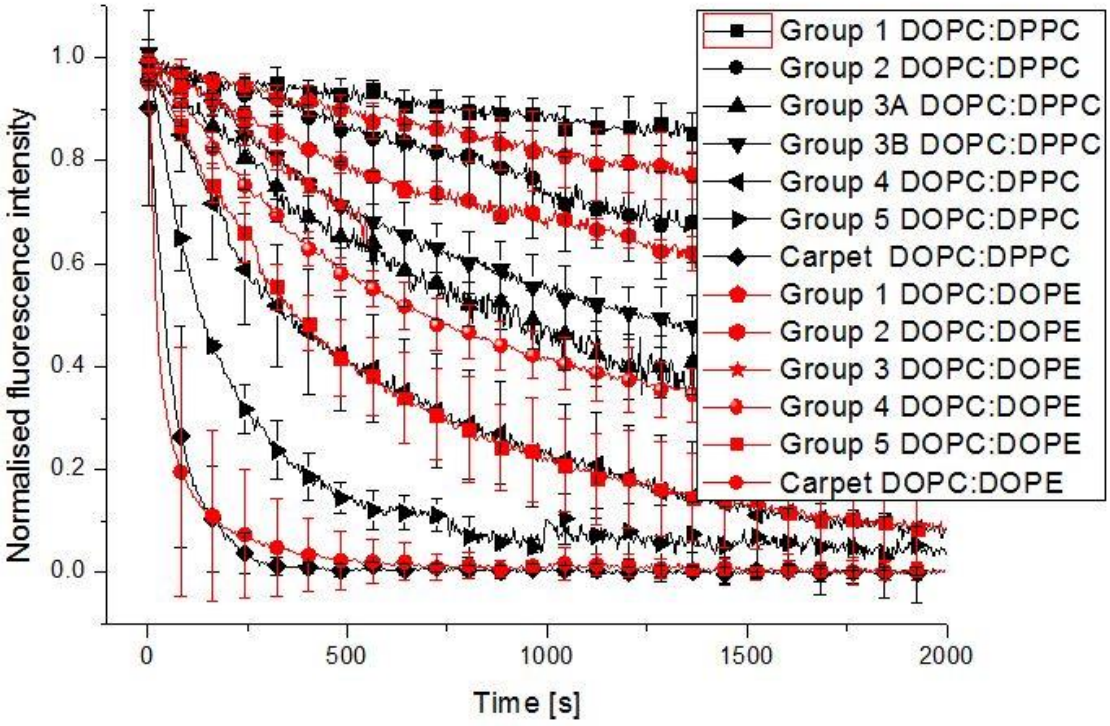

Figure 4.19: Comparison of the 1 µM melittin induced dye-efflux kinetics from the DOPC:DPPC (black) and DOPC:DOPE (red) membrane systems, which both contain 80 mol% of the cylindrical lipid DOPC and 20 mol% of either the positive curvature lipid DPPC or the negative curvature lipid DOPE. Groups 3B and 4 from the DOPC:DPPC data set show close kinetic matching with groups 3 and 5 from the DOPC:DOPE data set, with other groups demonstrating no close matches in the efflux kinetics across the two membrane systems.

4.2. Zwitterionic leakage kinetics summary

The grouping of leakage traces into sets is visible within all the zwitterionic membrane data sets, and suggests that pore formation can only occur within vesicle membranes possessing a tightly controlled set of boundary conditions. A membrane containing lipid-LCAMP interactions matching the required conditions can initiate leaking, and follow a defined leakage kinetic pathway connected to the initial boundary conditions. The multiphase leakage traces identified within the data sets, when split into their individual phases, fit within the framework of previously determined leakage groups, suggesting that the membrane is capable of switching between the established boundary conditions, presumably as a result of further peptide binding or intraleaflet association. The multiphase traces display two types of behaviour; switching back and forth between two adjacent leakage groups, or switching to faster kinetic groups until vesicle contents are depleted or vesicle failure occurs. There are several examples of adjacent leakage groups from the 3 kDa dextran leakage data, that combine within the 10 kDa data set, appearing as a single grouping. This behaviour is noticed within the DOPC, DOPC:DPPC and DOPC:DOPE membrane systems, and the most concise explanation for this is the simultaneous opening of two differently sized pores within the vesicle membrane. The larger pore allows efflux for both the larger and smaller dextrans, but the smaller pore only allows egress to the smaller molecule, resulting in increased leakage kinetics only within the 3 kDa data set.

Overlay of 1 and 5 µM melittin data shows that the leakages occur via very similar kinetics at both concentrations, indicating that within zwitterionic membranes, the rate of peptide binding to the vesicle does not exert a strong effect over the leakage kinetics. Overlay of the melittin induced leakage kinetics

within different membrane systems shows that the dye-efflux proceeds with strikingly similar dye efflux kinetics, but significantly different pore initiation timings. For example the average initiation time of pore-mediated leakage in DOPC membranes is approximately half (1961 s) the time in DOPC:DPPC membranes (3623.4 s); i.e. the addition of 20 mol% of the inverse-conical lipid DPPC dramatically increases the initiation time of pore formation. The PIE-profiles for these membranes also shows marked differences (figure 3.2), suggesting that the varying lipid-LCAMP interactions occulting within the membranes influence the pore energetics and likelihood of occurrence, but when pore formation is initiated it proceeds via almost identical kinetics; i.e. via pores with very similar pore size, number and opening times.

5. Pore-mediated leakage in anionic membranes

5.1. DOPC:DOPE:DOPG membrane system

The constituent lipids of the DOPC:DOPE:DOPG membrane system present cylindrical (DOPC) and conical (DOPE and DOPG) topographies. Exposure of the membrane system to 1 μM of the AMP melittin produced the dye-efflux kinetic shown in figure 5.1. The dye-efflux data from the anionic DOPC:DOPE:DOPG system continues to demonstrate some of the trends discovered within the zwitterionic membrane systems DOPC; DOPC:DPPC and DOPC:DOPE, notably the grouping of the kinetics data into quantised leakage states and the merging of the resulting kinetics groupings within the 10 kDa dye-efflux data. The averaged kinetic traces are compiled from the following number of individual leakage traces; group 1 is the average of two traces; group 2 is three traces; group 3 is three traces; group 4 is four traces; group 5 is five traces and the carpet mechanism group was compiled from five traces. Groups 3 and 4 are clearly defined within the 3 kDa data set, yet display almost identical dye-efflux kinetics within the 10 kDa data set.

Another point of similarity between the dye-efflux kinetic behaviour between the zwitterionic and anionic membrane systems is the presence of multi-component leakage traces, which can be split into their individual leakage components and overlaid with the grouped average leakage traces, as demonstrated in figure 5.2. The figure contains a four component dye leakage trace from the 10 kDa leakage data set, with each individual leakage component matched to one of the averaged leakage traces, demonstrating the quantised nature of the dye-efflux process.

Magainin was almost totally inactive within the DOPC:DOPE:DOPG membrane system, even at the higher peptide concentrations of 5 μM, interestingly proving that magainins least activity coincides with the presence of high fatty acid unsaturation and neutral to negative curvature.

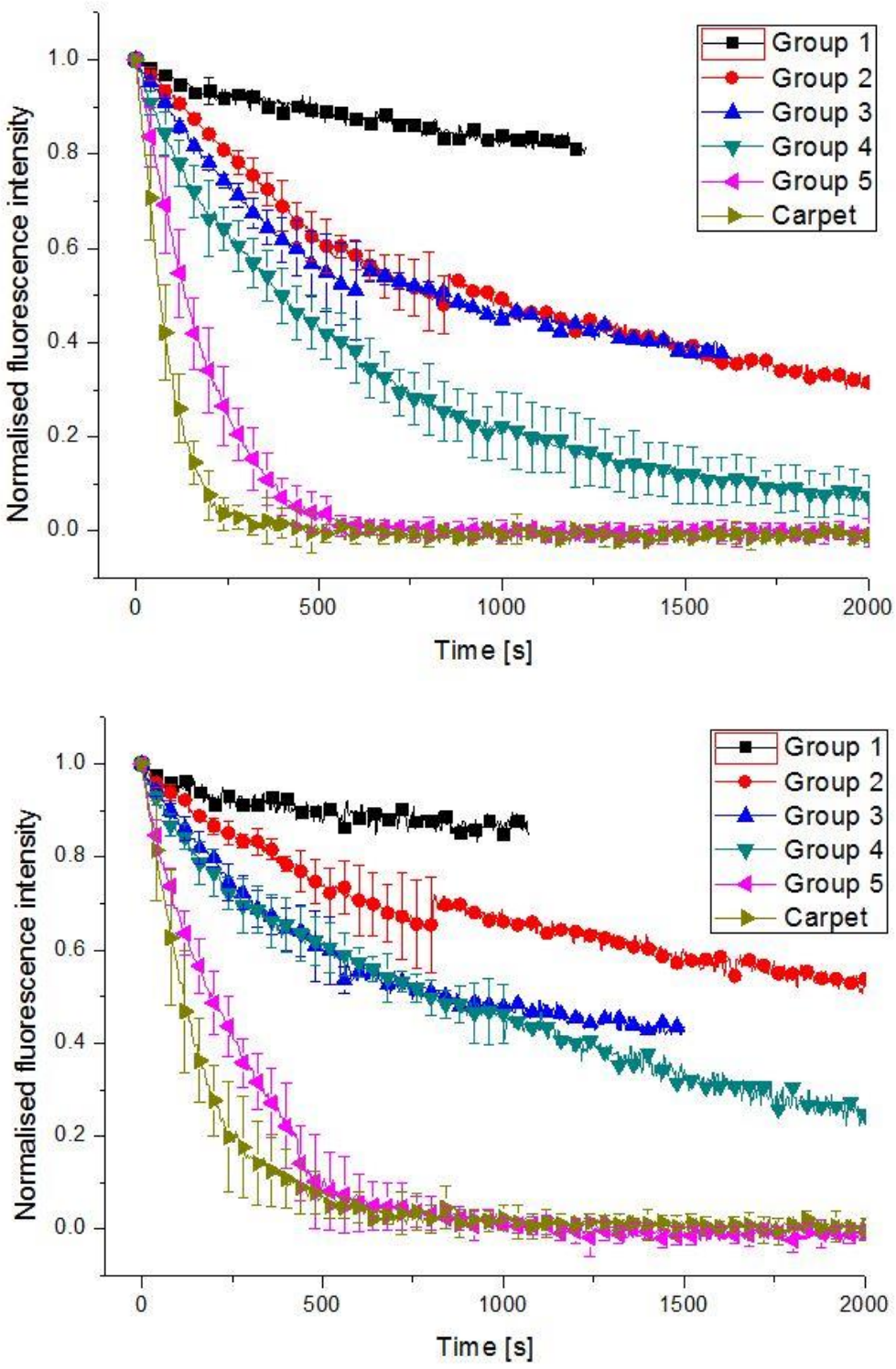

Figure 5.1: Averaged dye-efflux kinetics for the 3 (top) and 10 (bottom) kDa dextran-Alexafluor markers entrapped within DOPC:DOPE:DOPG vesicles, exposed to 1 μM melittin, with the error bars representing the standard deviation of the traces within each group. There are six groupings visible within the data, shown in the diagram key above. Five of the groups represent pore-mediated leakage, with the sixth leakage group, representing the carpet mechanism (green triangles). The 3 kDa data set contains five distinct kinetic groupings for pore-mediated leakage from the vesicles, while the 10 kDa data contains only four, with the 3 kDa groups 3 and 4 merging into one group within the 10 kDa data.

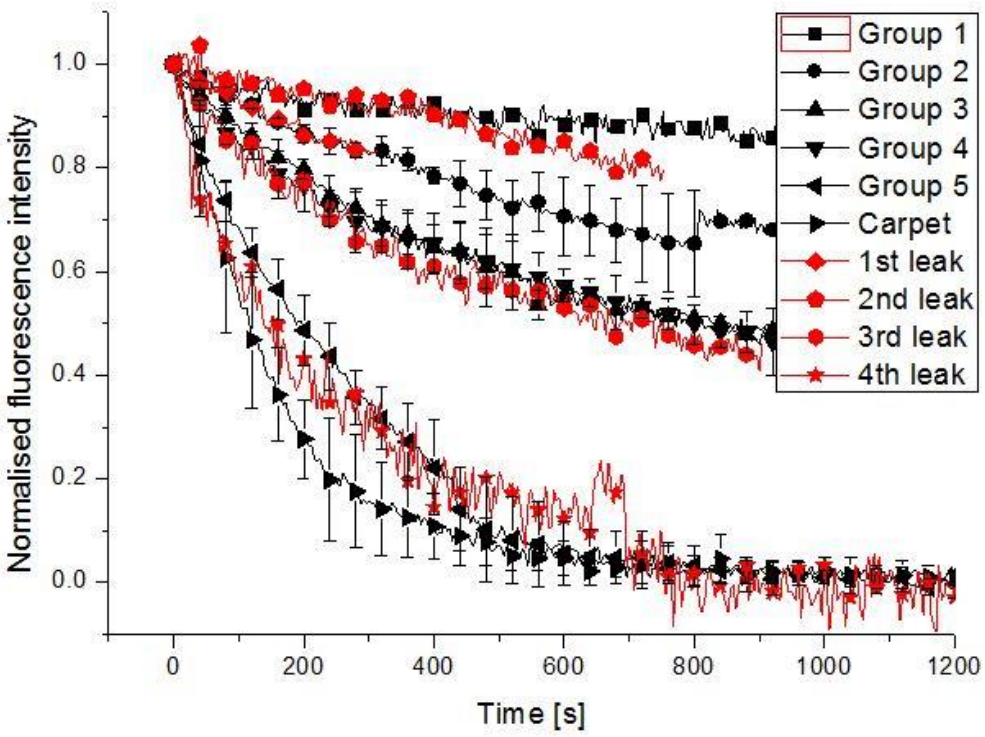

Figure 5.2: Overlay of the individual leakage components from a multi-component 10 kDa dye-leakage trace (red), with the averaged kinetic groupings of the entire 10 kDa data set (black). The initial leak from the multi-component trace (red diamonds) follows the leakage kinetics of group 2 for ~300 s, before the second leakage phase (red pentagons) switches to closely follow group 1 kinetics for ~400 s, with a further switch back to match group 1 kinetics for ~350 s (left in place to avoid obscuring the initial leakage trace). The third leakage phase (red hexagons) displays the leakage kinetics common to group 3/4 for around 900 s, before matching the kinetics of group 5 with its final leakage phase (red stars) until the vesicle contents are depleted.

5.2. DOPC:DOPE:DPPG membrane system

Replacing the DOPG from the previous membrane system with the inverse-conical shaped DPPG increases the variety of lipid geometry present within the membrane. The DOPC:DOPE:DPPG system therefore contains a wide mix of topography; DOPC is a cylindrical and zwitterionic lipid; DOPE is zwitterionic and conical and DPPG is anionic and inverse-conical. The inclusion of anionic positive topography lipids within the membrane system produces a large effect on the pore-mediated leakage displayed by 1 µM melittin, with the data for the efflux of the entrapped 3 kDa dextrans collected shown in figure 5.3. The inclusion of the positive curvature-inducing anionic DPPG substantially deactivated melittin action, proving to be the least activity membrane system for melittin, but the available data still demonstrated kinetic grouping.

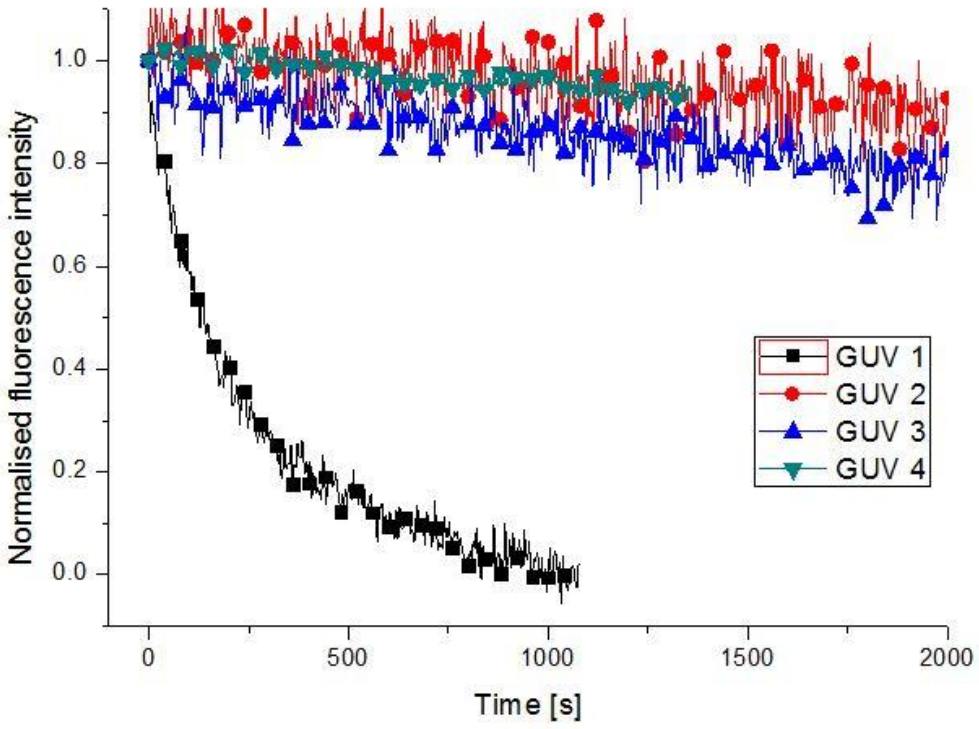

Figure 5.3: Dye leakage kinetics for the 3 kDa dextran-Alexafluor488 entrapped within DOPC:DOPE:DPPG vesicles, exposed to 1 μM melittin.

In contrast inclusion of DPPG produced the highest levels of magainin activity, and the dye-leakage kinetics for the DOPC:DOPE:DPPG membrane system exposed to 1 μM magainin are presented in figure 5.4. The average initiation time for the start of pore-mediated leakage in this membrane system was 289.5 s, the quickest initiation time for pore-formation recorded for any peptide, at any concentration in any membrane system. The grouped leakage traces are compiled from the following number of individual leakage traces; group 1 was a single trace; group 2A was produced by averaging four traces; group 2B from two traces; group 3 from four traces; group 4 from two traces; group 5 from four traces and the carpet mechanism was compiled from two traces. Both multi-component traces and merging of distinct 3 kDa groupings into identical 10 kDa groupings were present within this data set, with the merging of the 3 kDa groupings being particularly prominent within the DOPC:DOPE:DPPG membrane system. Four 3 kDa groups (2A, 2B, 3 and 4) merge in the 10 kDa data, with the groups 2A and 2B presenting parallel kinetics within the 3 kDa for a significant period of time (~450 s), before splitting to form separate kinetic groupings within the 3 kDa data. The parallel kinetics presented in the 3 kDa dye-efflux data at short timescales, suggests that continued binding of the peptide to the lipid membrane produced a change within the lipid-AMP system, that favoured a change in the pore-mediated leakage process. The change in the pore-formation process favoured the leakage of the smaller 3 kDa dextran, while the efflux of the larger 10 kDa dye remained unaffected.

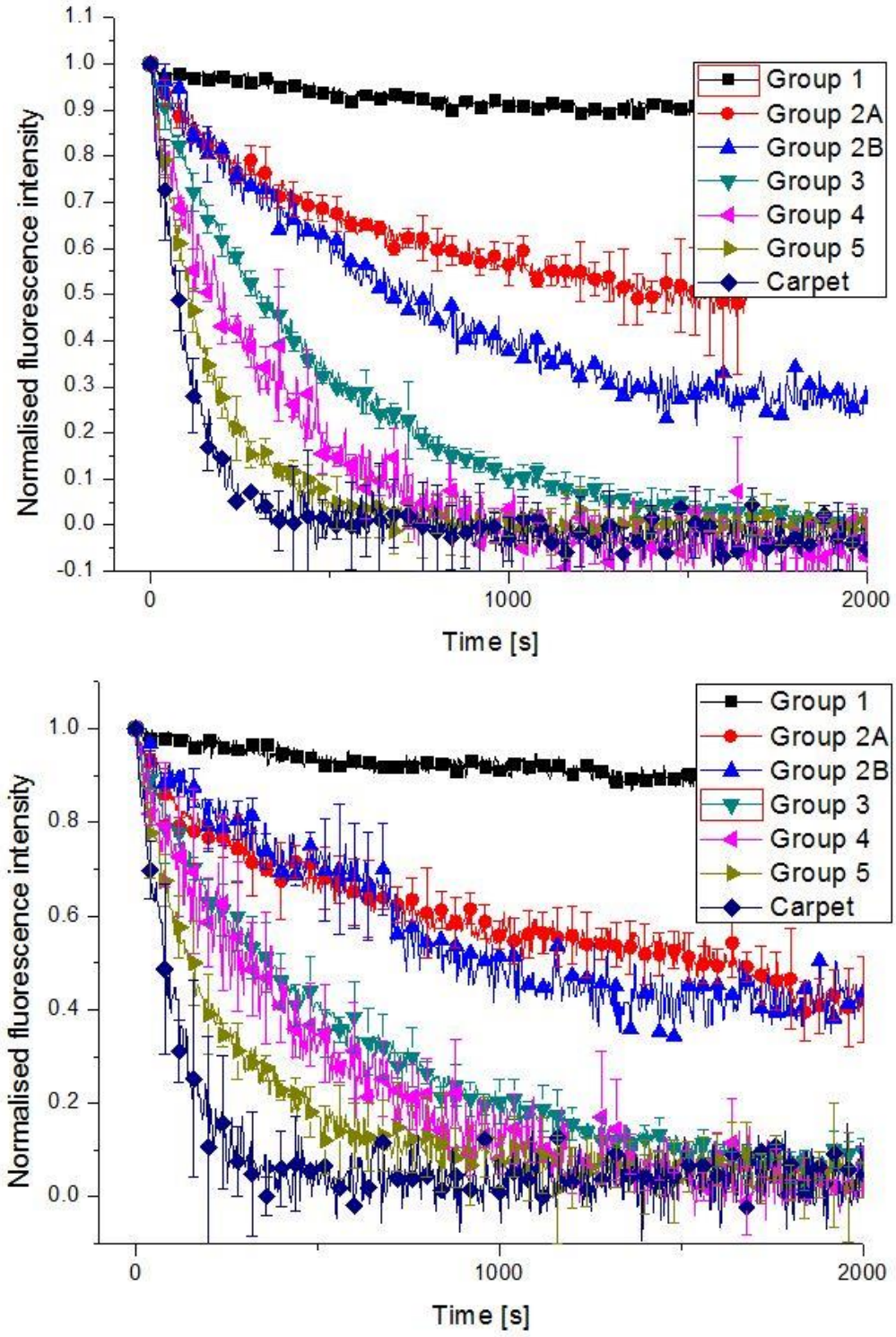

Figure 5.4: Dye leakage kinetics for the 3 (top) and 10 (bottom) kDa dextran-AlexaFluor markers entrapped within DOPC:DOPE:DPPG vesicles, exposed to 1 μM magainin, with the error bars representing the standard deviation for the individual leakage traces within each leakage group. The merging of two distinct 3 kDa leakage groupings into a single 10 kDa grouping occurs twice within this data set, with both the 3 kDa groups 2A and 2B merging within the 10 kDa data, as well as the 3 kDa groups 3 and 4. The 3 kDa groups 2A and 2B demonstrate merged kinetics within the 3 kDa data for ~450s, before they split into distinct groups, demonstrating a change in the lipid-AMP interactions producing the pore formation, but remain merged within the 10 kDa data.

Group switching in the DOPC:DOPE:DPPG membrane system exposed to 1 µM magainin is displayed in figure 63.

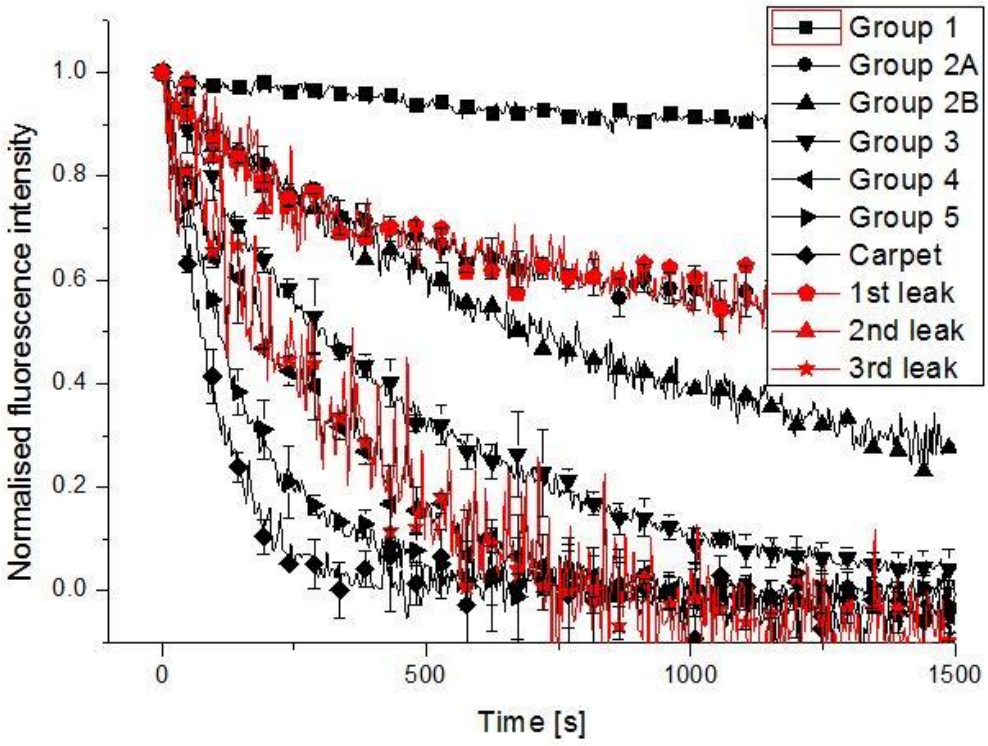

Figure 5.5: Graph presenting an example of group switching membranes, from the 3 kDa dye-efflux kinetics recorded after exposure of DOPC:DOPE:DPPG GUVs to 1 µM magainin. The first leakage phase (red pentagons) of a three component leak match the kinetics of the group 2A from the single component leakage data for ~1200 s, before the second phase (red triangles) reinitiates leakage at kinetics matching the groups 2A and 2B for ~300 s. The final leakage phase (red stars) switches groups to match the kinetics of group 4, until the vesicles dextran contents are completely depleted after ~750 s.

Exposure of the DOPC:DOPE:DPPG membrane system to the higher magainin concentration of 5 µM produces the grouped dye-leakage kinetics shown in figure 5.6. This combination of membrane system and peptide concentration produced the highest magainin activity, with 92.6 % of vesicles displaying a PIE under these conditions. The averaged leakage kinetic traces were compiled from the following number of individual traces; group 1 compiled from two traces; group 2 from four traces; group 3 from two traces and group 4 from three traces. The groups 2 and 3 within both the 3 and 10 kDa data sets display interesting kinetic behaviour, with both groups following similar kinetics at short timescales, before separating into distinct groups. However, the 10 kDa traces remain at similar kinetics for longer, taking ~450 s to separate, compared to ~300 s in the 3 kDa data. The separation between groups 2 and 3 is also less distinct within the 10 kDa data compared to the 3 kDa data set.

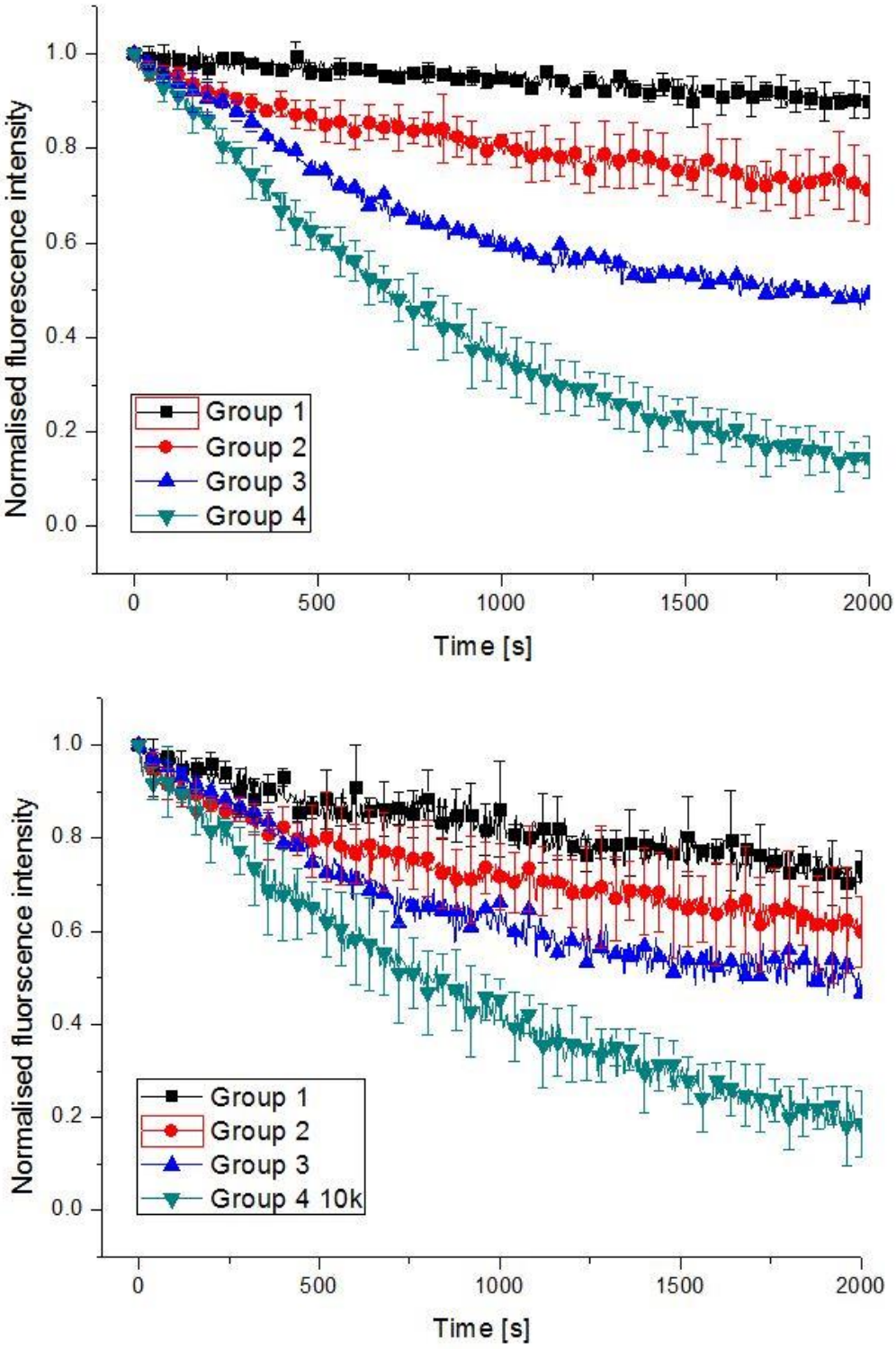

Figure 5.6: Grouped dye-efflux kinetics for the 3 (top) and 10 (bottom) kDa dextran-AlexaFluor markers entrapped within DOPC:DOPE:DPPG vesicles, exposed to 5 μM magainin, with the error bars representing the standard deviations of the individual leakage traces contained within each group.

The leakage pattern within the grouped traces at longer timescale within the DOPC:DOPE:DPPG membrane system is presented in figure 5.7. Groups 2 and 3 reduce their kinetics, until both groups run parallel to the slower leakage kinetics of group 1, after ~1500 s.

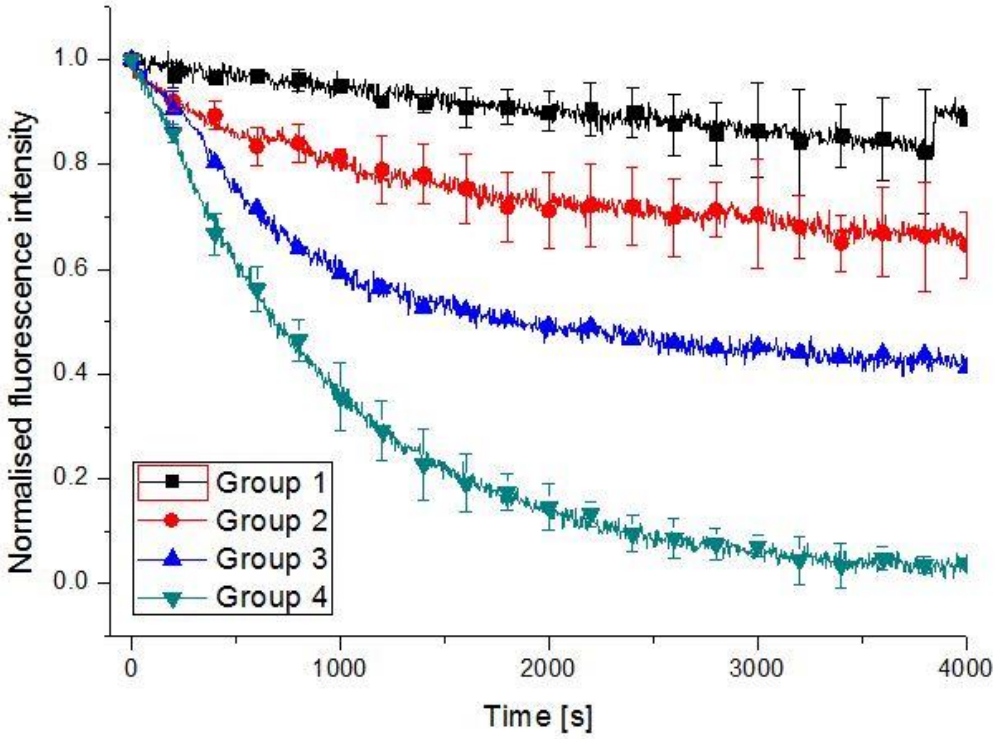

Figure 5.7: Dye leakage kinetics for the pore-mediated events of the 3 kDa dextran-Alexafluor488 entrapped within DOPC:DOPE:DPPG vesicles, exposed to 5 µM magainin, over a longer timescale of 4000 s. All the leakage groupings run parallel to group 1 kinetics, after ~1500 s, after an initial phase of following different kinetics.

DOPC:DOPE:DPPG membranes exposed to 5 µM magainin demonstrate group switching in the individual leakage phases of the multi-component leakage traces, that has proved a common thread running through the dye-efflux kinetics of all the membrane systems and AMPs tested. An overlay of the average dye-efflux kinetics for the 3 kDa dextran marker contained within DOPC:DOPE:DPPG vesicles, exposed to magainin at 1 and 5 µM concentrations, is presented in figure 5.8. The exposure of DOPC:DOPE:DPPG GUVs to the higher concentration of magainin, produces a change in the efflux kinetics of the system, when compared to the 1 µM data set. The averaged leakage traces are shifted towards slower leakage kinetics, and the average initiation time for pore-mediated leakage in these vesicles is 2577.5 s, considerably longer than the 1 µM systems time of 289.5 s, the fastest initiation time for pore mediated leakage displayed by any membrane system or peptide. The other PIE initiation times for the higher concentration of magainin are significantly reduced compared to the lower concentration; the discrepancy in the initiation time for pore-mediated leakage must be explained. One of the groupings within the 5 µM data set follows almost identical kinetics to a group within the 1 µM data set, but the remaining three groups follow their own unique kinetics.

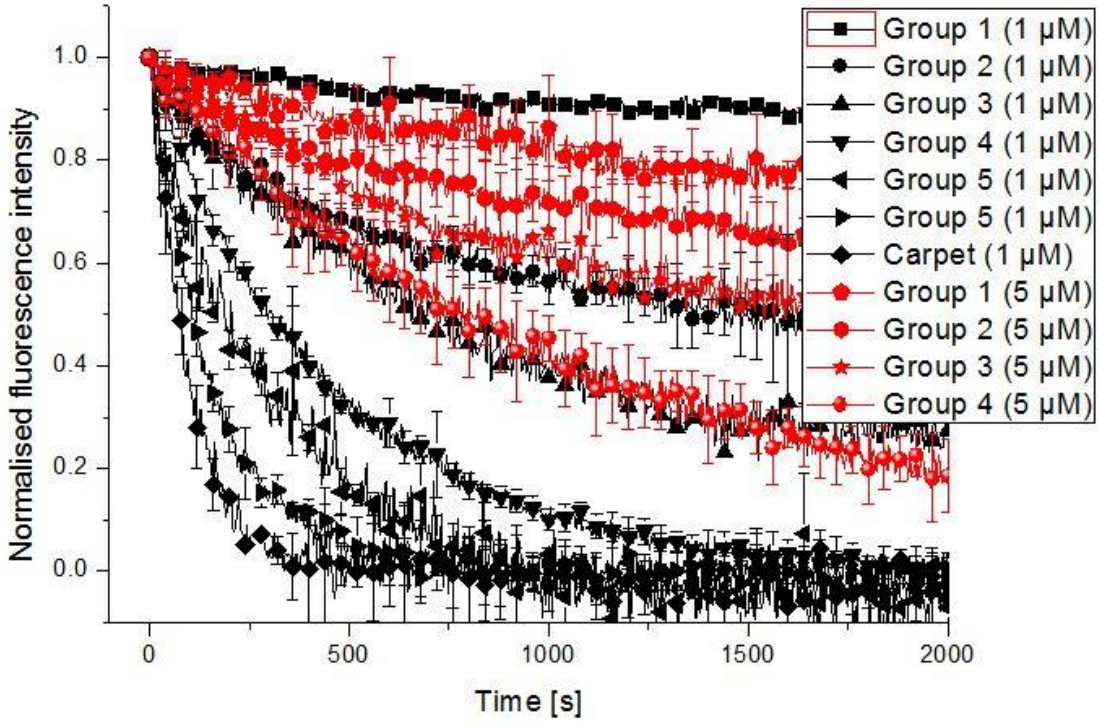

Figure 5.8: Overlaid averaged dye-leakage data for the DOPC:DOPE:DPPG membrane system, with 1 µM magainin traces shown in black, and 5 µM magainin traces depicted in red. Groups 2/3 for both concentrations show similar behaviour, initially identical leakage kinetics, before branching into two separate groups. The fastest group within the 5 µM data is group 4, and is significantly slower than the fastest leakage kinetics of displayed by the 1 µM magainin data. Group 4 of the 5 µM data set follows almost identical kinetics to group 3 of the 1 µM data set, but the other averaged traces do not match across the peptide concentration data sets.

5.3. DOPC:DOPE:LPG membrane system

LPG is an anionic lipid possessing extremely pronounced inverse-conical geometry, and the DOPC:DOPE:LPG (60:20:20 mol%) membrane system contains a large variation in lipid charge topography; DOPC is a zwitterionic cylindrical lipid and DOPE is a zwitterionic conical lipid. Exposure of GUVs with this lipid composition produces the grouped dye-efflux kinetics displayed in figure 5.8. The grouped leakage kinetics were averaged from the following number of individual leakage traces; group 1 averaged from two traces; group 2 from three traces; group 3 from three traces; group 4 from two traces; group 5A from two traces; group 5B from two traces and the carpet mechanism was compiled from the averaging of five traces.

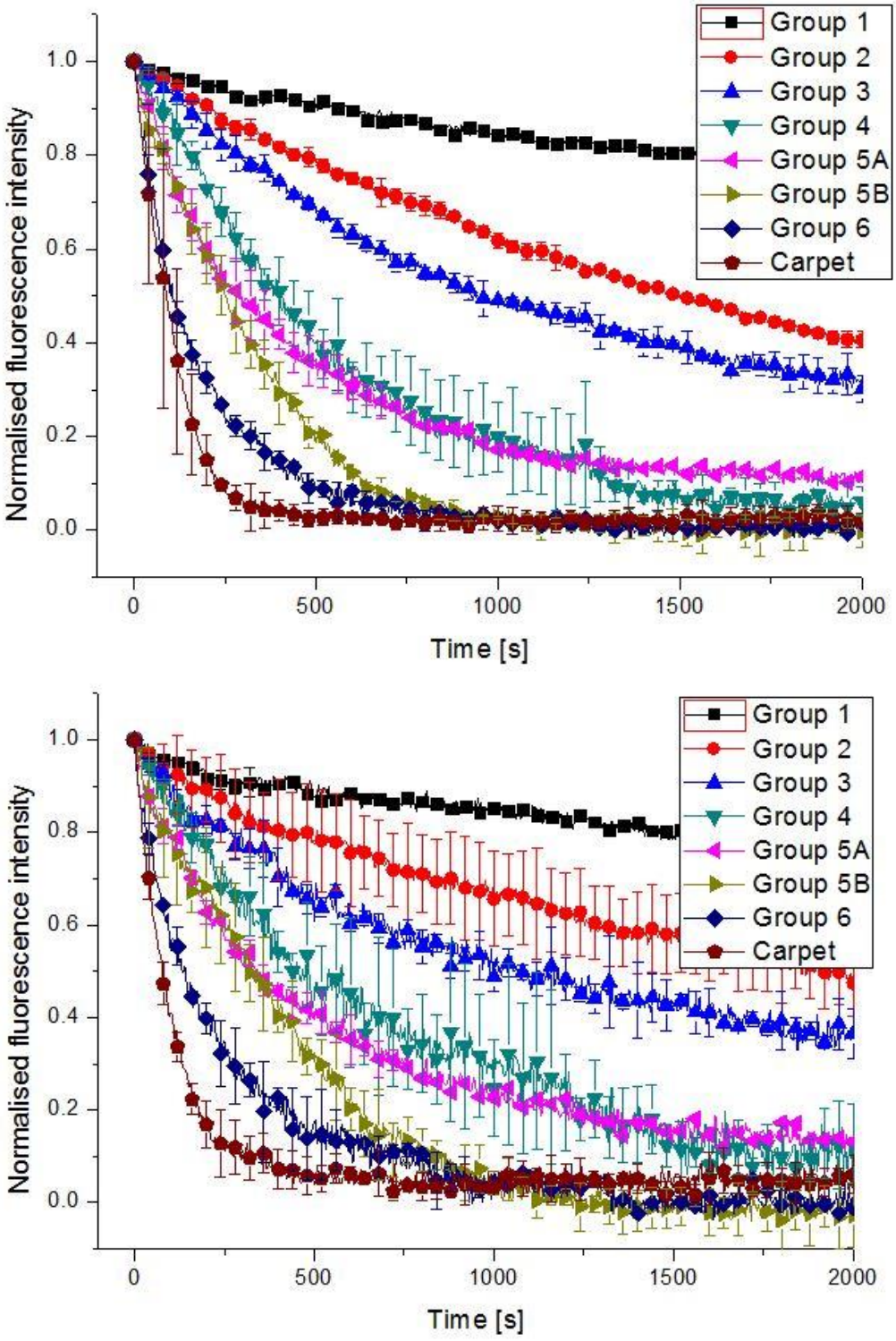

Figure 5.9: Dye leakage kinetics for the 3 and 10 kDa dextran-Alexafluor488 entrapped within DOPC:DOPE:LPG vesicles exposed to 1 μM melittin, with the error bars representing the standard deviation of the individual leakage traces contained within each group. The 10 kDa data set displays much larger error bars than the 3 kDa data, suggesting an increased amount of variability within the efflux of the larger dextran marker. Group 5 for both dextrans splits into two distinct kinetic groups, after following a phase of initially identical leakage kinetics, with the 3 kDa identical phase lasting ~250 s, and the 10 kDa identical phase lasting slightly longer at ~400 s.

Multi-component leakage trace group switching was again evident within this membranes dye-efflux kinetics, with the individual leakage phases recovered from one such multi-component trace presented in figure 5.10.

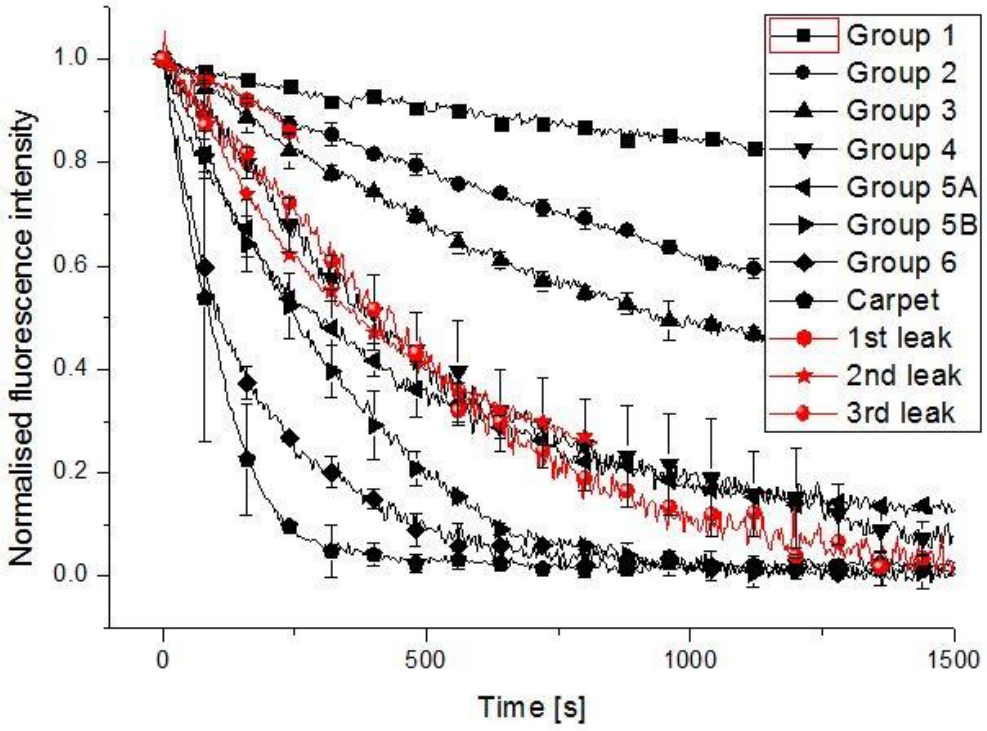

Figure 5.10: Graph demonstrating group switching for 3 kDa data, within a multi-component leakage trace recorded after exposure of a DOPC:DOPE:LPG vesicle to the AMP melittin, at a concentration of 1 µM. The first leakage phase (red hexagons) follows the kinetics of group 2 for ~250 s, before the second phase (red stars) switches to match the kinetics of group 4 for ~750 s. The third leak (red circles) then reinitiates leakage at the kinetics of group 4, until the dextrans within the GUV are completely depleted.

Exposure of the DOPC:DOPE:LPG membrane system to 1 µM of the bacteria selective and positive curvature-inducing AMP magainin, produces the averaged dye-leakage kinetics presented within figure 5.11. The leakage groups were averaged from the following numbers of individual leakage traces; group 1 compiled from a single trace; group 2 from two traces; group 3 from two traces; group 4 from two traces and the carpet mechanism group contains a single trace. The magainin-induced dye-efflux from DOPC:DOPE:LPG GUVs produces uneven leakage of vesicle contents, although this may be a result of the low number of individual traces the averaged groups are compiled from.

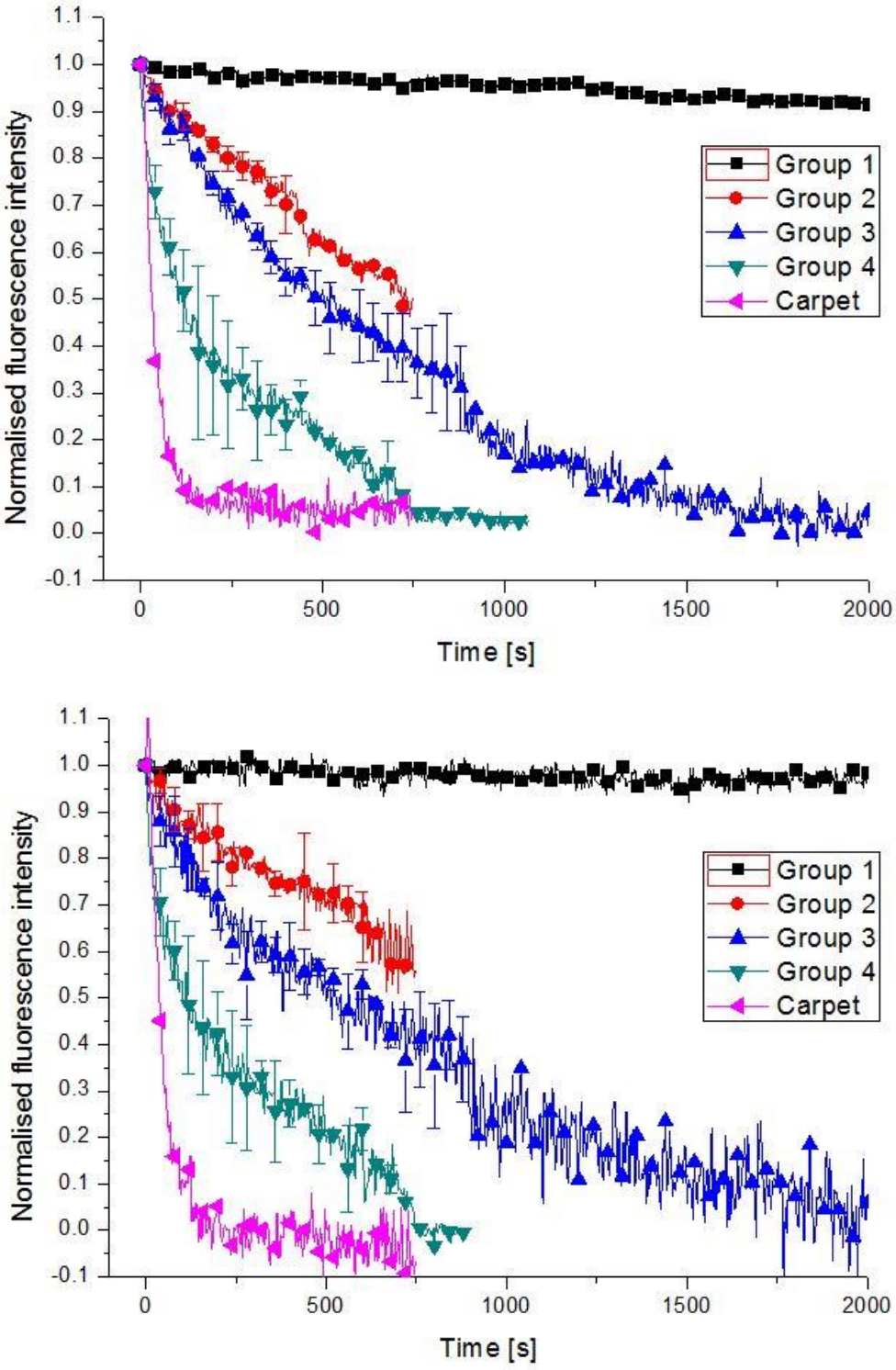

Figure 5.11: Dye leakage kinetics for the 3 and 10 kDa dextran-Alexafluor dextran markers entrapped within DOPC:DOPE:LPG vesicle, exposed to 1 μM magainin, with the error bars representing the standard deviation of the individual leakage traces within each group. Group 1 displays a low (~10%) level of leakage in the 3 kDa data over the 2000 s of data presented, but shows no decrease in the levels of the 10 kDa dextrans entrapped within the vesicle.

5.4. DOPC:DOPE:POPG membrane system

Inclusion of 20 mol% POPG within the DOPC:DOPE membrane system, results in a mixture of lipid charge, topography and fatty acid unsaturation. POPG is anionic with a slightly inverse-conical

geometry, which contains one saturated 16:0 palmitoyl fatty acid and one mono-unsaturated 18:1 (9Z) oleic fatty acid, while DOPC and DOPE display zwitterionic cylindrical and conical geometries respectively. However, not enough good quality traces were recovered to construct leakage kinetics for the pore-mediated leakage process for either peptide for this membrane system.

5.5. DOPC:DPPC:DOPG membrane system

The DOPC:DPPC:DOPG presents a large variation in lipid topography, with the presence of DOPG ensuring the immediate environment of the cationic membrane-bound AMP helix is enriched with the cylindrical anionic lipid. Clear and distinct groups were unable to be detected within this membrane system exposed to 1 µM melittin, as can be seen within the dye-efflux kinetic data presented in figure 5.12, although the leakage traces were concentrated at faster kinetics.

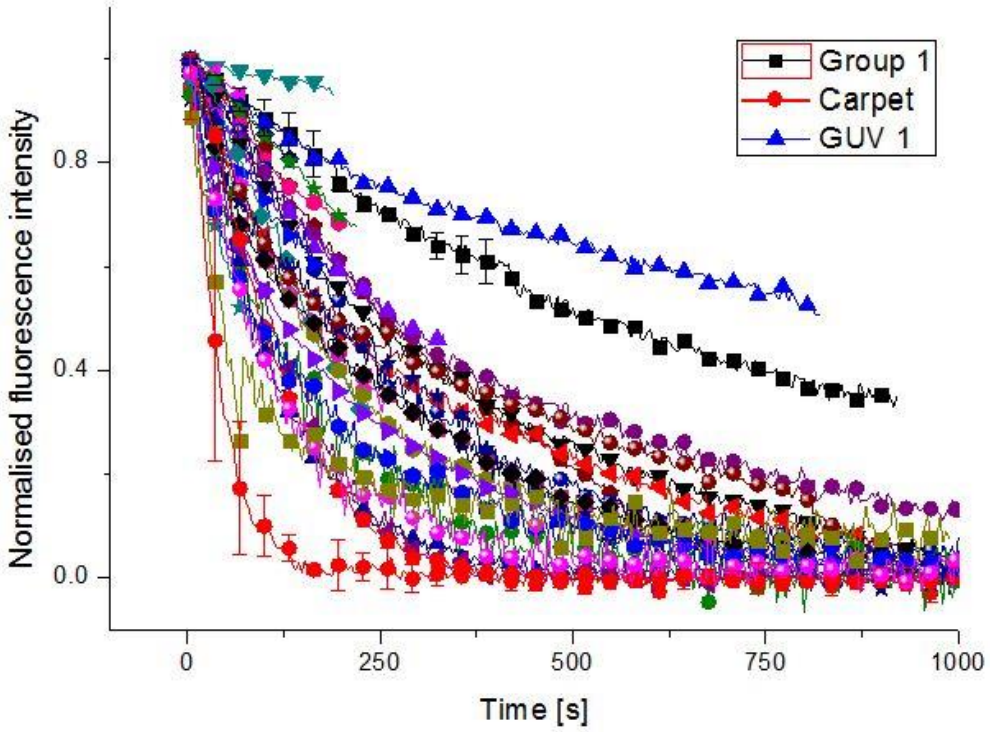

Figure5.12: Dye leakage kinetics for the 3 kDa dextran-Alexafluor488 entrapped within DOPC:DPPC:DOPG vesicles, exposed to 1 µM melittin. Only one pore-mediated leakage grouping could be detected within the data, indicated as group 1 (black squares), with the error bars representing the standard error for the individual leakage traces making up the grouped trace. The leakage trace of GUV 1 (blue triangles) appears to match the kinetics of group 1, for ~200 s, before demonstrating a group switching to slower kinetics. The carpet mechanism grouped trace is depicted as red circles, and the majority of the leakage traces are concentrated at faster kinetics.

DOPC:DPPC:DOPG GUVs exposed to 1 µM melittin produced high levels of pore-mediated leakage events, with > 55 % of vesicles responding to exposure to the AMP by the formation of pores, but the leakage data does not present the clear distinct grouping of the leakage traces displayed by the other membrane systems. The lack of clear dye-efflux grouping within the DOPC:DPPC:DOPG membrane data set, indicates that the leakage events are either unquantised within this membrane system, or the group switching demonstrated within this membrane obscures the quantised leakage kinetics. There were too

few high quality leakage traces to assemble the dye-efflux kinetics for DOPC:DPPC:DOPG membranes exposed to 1 μM magainin, with activity < 10 %.

5.6. DOPC:DPPC:DPPG membrane system

Replacing the cylindrical anionic lipid DOPG, which features two 18:1 (9Z) mono-unsaturated fatty acids, with the anionic inverse-conical DPPG featuring two 16:0 saturated fatty acids, produces a significant change in the dye-efflux kinetics of the system upon exposure to 1 μM melittin. The change of anionic lipid topography and fatty acid composition produced the dye-efflux kinetics displayed in figure 5.13, with clearly distinct groupings of the leakage data again visible. The grouped leakage kinetic traces depicted in figure 5.13 are compiled from the following number of individual leakage traces; group 1 averaged from five traces; group 2 from four traces; group 3 from five traces; group 4 from five traces; group 5 form eight traces and group 6 from four traces. The carpet mechanism was compiled by averaging two traces, and is included for comparison only. In addition to the leakage kinetic grouping, the DOPC:DPPC:DPPG membrane system also demonstrates the group switching phenomenon (do-doo-do-do-do), where multi-component leakage traces can be split into individual leakage phases, which can then be overlaid with the leakage groupings compiled from single-component leakage traces. An example of a two component leakage trace overlaid with the averaged grouped leakage kinetics is presented in figure 5.14. The close match between the separated leakage phases of the multi-component traces, and the averaged leakage traces compiled from the single component traces, again demonstrates the quantised nature of the leakage kinetics induced by AMPs. The dye-efflux from vesicles not only follow predictable and quantised kinetics, but conditions within the lipid-AMP system can change during the process of pore-formation, causing the leakage kinetics to switch from one quantised leakage state to another.

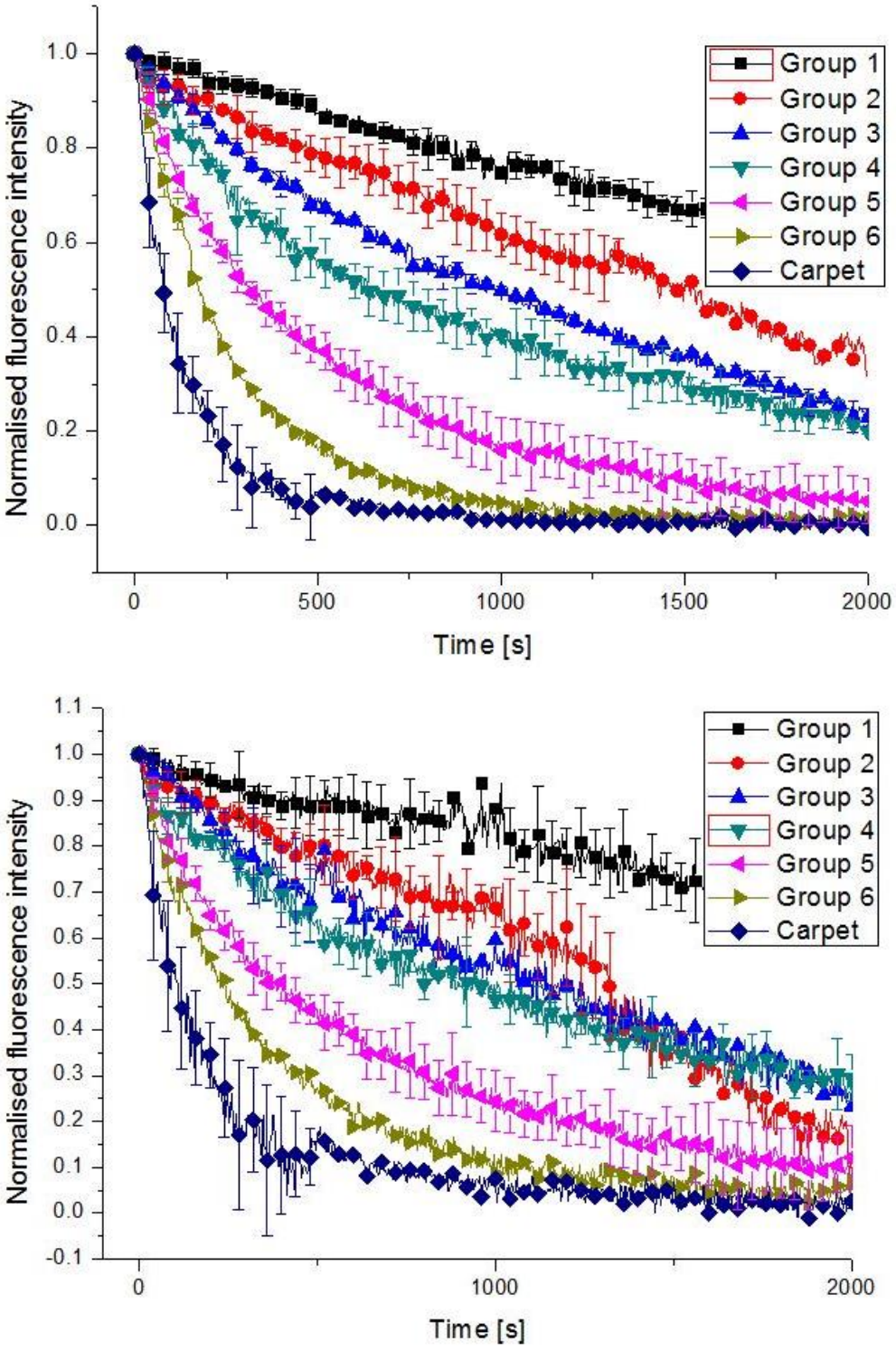

Figure 5.13: Averaged dye-leakage kinetics for the 3 (top) and 10 (bottom) kDa dextran-AlexaFluor markers entrapped within DOPC:DPPC:DPPG vesicles exposed to 1 μM melittin, with the error bars representing the standard error for the individual leakage traces making up the group. The 3 kDa data set contains six clearly separated groups of leakage kinetics, labelled 1 to 6, with a seventh group identified as operating under the carpet mechanism.

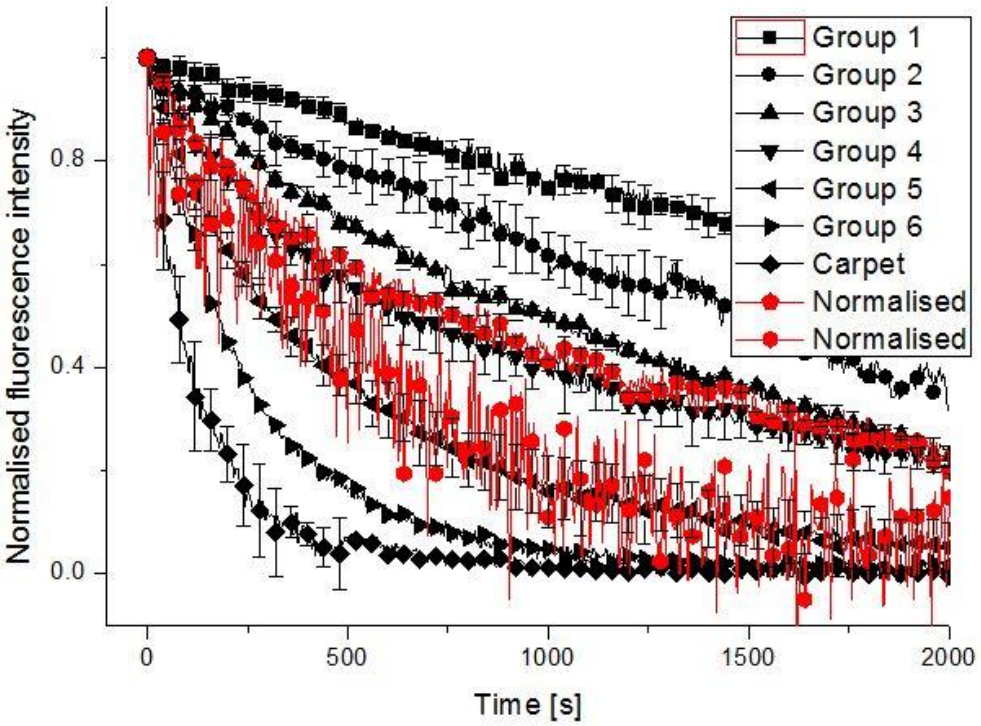

Figure 5.14: Graph depicting the group switching, of a multi-component leakage trace of the 3 kDa dextran marker enclosed within a DOPC:DPPC:DPPG GUV, after exposure to 1μM melittin. The first leakage phase of the multi-component leakage trace (red pentagons) follows the kinetics of group 4 for ~2200 s, before the second leakage phase (red hexagons) switches to follow the kinetics of group 5, until the vesicles contents are completely deleted.

Exposure of the same membrane system to 1 μM of the AMP magainin, produced the dye-efflux kinetics shown in figure 5.15, which presents the single-component leakage traces and the first leakage phases of multi-component traces. The grouped leakage kinetics are compiled from the following number of individual leakage traces; group 1 is the average of three traces; group 2 is the average of five traces; group 3 is the average of two traces and the carpet mechanism grouping is the average of three traces. When the full complement of leakage traces from the 3 and 10 kDa data sets are included within the analysis, i.e. both the single component traces and all the leakage phases from the multi-component traces, the grouped dye-efflux kinetics shown in figure 5.16 are produced. The traces in figure 74 were compiled by averaging the following amount of individual leakage traces; group 1 is the average of three traces; group 2 is the average of five traces; group 3 is the average of five; group 4 is the average of four traces; group 5 is the average of six traces and group 6 is comprised of a single trace. The carpet mechanism group is compiled from the average of five traces.

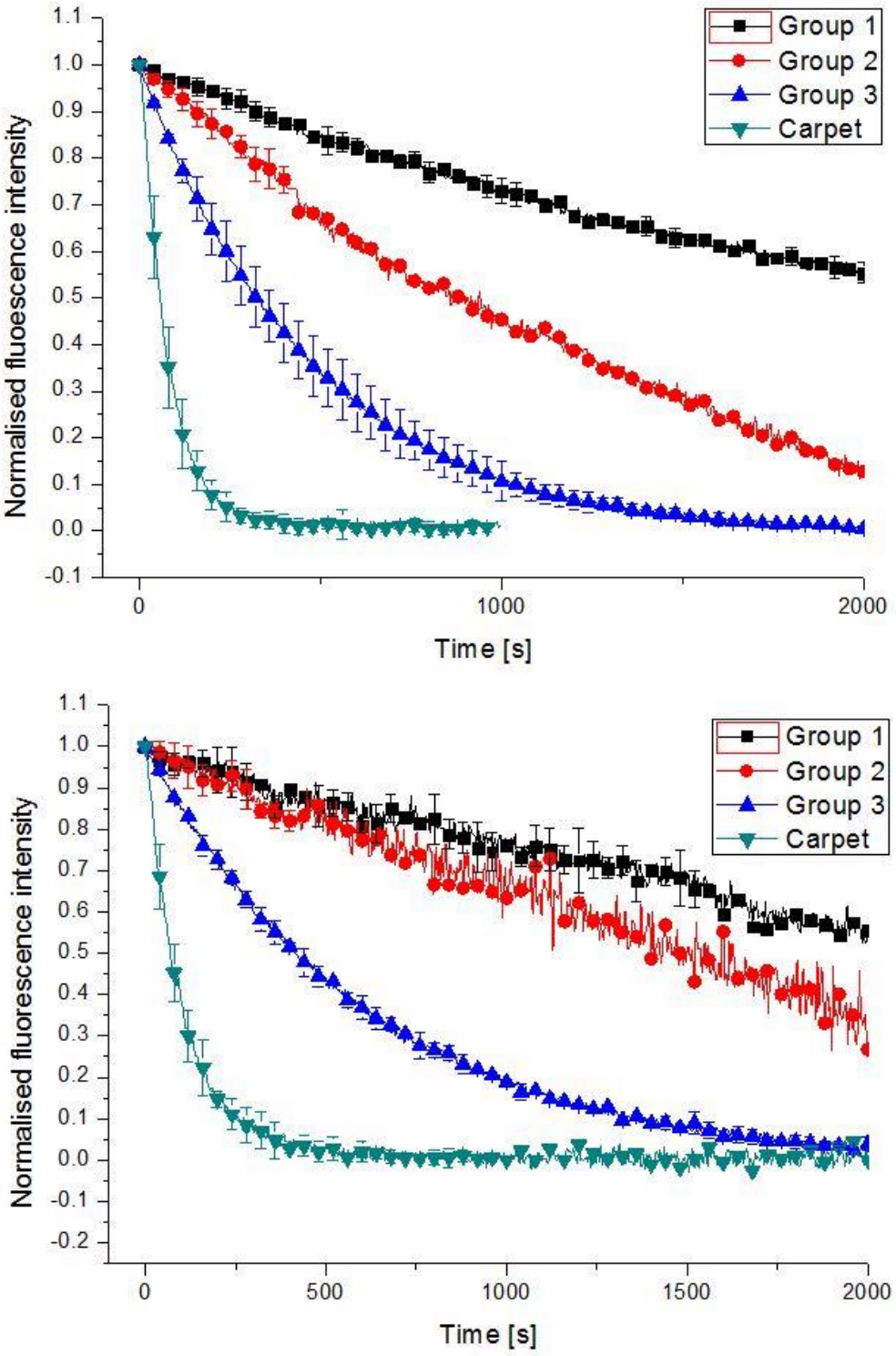

Figure 5.15: Initial dye leakage kinetics for the 3 (top) and 10 (bottom) kDa dextran-Alexafluor markers entrapped within DOPC:DPPC:DPPG vesicles exposed to 1 μM magainin, with the error bars representing the standard deviation of the individual leakage traces contained within each group. There are three pore-mediated leakage kinetic groups visible, and a fourth group at faster kinetics, representing leakage occurring via the carpet mechanism. Groups 1 and 2 are clearly distinct within the 3 kDa data, but the groups display much closer kinetics within the 10 kDa data set.

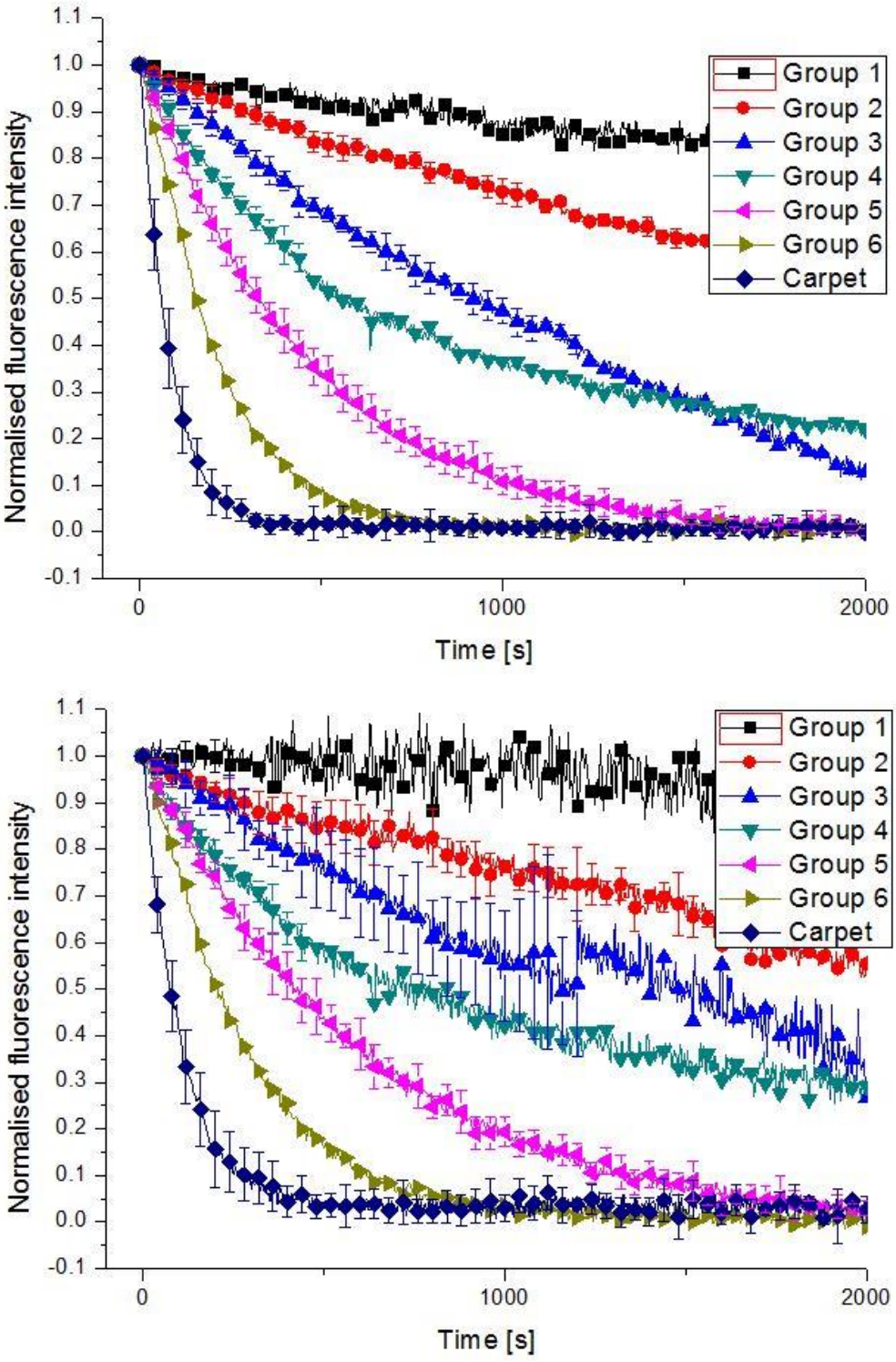

Figure 5.16: Complete set of grouped dye-leakage kinetics for the 3 (top) and 10 (bottom) kDa dextran-Alexafluor markers entrapped within DOPC:DPPC:DPPG vesicles exposed to 1 μM magainin, with the error bars representing the standard deviation of the individual leakage traces contained within each group. The number of kinetic groupings for pore-mediated leakage increases, from three to six, compared to the initial leakage graph shown in figure 5.15, with groups 1, 4 and 6 being unique to the complete data set.

Note that the complexity of the dye-efflux kinetics significantly increases within the complete data set, as compared to the grouped kinetics assembled from only the single component and initial phases

of multi-component traces. The number of groups increases from three to six, suggesting that the pore-formation process can be complicated, by the translocation of magainin across the membrane as part of initial pore formation. The translocated peptide then goes on to participate in pore formation from the inner membrane leaflet, resulting in the creation of novel leakage kinetics. The group 1 of the complete data set shows ~ 20 % loss of vesicle contents for the 3 kDa dextran, but displays 100 % retention for the 10 kDa dextran. This provides additional evidence for the formation of a population of small pores, able to expel the smaller dextran, but too small to expel the larger molecule. This defines the size of the group 1 pore as between the diameter of the 3 kDa dextran as a minimum, and the diameter of the 10 kDa as a maximum; i.e. the pore diameter lies somewhere between 2.26 and 4.13 nm. Groups 1, 4 and 6 are unique to the complete data set, and together comprise one third (8/24) of the total leakage traces, and the fact that it only appears within the later leaks of multi-component traces, suggests a role for translocated peptide within the pore-formation process for these leakage groups. Group switching behaviour is again present in the multi-component dye-leakage traces of DOPC:DPPC:DPPG membranes exposed to 1 µM magainin, with the overlay of a five component traces overlaid with the complete data set, using the 3 kDa leakage data presented in figure 5.17.

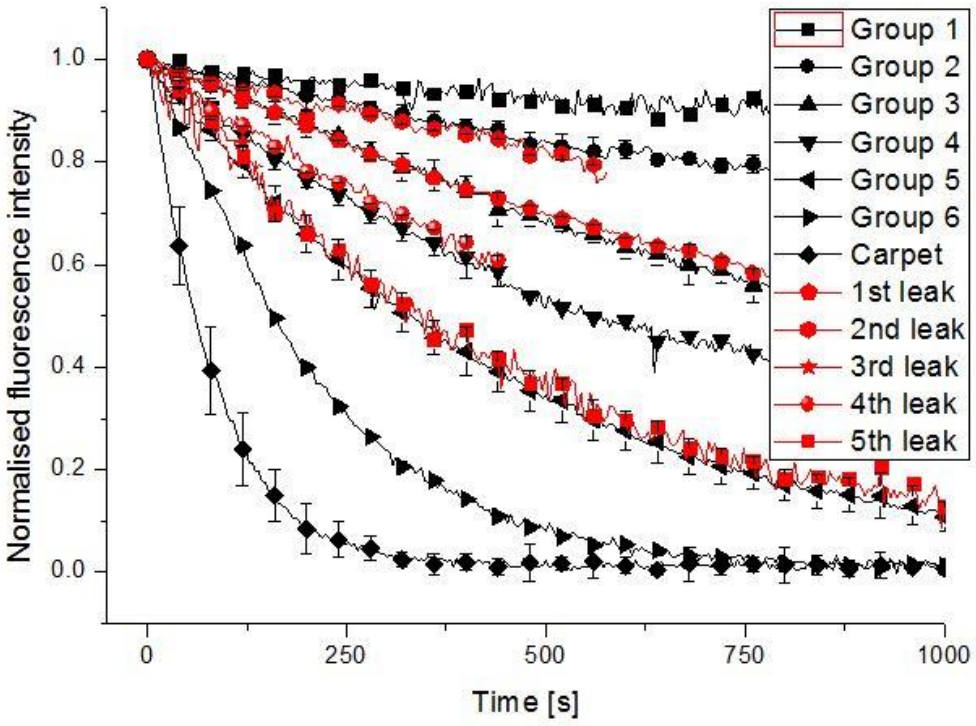

Figure 5.17: Graph showing the group switching behaviour of a five-component leakage trace, from a DOPC:DPPC:DPPG GUV exposed to 1 µM magainin, with the individual leakage phases of the multi-component trace shown in red, and the averaged leakage kinetics shown in black. The first leakage phase (red pentagons) follows the leakage kinetics of group 3 for ~800 s, before the second leakage phase (red hexagons) switches to group 2 kinetics, for ~ 550 s. The third leakage phase (red stars) matches the kinetics of group 5 for ~150 s, before the four leakage phase (red circles) switches to match the kinetics of group 4 for ~450 s. The final leakage phase of the multi-component trace, then changes from following group 4 to following group 5 kinetics, until vesicle contents are completely depleted.

The group switching behaviour noted for the multi-component traces displays a general trend towards faster kinetics, but may switch back and forth between faster and slower leakage groups. The traces displayed in figure 5.17 for example, show that the leakage kinetics of the multi-component trace

follow a complex path through the quantised leakage kinetic landscape, moving first from a faster leakage group (group 3) to a slower group (group 2). The leakage kinetics of the multi-component trace then switches to a faster leakage kinetic group (group 5), then back to the slower kinetic group (group 4), before returning to the faster kinetics of group 5. To compare the leakage kinetics produced by exposure of the DOPC:DPPC:DPPG membrane system, to 1 µM of the AMPs magainin and melittin, the averaged leakage traces obtained for both peptides was overlaid, and the 3 kDa data set is presented as figure 5.18.

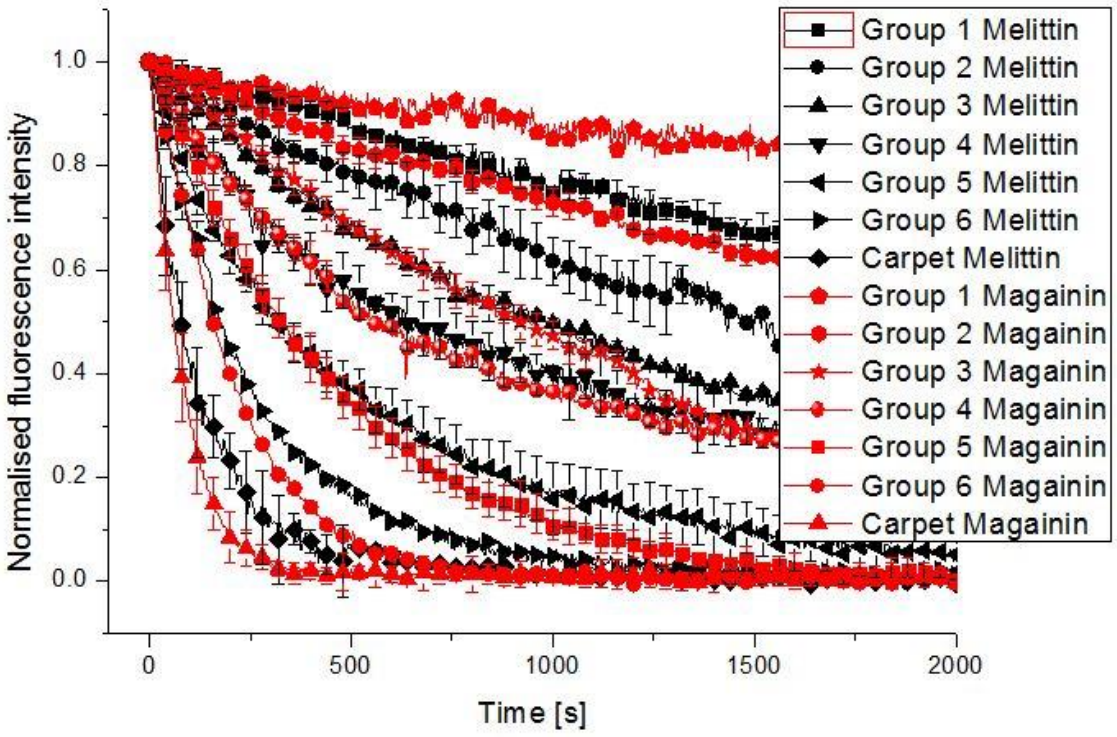

Figure 5.18: Graph of the overlaid averaged kinetic data for the 3 kDa dextran marker, for the DOPC:DPPC:DPPG membrane system exposed to 1 µM of the AMPs melittin (black) and magainin (red). Some averaged dye-efflux kinetic groups display closely matched leakage kinetics between the data sets for both AMPs, with groups 1, 3, 4, 5, and 6 for the melittin data set closely matching to the groups 2, 3, 4, 5 and 6 respectively, from the magainin data set. The kinetic groupings within the magainin data set display smaller standard errors, than the groupings contained within the melittin data, indicative of the tighter grouping of the individual leakage traces, within each leakage group produced by the AMP magainin.

The overlaid averaged kinetics both AMPs show similarities, with five of the six groups following similar kinetics, for both peptides. This close matching between the grouped leakage kinetics has profound implications for the mechanism of action of LCAMPs (see discussion), although it must be noted that significant differences exist in the initiation times of the pore-mediated leakage process. In the DOPC:DPPC:DPPG membrane system, melittin initiates the leakage process an average of 2541.0 s after first exposure of the vesicles to the peptide, while magainin returns a longer average initiation time of 3255.4 s. This suggests magainin takes a longer time to establish the lipid-AMP interactions in the DOPC:DPPC:DPPG membrane system, which result in the formation of pores than melittin. Magainin also displays lower levels of activity compared to melittin, within the DOPC:DPPC:DPPG membrane system, as demonstrated by the PIE profiles for the two AMPs presented in figure 5.19.

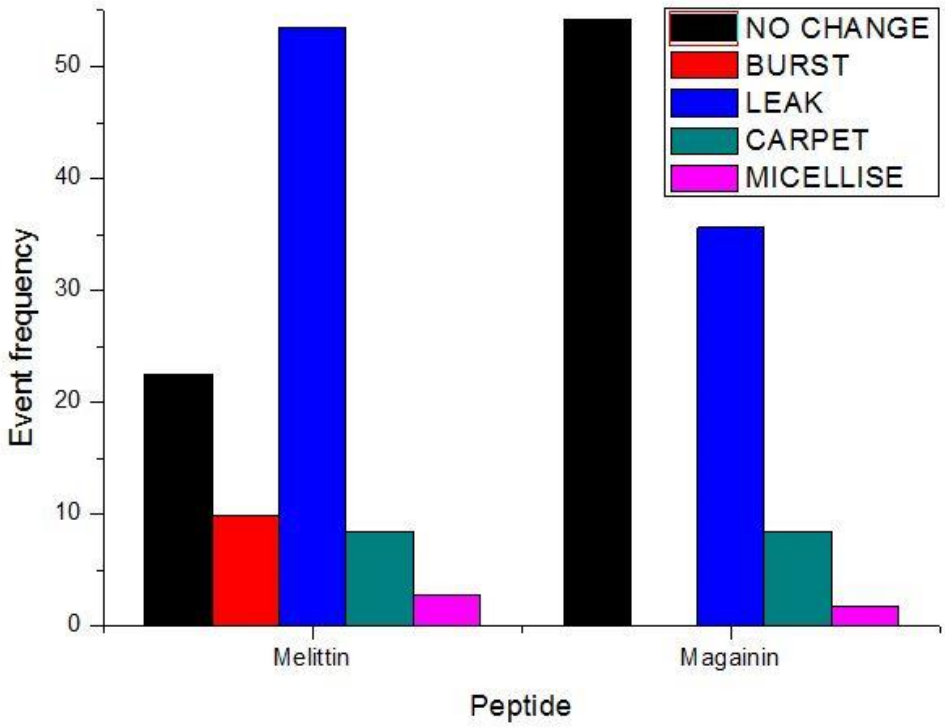

Figure 5.19: Comparison of the PIE profiles for the LCAMPs melittin and magainin, obtained by their interactions with the DOPC:DPPC:DPPG membrane system, at a peptide concentration of 1 µM. Although melittin is significantly more active within the membrane system than magainin, with 77.5 % of vesicles exhibiting a PIE during the time course of the experiment (8000 s) compared to 45.8 % of vesicles exposed to magainin, the profiles for the two peptides are remarkably similar. Both profiles are dominated by pore-mediated leakage events, with 53.5 % of the GUVs exposed to melittin displaying the behaviour, compared to 35.6 % of the GUVs exposed to magainin. The other PIEs display < 10 % activity within this membrane system for both LCAMPs.

Marked similarities exist between PIE profiles of magainin and melittin within the DOPC:DPPC:DPPG membrane system, with both profiles displaying high levels of pore-mediated leakage, with 53.5 and 35.6 % of the GUVs exposed to melittin and magainin respectively producing pore-mediated leakage as their dominant PIE. With melittin being more active within the membrane, displaying >75 % activity compared to 46.3 % for magainin, the selective AMP magainin is actually proportionally more effective at producing pore-mediated leakage events within active vesicles than melittin. Magainin produced 76.9 % of active vesicles displaying pore formation, compared to melittin, which results in 70.2 % of active vesicles displaying pore-formation.

5.7. mGUV membrane system

The mGUV membrane system contains DOPC, a cylindrical zwitterionic lipid; DPPC, a zwitterionic lipid with inverse-conical geometry and cholesterol, a zwitterionic negative curvature inducing lipid. When mGUV vesicles containing fluorescently tagged dextran markers were exposed to melittin, at a concentration of 1 µM, the dye-efflux kinetics shown in figure 5.20 were produced.

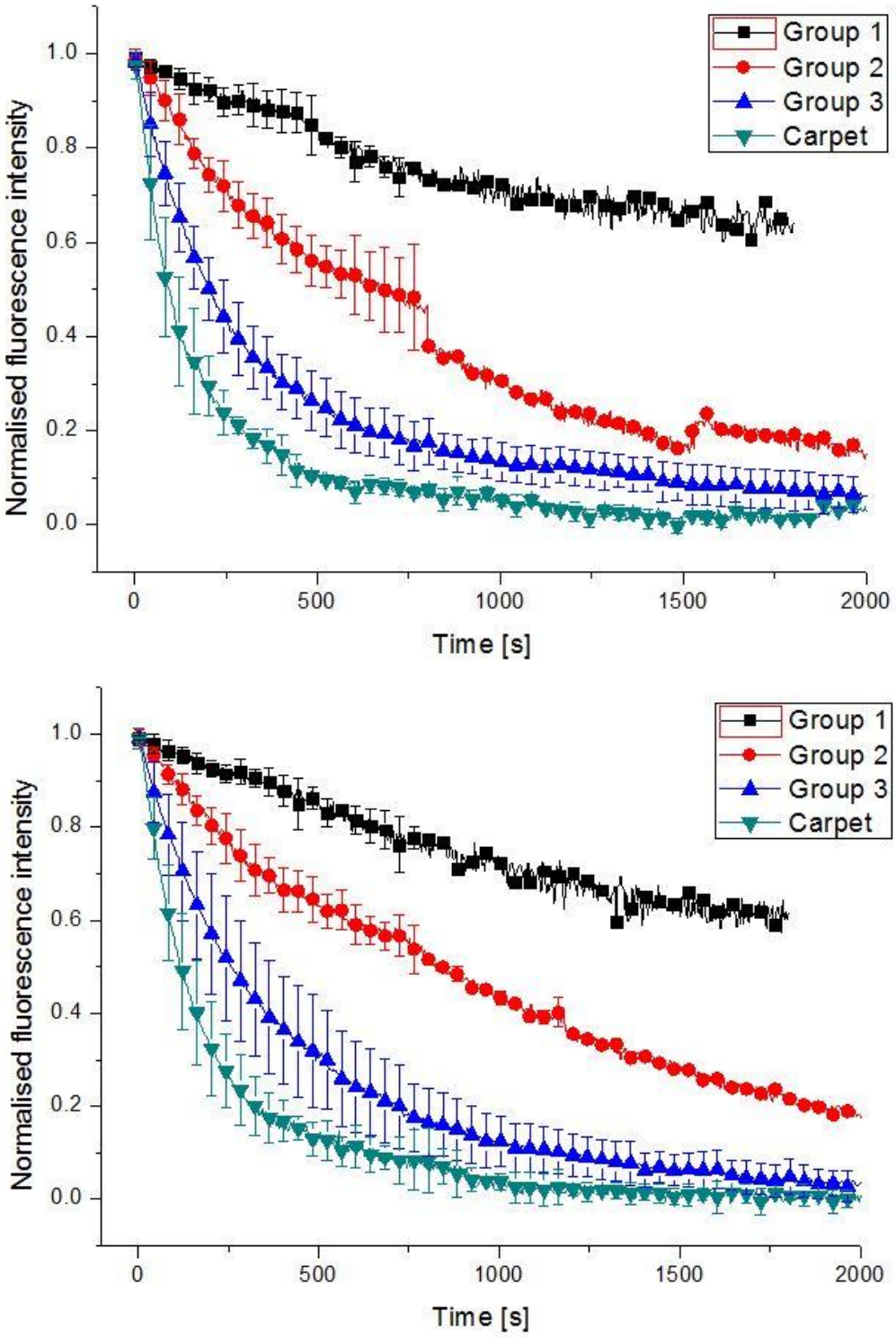

Figure 5.20: Dye-leakage kinetics for the 3 and 10 kDa dextran markers entrapped within mGUV vesicle, exposed to 1 µM melittin, with the error bars representing the standard deviation of the individual leakage traces contained within that group. There are three distinct pore-mediated leakage groupings within the dye-efflux data, with the carpet mechanism (turquoise triangles) included for comparison only.

The averaged traces depicted in figure 5.20 were compiled from the following number of individual traces; group 1 from nine traces; group 2 from seven traces; group 3 from eighteen traces and the carpet mechanism trace is compiled from six traces. In addition to the grouping of the leakage data into

quantised kinetic groupings, the membrane system also displayed group switching behaviour within multi-component traces, when the mGUV membrane system was exposed to 1 µM melittin. The individual 3 kDa leakage phases of a three component trace are displayed in figure 5.21, overlaid with the averaged kinetic grouping data from the relevant preceding figure.

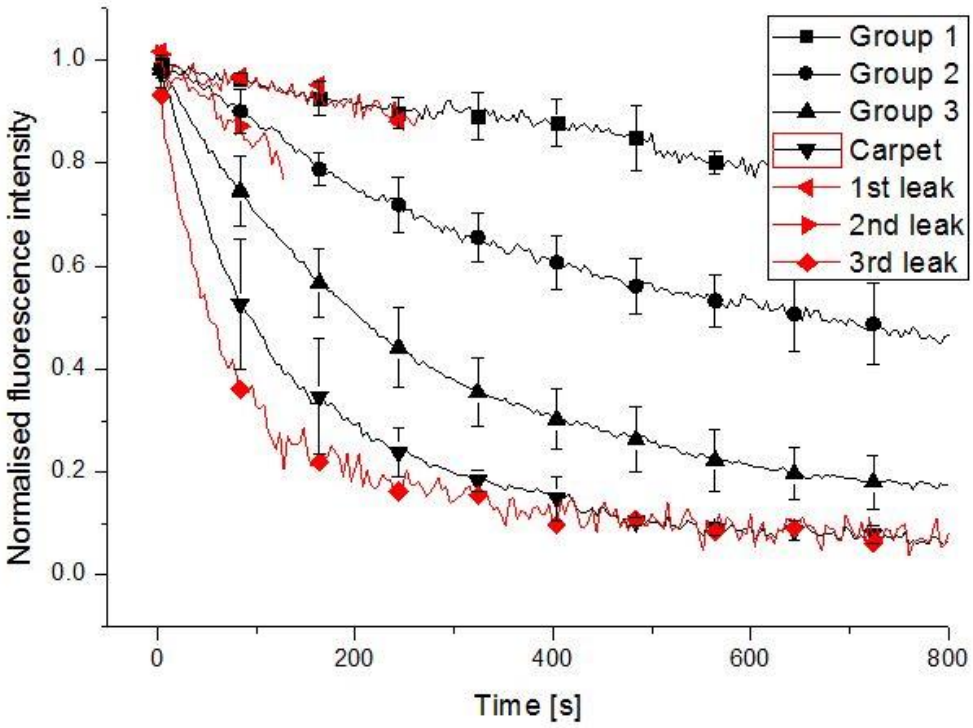

Figure 5.21: Group switching exhibited by the 3 kDa dextran dye-efflux kinetics, produced by exposure of mGUVs to 1 µM melittin, with the averaged leakage grouping depicted in black and the individual leakage phases of the multi-component traces shown in red. The first leakage phase of the multi-component trace (red left-facing triangles) follows the leakage kinetics of the averaged group 2 for ~150 s, before the second leakage phase (red right-facing triangles) shifts to follow group 1 kinetics for ~250 s. The third and final leakage phase of the multi-component leak (red diamonds) leaks via the carpet mechanism until the vesicles contents are completely depleted.

In common with most other membrane systems, the overlaid data from the multi-component leakage traces shows a very close match to the existing averaged leakage groups. Exposure of the mGUV membrane system to the higher 5 µM melittin concentration produced the dye-efflux kinetics shown in figure 5.22. Unlike the 1 µM data, only part of the data could be resolved into distinct kinetic groups, with the majority of the data occurring at fast kinetics. The 5 µM melittin data for the 3 kDa dextran efflux-kinetics displayed only one clearly delineated grouping of leakage traces, with a loosely grouped number of leakage traces at slower kinetics, but the majority of leakage occurring at faster kinetics, with no clear leakage groups. The 10 kDa data show a more distinct leakage pattern, with the slower kinetic traces more tightly grouped, and two leakage groups at faster kinetics, as well as a distinct carpet mechanism group. The data is still lacks enough clarity for the individual leakage groups to be reliably established however, and the ungrouped data is presented.

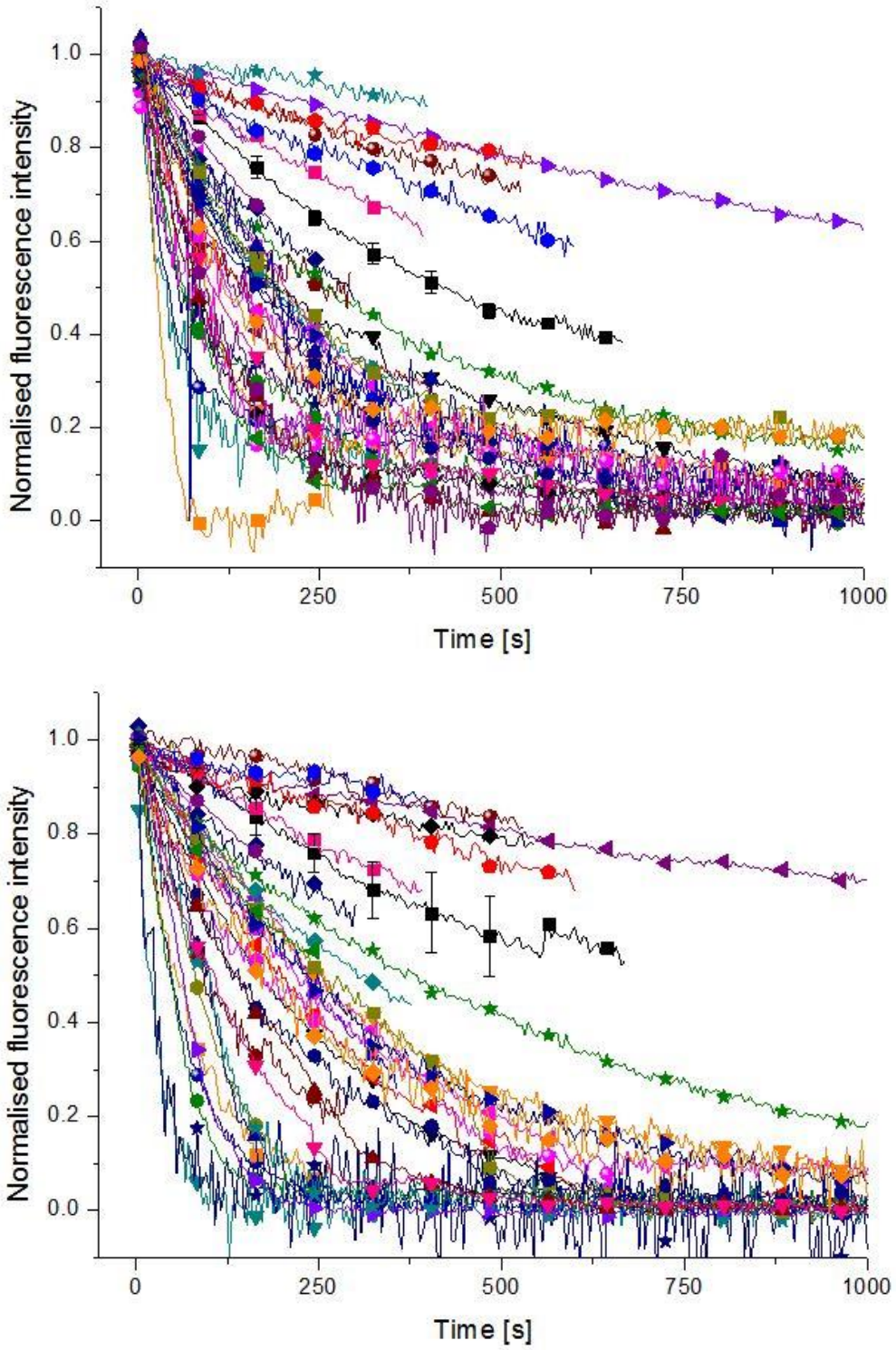

Figure 5.22: Graph showing the 3 and 10 kDa dye-efflux kinetics for the mGUV membrane system, after exposure to 5 μM of the AMP melittin. One closely matched group of leakage kinetics was identified within the 3 kDa data, and averaged to create a leakage group, represented by the black squares. The error bars represent the standard deviation of the individual leakage traces comprising the group. The remainder of the leakage kinetics feature no resolvable groups within the 3 kDa data. The 10 kDa data presents improved separation and grouping of the kinetics data compared to the 3 kDa data set, with three possible kinetic groupings visible; a slower kinetic group (A); two faster kinetic groups (B and C) and the carpet mechanism (D). However these groups are not clearly delineated from one another to establish the presence of leakage groups.

The closer grouping of the 10 kDa dextran data suggests that less variability exists within the pore-mediated leakage for the larger 10 kDa marker, while the smaller 3 kDa data encounters higher diversity in efflux through the pore structures. The unresolved traces contain 44 individual leakage events, while the leakage group is the result of averaging five traces. In common with most data sets, the 5 µM melittin mGUV data contained multi-component leakage traces that overlay with the leakage groups from the single-component data, with an example of a three component leakage trace presented in figure 5.23.

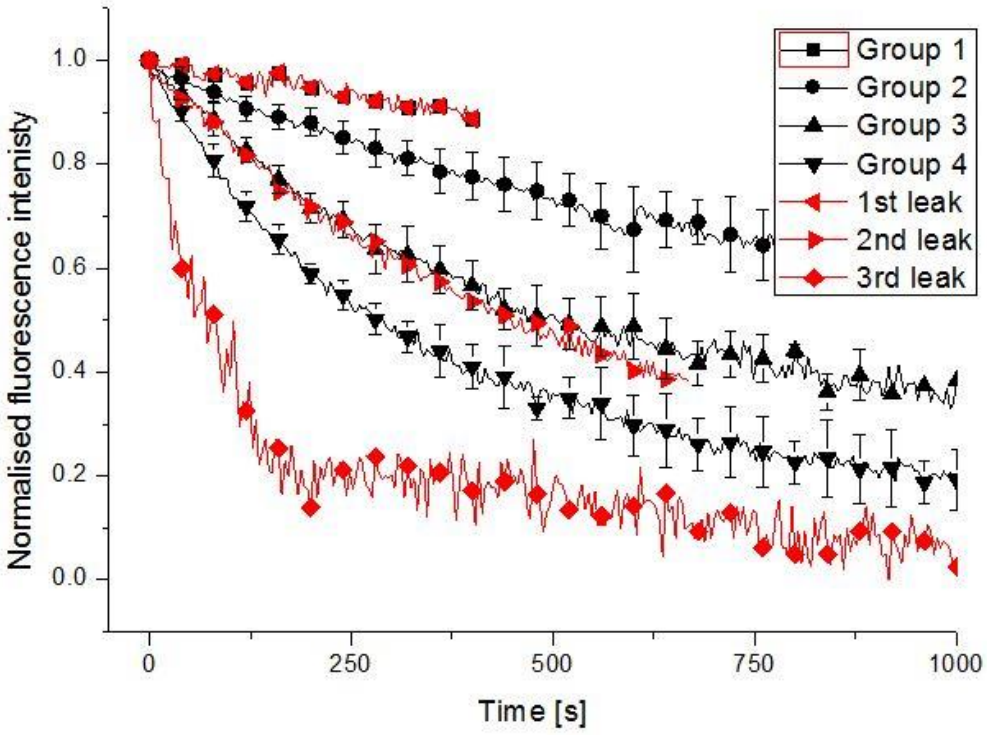

Figure 5.23: Graph demonstrating the group switching of a three component leakage trace, recorded from an mGUV after exposure to 5 µM melittin, with the averaged data presented in black and the individual leakage phases of the multi-component trace shown in red. The first leakage phase (red left-facing triangle) presents closely matched kinetics to that of group 1 for ~400 s, before switching to run parallel to the kinetics of group 3 for ~650 s for the second leakage phase (red right-facing triangles). The third leakage phase of the multi-component trace displays faster kinetics, possibly via the carpet mechanism, until the vesicle contents are completely depleted.

In addition to the multiphase leak group switching, the mGUV membrane system also displayed closely matching kinetics between the 1 and 5 µM data sets, but with differing event initiation timings. Both melittin concentrations display 100 % activity within the mGUV membrane system, with very similar PIE profiles. Melittin at a concentration of 1 µM produces 25.6 % pore-mediated leakage events, with an average initiation time of 1572.2 s after exposure to the peptide. At the higher concentration of 5 µM melittin produces 29.1 % pore-mediated leakage events, occurring on average of 624.1 s after exposure. The overlaid data for the mGUV membrane system exposed to 1 and 5 µM melittin is presented in figure 5.24.

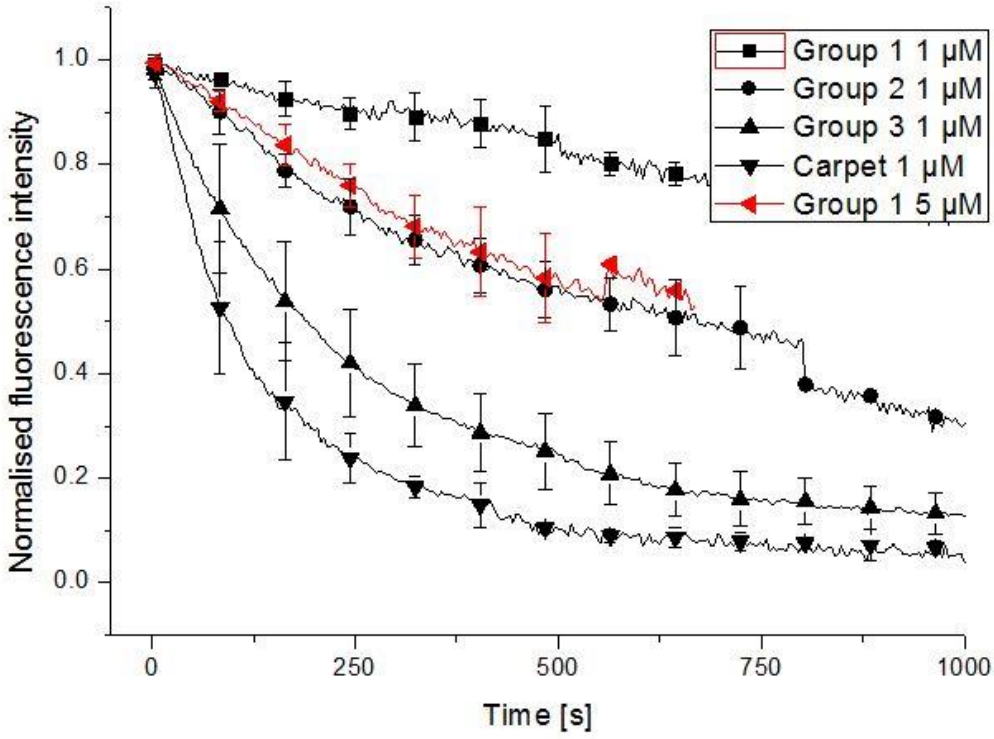

Figure 5.24: Graph presenting the overlaid data for the dye-efflux kinetics, induced by the exposure of the mGUV membrane system, to different concentrations of the AMP melittin. The 1 µM peptide concentration data is presented in black, and the 5 µM concentration in red, with the error bars displaying the standard deviation of the individual leakage traces within each group. The 5 µM leakage group presents a close match to the kinetics of the 1 µM group 2.

The close match between the 1 and 5 µM melittin data, suggest that identical pore forming processes are occurring within the mGUV membranes, at both concentrations of AMP. It can be speculated that the loose grouping of leakage traces displaying slower kinetics than group 1 within the 5 µM data correspond to group 1 of the 1 µM data, and the two ill-defined groups visible within the 5 µM data are the group 3 and carpet mechanism groups seen in the 1 µM data set. The increase in peptide concentration increases the variability of the leakage data, especially within the 3 kDa data, which suggests the presence of additional smaller pores at the higher concentration. Exposure of mGUVs to the AMP magainin at a concentration of 1 µM produced much lower levels of PIEs than melittin, with 31.1 % of vesicles producing activity, with only 2.3 % displaying pore-mediated leakage and the PIE profile dominated by bursting (17.2 %) and the carpet mechanism (9.9 %). The large data set size (354 mGUVs) allowed grouped leakage kinetics to be established, and produced the grouped dye-leakage kinetics shown in figure 5.25. The averaged groups were compiled by averaging the following amount of individual leakage traces; group 1 is the average of two traces; group 2 is the average of three traces and the carpet mechanism group is the average of seventeen traces.

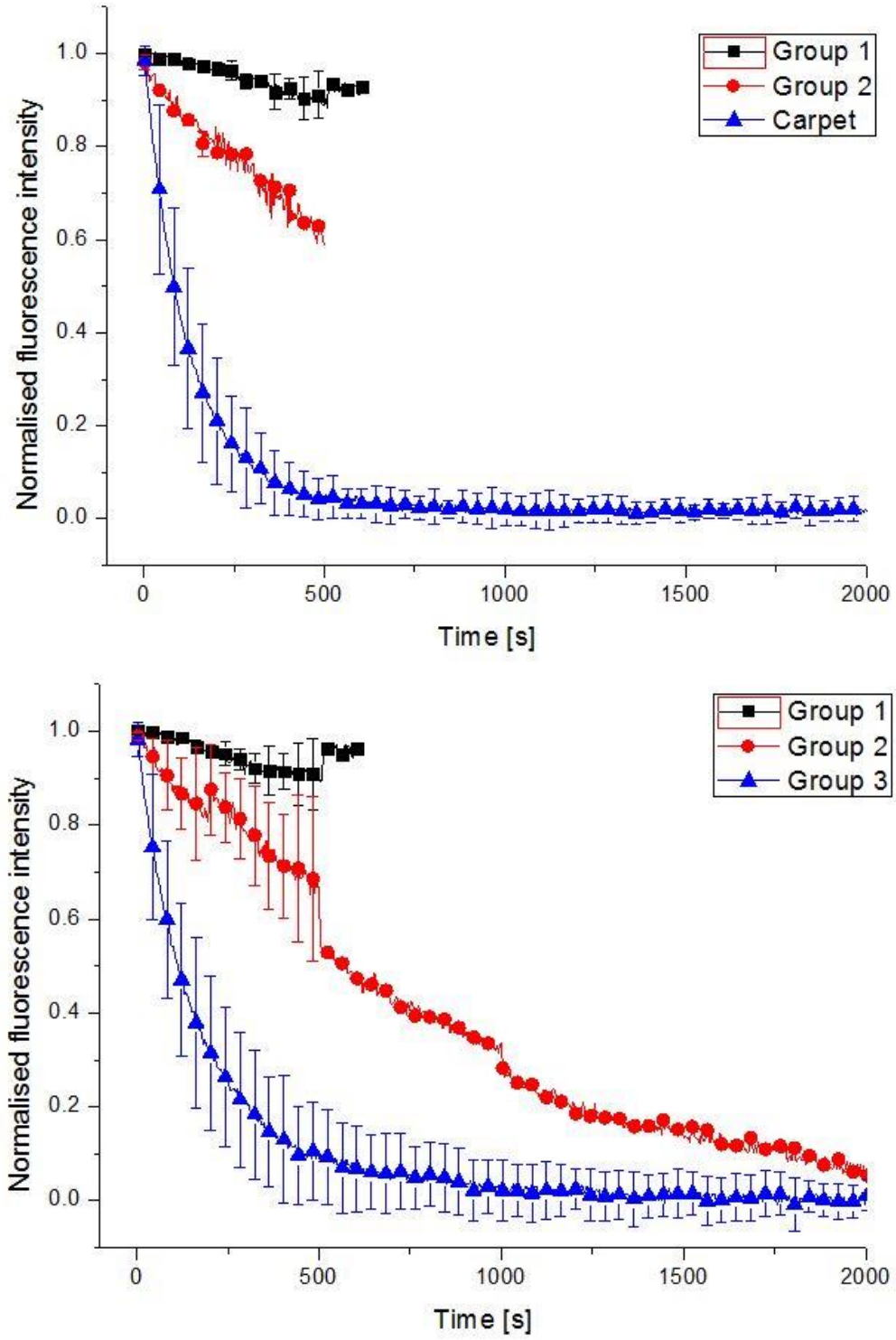

Figure 5.25: Averaged leakage groups displayed by the mGUV membrane system, after exposure to 1 µM of the AMP magainin, with the error bars representing the standard deviation of the individual leakage traces contained within each group. Two pore-mediated leakage kinetic groupings were produced by the efflux of the 3 kDa (top) and 10 kDa (bottom) dextran markers, with the groupings noticeably tighter within the smaller 3 kDa data set, as demonstrated by the reduced error bars.

The data collected for the mGUV system exposed to 1 µM magainin showed an interesting set of multicomponent leakage traces, with an example presented in figure 5.26.

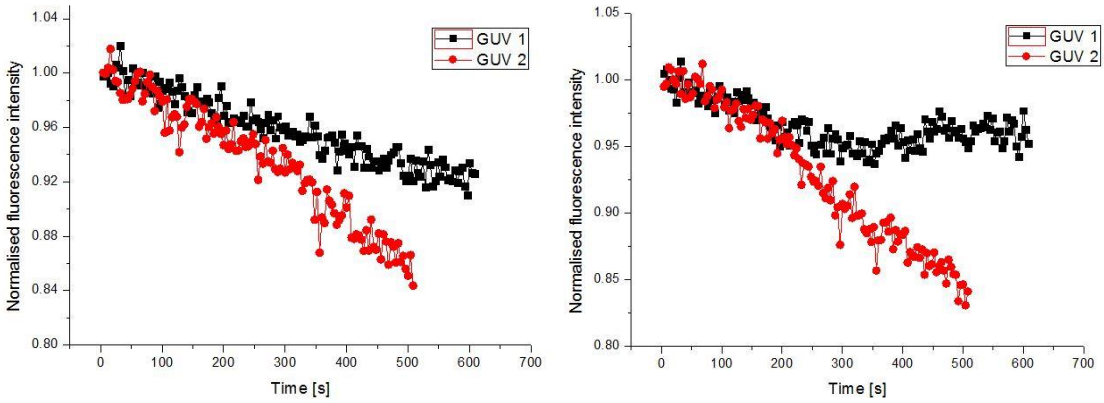

Figure 5.26: Graph depicting the changes within group 1 kinetics during the pore-mediated leakage event, for 3 (left) and 10 (right) kDa dextran-Alexafluor entrapped within mGUV vesicles, exposed to 1 µM magainin. The 3 kDa data shows that while the efflux rate for the smaller dextran remains constant for GUV 1, there is a pronounced increase in rate of release for GUV 2 after ~200 s. The 10 kDa data for GUV 2 indicates that the 10 kDa dextran efflux rate increases at the same timepoint as the 3 kDa data, but that the 10 kDa dextran leakage ceases at ~ 250 s.

The contrasting picture presented in figure 5.26, where leakage kinetics from the same group present opposing leakage behaviour, paints a complex picture of the dynamic interactions producing the pores within the mGUV membrane. The rate of dextran release from GUV 1 undergoes an increase after ~200 s for both the 3 and 10 kDa markers, indicating that an increase in the number, size or opening time for the pores has occurred. The dye-efflux data for GUV 2 also shows a change occurring at approximately the same time point as GUV 1, but with remarkably different results. The 3 kDa leakage rate appears to be unaffected, but the leakage rate for the larger 10 kDa dextran completely ceases. This indicates that a change within the lipid-AMP system has taken place, which stops the larger dextran from passing the lipid membrane barrier, while having little effect on the escape of the smaller 3 kDa dextran. Exposure of the mGUV membrane system to the higher magainin concentration of 5 µM produces the grouped leakage kinetics displayed in figure 5.27. The Data shown in figure 5.27 was compiled by averaging the following number of individual leakage traces; group 1 is the average of two traces; group 2 is a single trace; group 3 is the average of three traces and the carpet mechanism group is the average of seven traces.

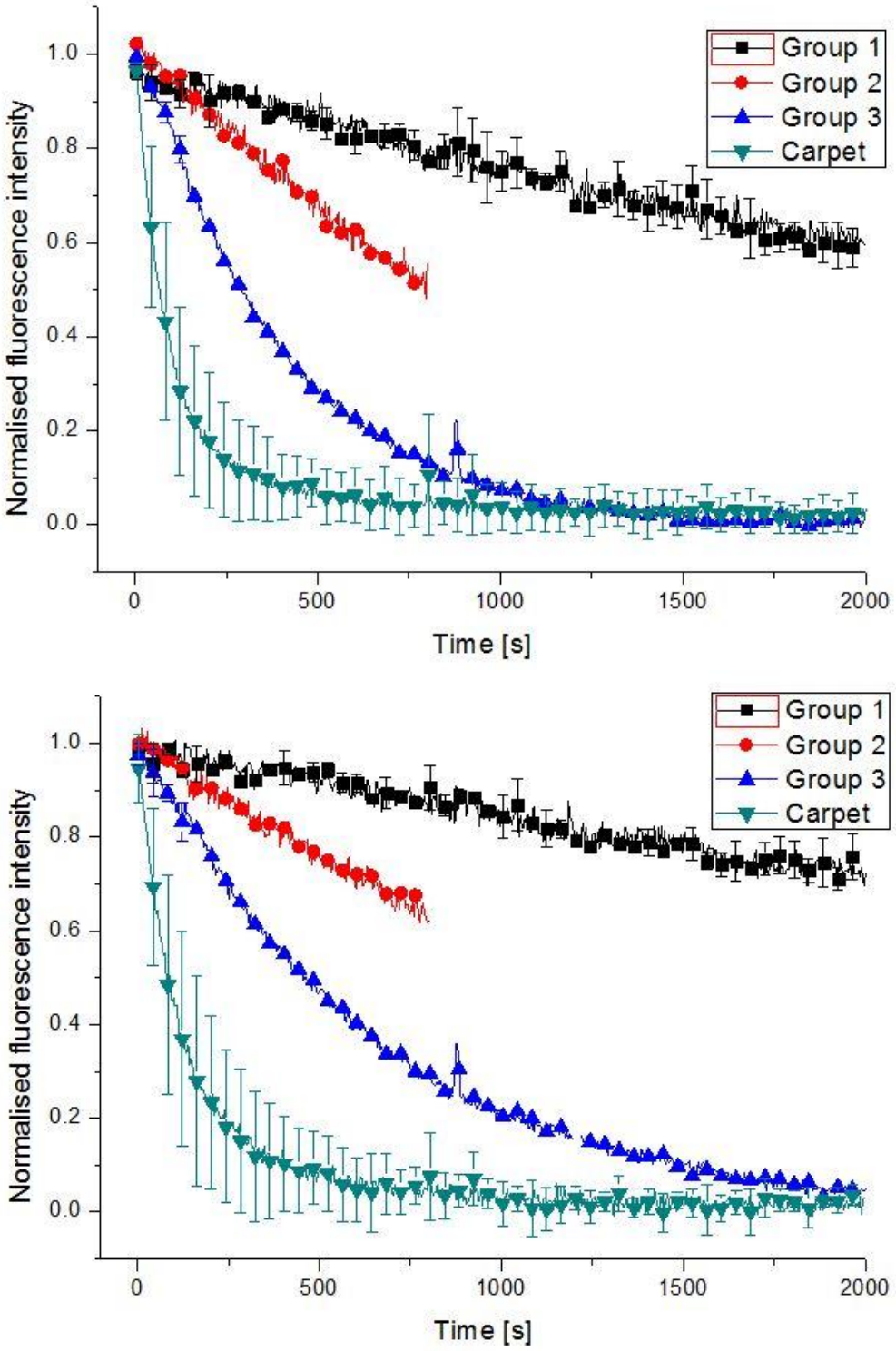

Figure 5.27: Graph depicting the averaged leakage groups for the mGUV membrane system, after exposure of the vesicles to 5 μM of the AMP magainin, allowing the efflux of entrapped 3 (top) and 10 (bottom) kDa dextrans through the peptide induced pores. Both dextran markers produce quantised leakage kinetics, with four clearly distinct leakage kinetic groups present, with the error bars representing the standard deviation of the individual leakage traces that comprise each group. Three of the groups are produced by pore-mediated leakage events, and one group is the result of leakage via the carpet mechanism.

The 5 μM magainin system also displayed the multi-component leakage group switching seen in the 1 μM system, as well as previous membrane systems. A two component leakage traces is presented in

figure 5.28, with both leakage phases from the multi-component trace separately overlaid onto the complete leakage data set.

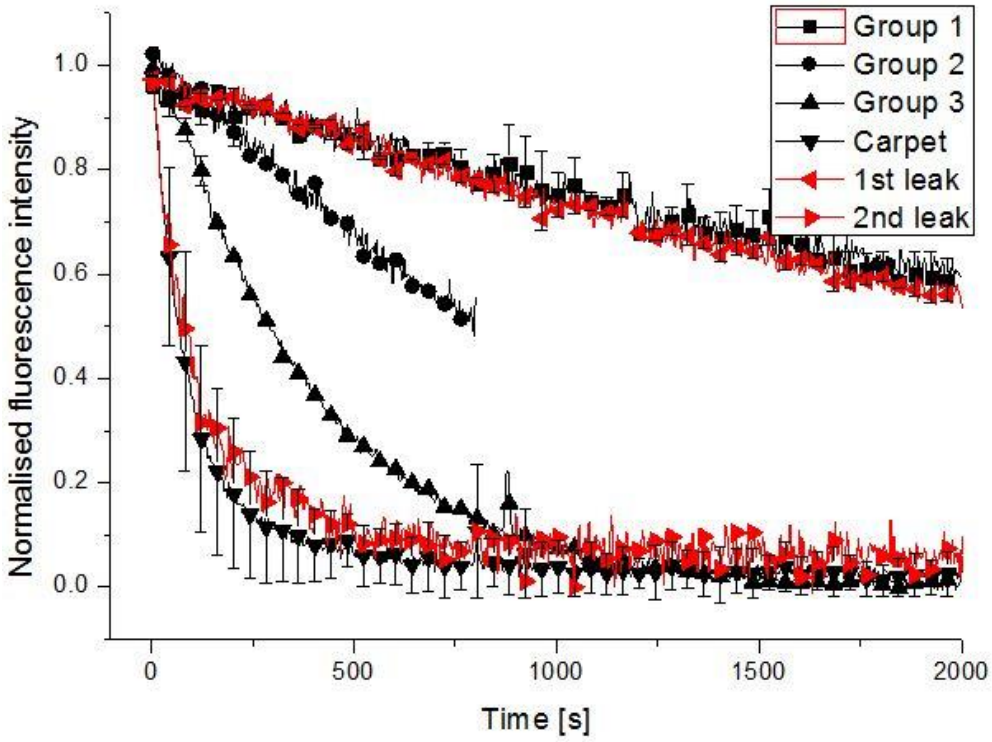

Figure 5.28: Graph showing the group switching of a two component leakage trace, displaying the 3 kDa averaged grouped leakage data for the mGUV system (black) exposed to 5 μM magainin, overlaid with the individual leakage phases from the two component trace (red). The first leakage phase (red left-facing triangles) presents a close match to the efflux rate of group 1 from the averaged leakage data, matching kinetics for ~2200 s, where upon the leakage trace switches between leakage modes. The GUV then follows the kinetics of the carpet mechanism (red right-facing triangle), until the 3 kDa dextran entrapped within the vesicle is completely depleted.

To compare the pore inducing effects of the two magainin concentrations within mGUV membranes, the grouped dye-leakage traces for both the 1 and 5 μM data sets were overlaid, and presented in figure 5.29. The 1 and 5 μM data sets for the dye-efflux kinetics induced by the exposure of mGUVs to the relevant concentrations of the peptide, again display close kinetic matching of the averaged leakage groups, indicating that the pore-formation process occurring within the mGUV membranes is independent of the peptide concentration. The presence of a unique group of faster leakage kinetics at the higher peptide concentration (group 3) suggests that the increase in the rate of peptide binding can induce faster kinetics, seemingly at odds with the previous statement, unless the pore-formation process is the same, but only the number of pores changes. All three groups from the 5 μM data set follow the kinetics of group 2 for the first 150 s of the leakage process, before diverging to create three separate groups; a slower kinetic group which matches with the kinetics of group 1 from the 1 μM data, and faster group 3 which is unique to the higher concentration data set.

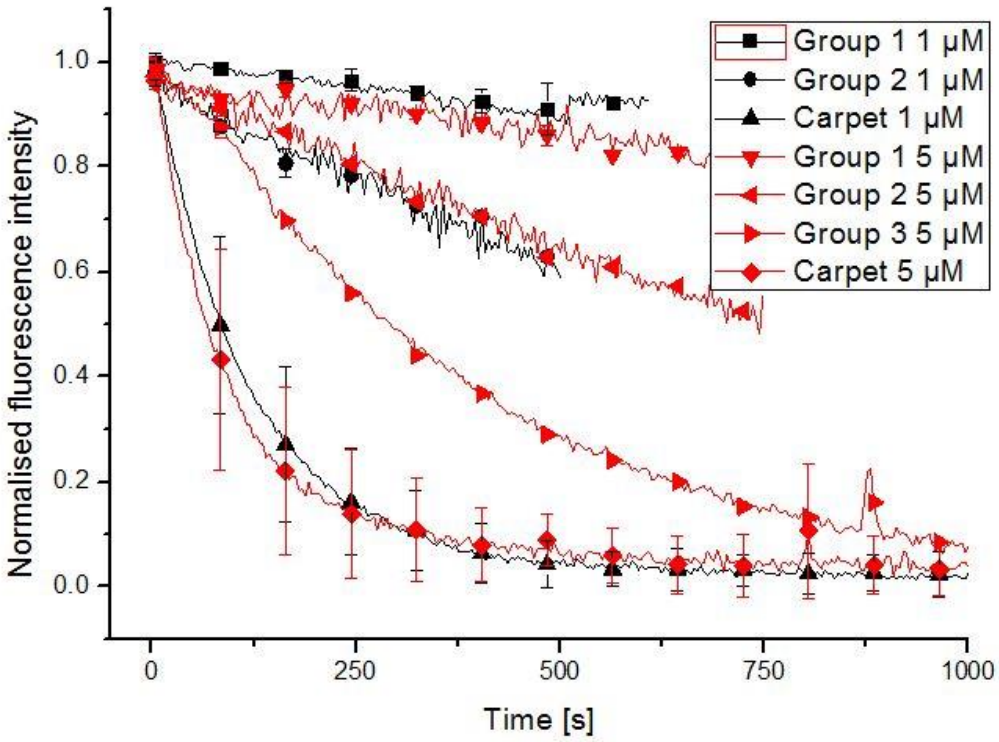

Figure 5.29: Graph showing the overlaid 3 kDa dextran data for the averaged grouped dye-efflux kinetics produced by the exposure of mGUVs to the AMP magainin, at concentrations of 1 µM (black) and 5 µM (red), with the error bars representing the standard deviation for the individual leakage traces contained within each group. The traces show a good match for the averaged grouped leakage kinetics across the two peptide concentrations, with both groups 1 and 2 of the 1 µM magainin data set mapping onto their corresponding groups from the 5 µM data. The carpet mechanism groups also show a close match for the kinetics of the two peptide concentrations, but the higher 5 µM concentration contains a unique leakage trace (group 3), that is not present within the lower magainin concentration data. The 5 µM data contains an interesting phenomenon, with all three groups appearing to follow group 2 kinetics for ~150 s, before branching out, to create both slower (group 1) and faster (group 2) kinetic groups.

The primary difference between the 1 and 5 µM magainin data sets is the initiation time of the leaks, with the lower concentration producing leaks after an average of 3036.4 s, and the higher concentration leaking after an average of 3538.0 s. The other PIEs at the higher concentration of magainin are all produced faster than at the lower concentration, in line with expectations. This phenomenon is not unique to the interaction of magainin with mGUV membrane systems, and was also noted within the interactions of magainin with DOPC:DOPG:DPPG vesicles, and for the interactions of melittin with DOPC:DPPC:DOPG membranes. The actions of the selective magainin peptide, with the non-selective melittin peptide, within mGUV membranes can be compared to provide information on the mechanism of selectivity of the two AMPs. The overlaid data of their 3 kDa leakage kinetics is presented in figure 5.30, for the m GUV system exposed to 5 µM of each peptide.

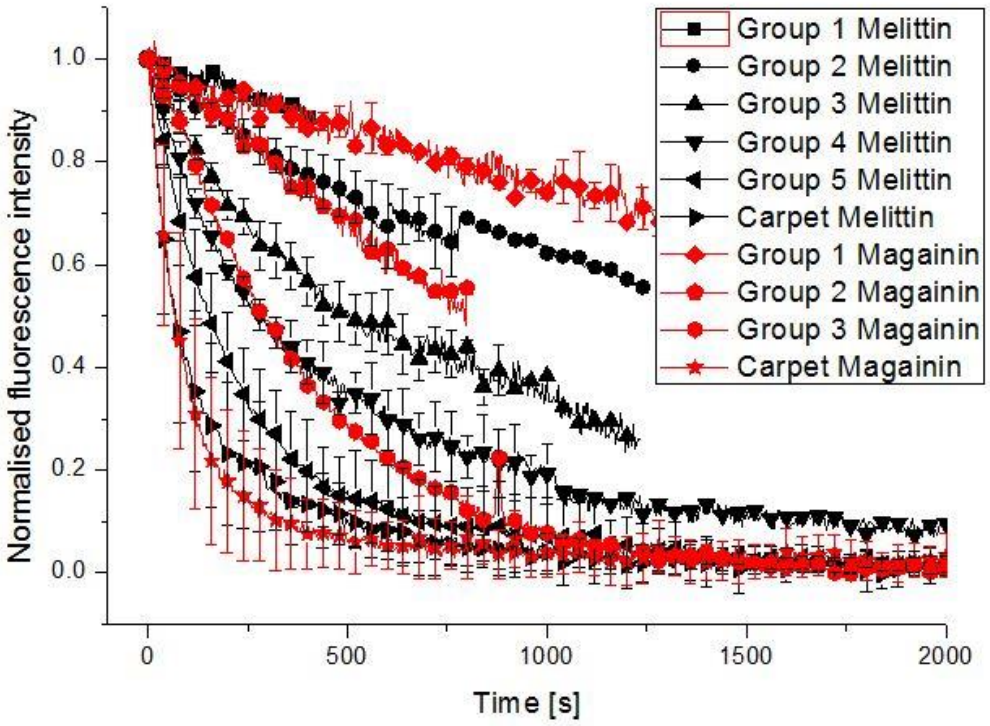

Figure 5.30: Comparison of the 3 kDa leakage data for the mGUV membrane, for the AMPs melittin (black) and Magainin (red), at a peptide concentration of 5 µM. The first groups for both peptides show a close match between their leakage kinetics, but the remainder of the leakage groups do not display kinetic matching.

In contrast to the magainin and melittin overlays within the anionic DOPC:DPPC:DPPG membrane system, the two AMPs do not display similar leakage kinetics, with both fewer groups within the mGUV data and dissimilar kinetics between the averaged leakage groups. The anionic membrane produced both the same number of averaged leakage groups for the two peptides (6), it also displayed matching kinetics for five of the six groups, suggesting that the pore-formation process of both magainin and melittin was similar within these bacterial facsimile membranes. The zwitterionic mGUV membrane system not only presented dissimilar average groupings for each peptide, with the magainin data containing three pore-mediated leakage groupings, and melittin five, it also displayed low levels of matching between the kinetic groups, with only the first of melittins five groups presenting a close match to the first group of magainin. It is interesting to note, that while in the DOPC:DPPC:DPPG membrane system it was the slowest kinetic groups that did not match, within the mGUV membrane system only the slowest group matched kinetics between the two peptides. Other points of contrast between the action of magainin and melittin within the mGUV system include the difference in the average timings of the pore-mediated leakage events, with the higher 5 µM concentration of melittin producing faster initiation of the pore formation process than the lower 1 µM concentration, returning times of 1614.8 and 695.1 s respectively. Together with the differences in leakage kinetics, this indicates that the pore formation processes of the selective magainin and non-selective melittin peptides, differ within the mammalian facsimile membrane system. In addition, both the peptides showed the expected difference in activity between the membrane systems, with melittin proving to be 100 % active within the mGUV system at both peptide concentrations test. In contrast magainin proved to be significantly less active, returning activity levels of 31.1 % at 1 µM and 52.2 % at 5 µM, within the mGUV system. The pore-mediated events within mGUVs exposed to melittin also occurred considerably faster than within

mGUVs exposed to magainin, taking place almost twofold faster for the 1 μM melittin vesicles, and showing over fivefold quicker initiation of leakage at the higher 5 μM concentration.

5.8. DOPC:DOPE:DOPG:DPPG membrane system

The DOPC:DOPE:DOPG:DPPG membrane system contains a mix of anionic and zwitterionic topographic lipids, with DOPC and DOPE presenting zwitterionic cylindrical and conical geometry respectively, and DOPG and DPPG presenting anionic cylindrical and inverse-conical geometry respectively. Exposure of DOPC:DOPE:DOPG:DPPG vesicles to 1 μM melittin produces the averaged leakage kinetic groups presented in figure 89. The membrane system demonstrates the quantised leakage behaviour established within the other lipid-AMP systems. The averaged leakage groups were compiled from the following number of individual traces; group 1 is the average of 3 traces; group 2 is the average of six traces; group 3A is the average of four traces; group 3B is the average of seven traces; group 4 is the average of twelve traces and the carpet mechanism group is compiled from six traces. Two of the leakage groups identified within the DOPC:DOPE:DOPG:DPPG data set (groups 3A and 3B) present identical leakage kinetics for a short time after the initiation of pore-mediated leakage, then diverging to form unique leakage groups after ~400 s. The change in leakage kinetics indicates that the continued binding of melittin to the vesicles during the pore-formation process, and/or the translocation of lipid and peptide to the inner membrane leaflet, induce changes within the lipid-AMP dynamics that favour changes in the pore-formation process within the vesicles of group 3A that reduce the rate of dye-efflux. Large number of traces followed the pattern, suggesting that the changes to the lipid-AMP system producing the change in leakage kinetics, are robust and reproducible. The kinetics of group 3A appear to run parallel to the group 1 kinetics at longer timescales; i.e. >1500 s.

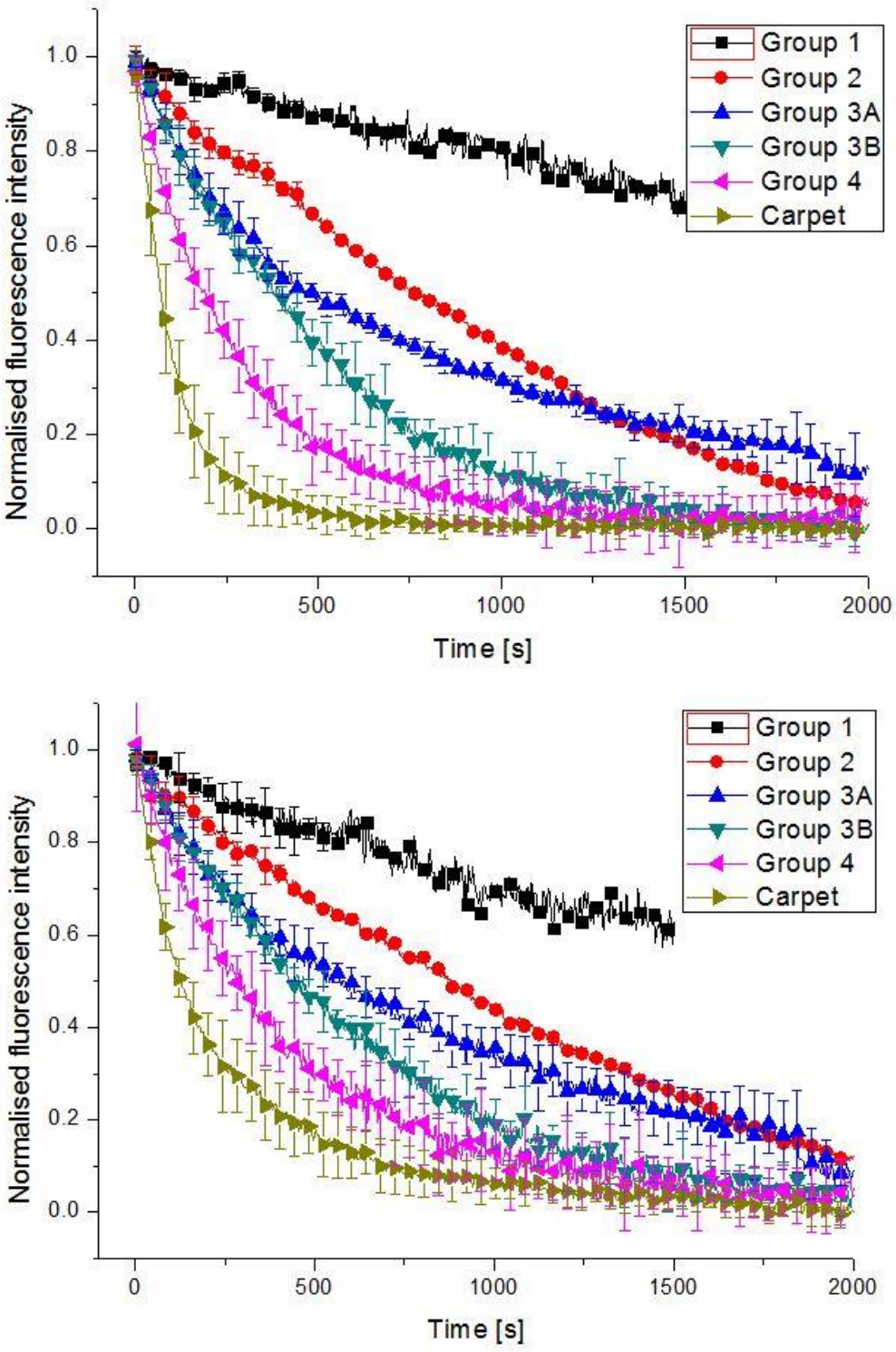

Figure 5.31: Averaged leakage groups for the 3 (top) and 10 (bottom) kDa dextran-AlexaFluor markers, entrapped within DOPC:DOPE:DOPG:DPPG vesicles exposed to 1 μM melittin, with the error bars representing the standard deviation of the individual leakage traces comprising each group. Five distinct pore-mediated leakage groups were detected, along with a sixth group leaking via the carpet mechanism, identified as in the diagram key. Two of the leakage groups (3A and 3B) present similar kinetics within both data sets for ~400 s, before separating to form unique groups. The 3 kDa leakage traces display less variation between intragroup traces, as demonstrated by their smaller error bars.

The membrane system also demonstrates the multi-component trace group switch displayed by almost every lipid-AMP system examined, with the 3 kDa dextran dye-efflux data for a three-component leakage trace presented in figure 5.32, overlaid with the averaged leakage groups.

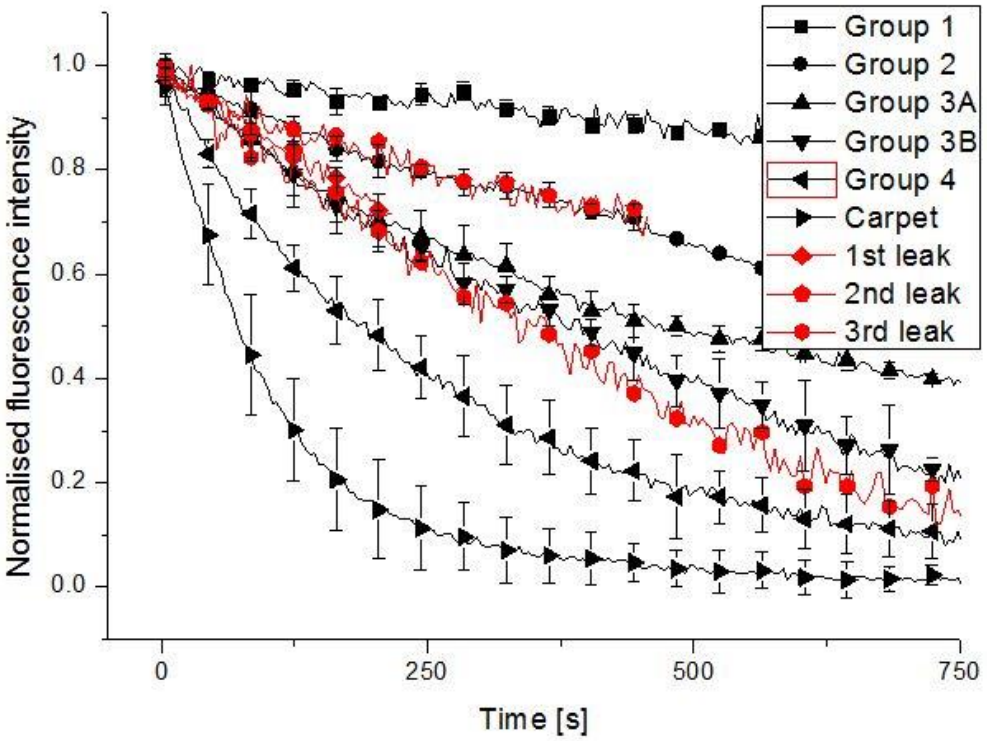

Figure 5.32: Group switching graph of a three component leakage trace, with the individual leakage phases of the multi-component leak shown in red, and the averaged leakage groups for the DOPC:DOPE:DOPG:DPPG membrane system shown in black. The first leakage phase of the multi-component traces (red diamonds) presents similar kinetics to group 3A/B for ~ 200 s, before switching groups to match kinetics with groups 2 for ~450 s (red pentagons). The final leakage phase of the multi-component trace (red hexagons) switches back to group 3B kinetics until the vesicle contents are depleted.

Exposure of the DOPC:DOPE:DOPG:DPPG membrane system to 1 µM of the AMP magainin, produces the averaged leakage groups presented in figure 5.33. The averaged leakage groups were compiled by averaging the following number of individual leakage traces; group 1 is the average of three traces; group 2 is the average of two traces; group 3 is the average of three traces and the carpet mechanism group is the average of four traces. Groups 1 and 2 of the 3 kDa data set are merged within the 10 kDa data, which suggests a difference within the pore-formation process within the group 2 membranes, which favours the release of the smaller entrapped dextran, while producing no effect on the leakage of the larger dextran.

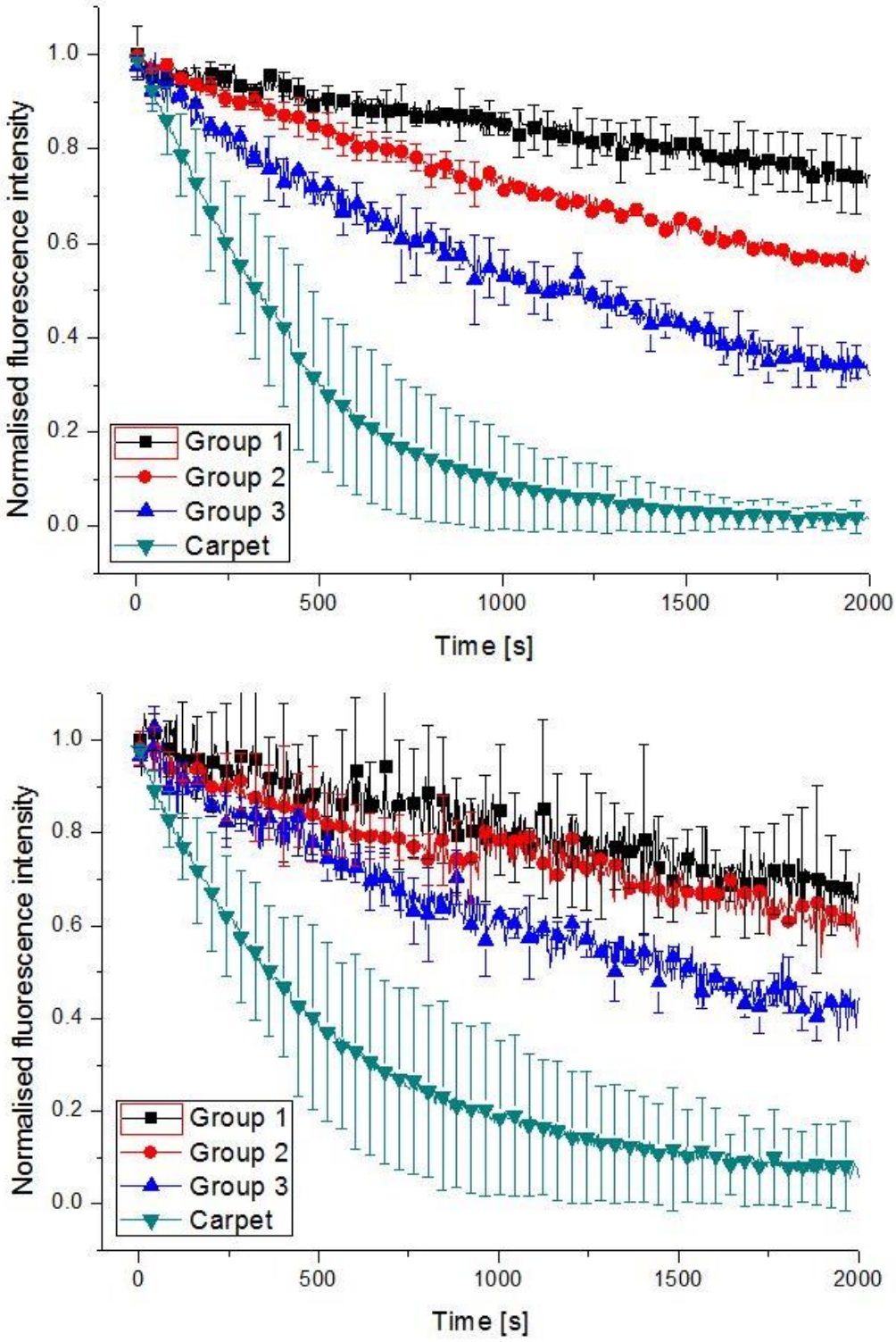

Figure 5.33: Grouped dye-efflux kinetics for the 3 (top) and 10 (bottom) kDa dextran markers, enclosed within DOPC:DOPE:DOPG:DPPG vesicles after exposure to 1 μM magainin, with the error bars representing the standard deviation of the individual leakage traces within each group. Three pore-medaited leakage groups are present within the 3 kDa data set, with a fourth group demonstrating leakage via the carpet mechanism, identified as in the diagram key. Two of these groups are merged within the 10 kDa data, with groups 1 and 2 displaying similar leakage kinetics within the data for the larger dextran.

The data set for the DOPC:DOPE:DOPG:DPPG membrane system after exposure to 1 µM magainin, also contains multi-component leakage traces, and figure 92 presents a two component traces, overlaid with the averaged leakage groups.

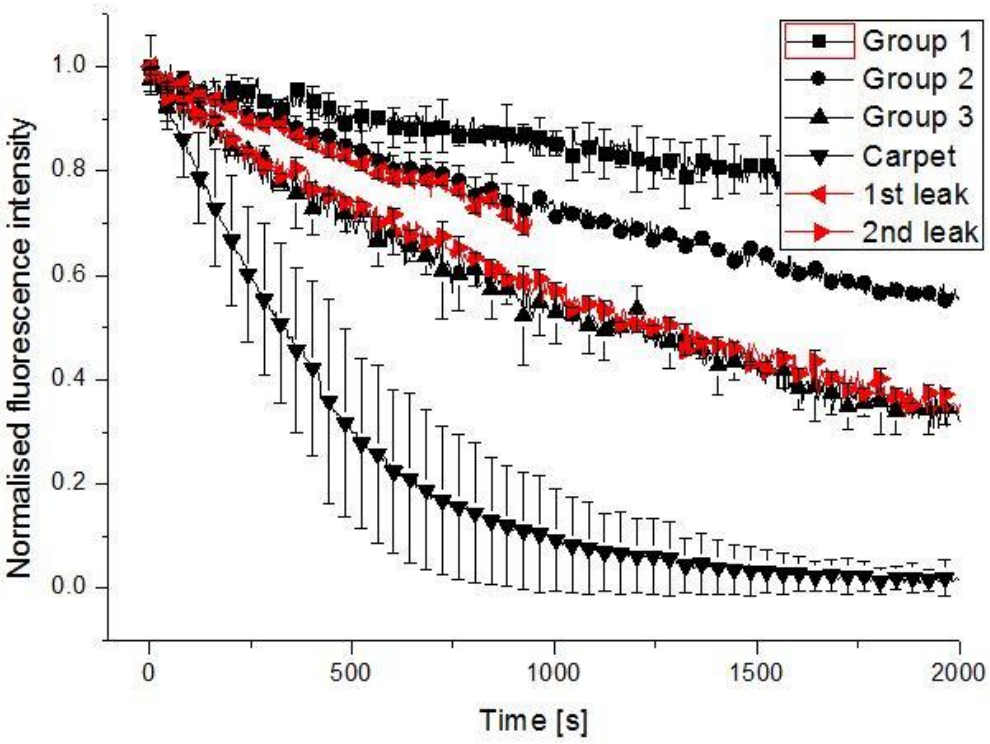

Figure 5.34: Graph presenting the overlay of a two component 3kDa leakage trace, produced by the exposure of a DOPC:DOPE:DOPG:DPPG vesicle to 1 µM magainin, with the averaged leakage kinetic groups for the same membrane. The first leakage phase of the two component trace (red left-facing triangles) initially follows the efflux kinetics of group 2, for ~900 s, before the second leakage phase (red right-facing triangles) switches groups, to match leakage kinetics with group 3 until the vesicles contents are depleted.

To compare the pore-formation process and its effect on dye leakage kinetics, for the AMPs magainin and melittin within the DOPC:DOPE:DOPG:DPPG membrane system, the grouped 3 kDa dextran leakage kinetics for the peptides were overlaid, with the result presented in figure 5.35. In contrast to the data from the anionic membrane system DOPC:DPPC:DPPG, the data for the anionic DOPC:DOPE:DOPG:DPPG membrane system displays a poor match between both number of quantised leakage groups and leakage kinetics between the two peptides. This suggests that the pore-formation process is significantly different within this membrane system for the two peptides, more in line with the results for the mGUV membrane system, where the selective AMP magainin demonstrated a poor kinetics match with the non-selective AMP melittin.

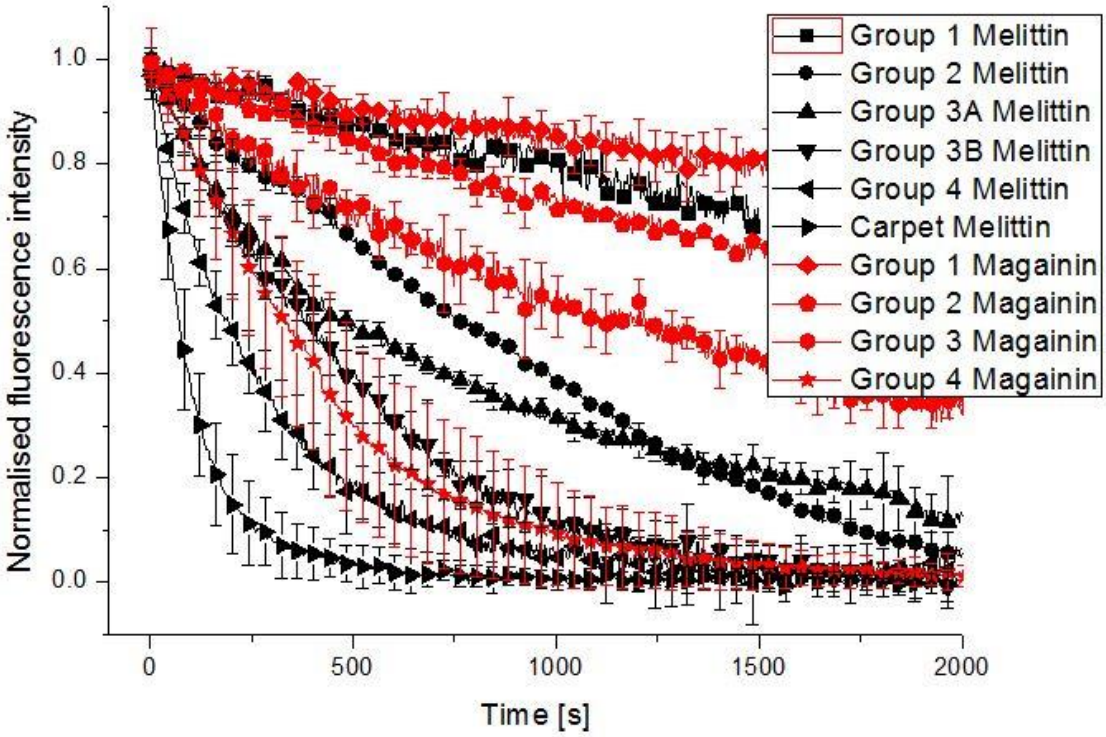

Figure 5.35: Comparison of the 3 kDa leakage data for the DOPC:DOPE:DPPG:DOPG membrane system, for the AMPs melittin (black) and Magainin (red), at a peptide concentration of 1 µM. The kinetics for the dye-efflux induced by the AMP magainin generally occurring at slower kinetics than those generated by the AMP melittin. The averaged kinetic groupings show a poor level of matching between the peptides, with only group 4 in the magainin data set showing a slight match to group 3B within the melittin data.

5.9. Summary

The leakage traces from the anionic bGUV and zwitterionic mGUV membrane systems follow the pattern established by the zwitterionic membranes, by arranging into distinct kinetic groups, again suggesting that leakage from vesicles can only occur via a limited set of allowed leakage conditions, likely to be related to the specific lipid-peptide interactions occurring within that particular membrane. The multiphase leakage traces from the bGUV data set again fit into the previously established groupings, indicating that further binding of peptide to the membrane can move the lipid-LCAMP system from one allowed leakage condition to another. The simultaneous opening of differently sized pores within a membrane, is again demonstrated by the merging of separate but adjacent traces from the 3 kDa data set, in the 10 kDa data set.

Overlays of the data for the two LCAMPs magainin and melittin display good matching between the grouped leakage kinetics, suggesting that the leakage process induced by both peptides is occurring through pores with similar sizes, numbers and opening times. The PIE-profiles and initiation times for the two peptides show significant variation however; e.g. in the DOPC:DPPC:DPPG system, magainin displays an average initiation time for pore-mediated leakage of 3255.4 s, while melittin displays an average initiation time of 2541.0 s. The quicker initiation of pore formation indicates that melittin can form pores via fewer membrane-bound monomers than magainin; i.e. is more effective at generating pores within the DOPC:DPPC:DPPG membrane system. Once pore formation has been initiated

however, the pores formed allow dye efflux according to almost identical kinetics. When compared to the anionic DOPC:DPPC:DPPG membrane, an overlay for magainin and melittin leakage data for the mGUV system shows lower levels of matching, between the averaged leakage groups. This suggests that the lipid-LCAMP interactions that establish the conditions that allow leakage in the bGUV membrane, and the conditions that allow leakage in the mGUV membrane, are different.

6. Discussion

Interactions between lipids and AMP helical faces appear to be a versatile director of membrane conformation, able to induce a heterogeneous catalogue of effects, including micellisation, pore-formation and vesicle bursting. The mosaic of peptide-induced behaviours determined by the high-throughput exposure of GUVs to AMPs, both selective for bacterial cells (magainin) and non-selective between mammalian and bacterial cells (melittin), indicates that a complex set of lipid-peptide interactions governs the bactericidal effects of these peptides. The influence of lipid charge and topography on the mechanism of action of AMPs is both ill-defined within the literature, and of crucial importance to the future development of these peptides as novel antimicrobial agents. This discussion contains a new model for LCAMP activity, which considers membrane free energy as the keystone to the mechanism of action of the peptides. The model proposes a novel pore structure, and explains the PIEs of the LCAMPs magainin and melittin within the different membrane systems. The model was constructed using the peptide behaviour presented within this thesis, combined with literature knowledge about lipid-peptide interactions, and possesses both explanatory and predictive power.

6.1. The free energy of lipid-LCAMP interactions

Lipid membrane bilayers can adjust their molecular shape and supramolecular structure in order to minimise their free energy.[123] Given the fact that the forces involved in lipid-peptide interactions are typically stronger than those involved in lipid-lipid interactions,[46] lipid interactions with membrane proteins will take precedence over interactions with other lipids, allowing membrane proteins the dominant role in the modulation of the physiochemical properties and free energy of the surrounding lipids.[30] The free energy change (ΔG^0) associated with the membrane binding of LCAMPs from aqueous solutions is comprised of several components, shown in equation 2.[124]

$$\Delta G^0 = \Delta G^0_{np} + \Delta G^0_{elc} + \Delta G^0_{qE} + \Delta G^0_{con} + \Delta G^0_{imm} + \Delta G^0_{lip}$$

Where ΔG_{np} = non-polar interactions formed by the expulsion of non-polar amino acid residues from water; ΔG_{qE} = electrostatic interactions between basic amino acid residues and anionic lipids; ΔG_{elc} = effects related to the hydrogen bonding of the peptide backbone; ΔG_{con} = energy from protein conformational change; ΔG_{imm} = motional degrees of freedom from immobilisation in membrane and ΔG_{lip} = energy to perturb the lipid bilayer. In a similar manner to how lipid-lipid interactions produce lipids rafts at local minima in the energy landscape, lipid-peptide interactions will search the available

landscape to achieve minimal energy conformations.[103][125] Applied to LCAMPs, this concept leads to membrane inserted peptides sitting within a free energy minimum in the energy landscape of the membrane, determined by its interactions with both the polar lipid headgroups and the membranes hydrophobic core.[124][126] To minimise the free energy of the LCAMP-lipid system, both conformational and organisation changes can take place; the proteins conformation and orientation can change;[127] the lipids can deform can deform via chain splay or headgroup tilt[128][129] and selective lipid clustering can take place.[113] The process of LCAMPs binding to membranes is strongly exothermic, but pore formation requires the input of energy; i.e. it is endothermic.[118][130] This discussion suggests that the required energy for pore formation is contained within the free energy of the lipid-LCAMP interactions. We will look at each term from equation 2, and examine the influence of the physiochemical and structural properties of LCAMPS, on the free energy of the bilayer during the peptides membrane-bound monomer and pore-formation states.

6.1.1. Membrane partitioning $\left(\Delta G_{np}^{0}\right)$

Before the partitioning process can be discussed, the energetics of the LCAMP in aqueous solution must be considered. LCAMPs are typically highly soluble in water, due to the high positive charge density conferred upon the molecule by the presence of lysine and arginine amino acid residues, but the peptides also contain a high proportion of non-polar residues. Non-polar amino acids interaction with water is thermodynamically unflavoured, and prefer to partition into the hydrocarbon core of the membrane bilayer. The energetics of the membrane partitioning process are often studied using the thermodynamics of individual amino acid residues, partitioning into hydrocarbons like n-octanol, which gives a good approximation of the partitioning energies into a lipid membrane core,[70][124] and it is found that the amount of partitioning is dependent on the potential energy of the peptide in the membrane.[128] A rough approximation of the partitioning energy of a LCAMP into a membrane leaflet, can be obtained by consideration of their amino acid sequence. From the partitioning studies mentioned above, we know that certain hydrophobic amino acids commonly encountered in the sequence of LCAMPs favour partitioning into the hydrophobic core of the bilayer, in the order of preference W > F > L > I > M > Y.[88] Consider the LCAMP melittin with the amino acid sequence GIGAVLKVLTTGLPALISWIKRKRQQ; it contains 1 x W, 4 x L, 3 x I, all residues which display a large preference for non-polar environment like the hydrocarbon bilayer core, and thus contribute a large negative energy to the binding process. The energy of partitioning for melittin, from aqueous solution into a membrane leaflet has been calculated as –2 kcal/mol.[70]

6.1.2. Secondary structure formation $\left(\Delta G^{0}_{elc}\right)$

Protein secondary structures, e.g. α-helices, involve the formation of hydrogen-bonds, a large negative energy contributor to the binding energetics of LCAMPs to lipid membranes. For LCAMPs we must only consider the energetics of α-helix formation, with each amino acid residue reported to contribute -0.4 to -0.6 kcal/mol of residue involved in secondary structure hydrogen bonding.[70][131] Again using melittin as an example, there are approximately 18 residues involved in helix formation, and the formation of the α-helix contributes -9 kcal/mol.[70] Hydrogen bonding of the peptide backbone during secondary structure formation, also reduces the energy cost of inserting the polar groups within the membrane core.[70] The random coil to helix transition provides the majority (~65 %) of the negative enthalpy that drives the spontaneous binding of LCAMPs to lipid membranes.[118] The AMP helix is believed to remain in largely helical form in both its monomer and pore states, and thus this term is unlikely to exert a significant influence of the transition between the two states.

6.1.3. Electrostatic interactions $\left(\Delta G^{0}_{qE}\right)$

Electrostatic interactions will make a significant negative contribution to the free energy of the lipid-peptide system in anionic membranes,[132][133] with the contribution for one lysine binding to an anionic lipid estimated at 1 kcal/mol. Magainin contains four positively charged amino acids at physiological pH, and the contribution to the free energy can be approximated at -4 kcal/mol, while melittin contains six cationic residues at identical pH, and electrostatics will contribute -6 kcal/mol towards the total free energy of the lipid-LCAMP system. It should be noted here, that the electrostatic force is much greater than the other forces encountered in lipid-LCAMP interactions, on a per lipid basis.[134] The interaction of the LCAMPs cationic amino acid residues can therefore be expected to dominate the accumulation of lipids around the LCAMP in anionic membranes,[113] but to change little on transition from membrane-bound monomer to pore peptide states.

6.1.4. Protein conformation $\left(\Delta G^{0}_{con}\right)$

Protein conformation is coupled to the mechanical and physiochemical properties of the bilayer, through interactions between the membrane-bound LCAMP and the lipids hydrocarbon core and polar headgroups. In relation to LCAMPs, the protein is primarily helical in both monomer and pore-associated states, so this term will have little influence on the pore-formation energetics.

6.1.5. Peptide immobilisation $\left(\Delta G^{0}_{imm}\right)$

While the partitioning energy is negative, and thus the process is spontaneous for LCAMPs, the binding of the peptide to membranes involves an increase in entropy. Enthalpy drives the spontaneous binding process, whereas entropy counteracts binding.[118]This is due to the loss of translational and rotational freedoms of the peptide, from moving from random coil conformation to membrane-bound helical form. Moving from aqueous solution to membrane-bound monomer involves a change from 3D to 2D diffusion, incurring an entropic penalty. The pore-associated AMP helix may be a permanent fixture in the pore structure, again suffering an unfavourable entropic contribution to the free energy of the pore state.

6.1.6. Lipid perturbation $\left(\Delta G^{0}_{lip}\right)$

One of the largest contributors to the free energy of the lipid system is elastic deformation induced by lipid-lipid and lipid-peptide interactions. Non-bilayer lipids like PE within membranes induce curvature in the surrounding lipids, producing packing frustration and increasing the free energy of the bilayer.[30] The concept can also be applied to the interaction of lipids with membrane proteins, where it is possible to induce both membrane bending and stretching through hydrophobic mismatch, between helix length and hydrophobic core thickness.[31] The equations governing the energy cost of the bilayer deformations are given below in equations 3 and 4.[31]

$$Energy\ cost\ of\ stretching = \frac{1}{2}\ x\ K_a\ x\ \left(\frac{2u}{d_0}\right)^2$$

$$Energy\ cost\ of\ bending = \frac{1}{2}\ x\ K_c\ x\ (\nabla^2 u - \ c_0)^2$$

Where K_a = bilayer compression moduli; u = change in bilayer thickness; d_0 = original bilayer thickness; K_c = bilayer bending moduli; $\nabla^2 u$ = Laplacian operator of the change in membrane thickness and c_0 = intrinsic monolayer curvature. The energy costs for membrane deformation are dependent on the bilayer compression and bending moduli, which in turn rely on the constituent lipids. It is clear that it is energetically preferable to surround the protein with lipids which minimise the energies of compression and bending. To minimise the energy cost of stretching the bilayer in response to the deformation around an inserted protein, it is necessary to reduce the influence of the terms K_a and d_0, by enriching the annulus around the protein with lipids with low compression moduli and longer chain lengths. The change of acyl chain length will produce the most significant effect, as d_0 has a squared relationship with

the energy cost of stretching. The bending cost is also dependent on the intrinsic curvature of the surrounding lipid, with the best way to minimise this energy is to minimise the $(\nabla^2 u - c_0)^2$ term, by surrounding the protein with lipids that possess intrinsic curvature that efficient packs the lipids into the required curve. Applied to the membrane interactions of the AMPs magainin and melittin, we can see that this concept results in a preference for opposite curvature lipids to accumulate around each peptide, in order to minimise the energy of the lipid-LCAMP system. One significant difference between magainin and melittin, is the opposite curvature induction produced by the membrane-bound AMP helix, with magainin producing positive curvature and melittin inducing negative curvature. To maintain the free energy landscape of the lipid-AMP system at a local minima, melittin will preferentially interact with positive curvature (i.e. inverse-conical geometry) lipids like DPPC, and magainin with negative curvature (i.e. conical geometry) lipids like DOPE. We can therefore expect the curvature of the surrounding lipids to play a major role in the lipid-AMP dynamics surrounding the membrane-bound peptide, influencing both the pore-formation and selectivity mechanism of the two peptides. The degree of lipid perturbation is considerable different moving from the membrane-bound monomer to the pore state peptide, and this will likely exert a considerable influence on the energetics of the pore-formation process.

6.2. Membrane free volume and packing frustration

One pitfall associated with considering lipids as purely geometrical rigid shapes according to the Helfrich packing model, is that strict application leads to poorly packed lipid membranes containing membrane free volume, or interstices, between the constituent lipids.[39][135] In reality these volumes are minimised; the membrane will deform in order to minimise the intrusion of water into the free space, and hence into contact with the hydrophobic membrane core. To fill the free volume, the constituent lipids of the bilayer can perform several conformational adjustments, including tilting of the whole lipid[136] or the headgroup[137] and splaying of the lipid acyl chains.[128][129] Conformational changes of the lipids in response to bilayer stress is termed “packing frustration”, representing a deviation from the idealised packing situation, and increasing the free energy of the bilayer.[128][135]

6.3. LCAMP behaviour during pore-formation

At this point, it is worth revisiting the behaviour of LCAMPs within lipid membranes, which are widely reported in the literature.[87][58] LCAMPs display random coil conformation in aqueous solution, and spontaneously bind to lipid membranes, adopting a pronounced helical character. The helix initially orientates parallel to the membrane plane, and increases the area of the outer membrane leaflet, thinning and weakening the membrane. Once a critical peptide/lipid ration is achieved, peptide

monomers change orientation, from parallel to the membrane plane to parallel to the membrane normal plane. The reorientation of peptide helices is associated with the process of pore formation, as prior to reorientation, no pores can be detected within the system. Positive curvature lipids greatly increase the pore formation activity of LCAMPs. The leakage kinetics are often described as biphasic, with both slow and fast components.[58][77] Any new model must explain these facts, and make successful predictions about future experimental results.

6.4. Energy of the membrane-inserted monomer

Interactions of membrane-inserted AMP monomers with their surrounding lipids are not homogeneous, factors including lipid curvature, charge and fatty acid configurations will affect the energy of the lipid-AMP system. Interactions of peptide helices with lipids generating matching curvature to the peptide-induced curvature will create larger defects within the membrane, increasing the bilayer free energy and speeding the initiation of PIEs, and *vice versa*. For example, interactions between magainin, a positive curvature inducing peptide and DOPE, a negative curvature inducing conical lipid, would result in a reduced packing defect than the interaction of magainin with DPPC, a positive curvature inverse-conical geometry lipid. Close proximity of the shallowly-inserted magainin helix and the large hydrophobic volume of the lipid DOPE (S = 1.41), reduces the membrane disruption surrounding the peptide helix, decreasing the bilayer free energy. Strandberg and colleagues (2013) unequivocally show that the surface-associated helical form of magainin is stabilised by negative curvature lipids. In contrast, interactions between magainin and DPPC lead to an increase in the free energy of the lipid annulus surrounding the peptide helix. The reduced hydrophobic volume of DPPC (S = 0.78) and its large PC headgroup, coupled to the positive curvature inducing magainin helix, creates a mismatch between the volume occupied in the polar headgroup region, and the hydrophobic volume occupied by the lipid-AMP raft. The concept of lipid topography controlling the free energy of lipid-AMP interactions is presented in figure 6.1,

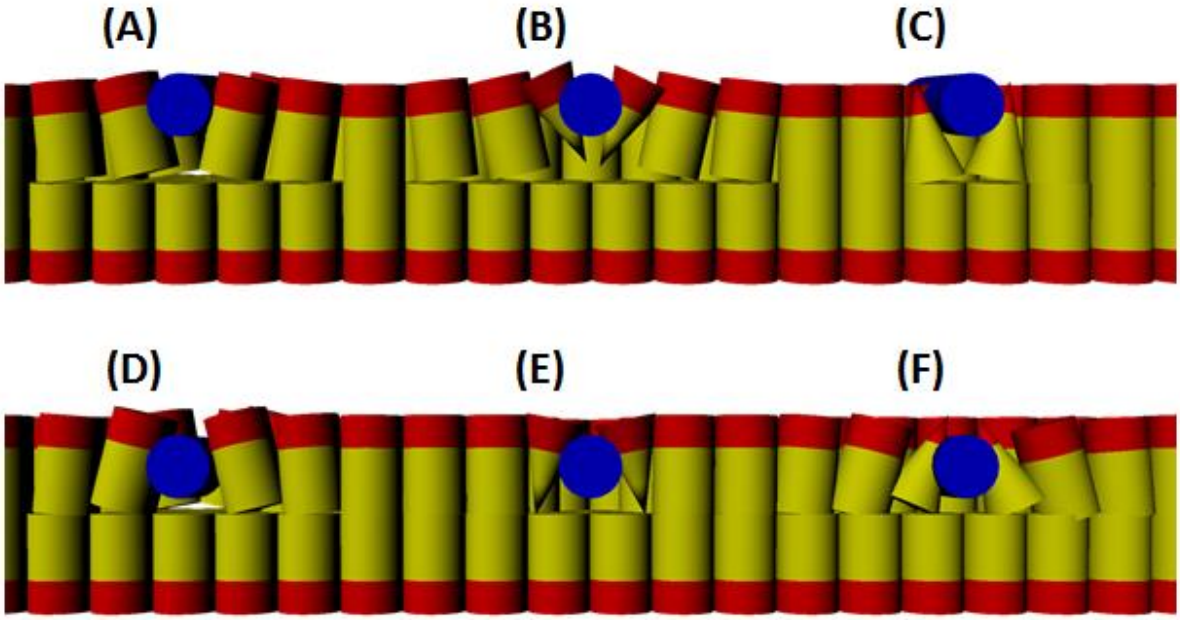

Figure 6.1: Diagram depicting the interaction of deep (melittin) and shallow (magainin) penetrating AMP helices, with membranes of varying topography, with the peptide helices shown as blue cylinders. The polar lipid headgroups are depicted in red, and the non-polar tailgroups in yellow. (A) The interaction of a magainin helix with cylindrical geometry lipids (i.e. DOPC) leads to disruption in the membrane packing of the surrounding lipids, as the peptide occupies a large volume of the polar headgroup area, and induces positive membrane curvature. (B) A magainin helix surrounded by positive curvature lipids (i.e. DPPC) induces a larger packing defect than (A), caused by the mismatch between hydrophobic and hydrophilic volumes occupied by the lipids and peptide, leading to crowding of the interfacial region. (C) Magainin surrounded by negative curvature lipids (i.e. DOPE) produces a smaller packing defect than (A), the smaller headgroup of the negatively curved lipid easing the crowding at the interfacial region. (D) A membrane-bound melittin helix surrounded by cylindrical lipids produces a packing defect and negative curvature, caused by the deep penetration of the helix into the bilayer, which expands the hydrophobic volume of the membrane. (E) Lipids with positive topography will pack closely around the deeply penetrated melittin helix, reducing the leaflet area increase, and minimising the energy of the packing defect. (F) Melittin surrounded by negative curvature lipids will result in larger packing defects, caused by overcrowding in the hydrophobic region of the membrane leaflet. It is clear that the two peptides will display their maximal packing defect energies in membranes with opposite topographies; magainin in membranes featuring positive topography (B), and melittin in membranes containing negative topography lipids (F).

Figure 6.1 depicts the influence of lipid topography on the scale of the lipid-AMP packing defect, by contrasting a shallow penetrating peptide (magainin) surrounded by lipids featuring cylindrical, conical and inverse-conical geometries, with a deep penetrating peptide (melittin) interacting with the same membrane. The tendency of lipid-AMP systems to minimise their free energy, can be illustrated using the membrane systems DOPC; DOPC:DPPC and DOPC:DOPE, interacting with the AMP melittin. Each peptide helix will form a dynamic lipid-AMP raft, with raft composition governed by the interactions between each lipid and the peptide helix, as depicted in figure 6.2.

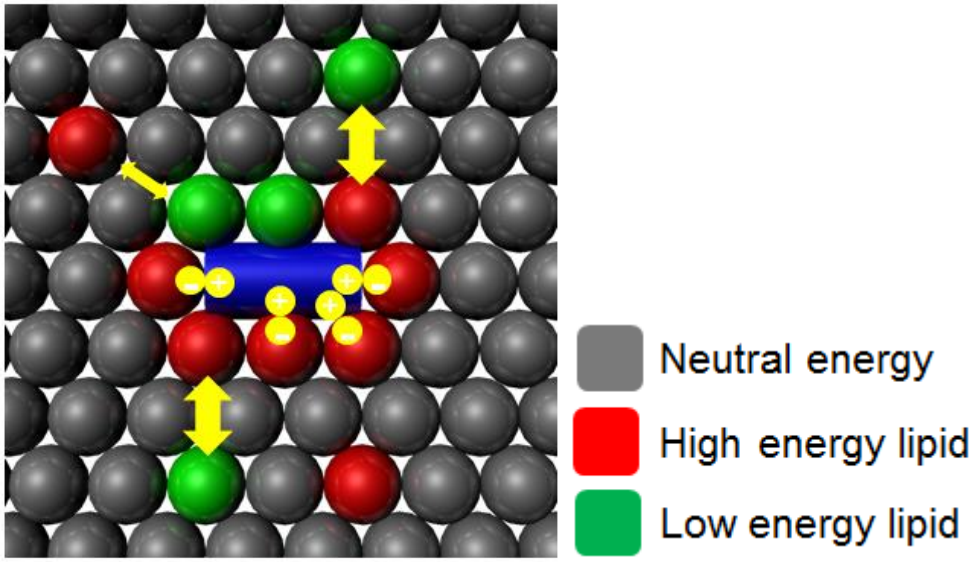

Figure 6.2: Top-down view of a membrane-bound AMP helical monomer, represented by the blue cylinder, embedded within a lipid membrane. The lipid headgroups are depicted as spheres, with the bulk components of the membrane shown in grey. Green spheres represent lipids which form favourable interaction with the peptide helix, reducing the free energy of the lipid-AMP system, while red spheres are lipids which form high energy interactions with the helix, increasing the membrane strain in the area surrounding the AMP helix. The yellow arrows represent the lipid exchange taking place in the dynamic lipid-AMP raft, with the replacement of a high energy lipid with a low energy lipid being favoured, with a corresponding large arrow. Replacement of a low energy lipid with a high energy lipid is disfavoured, resulting in a small arrow. The yellow circles represent positively charged residues of the AMP, and their counterpart high energy anionic lipids, forming strong electrostatics but unfavourable interactions with the peptide helix, resulting in a high membrane free energy.

Lipids which lower the raft free energy will be retained for longer within the raft than those lipids which produce higher energies, which has interesting implications for the mechanism of action of AMPs within heterogeneous membrane systems. Consider again the dynamic lipid-melittin raft interacting within a DOPC membrane, with all lipids presenting identical topographies and fatty acid saturation, the rafts will all possess almost identical free energies. Next consider the raft behaviour within DOPC:DPPC and DOPC:DOPE membranes; the inverse conical DPPC will suppress the negative curvature induction of the deeply-inserted melittin helix, while the conical DOPE will exaggerate the curvature induction of the AMP. Interaction with DPPC will reduce the free energy of the defect, and therefore it is thermodynamically favoured for DPPC to remain within the lipid-AMP raft for longer than DOPE. Within the DOPC:DPPC system the rafts are enriched with DPPC, while in the DOPC:DOPE system the raft will exclude DOPE and contain mainly DOPC. Electrostatics will play a disproportionately large role in determining the composition of the lipid rafts around each peptide, due to the strong nature of electrostatic interactions compared to the other forces involved in lipid-AMP interactions.[113][134] The large electrostatic interactions will dominate other considerations; e.g. curvature, topography and fatty acid saturation effects. This results in the forced retention of lipids with unfavourable interactions with the peptide helix within the dynamic lipid-AMP raft, increasing the available free energy of the bilayer.

In conclusion, the increases of both membrane free energy and leaflet area that occur upon LCAMP binding to lipid membranes, can by mediated via interactions with varying topography lipids.

6.5. Energy of the lipid-LCAMP raft

The low number of lipids directly interacting with the helix within a lipid-AMP raft, results in large local fluctuations in the system free energy, caused by the exchange of lipids between the bulk system and the raft. Consider a membrane bound melittin helix with a charge of +6 at physiological pH, with a helical content of around 70 – 80%.[58] Due to the small size of the peptide helix, only an estimated 7- 9 lipids can directly interact with the peptide, with each lipid contributing a specific free energy to the lipid-AMP raft free energy. Replacement of one lipid with a different lipid from the surrounding bulk system will result in a specific change in the energy of the lipid-melittin raft, dependant on the type of lipid introduced and its location along the peptide helix. Within the tightly controlled binary, tertiary and quaternary lipid systems featured in this work, the lipid-raft energies will be quantised, across the energy range covering the complete set of possible lipid-peptide interactions. The energy content of the set will range from the minima, where the peptide is completely surrounded with lipids featuring the lowest free energy interactions, to the maxima, where the peptide interacts only with lipids producing the highest possible increase in the membrane free energy. Due to the tendency of lipid-AMP rafts to minimise their free energy, the higher energy rafts will be present at low numbers within the total population, while the lower energy rafts will occur more frequently. Within anionic membranes electrostatic interactions, between the cationic melittin and the anionic lipids, result in practically permanent residents of the lipid-AMP raft.[113] In these membranes the set of possible lipid-AMP interactions is greatly reduced, and the energy states for the lipid-AMP raft will be considerably more quantised in nature. The concept is presented in figure 6.3, which features the energy minima and maxima, as well as intermediate lipid-AMP raft free energy levels.

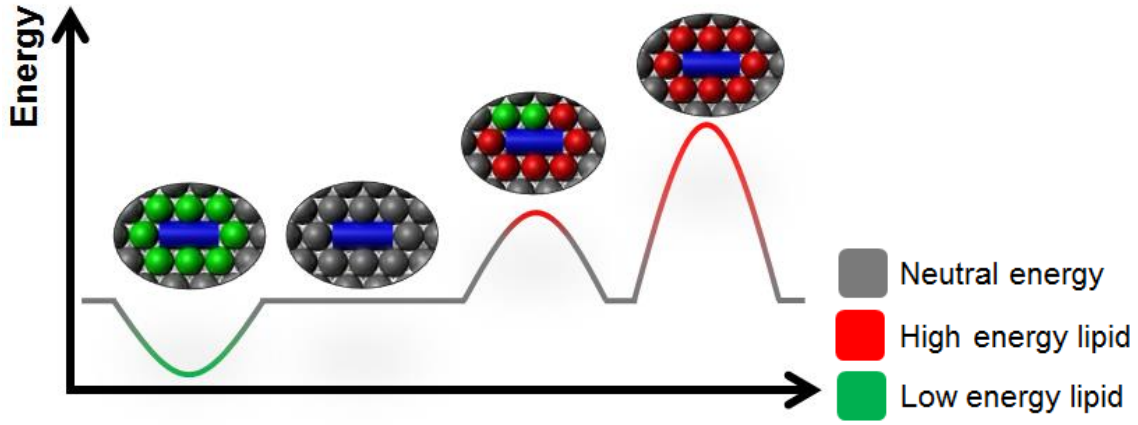

Figure 6.3: Graph depicting the variation in the membrane free energy of a lipid-AMP raft within a heterogeneous membrane system. Neutral lipids which neither raise nor decrease the energy of the raft, are represented in grey. Interactions with lipids which minimise the free energy of the lipid-AMP system (green) will be favoured, resulting in a lower aggregate free energy for the membrane-bound AMP helix and its associated lipids. Replacing neutral and low energy lipids with lipids featuring energetically unfavourable interactions with the helix (red), results in stepwise increases in the free energy of the lipid-AMP system.

6.6. Membrane penetration of LCAMP monomers

As an interacting coupled system, the lipids-AMP rafts will locate to a local energy minima within the free energy landscape of the system, where the peptides penetration depth may be affected by the topography of the surrounding lipids. DOPC:DPPC (80:20 mol%) membranes possess less hydrophobic volume than pure DOPC membranes, due to the reduced number of carbons and decrease unsaturation of the palymitoyl 16:0 fatty acids of DPPC (average packing parameter of 1.012). Melittin can initially be expected to penetrate deeper into the DOPC:DPPC membrane, as the energy penalty for deeper penetration will be reduced compared to the DOPC:DOPE membrane system, which possesses an averaged packing parameter of 1.144. The greater hydrophobic volume of the DOPC:DOPE hydrophobic membrane core will exert an energetic penalty on deeply-inserting peptides, pushing the lipid-AMP system away from the energy minima as the increased hydrophobic volume forces the surrounding lipids apart, and allows increased water penetration into the hydrophobic core. The local minima for the system will involve decreasing the peptide-insertion depth, suffering a penalty to the peptides partition energy (ΔG_{np}^{0}), but compensating through changes the energy of lipid perturbation (ΔG_{lip}^{0}).

The topography of the constituent lipids and the AMP therefore can be seen as components within a single system, that cooperatively find a local energy minima for the entire system, by altering properties such as peptide-insertion depth, lipid acyl chain splay and headgroup tilt. The penetration depth of melittin varies within membranes of different lipid composition, and by taking geometrical consideration into account it is possible to reconcile these differences within the same model, based on varying hydrophobic volumes and its effect on the location of the free energy minima of the lipid-AMP

system. Raghuraman and Chattopadhyay use DOPC membranes containing varying amounts of cholesterol,[119] creating a membrane with significantly more crowding within the hydrophobic region than the membranes utilised by Glukhov and colleagues, which feature DPPC and DPPG lipid membranes[139]. Within DOPC membranes the negative curvature inducing cholesterol results in increased lateral pressure within the hydrophobic core of the bilayer, and melittin trying to penetrate the outer leaflet faces a higher energetic penalty than within the DPPC/DPPG membranes, where the positively curved lipids leave considerable space within the bilayer core for AMPs to insert. The local free energy minima of the DOPC membrane will therefore see the peptide occupying a shallower position within the bilayer, compared to the deeper position allowed within the DPPC/DPPG system. Further supporting evidence is found within Raghuraman and Chattopadhyay,[115] which uses red edge excitation shift to probe the penetration depth of LCAMPs in response to lipid fatty acid unsaturation, where increased unsaturation disfavours peptide penetration due to the increased hydrophobic volume of the component lipids.

Lysine is a common residue within AMPs, featuring a positive primary amine (at physiological pH) located at the end of a four carbon chain, which prefers to locate at a depth within phospholipid membranes where it can interact with the anionic phosphate groups. The phenomenon of lysine snorkelling is the capability of the cationic amino acid lysine to utilise the four carbon chain to "reach up" to its preferred region of the bilayer, granting considerable flexibility to the membrane penetration of the inserted AMP helix, in order to achieve a local energy minima within the energy landscape of the lipid-AMP system. Planque and Killian present convincing evidence, in an elegant study of the interaction of transmembrane helices flanked with cationic and aromatic residues with heterogeneous lipid systems, for the snorkelling ability of lysine containing peptides to minimise the perturbation of surrounding lipids.[139] Again topographical influences exert a powerful influence on the snorkelling capability of membrane-bound peptides; PC systems were more likely to feature snorkelling helices compared to PE systems, with the smaller headgroup and larger hydrophobic volumes of PE exerting a penalty on deeper insertion into the membrane.

6.7. Helical steric asymmetry and membrane tension

Both magainin and melittin demonstrate steric asymmetry within their helices, i.e. one face is composed of amino acids with bulky sterically active side chains, while the opposite face contains smaller less sterically active residues. Magainin in particular displays pronounced differences in the steric activity of its faces; one face containing three phenylalanine amino acids, and the opposite face consisting of less bulky amino acids (L/I/V/A residues). The presence of steric imbalance will exert different influences on lipid interactions of the opposing faces of the membrane-bound peptide helix,

and that the aggregation of different lipids to the opposing faces may play a role in pore-formation. The sterically rough face will induce considerable packing frustration along one face of the helix, and also reduce the packing density and hence lateral pressure along one face. The helical steric imbalance present in magainin will force association with varying topography lipids on opposing helical faces, which may play a part in the selectivity mechanism of AMPs (see later). To link steric asymmetry to lipid-AMP raft energetics, it is necessary to consider the 3D structure of the membrane-inserted AMP helix, and in particular the location of the peptides cationic and sterically bulky amino acid residues. Consider a magainin 2 amide helix inserted into the plasma membrane of an *E.coli* bacteria, whose membrane composition is dominated by PE and PG lipids,[53] the steric asymmetry of the magainin helix is clearly visible in figure 6.4.

To examine the effect of the steric imbalance of the membrane-bound magainin helix within the *E.coli* membrane, the sterically bulky face of the helix is presented in figure 6.4, to display the spatial relationship between the cationic residues and the sterically bulky residues. The cationic lysine residues of magainin will interact preferentially with the anionic PG lipids, and form a strong association via their strong electrostatic interaction. Interaction of PG with the lysine residues available on the sterically bulky face of the magainin helix will force unfavourable steric interactions with the phenylalanine resides; PG lipids interacting with K11 will be forced into close proximity to the sterically bulky F12 residue. The large headgroup of the PG lipid will be sterically hindered by the position of F12 at the interface, increasing the energy of the lipid peptide raft. The other lysine available (K4) will also force interacting PG lipids into unfavourable steric interactions with the nearby F5 residues. If we replace the PG lipid with a PE lipid, its much smaller headgroup will suffer from much less steric hindrance from the phenylalanine residue than the bulky PG headgroup.

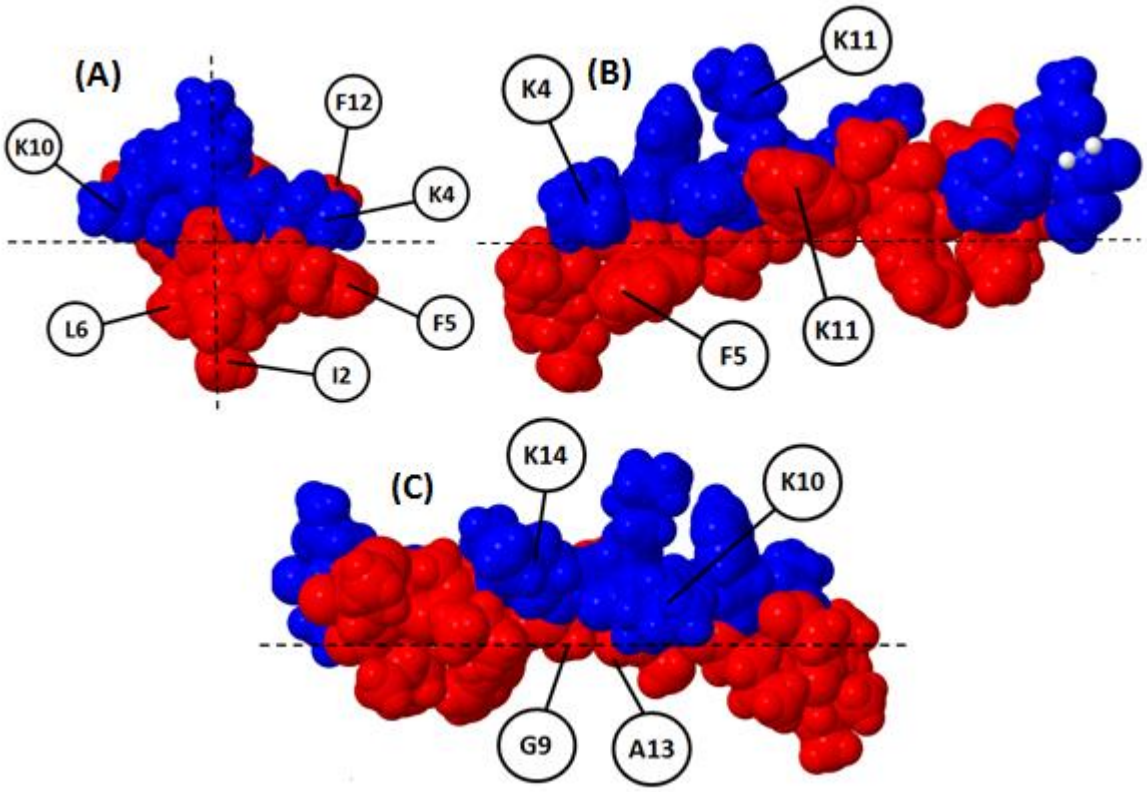

Figure 6.4: Space filling model of a membrane-bound magainin 2 helix, with hydrophilic residues shown in blue and hydrophobic residues in red. The dashed lines approximate the membrane plane (horizontal) and membrane normal plane (vertical), and are intended as a guide for the eye only. (A) Viewed down the helical axis, the helical asymmetry of the membrane-bound magainin helix is clearly visible, caused by the presence of bulky sterically active amino acids like phenylalanine (F5 and F12) and isoleucine (I2), and the residues to the left of the line comprising of less bulky and sterically active residues like leucine (L6). (B) Side view of the inserted helix, with both the cationic residues, K4 and K11, and the nearby sterically bulky amino acid residues, F5 and F12, are indicated. The anionic PG lipid will preferentially associate with the cationic lysine amino acid residues, due to electrostatic interactions, and the high volume PG headgroups will be sterically hindered by the bulky F12 residue, generating unfavourable interactions. (C) Opposing side view of the inserted helix, with cationic residues, K10 and K14, and the nearby low hydrophobic volume amino acid residues, G9 and A13, are indicated. The anionic PG lipids will preferentially associate with the cationic lysine amino acid residues due to electrostatic interactions, and the lack of steric crowding in the interfacial region will allow close energetically stable interactions between the lysine residues and PG lipids.

However the electrostatic interactions between the cationic lysines and the anionic PG lipids will dominate the polar/hydrophobic interactions offered by the PE lipids,[134] and the sterically bulky face will become enriched with PG lipids. The collection of large headgroup lipids along this face increases the free energy of the lipid-AMP raft, through greatly increasing the volume of the hydrophilic interfacial region between the bilayer hydrophobic core, and the surrounding aqueous solution. If the PG lipid possesses unsaturated fatty acids, then in addition to the greater negative curvature of the lipid opposing the positive curvature of the peptide, the kink in the acyl chain caused by the double bond allows the lipid to deform and fill the available space within the hydrophobic region, reducing the lipid-AMP raft energy. PG lipids with unsaturated acyl chains cannot adapt as readily to the increased interfacial volume, caused by the bulky PG headgroups and phenylalanine residues, and will possesses

more positive curvatures which synergise with the curvature induced by magainin, resulting in a higher energy defect. The opposing face of the peptide is comprised of much less bulky amino acid residues than the opposing face, namely G9 and A13, residues with small volume side chains with low steric activity. PG lipids interacting with the lysine residues available from this side of the membrane-bound magainin helix, K10 and K14, face greatly reduced competition for the interfacial region of the membrane leaflet compared to PG lipids interacting with K4 and K11 on the opposing face. The two closest amino acids to the lysine residues on this face are G13 and A9, which possess low volume side chains, which interfere with the lysine-PG electrostatic interactions to a lesser extent than the F residues on the opposing face. The large PG headgroups will "fit" much more closely to the peptide helical face, resulting in a lower energy interaction with less strain induced within the lipid-AMP system. The steric asymmetry exhibited by the membrane-bound magainin helix interacting with the *E.coli* membrane results in one face of the helix featuring higher energy interactions through forced electrostatic association with PG lipids, due to steric crowding at the leaflet interface between the F residues and the large PG headgroups.

6.8. Key residues – Tryptophan and Phenylalanine

The large sterically bulky W and F residues have been identified as key mediators of the activity of LCAMPs.[58][85][86] Both residues preferentially locate at the interfacial region, near to the glycerol backbones of the membrane lipids,[46][57][86][108] with a negative contribution to the free energy of the system of -4 kcal/mol.[140] This is a significant contribution to the thermodynamics of lipid-AMP systems, resulting in a substantial increase in the volume occupied by the peptide within the interfacial region. The 3D arrangement of residues around the magainin helix is also worthy of note, and is presented in figure 6.5. The arrangement fits well to the proposed leaflet fold structure of a toroidal pore, with the F5 and F16 residues located deeper into the membrane, and the F12 residue located at a shallower spot, leading to an improved fit to the fold structure.

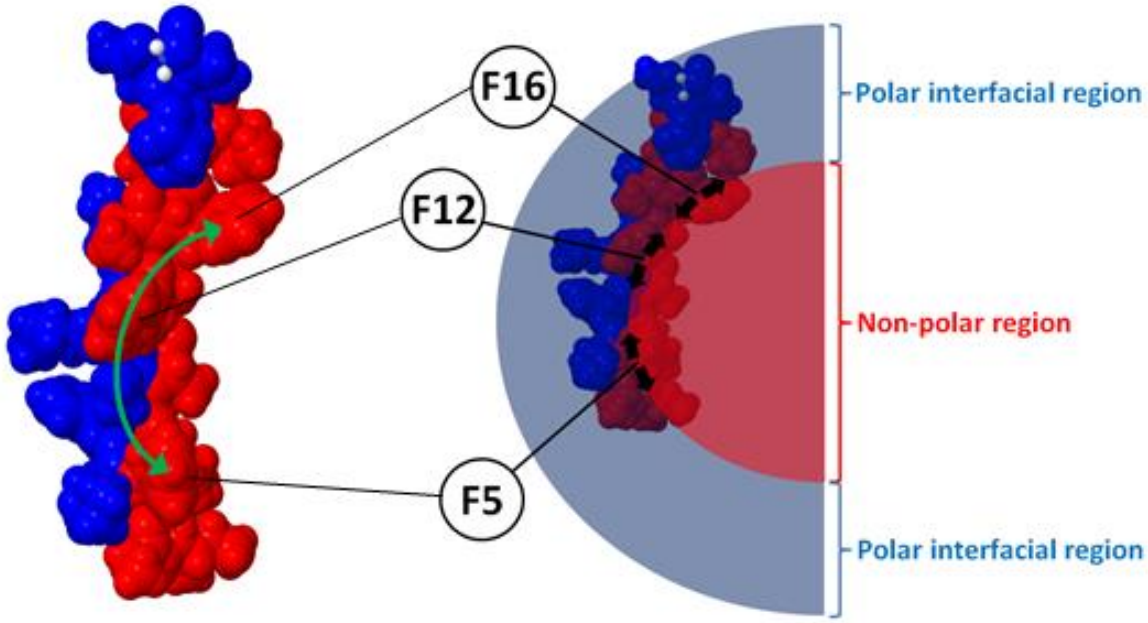

Figure 6.5: Diagram depicting the ability of magainin to stabilise the positive curvature of the leaflet fold structure of a toroidal pore. (Left) Space filling model of the helix bound to lipid membranes, with hydrophobic amino acid residues depicted in red, and hydrophilic residues in blue. The key residues F5/F12 and F16 labelled, and the green arrow depicts the curve created by the 3D location of the phenylalanine residues around the peptide helix. (Right) Identical magainin helix contained within the leaflet fold structure of the toroidal pore, with the transparent blue section representing the polar interfacial region of the bilayer, and the red showing the hydrophobic membrane core. The phenylalanine residues are labelled, and the black arrows indicate the residues occupation of the interfacial region, increasing the area and effectively acting as space fillers, stabilising the positive curvature required to form the leaflet fold structure.

An approximation of the effect of the interfacial region occupation by the peptides bulky phenylalanine residues, can be obtained by consideration of the effect on the packing parameter of the surrounding lipids. Consider the non-bilayer lipid DOPE, with a packing parameter of 1.41, calculated by dividing the lipid volume (1235.0 $Å^3$) by the product of the lipids molecular area at the lipid-water interface (50.0 $Å^2$) and the lipid length (17.5 Å). When DOPE is present within the lipid annulus surrounding a membrane-bound magainin helix, it will come into contact with the three phenylalanine residues along the length of the peptide helix, with approximately three DOPE lipids able to fit along one helical face. The side chain of the F residue occupies an area of 32 $Å^2$ at the interface, when orientated perpendicular to the bilayer normal plane; i.e. its minimal area within the bilayer interface, with 62 $Å^2$ being its maximal area when orientated parallel to the membrane plane. Due to the additive nature of packing parameters, it is reasonable to assume that the area occupied by the F residues can act in synergy with the lipid interfacial area, during consideration of the packing preference of the lipids surrounding the magainin helix.

Increasing the headgroup area parameter of DOPE in the packing parameter calculation by the minimal area of the F side chain gives a packing parameter of 0.86, while orientating the side chain to occupy its maximal interfacial area gives a packing parameter of 0.63. It is clear that small changes to the peptide conformation, i.e. changing the orientation of the phenylalanine residues with relation to the membrane plane, could exert a powerful influence on the packing preferences of the neighbouring lipids. For the case of the bilayer lipid DOPC (S = 1.08) the effect is even more pronounced, giving modified packing parameters of 0.72 and 0.56, for F orientated at its minimal and maximal interfacial areas respectively. As a packing parameter of S > 0.74 has been reported to be required for stable bilayer formation,[40] it is likely that occupation of the interface by the F residues of the peptide magainin is enough to destabilise the bilayer structure, and influence the formation of non-lamellar micellular phases. Geometrical parameter values of the lipids taken from [141]; [142] and [40]. The formation of non-lamellar phases normally results from the presence of large mismatch between the polar and non-polar regions of lipids, i.e. packing parameters with values 1<< S >> 1, and induction of non-lamellar phases has been reported for alpha-helices flanked with aromatic and cationic residues at high concentrations (>1:10 P/L ratios).[139] LCAMPs appear able to induce membrane reorganisation at significantly lower concentrations. The new model proposes that both F and W residues act as interfacial "space fillers", occupying headgroup area adjacent to the peptide, and altering the curvature properties of the surrounding membrane. The ability of W/F residues to stabilise leaflet fold will only extend a short distance from the edge of the membrane-bound peptide helix, and may play an important role in determining the size of the pore, as each peptide can only stabilise a short section of the pores central channel.

A further effect of the presence of W and F residues within the structure of LCAMPs, is their ability to preferentially associate with cholesterol, but disagreement exists on the effects of cholesterol on the membrane interactions of LCAMPs. Cholesterol has been reported to both decrease membrane penetration into membranes for AMPs,[119] and also to exert no effect on the penetration depth.[138] This can be explained using geometrical considerations, as the association of cholesterol with an LCAMP peptide will increase the lateral pressure within the hydrophobic volume of the membrane, disfavouring deeper insertion. W and F flanked transmembrane proteins show less sensitivity to hydrophobic mismatch between the thickness of the hydrocarbon bilayer core, and the non-polar residues of the membrane-spanning helix.[46][139] The large interfacial anchoring energy of the W and F residues changes the local energy minima for the lipid-peptide aggregate, forcing the membrane to distort to accommodate the transmembrane helix. The ability of W and F to act as buffers against hydrophobic mismatch can similarly stabilise the lipid-peptide pore induced by LCAMPs, through mediating between the bulk membrane thickness and the pore structure.

6.9. Reshaping the toroidal pore

By consideration of the properties of membrane-bound LCAMPs, namely their flexible membrane penetration, steric asymmetry and positive curvature stabilisation, it is possible to propose a novel structure for the pores formed by the peptides. Figure 6.6 presents a diagram of proposed pore structure, where the peptides and lipids are represented as simple geometrical shapes, as per Helfrichs theory. In a small but mechanistically important shift, the leaflet fold is prioritised as the key structure within the pore, as it enables the mass transfer between the outer and inner membrane leaflets, and the generation of the leaflet fold positive curvature is regarded as the primary mediator for pore formation within the model proposed in this thesis. The LCAMPs F and W residues enable efficiently packed leaflet fold structures by occupation of leaflet interfacial volume, reducing the pores energy. The lysine snorkelling capability of the peptide allows it to adjust its depth penetration in order to conform to the new minima in the membranes energy landscape, induced via the change in the membranes supramolecular organisation from bilayer to pore state, and allows it to fill in the pore geometry by generating the negative curvature for the pore lumen. An alternative structure for the pore includes peptide dimers, with the LCAMP helices interacting via the opposing face to the one containing the W and F residues, and allowing each leaflet fold structure to be stabilised via the W and F residues from two peptides. Interestingly, some support for this proposed structure exists within the literature, with several papers indicating that melittin dimers may be involved in the pore formation process.[77][143][98]

Many LCAMPs possess a leucine zipper motif, where every seventh residue is a leucine or isoleucine residue, and substitution of these leucine residues for other amino acids has the effect of reducing the peptides haemolytic activity, while retaining comparable antimicrobial activity to the parent peptide.[144][145] Leucine zipper motifs provide favourable energy interactions for helical association, and may overcome the electrostatic repulsion and allow dimerization within zwitterionic eukaryotic membranes. Within anionic prokaryotic membranes, the lipids shield the cationic residues from electrostatic repulsion, allowing peptide helical dimerization without the presence of a leucine zipper.

Figure XXX: (A) A section of a cylindrical geometry lipid membrane containing two of the proposed pore structures. Peptide helices are shown in blue, lipid polar headgroups in red, and lipid non-polar tailgroups in yellow. Note the varying dimensions of the two pore structures, each featuring differing numbers of peptide monomers. The pore size will be quantised due to the number of monomers, with each peptide helix capable of stabilising a tightly restricted section of pore. The proposed pore could be considerably more disordered than seen here, which depicts an idealised pore structure.

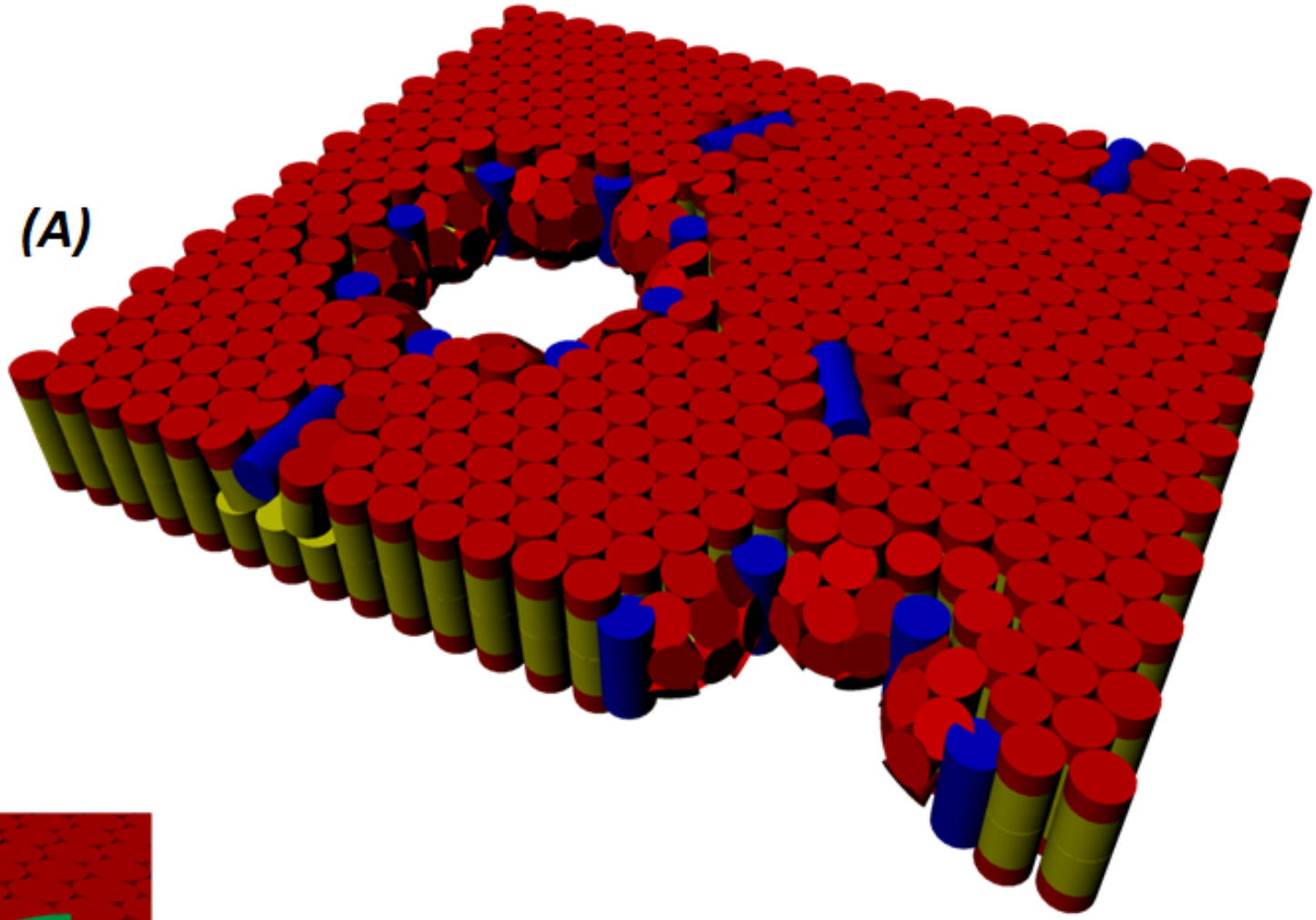

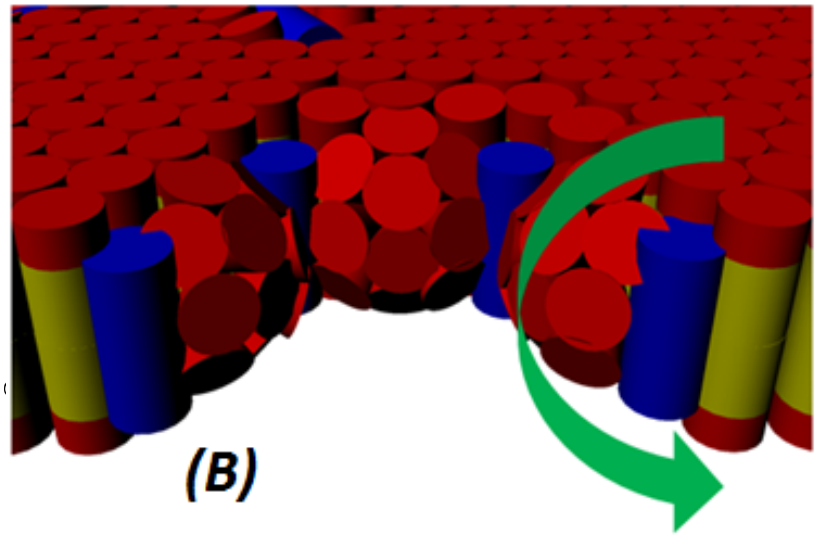

Figure XXX: (B) Closer view of the lipid-AMP arrangements within the pore structure, consisting of several leaflet fold structures, where one membrane leaflet is curved into the opposite leaflet. AMPs fulfil two functions within the structure, stabilising the positive curvature of the leaflet fold via occupation of the polar region with their bulky W and F residues, and providing the negative curvature of the pore lumen. The green arrow indicates the pore mediated mass transfer of lipids, from the outer membrane leaflet to the inner leaflet.

` It is possible that both the monomer and dimer pore types are possible, and can occur in membranes of different lipid compositions; anionic lipid membranes would reduce the electrostatic repulsion between the two cationic peptide helices for example. It is also conceivable that both pore types can exist within a membrane simultaneously. Another change to the classical pore occurs with the realisation that the pore is an active structure, mediating the transfer of lipids and peptides between membrane leaflets, with the constituent lipids (and possibly peptides) constantly changing. This results in a necessarily dynamic pore structure, with constant adjustments to pore size and shape in order to accommodate the inclusion of different lipids, and possible varying peptide monomer numbers) within its structure. This would lead to a significantly disordered pore, bringing the model into line with the latest literature on LCAMP toroidal pores. Interestingly, evidence exists for the retention of at least some lipids within the pore structure, as the rate of mass transfer between leaflets was found to increase if the charges on the headgroup of anionic lipids were neutralised by a low pH.[146] This suggests that anionic lipids are at least partially retained within the pore structure, perhaps serving to stabilise the pore.

6.10. Pore formation in peptide-free membrane

The structural parameters of the pore within the membrane will depend on properties of both the membranes constituent lipids, and the LCAMP monomers involved within the pore structure. Formation of the ideal pore requires remodelling of the lipid-AMP system into a new supramolecular organisation, with the formation of a tightly curved leaflet fold structure. Sakuma and colleagues demonstrate the formation of similar pores within peptide-free membranes, by the inclusion of non-lamellar lipids (DHPC) within DPPC lipid bilayers.[121] The lipid system demonstrated the formation of pores featuring a rolled rim resembling the leaflet fold structure, requiring only the cooling of a DPPC/DHPC membrane below the transition temperature of DPPC. The process is depicted in figure 6.7, and compared to the proposed mechanism for formation of LCAMP pores. DHPC possesses extreme inverse-conical geometry ($S < 1/3$), due to its short (6C) acyl chain and large PC headgroup, and forms micelles in aqueous solutions. Above the transition temperature of DPPC, the bilayer exists in a fluid liquid-disordered state, with DPPC and DHPC distributed at random throughout the membrane. Below its transition temperature, DPPC forms a gel-phase, excluding the DHPC from its liquid-crystalline lattice, and begins concentrating the inverse-conical geometry lipid within separate domains, increasing the membrane tension within those domains. . Pores then form with the inverse-conical geometry lipids acting as a cap for the pore rim, forming a leaflet fold structure, where one leaflet is bent into the other.

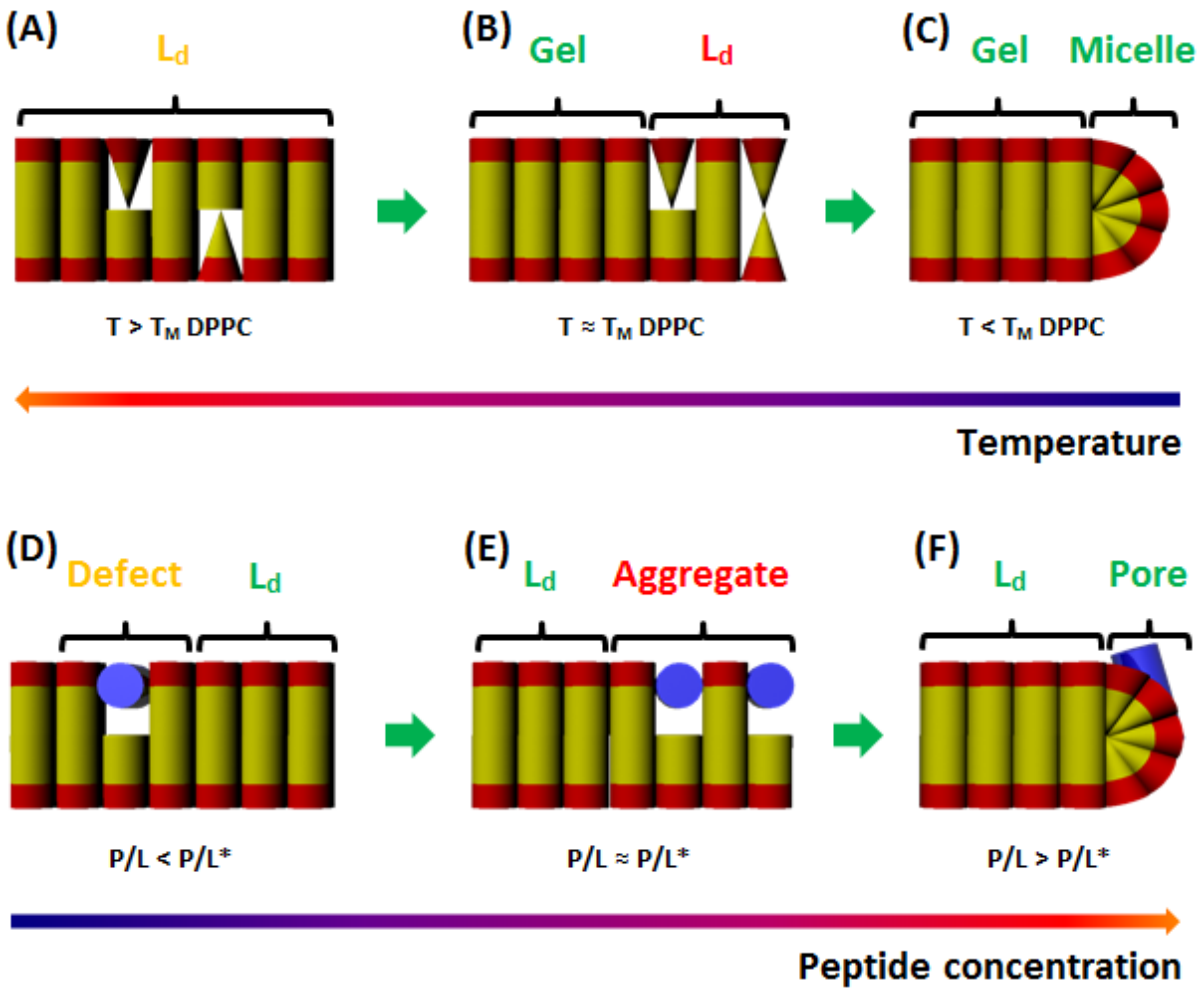

Figure 6.7: (A – C) Diagram depicting the supramolecular reorganisation reported by Sakuma and colleagues (2010), within DPPC:DHPC membranes, inducing the formation of macro-scale pores. The process is driven reduced free energy of lipids occupying their preferred geometrical arrangements; a bilayer in the case of DPPC, and micelle-like for DHPC. This section of the diagram is repeated from the introduction, while parts D –E show the application to the process of LCAMP pore formation, within a homogeneous membrane system comprised of cylindrical bilayer lipids. (D) At low peptide concentrations a small number of peptide-induced packing defects exist, with a higher energy than the surrounding liquid-disordered (L_d) phase, shown by the amber shading to the L_d label. (E) As peptide concentration increases, associations of lipid-peptide rafts occur, possessing significantly higher energies than the bulk membrane, indicated by the red shading to the aggregate label. (F) Above the critical P/L ratio the membranes supramolecular organisation as an L_d phase bilayer, is less energetically favourable than reorganisation of the lipid-peptide raft associations, into a pore structure. Bilayer reorganisation into a pore results in a lower total energy content than the initial lipid-peptide raft association, indicated by the green shading to the pore label.*

The work of Sakuma and coworkers presents direct evidence of strain energy within a bilayer structure resulting in membrane supramolecular reorganisation into a pore structure, moreover, it closely resembles the key leaflet fold from the proposed new pore structure. In this case the reorganisation of the membrane lipids operates at both the micron-scale, producing the diameter of the pore lumen, and at the nano-scale, producing the leaflet fold structure. Pore-formation in lipid-AMP systems results in much smaller pore diameters, suggesting that the presence of AMP stabilises the

formation of tighter pore lumen curves and/or allows the formation of pores at lower concentrations of strain energy; i.e. much lower numbers of involved lipids.

6.11. Energy of the pore structure

Lee and coworkers show that the energy difference (E_R) between a pore free bilayer and one with a pore, is determined as shown in equation 5.[107]

$$E_R = \gamma 2\pi R - \sigma\pi R^2$$

Where ϒ is the line tension, or energy cost per unit length of the pore rim; R is the radius of the circular pore; σ is the membrane tension of the vesicle. The first term represents the free energy cost of creating the toroidal pore structure, whereas the second term presents the work done against the membrane tension to create a pore of area πR^2. For energetically favourable pores to exist within the membrane, it is necessary to minimise the first term, and maximise the second term. Once $E_R \leq 0$ the pore structure becomes energetically favourable, and the membrane can reorganise into the pore state. Equation 5 can be applied to the formation of pores by AMP,[107][147] which together with the general behaviour of AMPs within lipid membranes, permits two conclusions to be drawn. Firstly the helical orientation change occurring on pore-formation indicates the peptide is integral to the pore structure, acting to stabilise the structure via reducing pore line tension (ϒ), and secondly that peptide binding to the membrane increases the energy of the bilayer in a similar way to membrane tension (σ).[147] The influence exerted on ϒ and σ by the AMP enables energetically stable pores to form within membranes, under much less extreme tensions than would otherwise be required in peptide-free membranes. The energy of stable pore structure equals an energy minimum for the lipid-AMP system, in a similar manner to the various packing configurations of peptide-free lipid systems in aqueous solution.[39]

The free energy of the toroidal pore within a membrane will be primarily determined by the efficiency of the lipid-AMP packing within the leaflet fold structure. Lipids that generate the required curvature without large scale deviations from their lowest energy geometries, will form pores that are more stable than if the pore structure requires significant deformation of the lipids. In combination with the occupation of interfacial volume be an LCAMPs W and F residues, positive curvature lipids will rsult in an efficiently packed pore with a low line tension. It has been proposed that a negative feedback loop exists within the energetics of the pore-formation process, which can partially explain the behaviour of the lipid-AMP pores.[107] Formation of pores reduces membrane tension though the changes in peptide

orientation that occurs during the transition from monomer to pore state, and through lipid and peptide transfer from the outer to the inner leaflet through the pore structure. Both these actions reduce the area of the outer leaflet, decreasing the membrane tension which disfavours pore formation, and causes the feedback loop. The feedback phenomenon can be understood by consideration of the terms within equation 5, where increased membrane tension results in a smaller difference between a pore-free and pore-containing membrane. Higher membrane tension induces pore formation, which involves more peptide transfer from monomer to pore state, which reduces the membrane tension and disfavours pore formation. The feedback loop has implications for the pore-forming activity of LCAMPs, which are discussed later.

6.12. Global versus local membrane tension

The membrane binding of AMP helices increases the membrane tension, and can be broken down into separate aspects; the global tension and local tension around each membrane-bound AMP helix. Addition of peptide helices to the outer membrane leaflet raises the global membrane tension (σ_G), by increasing the leaflet area through the accommodation of the AMP helix, resulting in the inner leaflet stretching to occupy the same area as the outer leaflet. The increase in tension per membrane-bound helix can be modulated via association with preferred lipids within the raft, but the total increase in the global tension will be in rough proportion to the total amount of peptide added. The global tension increase is not subject to large fluctuations, being comprised of the total membrane strain induced by the whole population of dynamic lipid-peptide rafts. Local membrane tension (σ_L) represents the lipid-AMP interactions occurring around each individual helix, and unlike the global tension, will be subject to large local fluctuations as individual lipids join and leave the raft. The local and global membrane tensions are interdependent in many membranes, a peptide which selectively associates with those lipids which minimise its impact on membrane packing, will display low increases per membrane-bound monomer to both the local and global tensions. For example, a magainin helix surrounded by DOPE lipids will contribute only minimal increases to the local and global membrane tensions. Magainins tendency to occupy interfacial volume in the membrane leaflet is compensated via selective aggregation with the conical DOPE lipids, leading to only modest increases in outer membrane leaflet area per bound peptide helix. Conversely, those peptides which associated with lipids that increase the scale of the membrane deformation induced by the AMP helix, will feature large increases to both local and global membrane tensions per bound monomer. Melittin surrounded by DOPE produces the opposite situation than magainin, with the deeper penetration of melittin into the bilayer and the large hydrophobic volume of DOPE leading to hydrophobic crowding in the bilayer. The total membrane tension within a defined membrane region, termed a pre-pore region, will be equal to the sum of the

global and local tension contained within the lipid-AMP interactions within that region, as shown in figure 6.8.

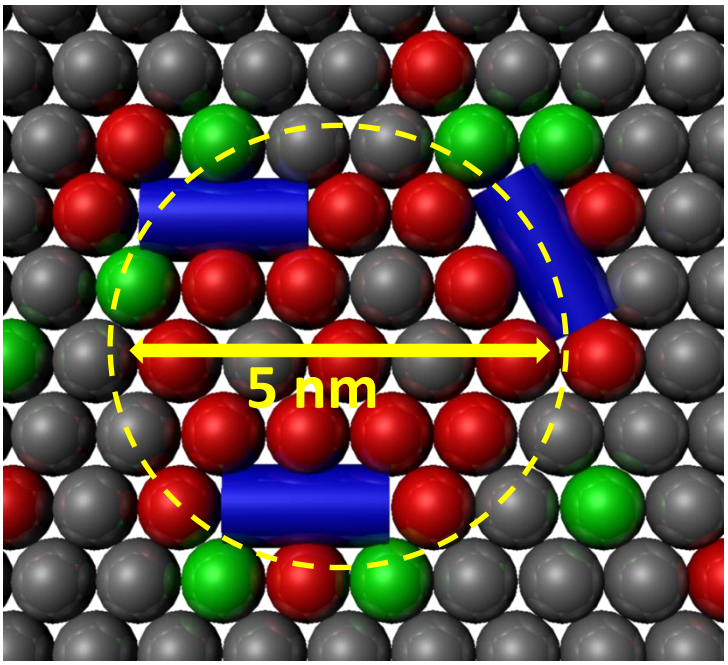

Figure 6.8: Top down view of a lipid membrane, containing laterally diffusing peptide helices. The peptides are depicted as blue cylinders, and the lipids as spheres. Grey spheres are lipids that form energetically neutral interactions with the faces of the helices, red spheres are anionic lipids forming unfavourable interactions that are held to the peptide via electrostatics, and green spheres are lipids which form favourable interactions with the helix. The yellow dashed line represents a 5 nm circle indicating an approximate size for AMP-induced pores, termed a pre-pore region, that can go on to undergo reorganisation into a lipid-AMP pore when the threshold energy is reached. It is clear that the random diffusion of AMP helices in the outer membrane leaflet can accumulate considerable local membrane tension within a small area – a transient raft assembly.

Applying the concept presented in figure 6.8 to equation 5, allows us to reformulate it as shown in equation 6, where several AMP helices have come into close association via lateral diffusion in the outer membrane leaflet.

$$E_R = \gamma 2\pi R - (\sigma_G \pi R^2 + \sum_{\pi R^2} \sigma_L)$$

Equation 6: Modified version of equation 5, to account for the global and local membrane tensions induced by the binding of AMP helices to a region of lipid membrane with area πR^2. σ_G represents the global tension in the membrane region, from the membrane thinning induced via the generation of leaflet area asymmetry, and $\sum_{\pi R^2} \sigma_L$ is the total local tension contained within the lipid-AMP rafts in the defined region. The local membrane tension increases the value of the second term, enabling the formation of pores at considerably lower global membrane tensions.

E_R represents the energy of a defined region of radius R that will end up containing the pore structure, ϒ the line tension of a translocating toroidal pore, and the second term is split into two components, σ_G and σ_L representing the global and local membrane tensions within the small defined region of the membrane respectively. A membrane containing several AMP helices in close proximity, either via random lateral diffusion within the membrane leaflet or through selective aggregation, is capable of generating a "hotspot" of membrane tension. This local tension can be far in excess of the average tension within the membrane, depending on the constituent lipids of the lipid-AMP raft. Associations of lipid-AMP rafts containing high energy interactions, possibly forced through electrostatics, will display considerably larger contributions to the second term of equation 6, than accumulations of peptides possessing low energy interactions. When the term $(\sigma_G \pi R^2 + \sum_{\pi R^2} \sigma_L)$ exceeds the term $\gamma 2\pi R$ then reorganisation of the bilayer structure into a pore-like structure becomes energetically favourable. As more peptide binds to the membrane the global membrane tension will increase, and more peptides will be contained within any defined region, leading to increasing numbers of lipid-AMP raft assemblies. Associations of high energy rafts will achieve the energetic situation $(\sigma_G \pi R^2 + \sum_{\pi R^2} \sigma_L) \geq \gamma 2\pi R$ needed to form the pore structure earlier than associations of low energy peptides, due to larger contributions of the high energy rafts to the local membrane tension.

Support for the concept of pore formation from raft aggregates at a specific spot within a membrane, rather than occurring due to peptide widely dispersed across the membrane can be found within the literature. Pore-formation occurs after the binding of as few as four melittin monomers to an LUV membrane,[99] indicating that low monomer numbers can achieve pore formation. The exact global tension required to allow raft assemblies to remodel into the pore state, will be dependent on the specific lipid-AMP interactions occurring in that raft, creating a range of threshold energies occurring within each peptide-exposed membrane. When the global tension reaches the threshold energy, the lipid-AMP raft assemblies within the membrane will reorganise into the pore structure. The pore will translocate material from outer to inner membrane leaflets, initiating the negative feedback loop already discussed. Several situations can now occur, as demonstrated by the multiple pathways for the membrane tension after this point within figure 6.9.

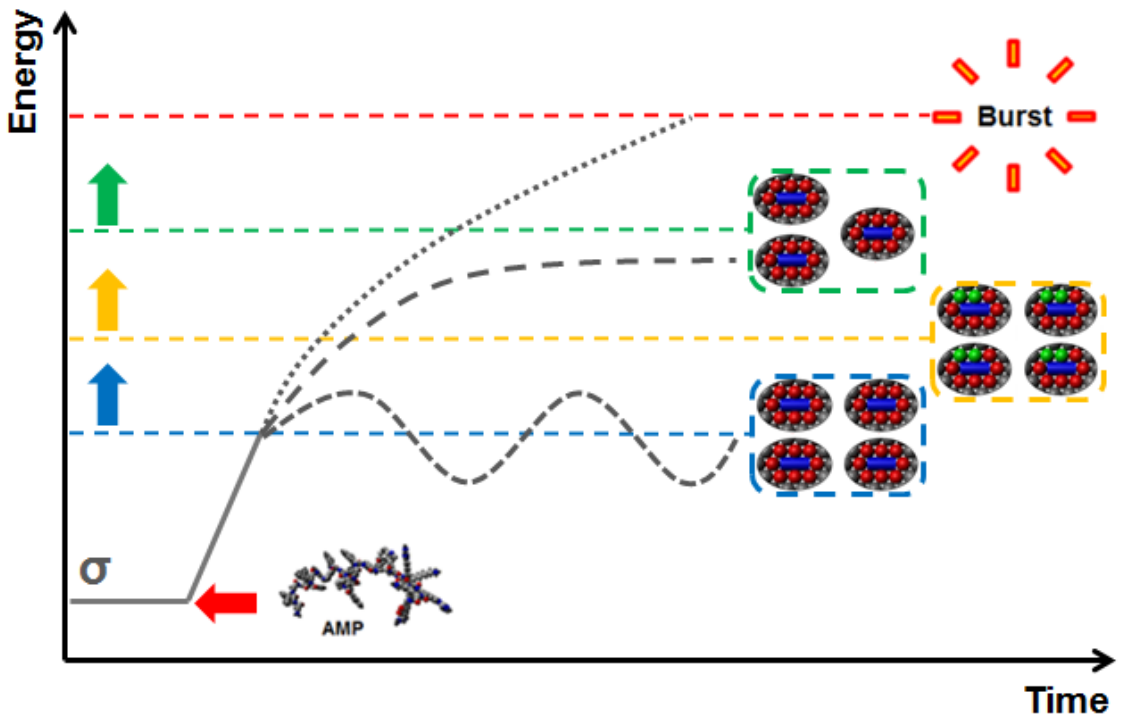

Figure 6.9: Energy level diagram depicting the effect of lipid-peptide raft aggregates on the formation of pores, and the release of membrane tension via lipid/peptide translocation to the inner membrane leaflet. σ represents the initial membrane tension prior to AMP exposure, which is indicated by the red arrow. The blue line represents the point where the global membrane tension plus the local contribution from an assembly of four maximal energy lipid-AMP rafts enables the energetically favourable formation of a toroidal pore. The yellow line indicates where pore formation can occur through the association of four intermediate energy rafts, and the green line where pore formation can occur via association of three maximal energy rafts within the same area, becomes favourable. The red line indicates the critical membrane tension whereupon the bilayer structure itself becomes energetically unfavourable, leading to complete failure. Several possible scenarios are represented, including cycling of pore opening and closing (narrow spaced dashed line), steady state pore opening (widely spaced dashed line) and consecutive pore openings followed by membrane failure (dotted line).

If the rate of material translocation is able to lower the total tension below the threshold line required for pore formation from this assembly of rafts, the pore will close, indicated by the closely spaced dashed line. Closure of the pore allows the global membrane tension to increase back towards the threshold level, leading to a pore opening and closing cycle around the same threshold energy, so long as the required lipid-AMP assemblies remain present within the membrane. Alternatively, the translocation of material may not be sufficient to prevent the accumulation of strain within the membrane, which increases to the next lowest threshold level. The corresponding lipid-AMP assemblies will then be free to reorganise into a pore structure, leading to increased levels of mass transfer between leaflets. If this increase in strain relief from the outer leaflet is sufficient to ensure that the tension never achieves the threshold level required to activate the next highest energy accumulation of assemblies, the pore situation will remain unchanged. The final situation depicts the phenomenon where the consecutive opening of all the featured pores and their associated mass transfer, is not sufficient to overcome the increase in membrane tension, and the next threshold energy level is

reached. The red line represents the critical failure energy of the membrane bilayer, and the vesicles structure will fail at this point, resulting in bursting. It should be noted that not all the potential threshold energies will be occupied within any particular membrane, as the highest energy lipid-AMP raft assemblies are likely rare within the total population, being composed of lipid-peptide rafts with unfavourable lipid-AMP interactions. The global membrane tension can then pass through the threshold energy without triggering pore formation, although once past the threshold, a pore will form should the required raft assembly occur.

6.13. LCAMP modulation of bulk membrane tension

Presence of non-bilayer lipids within membranes leads to increased strain, which can be mediated via interactions with membrane-bound LCAMP helices. Consider the interactions of magainin within the DOPC:DOPE (80:20 mol%) system, where the peptide will selectively associate with the DOPE to minimise the lipid-AMP raft free energy. The non-bilayer DOPE lipid induces a strain within the bilayer, due to its large packing parameter (S = 1.41), resulting in inefficient packing with the bulk DOPC membrane. Aggregation with magainin removes DOPE from the bulk membrane, and replaces its previously unfavourable interactions with favourable interactions with the magainin helix, lowering the global membrane tension. Conversely, within the same DOPC:DOPE system, melittin would increase the energy content of the bulk membrane surrounding the peptide defects. The peptides unfavourable interactions with DOPE, due to steric crowding in the hydrophobic bilayer core, would act to exclude DOPE from the lipid-peptide rafts, increasing its relative concentration within the bulk membrane, and increasing the strain energy.

6.14. Selectivity mechanism

Consider the impact of the steric asymmetry, and forced electrostatic interactions, on the selectivity of magainin between prokaryotic and eukaryotic membranes. Within the bacterial *E.coli* membrane the AMP exploits the strong nature of the electrostatic interaction, between cationic lysine residues and the anionic PG lipids, to force high energy sterically hindered interactions along one face of the helix. The *E.coli* membrane contains lipids which would allow the lipid-magainin raft to locate at much lower energy minima, for example the negative curvature inducing PE lipids, which would both oppose the positive curvature induced by magainin, and reduce the steric crowding at the leaflet interface, due to its smaller headgroup. The opportunity to locate to a lower energy minima is lost however, through the exclusion of PE lipids in favour of anionic PG lipids. The outer leaflet of mammalian membranes, for example erythrocytes, are comprised mainly of the electrically neutral lipids SM, PC and cholesterol. With no forced electrostatic interactions, the lipid-AMP raft is free to locate to much lower energy

minima within the energy landscape of the membrane, free from the steric crowding seen in the bacterial membrane. Cholesterol is a negatively curved membrane component, and is known to associate with the aromatic phenylalanine residues of proteins. Not only are lipid-magainin rafts free from forced sterically hindered electrostatic interactions, they are instead forced into interactions with membrane components which oppose the peptides positive curvature, resulting in reduced energy rafts. Lipid-magainin rafts will therefore exist at higher energy levels in bacterial membranes than mammalian membranes, with increased contributions to the membrane tension-like energy induced by each lipid-AMP raft.

The membrane disruptive effects of LCAMPs increase with membrane penetration (Glukhov et al, 2005), indicating that the deep penetrating melittin has been evolutionary designed to exert maximal strain within target membranes, through insertion of its entire helical length into the outer membrane leaflet. The shallow penetrating magainin is less disruptive, only inserting ~50 % of its helix into the leaflet. With bacterial membranes containing high levels of non-bilayer lipids, like DOPE and CL, they operate much closer to the lamellar to non-lamellar phase transition boundaries than mammalian membranes.[54] The LCAMP selectivity mechanism operates within the energy gap of prokaryotic vs eukaryotic membranes, with mammalian membranes able to take significantly more internal tension before passing through the lamellar to non-lamellar transition boundary.

6.15. Charge distribution

The differences in the charge distribution between melittin and magainin are displayed in figure 6.10. Of the six positive charges at physiological pH possessed by melittin, five are clustered at the ends of the helix, the N-terminus and the KRKR motif, with only one located along the length of the melittin helix. In contrast magainin has four cationic residues located along its helical length.

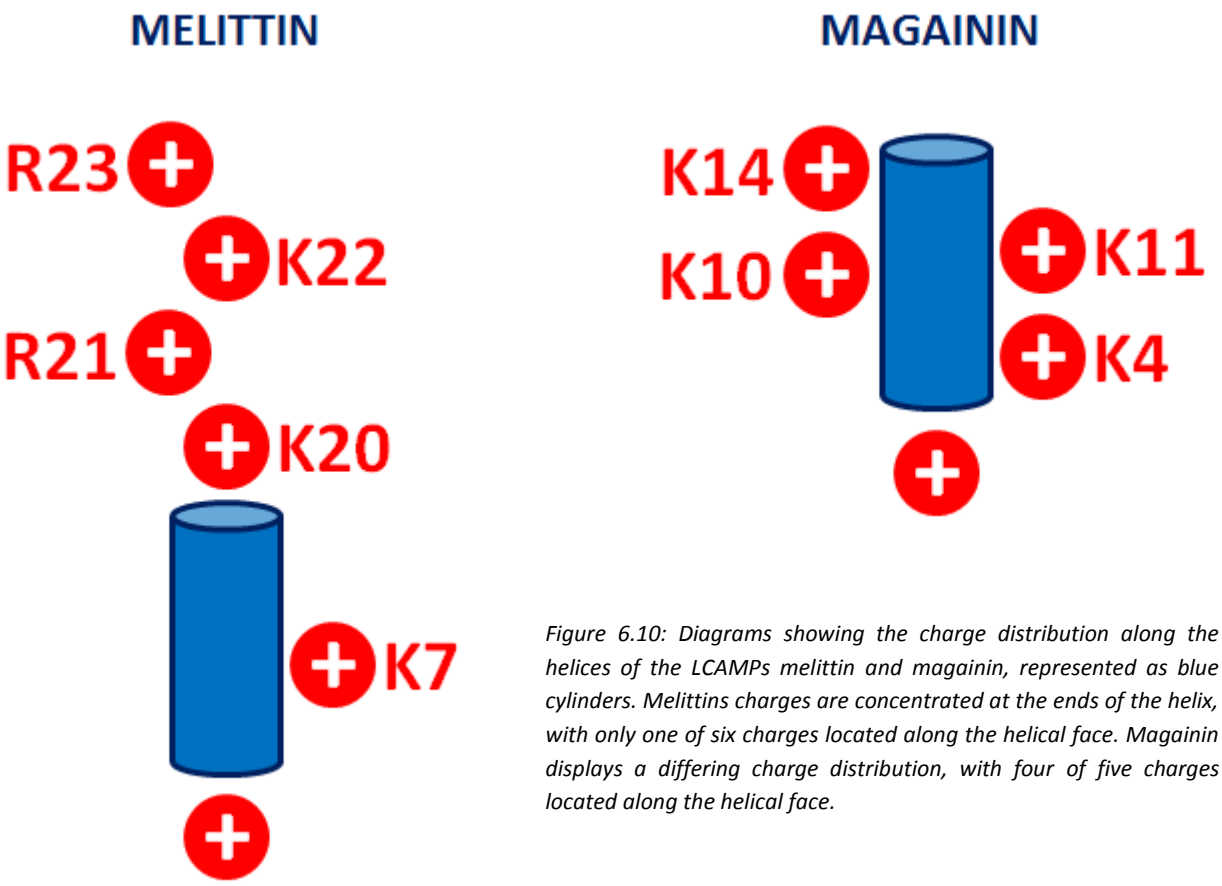

Figure 6.10: Diagrams showing the charge distribution along the helices of the LCAMPs melittin and magainin, represented as blue cylinders. Melittins charges are concentrated at the ends of the helix, with only one of six charges located along the helical face. Magainin displays a differing charge distribution, with four of five charges located along the helical face.

Melittin possesses a larger helical face available for interaction with zwitterionic lipids than magainin within anionic membranes, of the 7 – 9 lipids that magainin can directly interact with, five will be anionic lipids with only 2 – 4 being zwitterionic. Only one anionic lipid is electrostatically recruited along the helical face of melittin, allowing more neutral lipids access to the helical face of the membrane-bound peptide. Melittin should therefore show increased sensitivity to zwitterionic lipids than magainin, whose PIEs should be dominated by interactions with anionic lipids.

6.16. Model predictions

The model can be used to make several predictions about LCAMP pore activity within lipid membranes. These predictions are listed below, and briefly discussed. We will then review the data presented within this thesis, to match the predictions to the experimental data.

6.16.1. Prediction 1 - Lipid-AMP raft energetics

Lipid-AMP raft energetics will vary depending on the precise lipid composition of each raft, with lipid topography exerting a strong influence of raft energetics. Lipids with exert similar topography to the membrane-bound LCAMP helix will synergise with the peptide, and produce large high energy membrane defects. This will result in high peptide activity, especially within those membranes where the high energy interactions can be forced via electrostatic interactions.

6.16.2. Prediction 2 - Pore energetics

The lower the energy of the leaflet fold structure, the more energetically favoured the pore becomes. Since the leaflet fold structure is the primary structural component of the pore, and is tightly positively curved, membranes containing positive curvature lipids will minimise the pore energy. AMPs which will associate with positively curved lipids when inserted into the lipid membrane should therefore produce higher levels of pore activity, than those peptides which associate with negatively curved lipids. Magainin offers the greatest stabilisation to the leaflet fold structure, from its three phenylalanine residues, and so should display higher relative proportions of pore activity than melittin, which can only stabilise the fold structure with a single tryptophan.

6.16.3. Prediction 3 - Stochastic behaviour

The formation of pores should not be deterministic, but instead stochastic, as the formation of pores depends on the probability of lipid-AMP rafts with required energies coming into close association with each other. It is possible that pore formation requires the presence of one or more specific high energy lipid-AMP interactions; i.e. a specific topography lipid interacting with a particular residue of the membrane-bound AMP helix. The energy required for pore formation will depend on the length of time the membrane is exposed to peptide, with quick pore formation requiring the presence of many high energy lipid rafts within a small raft population, and therefore a low probability event. Slower pore formation allows more time for the global tension to accumulate within the system, and facilitates pore formation from the association of lower energy rafts.

6.16.4. Prediction 4 - Pore behaviour

The negative feedback loop between pore formation and global membrane tension should allow repeated opening and closing of similar pores, when the rate of material added to the outer membrane is less than the rate of material transfer through opened pores, as the global membrane tension cycles across the threshold energy of a particular lipid-AMP raft energy threshold. Consecutive opening of

pores followed by a stable pore situation can occur, caused by the membrane tension passing through consecutive thresholds, when the rate of translocation of material from outer to inner leaflet is similar to the rate of material addition to the outer leaflet.

6.16.5. Prediction 5 - Pore size and quantisation

The leaflet fold is the key component of the pore structure, and the peptide acts to both stabilise the positively curved fold structure through its W and F residues, and to supply the negative curvature required to form the pore lumen. Peptide helices within a pore are capable of supporting only a defined section of the structure, exerting tight control over pore size. Pore size will therefore depends only on the number of monomers within the pre-pore region, and it is likely that pore sizes will be similar across membranes of varying composition, and for the pores induced by different AMPs. Although pore size and leakage kinetics may be similar, the overall activity and initiation times for pore formation may vary widely for different peptides. The differing lipid-peptide interactions occurring within different membranes, produce significantly different effects on the defect energy and local/global membrane strains, while contributing towards the opening of very similar pore structures. The model permits the formation of differently sized pores within single membranes, as both low monomer number assemblies of high energy rafts and high monomer number assemblies of low energy rafts can display similar contributions to the local free energy within the pre-pore region, permittin pore formation at similar global energy levels.

6.16.6. Prediction 6 - Pore number

The model predicts that multiple pores will open consecutively during the pore leakage process, as lower and lower energy lipid-AMP raft assemblies achieve the energy required to remodel the bilayer into the pore structure. Multiple pores can open at once upon crossing a single energy threshold, as several raft assemblies with the required energy could exist within the membrane simultaneously. Multiple pore openings would occur more frequently for lower energy raft assemblies, which are more common within the raft population.

6.17. Application of model to experimental data

The proposed model can be used to explain the patterns of activity seen within the experimental data within this thesis.

6.17.1. Pore-mediated leakage data

The pore-mediated leakage events occur within strongly grouped kinetics modes, where individual GUVs will display dye leakage through a limited set of dye-efflux kinetics. The average time of initiation of the leakage process following exposure to peptide varies widely, yet the dye still follows tightly controlled efflux kinetics groups. An example is shown in figure 6.11, for the exposure of the DOPC:DPPC:DPPG membrane system, to 1 µM of the LCAMP magainin. The leakage events for this system initiate over a large time frame, from about 250 s to 5600 s, with no discernible pattern between initiation time and the leakage kinetics followed by the individual vesicle. The probabilistic nature of the pore formation can be explained by consideration of the lipid-peptide interactions required to form a pore; in a low percentage of lipid-peptide systems, high energy raft assemblies will occur, as the random lateral diffusion of the peptide within the outer membrane leaflet brings a large number of peptide monomers together. If these raft assemblies contain high energy lipid-peptide interactions, then the raft assembly can quickly achieve the threshold energy needed to initiate pore formation. In some membranes, the high energy raft assemblies will not occur rapidly, as the diffusion of the peptide monomers in the outer membrane never brings large numbers of peptides together, or high energy lipid-peptide interactions are not present within the assembly.

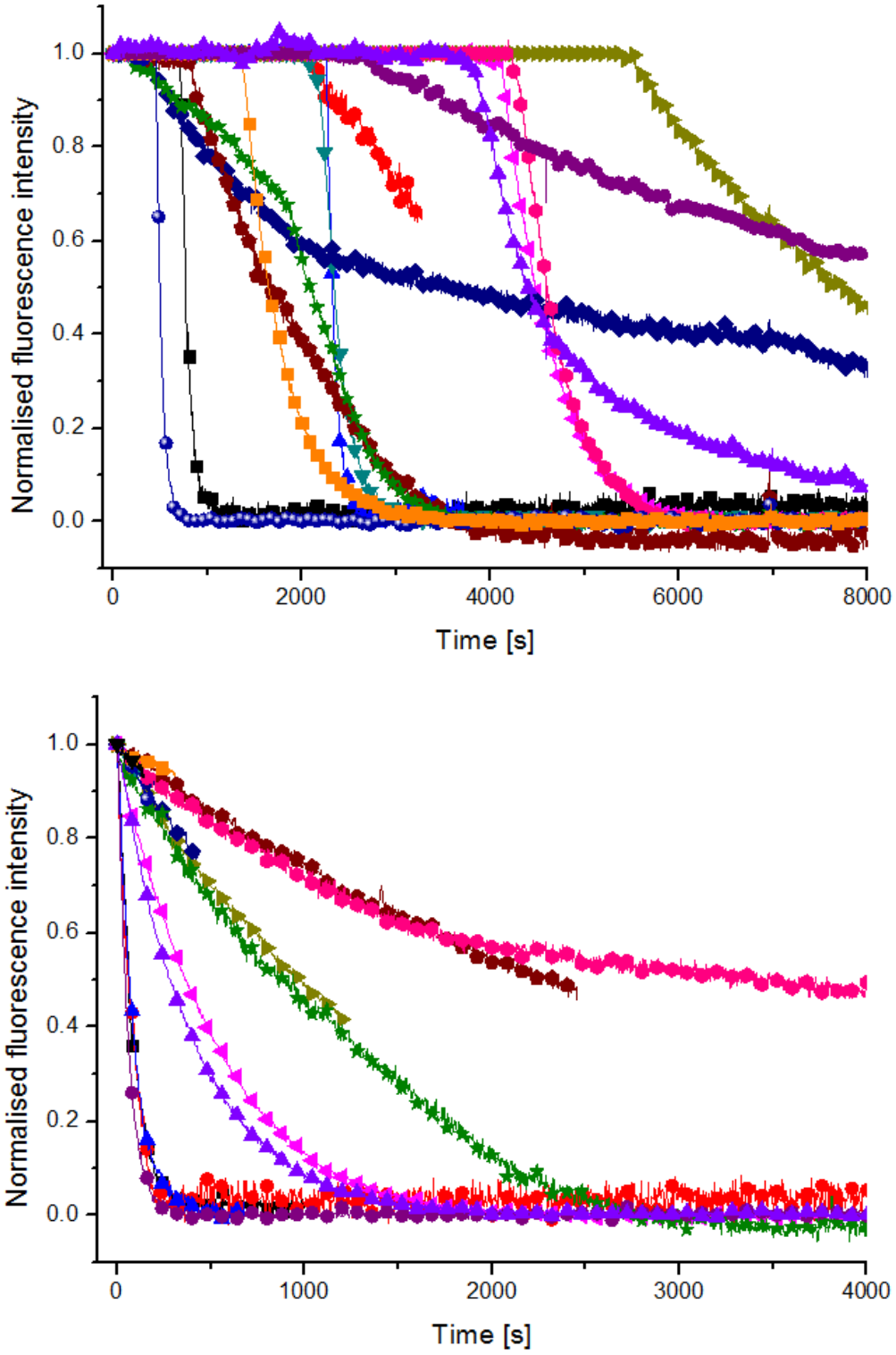

Figure 6.11: (Top) Normalised leakage data demonstrating the stochastic nature of the pore-mediated leakage induced by exposure of 12 DOPC:DPPC:DPPG GUVs to 1 µM of the LCAMP magainin. The initiation time of the pore-mediated leakage varies between <300 s to > 5500 s, with no clear pattern in the data. (Bottom) Data from the same 12 GUVs after correcting for initiation time, showing that although the timings are widely separated, the kinetics are closely grouped after accounting for the differing initiation times.

In these membranes, pore formation will occur later, when the increased number of peptides bound to the membrane make achieving the threshold energy easier, without requiring high energy unflavoured lipid-peptide interactions. If pore formation relies on the formation of a particular lipid-peptide raft assembly within the membrane, then pore-mediated leakage can be expected to be stochastic, and to follow the type of leakage pattern shown. That the data follows this pattern acts as evidence in support of prediction 3 of the new model. The model also predicts that pore opening and closing cycles should be present within the data, caused by the negative feedback loop between membrane tension and interleaflet material transfer through open pores, inducing the membrane tension to pass back and forth over an energy threshold. An example of this phenomenon is shown in figure 6.12, which demonstrates a pore opening and closing cycle within a DOPC:DOPE:DOPG GUV, exposed to 1 µM of the LCAMP melittin.

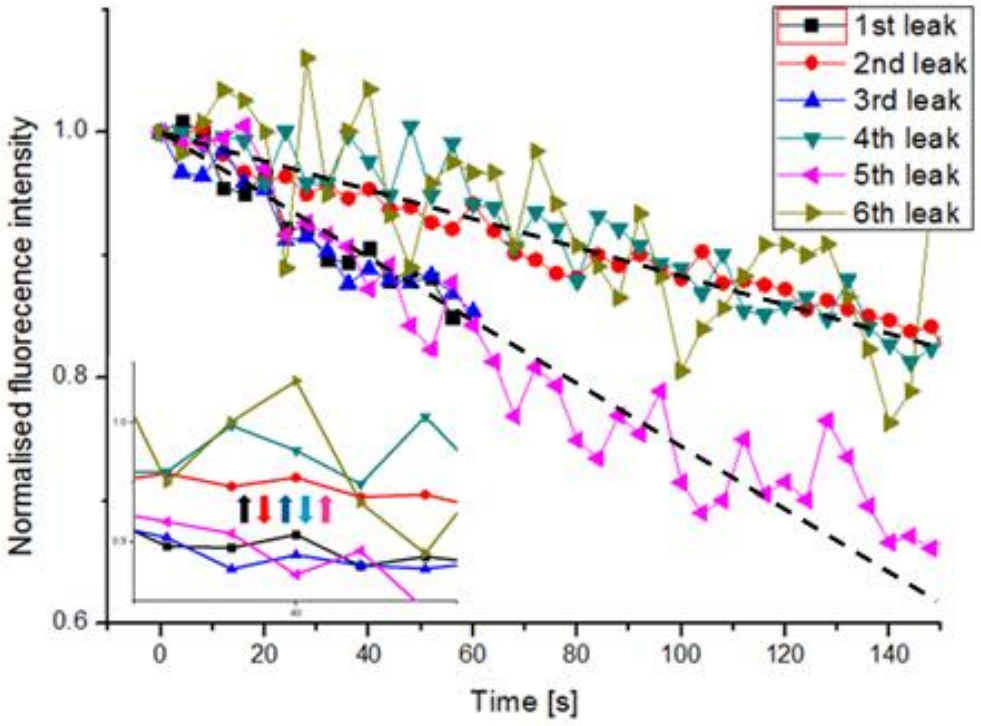

Figure 6.12: Leakage data presenting the pore-mediated leakage behaviour of an individual DOPC:DOPE:DOPG GUV, after exposure to 1 µM of melittin, depicting the negative feedback loop between pore formation and membrane tension. Pore formation requires a specific energy threshold to be achieved in the membrane, and as the formation of pores reduces the membrane tension it can lower the membrane energy to below the threshold, rendering the formation of that specific pore unfavourable. The black dashed lines indicate the two leakage kinetic groups, and are a guide for the eyes only. The inset (bottom left) shows the switching of the leakage phases, between a slow and fast kinetic group, as the membrane energy repeatedly crosses an energy threshold, leading to repeated cycling of pore opening and closing and confirming prediction 4. The coloured arrows indicate the direction of the groups switching, between the faster and slower leakage groups.

TheDOPC:DOPE:DOPG vesicle demonstrates a total of five sequential switches between two leakage kinetic modes, as the lipid-AMP system cycles back and forth across a threshold energy. The

GUV initially leaks following the faster of the two leakage groups, then as material transfers between the leaflets through the open pore, the membrane tension falls below the threshold energy needed to render this size pore energetically favourable. The pore structure adjusts by adapting to a lower energy organisation, potentially by reducing the number of peptide monomers within its structure, reducing both the leakage rate to follow the slower leakage group and the rate of interleaflet material transfer. The reduced flow material flow between the outer and inner leaflet allows the membrane tension to build up again, until it recrosses the threshold energy needed for the larger pore. The pore structure then resumes its prior form, with increased leakage and material transfer rates, and the cycle repeats.

The cycling of pore activity as the negative feedback loop moves the membrane tension back and forth across a threshold energy serves as conformation of the 4th prediction of the proposed model. The 5th prediction of the model is that pore size and leakage kinetics will be similar for LCAMPs in identical membrane systems, as each peptide monomer within a pore is capable of stabilising only a short stretch of leaflet fold structure. This can be seen within the data in figure 6.13, which displays the grouped leakage modes for the LCAMPs magainin and melittin, within the DOPC:DPPC:DPPG membrane system, exposed to 1 μM of the peptides. Both LCAMPs present similar dye-leakage kinetics within the DOPC:DPPC:DPPG membrane system, showing six kinetic groups and a carpet mechanism group. Of the six leakage groups, five show a very good match between the peptides, indicating that the pore activity within the membrane is very similar, despite the different lipid-peptide interactions occurring in the membrane. Although the leakage kinetics are similar, the peptide activity, initiation times and PIE-profiles are significantly different between the two peptides. The peptide activities within the membrane are 75.5 and 45.8 %, for melittin and magainin respectively, and the pore-mediated average initiation times are 1961.1 and 3255.4 s. The similarity in leakage kinetics represents the formation of similar pore structures by the two peptides, while the other factors vary due to the different nature of the lipid-peptide interactions leading to pore formation, and is supporting evidence for prediction 5 of the proposed new model.

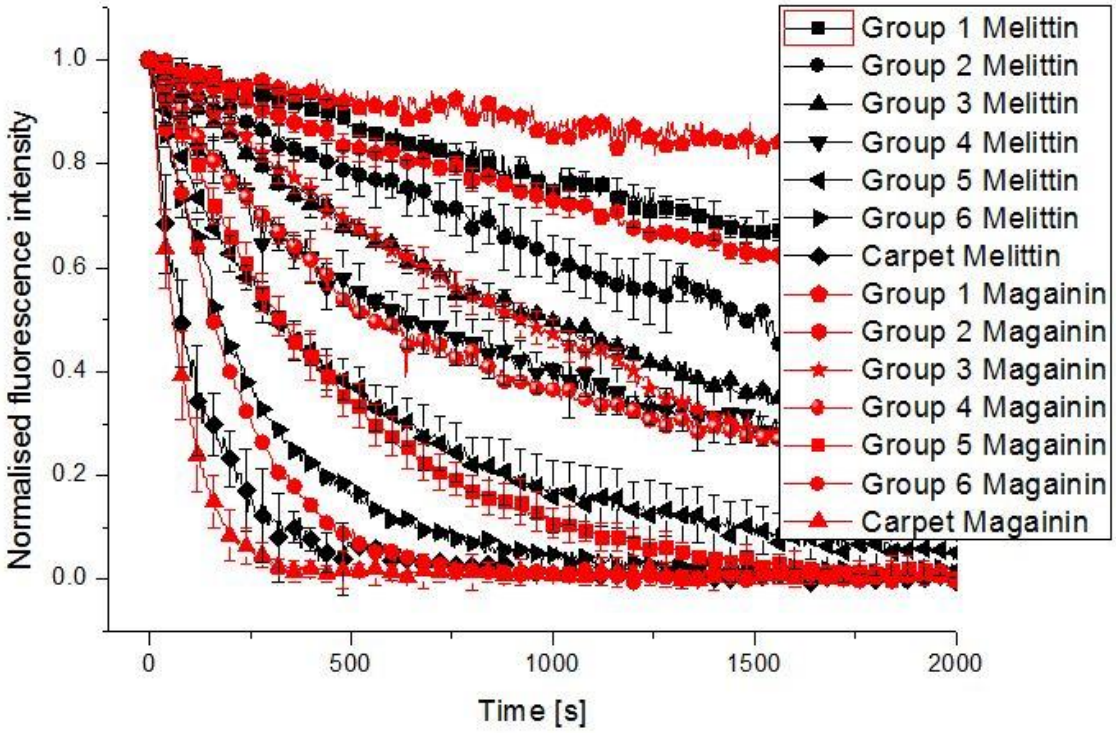

Figure 6.13: Tightly grouped leakage traces occurring within the DOPC:DPPC:DPPG membrane system after exposure to 1 µM of melittin and magainin confirm prediction 5, which states that the pores induced through the interaction of different LCAMPs should be very similar in size/leakage kinetics. With each peptide only capable of supporting a limited section of leaflet fold, the pore size depends only on the number of monomers contained within the pore structure, it is the energetics of the process that change across different peptides and membranes.

Further evidence to support this prediction comes from the data shown in figure 6.14, which depicts the opening of differently sized pores with the same membranes, within the DOPC:DOPE:DPPG GUVs exposed to 1 µM of magainin. The opening of a second pore within the membrane, with a smaller diameter than the existing pore, is seen within the leakage data. The second pore allows the efflux of the smaller 3 kDa dextran, which has a diameter of 2.13 nm, but retains the larger 10 kDa dextran, which has a diameter of 4.23 nm. This places the limit of the second pore diameter of between these two values, while the first pore remains open. Further evidence for the differential escape of the smaller tagged dextran can be found in several other data sets for both peptides, including the DOPC:DOPE:DOPG, DOPC:DOPE:LPG, DOPC:DOPE:DOPG:DPPG and mGUV membrane systems, where leakage groups display efflux for the 3 kDa dextran but retention of the larger 10 kDa molecule.

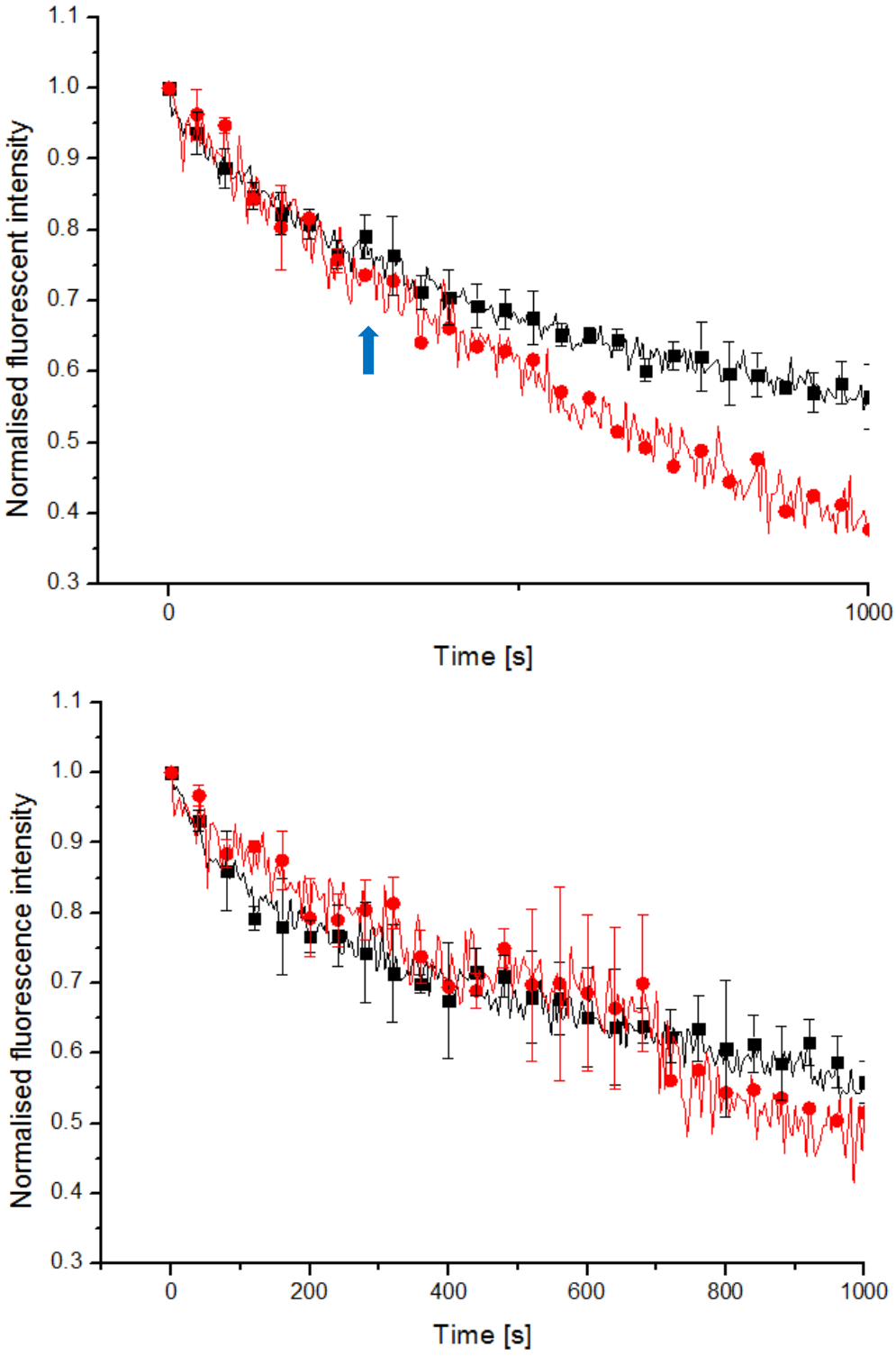

Figure 6.14: Leakage kinetics demonstrating the sequential opening of differently sized pores within the DOPC:DOPE:DPPG membrane system exposed to 1 µM magainin, showing the grouped leakage kinetics of the 3 (top) and 10 kDa (bottom) dextran markers. The 3 kDa data clearly depicts a second pore opening event after ~350 s, indicated by the arrow, while the kinetics of the 10 kDa trace remain unaffected. This situation is only possible if a second pore state has become energetically viable within the membrane, of a diameter larger than the diameter of the 3 kDa dextran and smaller than the diameter of the 10 kDa dextran. This allows the egress of the smaller dextran, but retains the larger molecule.

6.17.2. PIE data

This section reviews the data from the biomimetic membranes in the light of the new model, allows us to map the relevance of lipid and LCAMP topography to the membrane activity of the peptides melittin and magainin. Interpretation of the data in this way allows us to determine the factors controlling the behaviour of the lipid-LCAMP system, with relevance to equation 6.

$$E_R = \gamma 2\pi R - (\sigma_G \pi R^2 + \sum_{\pi R^2} \sigma_L)$$

Lipids which lower ϒ will decrease the free energy of the pore structure, and increase the likelihood of pore formation within the lipid-AMP system. The second term has two components, the local and global membrane tensions σ_L and σ_G; lipids which increase these terms will result in increased membrane disruption, but the likelihood of pore formation will depend on the ϒ value. Lipid-AMP rafts that possess the possibility of very high σ_L energies, for example a membrane-bound magainin helix featuring interactions between a large headgroup/small tailgroup lipid and its sterically bulky side, should display high levels of pore formation. The concentration of energy within a raft assembly in a small membrane region, will exert a much more powerful effect on the activity of LCAMPs, than the small increase in global tension caused by one peptide monomer.

6.18. Bacterial biomimetic membranes and melittin

The three membranes designed to replicate bacterial membranes containing lipids of opposing charge and topography were the systems DOPC:DOPE:DOPG, DOPC:DOPE:DPPG, DOPC:DPPC:DOPG and DOPC:DPPC:DPPG. Comparison of the PIE-profiles for these systems produced by exposure to 1 μM of the LCAMP melittin, presented in figure 6.15, it is clear that the individual PIEs are controlled primarily by the presence of one specific lipid within the membrane system.

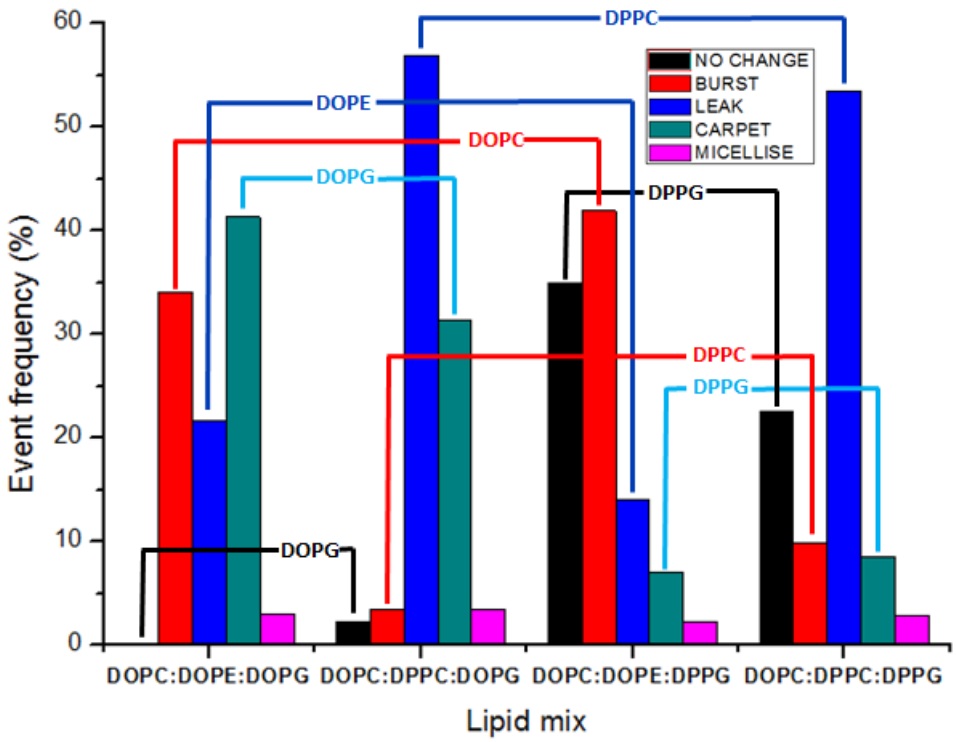

Figure 6.15: PIE-profiles for the bacterial biomimetic membrane systems, produced by exposure to 1 μM of the AMP melittin. The individual PIEs are colour coded according to the diagram key. The specific lipid interactions controlling the occurrence of each PIE, are indicated within the colour keyed lines connecting the bars on the graph. Certain lipids within the membrane system controls the level of the PIE that occurs, for example; the presence of the anionic DOPG lipid influences the PIE-profile towards containing carpet mechanism events, and increases overall activity.

6.18.1. Activity

The most active systems were the DOPC:DOPE:DOPG and DOPC:DPPC:DOPG membranes, displaying 100 and 97.7 % activity respectively. Within both of these membrane systems and in line with prediction 1 of the proposed model, the lipid-melittin rafts can be expected to be enriched with the anionic DOPG, forced into interactions through the strong electrostatic attraction between the cationic peptide and anionic lipid. The secondary lipid interactions differ however, with the DOPC:DOPE:DOPG raft expected to contain more DOPC than DOPE, and the DOPC:DPPC:DOPG raft expected to contain more DPPC than DOPC. This difference is caused by the deep penetration of the melittin helix into the membrane leaflet, where it prefers to interact with low hydrophobic volume lipids, which reduce steric crowding in the hydrophobic region. The electrostatically forced interaction of melittin with a lipid featuring a high hydrophobic volume, i.e. DOPG, produces a large amount of packing frustration within the bilayer; i.e. high values for σ_L and σ_G. The high energy level of the lipid-melittin rafts in these membranes explains the overall high activity of the peptide in these systems. Association with the lipid DPPC reduces the energy of the lipid-melittin raft, and hence the DOPC:DPPC:DOPG membrane displays slightly less activity than the DOPC:DOPE:DOPG system. The two lowest activity systems are DOPC:DOPE:DPPG and DOPC:DPPC:DPPG, which display 65.1 and 77.5 % activity respectively. In contrast

to the two previous membranes, these systems will possess forced electrostatic interactions between the negative curvature-inducing melittin, and the positive curvature-inducing DPPG lipid. This lowers the energy of the lipid-AMP raft, reducing the peptides activity considerably compared to the DOPG containing systems.

6.18.2. Bursting

High levels of bursting were seen within the DOPC:DOPE:DOPG and DOPC:DOPE:DPPG membranes, which displayed 34.1 and 41.9 % of the PIE respectively. The systems feature forced electrostatic interactions with opposite curvature lipids (DOPG and DPPG), and will preferentially associate with DOPC rather than DOPE. The lipid DOPC was assigned to be controlling the bursting, as melittin will preferentially associate with the cylindrical DOPC over the conical DOPE. The large hydrophobic volume of DOPC will increase Υ, but compensate via moderate increases to σ_L and σ_G. The influence of the zwitterionic DOPC appears to override that of the anionic lipids, which possess opposing curvatures, but can be explained by considering the greater effect of zwitterionic lipids on the activity of melittin due to the charge distribution. This hypothesis is given weight by the high degree of similarity between these systems, and the PIE-profile of pure DOPC membranes exposed to 1 µM melittin, which also displays a high level of 33.3 % of the bursting PIE. The two lowest membranes for bursting both contained DPPC as the most likely secondary interaction, which will result in a significant decrease in Υ, but also drops within σ_L and σ_G. Bursting within membranes exposed to melittin is controlled by associations with zwitterionic lipids possessing large hydrophobic volumes, in this case dioleoyl unsaturated 9Z chains, a fact supported by the DEPG results. Confirmation of the model validity comes from consideration of the average timings of the events, with DOPC:DOPE:DPPG taking over threefold longer to burst than the DOPC:DOPE:DOPG system. The presence of DPPG reduces the raft energy, and it therefore takes more membrane-bound peptides before the membrane reaches the critical failure point.

6.18.3. Pore-mediated leakage

The membrane systems with the lowest levels of pore formation were DOPC:DOPE:DOPG and DOPC:DOPE:DPPG, displaying 21.6 and 14.9 % respectively. Both systems are DOPE containing membranes, and the large negative curvature of the lipid will significantly increase the tension within the leaflet fold structure of the pore (Υ), disfavouring pore formation, and resulting in the membrane systems returning low pore activity. The large hydrophobic volumes of both DOPC and DOPE increase σ_L and σ_G, due to the deep insertion of the melittin helix into the bilayer. Although melittin can be expected to preferentially associate with DOPC in both these systems, lipid-melittin rafts associated with DOPE will occur within this system, giving rise to raft assemblies with high energies. In contrast, the

membranes displaying the highest level of pore-mediated leakage are linked by the lipid DPPC, with the DOPC:DPPC:DOPG and DOPC:DPPC:DPPG membranes featuring 54.7 and 52.1 % pore activity respectively. DPPC is a positive curvature lipid, which will reduce both σ_L and σ_G and the pore leaflet fold tension (ϒ), and overall favours pore formation. Again the reliance of melittin of secondary zwitterionic interactions to control pore formation can be explained by the charge distribution along its helix (refer to figure 6.10), with pore formation requiring the presence of positive topography lipids along the helical face, lowering the tension within the leaflet fold structure. The presence of the positively curved lipids DPPC and DPPG within the pore active membranes confirms prediction number 2 of the proposed model.

6.18.4. Carpet mechanism

The DOPC:DOPE:DOPG and DOPC:DPPC:DOPG membrane systems returned 41.3 and 31.4 % respectively for the carpet mechanism PIE, considerably higher than the DOPC:DOPE:DPPG and DOPC:DPPC:DPPG systems, which returned 7.0 and 8.5 % respectively. The carpet mechanism for melittin appears to be controlled by the presence of the ionic DOPG lipid within the lipid-melittin raft, and suppressed by the anionic DPPG. Membrane disruption via this mechanism requires the presence of large hydrophobic volume anionic lipids, in this case double oleoyl fatty acids, possessing a single 9Z unsaturation. Several papers link the disruption of membranes via the carpet mechanism to the intrinsic curvature of the target membrane (Bechinger and Lohner, 2006; Brogden, 2005). In the case of melittin, a membrane possessing high hydrophobic volume lipids, like DOPG and DOPC, is more likely to exhibit the carpet mechanism.

6.18.5. Micellisation

The micelle PIE is present at low levels (< 5 %) for all membrane systems tested, and is not strongly influenced by the lipid composition of the membrane. Note however, that the micelle PIE is completely absent from control membranes, and is therefore induced by lipid-melittin interactions.

6.19. Bacterial biomimetic membranes and magainin

The PIE-profiles for the bacterial biomimetic membrane systems, produced after interaction with 1 μM of the AMP magainin, are presented in figure 6.16.

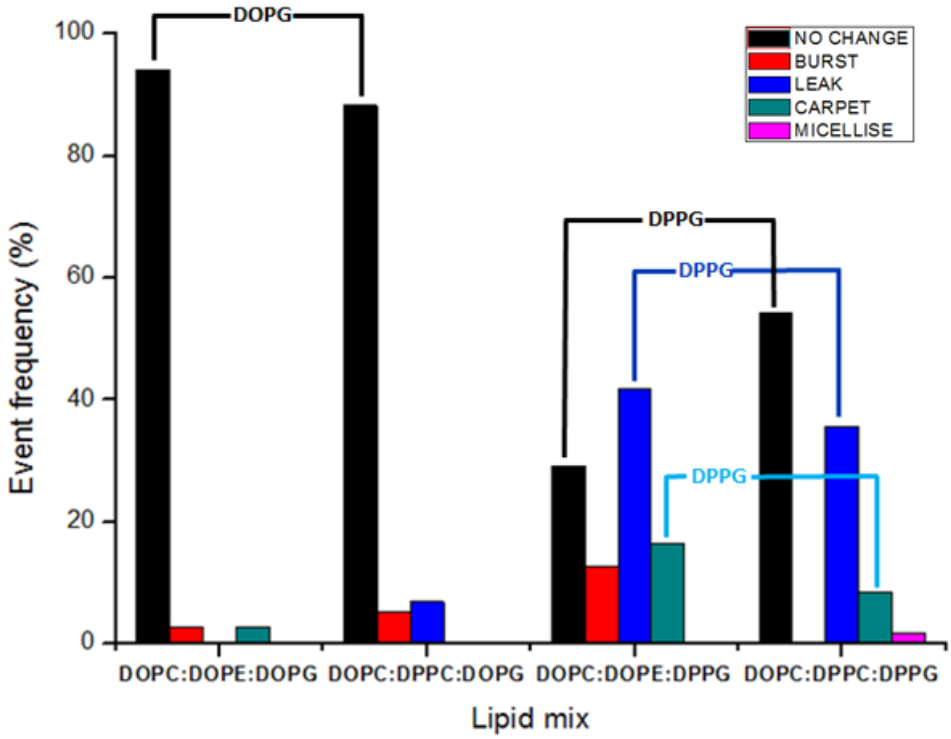

Figure 6.16: PIE-profiles for the bacterial biomimetic membrane systems, produced by exposure to 1 μM of the AMP magainin. The individual PIEs are colour coded according to the diagram key. The specific lipid interactions controlling the occurrence of each PIE, are indicated within the colour keyed lines connecting the bars on the graph. Within the active membrane systems, DPPC appears to control peptide activity.

6.19.1. Activity

Magainin is significantly less active than melittin in three of the four bacterial membranes, showing higher activity in only DOPC:DOPE:DPPG vesicles. The shallow insertion of magainin into the outer leaflet, causes a smaller increase in the area of the outer leaflet per monomer compared to melittin, and hence a smaller rise in σ_G. Magainin activity is controlled by DPPG, an anionic lipid, with a large PC headgroup and low hydrophobic volume in line with prediction 1 of the proposed model. Within DOPC:DOPE:DPPG and DOPC:DPPC:DPPG membrane systems, magainin displays activity of 70.1 and 45.8 % respectively. The lipid-magainin raft in both of the high activity systems will be enriched with DPPG, due to the distribution of cationic residues along the helical face of the peptide. The positive curvature of the peptide and lipid, combined with steric crowding in the bilayer interfacial region, caused by the three phenylanlanine residues of the peptide interacting with the large lipid headgroup, causes large increases to σ_L and σ_G but decreases Υ.

The DOPC:DOPE:DPPG system is more active, as the presence of DOPE within the bulk membrane increases its base energy prior to peptide binding, and the peptide needs to contribute a much lower level of σ_L and σ_G to cause a PIE. The systems displaying low activities, DOPC:DOPE:DOPG and DOPC:DPPC:DOPG, both contain the anionic lipid DOPG, and display activities of 5.9 and 11.8 %

respectively. The presence of the DOPG surrounds the magainin helix with lipids possessing large hydrophobic volumes, able to distort and reduce the packing frustration around the membrane-bound magainin helix. The reduction in raft free energy decreases both σ_L and σ_G, with the higher activity of the DOPC:DPPC:DOPG system caused by the presence of the positive curvature lipid DPPC. Although DPPC within lipid-magainin rafts will be disfavoured, it will exist in low population number rafts, which feature considerably higher σ_L than rafts surrounded by the preferred DOPG and DOPC lipids. This explains the increase in activity seen in the DOPC:DPPC:DOPG system compared to the DOPC:DOPE:DOPG system, which contains only lipids with large hydrophobic volumes and neutral to conical geometries. Interestingly, the DOPC:DOPE:DOPG membrane system shows lower activity than obtained from pure DOPC membranes in peptide-free conditions. This suggests that the addition of magainin to the membrane increases membrane mechanical properties, resulting in reduced membrane failure during the timecourse of the experiment. It is suggested that the association of membrane-bound magainin helices with the conical lipid DOPE both reduces the σ_L and σ_G induced by the peptide, but also removes DOPE from the bulk membrane, resulting in decreased tension. A similar phenomenon has been reported to occur for detergents, where low volumes of detergent was found to stabilise the membrane.[62]

6.19.2. Bursting

Of the two active membrane systems, only the DOPE:DOPE:DPPG displays any bursting behaviour, with 12.7 % of total activity resulting in bursting events. The lipid-magainin raft will be primarily enriched with DPPG, through forced electrostatic interactions, resulting in high σ_L and σ_G induction. The raft will also become enriched with DOPE through secondary lipid interactions, acting to reduce the σ_L and σ_G of the system. The DOPE present within the bulk membrane results in a higher starting membrane tension, narrowing the “energy gap” that magainin operates in; i.e. the energy difference between the starting membrane tension, and the critical failure energy of the membrane. The DOPC:DPPC:DPPG system has a lower starting membrane tension of the DOPE containing system, but lacks the σ_L and σ_G reducing effect of DOPE within the lipid-magainin raft, and demonstrates zero bursting activity. With the lower starting membrane tension, the system possesses a larger energy gap, giving more time for magainin to bind to the membrane, accumulate lipids and form active raft assemblies. It is clear that the presence of the non-bilayer DOPE rather than DPPC in the bulk membrane induces bursting, indicating that it is easier for raft assemblies to achieve the critical failure energy in DOPC:DOPE:DPPG membranes, without activating other PIEs.

6.19.3. Pore-mediate leakage

The two active lipid-magainin systems DOPC:DOPE:DPPG and DOPC:DPPC:DPPG produced high levels of pore-mediated leaking, with 53.9 and 74.1 % of the total PIEs produced being pore-mediated leakage events respectively. The controlling factor is the forced electrostatic enrichment with the positive curvature lipid DPPG, resulting in a lower ϒ which favours pore formation, with the DOPC:DPPC:DPPG system displays the highest level of PIEs as pore-mediated leakage events for any lipid-AMP system tested. The lack of DOPE in this system lowers the initial membrane tension reducing the overall activity compared to the DOPE containing membrane, but the presence of the positive curvature DPPC lipid enables more efficient packing within the leaflet fold structure. Combined with the higher energy raft assemblies formed through steric interactions between DPPC and the F residues of magainin, this leads to the high level of pore-formation. The DOPE containing system returns the fastest average time to leakage initiation of any membrane-peptide system tested, resulting in a fascinating situation, where one of the two active systems returns the highest levels of pore-mediates leakage and the other returns the fastest initiation of leaks.

This can be explained by consideration of the effect of the lipid composition on the terms contained within equation 6. The DPPC containing membrane has a high proportion (40 mol%) of inverse-conical geometry, positively curvature inducing lipids, which together with the curvature stabilisation of the three F residues of magainin, results in a very low leaflet fold energy, and greatly reduces the pore energy. The DOPE containing membrane has higher ϒ, resulting in lower pore formation, but a higher initial membrane tension due to the presence of the non-bilayer lipid DOPE. This results in faster initiation of pore-mediated leakage events, indicating that the membrane strain induced by non-bilayer lipids can play an important part in pore formation by magainin. Non-bilayer lipids that reside near a pre-pore region may contribute their strain energy towards pore formation, playing a role in the peptide selectivity mechanism, as eukaryotic membranes lack non-bilayer components. Within the active magainin membranes the LCAMP melittin displays 54.7 and 52.1 % pore-mediated leakage activity, with magainin producing higher levels of pore activity despite being less active overall, thus confirming prediction number two of the new model.

6.19.4. Carpet mechanism

The two active systems produce similar amounts of carpet mechanism events, demonstrating 23.1 and 18.5 % of total PIEs respectively. It is likely then that the carpet mechanism is controlled via the association of the positive curvature magainin with the positive curvature lipid DPPG, with its large headgroup and low volume acyl chains. Magainin demonstrates the opposite curvature preference from the negative curvature melittin, indicating that carpet mechanism is induced via the aggregation of

excess curvature strain within the membrane. This fits with the generation of micelles, which are high curvature structures.

6.19.5. Micellisation

Magainin demonstrates no significant levels of micellisation within any membrane system, with only the DOPC:DPPC:DPPG system displaying any micelle activity.

6.20. Mammalian biomimetic membranes and LCAMPs

Similar dissection of the likely Υ, σ_L and σ_G values of magainin and melittin within the mGUV membranes, allows assessment of the influence of lipid topography on peptide selectivity, for bacterial versus mammalian membranes. The PIE-profiles produced by the mGUV membrane system after exposure to the peptides, at concentrations of 1 and 5 µM, are presented in figure 6.17.

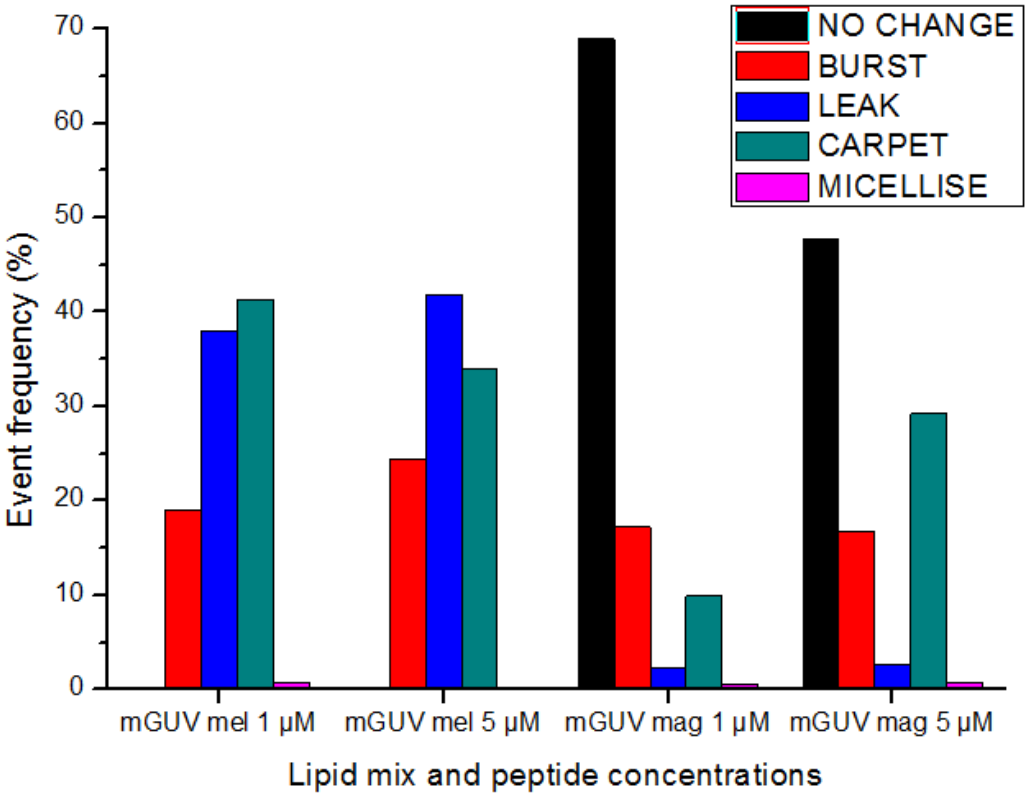

Figure 6.17: PIE-profiles for the mammalian biomimetic membrane systems, produced by exposure to the LCAMPs magainin (mag) and melittin (mel), at concentrations of 1 and 5 µM. The individual PIEs are colour coded according to the diagram key. The selective magainin is significantly less active in mGUV systems compared to melittin, and both peptides produce consistent profiles across the two different peptide concentrations.

6.20.1. Melittin and mGUV membranes

Melittin inserts its helix deeper into the membrane than magainin, resulting in greater increases in σ_L and σ_G per membrane-bound monomer, and therefore greater activity. The high levels of both pore-mediated and carpet mechanism within the PIE-profiles indicate that the lipid-melittin raft can both contain positive curvature lipids, capable of supporting the curvature of the leaflet fold, and negative curvature lipids to generate the carpet mechanism. The mGUV membrane is comprised of DOPC:DPPC:cholesterol (35:35:30 mol%), all zwitterionic lipids, and the membrane-bound melittin helices are free to locate to a local energy minima, without forced electrostatic interactions. Melittin helices can be expected to preferentially associate with the lipid DPPC, due to its lower hydrophobic volume compared to DOPC. This association lowers the σ_L and σ_G energies, but decreases Υ, as the positively curved DPPC associated with the peptide helix has been shown to initiate pore formation. Melittins PIE-profile displays a high level of pore formation at both the 1 and 5 μM concentrations of melittin, producing 38.0 and 41.8 % of PIEs as pore-mediated leakage events respectively.

The lipid-melittin raft may also be enriched with cholesterol, through π-electron interactions between melittins tryptophan residue and cholesterol. This will bring a strongly negatively curved membrane component into contact with the negative curvature inducing melittin, increasing σ_L and σ_G values. Melittin only contains one W residue compared to the three F residues of magainin, and thus the increase in Υ should be much greater for the selective magainin, and PIE activity more strongly disfavoured. Although interactions with DOPC will be disfavoured within lipid-melittin rafts, the potential for large σ_L energies exist, as 9Z mono-unsaturated acyl chains have been shown to induce PIEs, as previously discussed. As the exact PIE produced likely depends in a stochastic manner on the presence of specific raft assemblies within the membrane, it is possible to suggest potential lipid-melittin interactions which could result in the production of high levels of both pore-mediated leakage and carpet mechanism events. Lipid-melittin rafts enriched with DPPC will be lower energy, and thus more common, than those enriched with DOPC and cholesterol. The lower σ_L energy means that, although pore formation will be favoured by the lipid content of the raft, it will require more melittin monomers within a raft assembly to accumulate enough local energy to generate a pore event. The DOPC:cholesterol enriched raft is less common within the raft population, but the significantly higher σ_L will result in fewer monomers being required to initiate a PIE. It is likely that cholesterol present in the bulk membrane aggregates with membrane-bound LCAMPs, as it has been shown that cholesterol in non-raft containing systems affects peptide activity, but has no effect when the cholesterol is sequestered within l_O lipid rafts.[92]

6.20.2. Magainin and mGUV membranes

The expected lipid interactions for magainin interacting within mGUV membranes are very different to those expected for melittin. Magainin helices can be expected to form dynamic lipid-AMP rafts enriched with DOPC, whose high volume hydrophobic tails can counter the positive curvature induction of the shallowly-inserted peptide. This lowers σ_L and σ_G energies but increases Υ, resulting in low peptide activity with strongly disfavoured pore-formation. The presence of three F residues enriches the raft with the negative curvature cholesterol lipid, again lowering the σ_L and σ_G energies but increasing Υ. In contrast to melittin, whose preferential lipid aggregations favour pore formation, the formation of magainin-induced pores within mGUV membranes is strongly disfavoured due to lack of association with positive curvature lipids. Within anionic bacterial systems, the presence of positive curvature lipids can be forced through electrostatic interactions, causing high magainin activity in systems containing the positively curved anionic lipid DPPG.

6.21. Application to *in-vivo* membranes

Bacterial strains have membrane lipid compositions that are somewhat characteristic for the individual strains, for example *E.coli* typical displays a membrane composition of 80 and 20 % of the lipids PE and PG respectively.[53] However the membrane compositions of different strains can vary widely, with the complete set of *in*-vivo bacterial membranes encompassing a large heterogeneous population of lipids, with variations in lipid topography, fatty acid unsaturation and headgroups, unlike the tightly controlled composition of artificial biomimetic membrane systems.[13] The possible set of lipid interactions surrounding a membrane-bound LCAMP helix is therefore much broader, and the complex influence of lipid topography on LCAMP activity would be hard to decipher *in-vivo*, making the utilisation of artificial biomimetic membrane platforms necessary. The *in-vivo* bacterial plasma membrane is extremely fluid in composition, responding to changes in the environment like temperature and available fatty acids.[52][53][54] The membrane responds to changes in environment through changes in the headgroup composition and fatty acid length and unsaturation of the membrane, although the average packing parameter is maintained within a narrow range,[54] close to the lamellar to non-lamellar phase transition boundary.

Such energetically taxing manipulation of membrane composition, in order to maintain the membrane close to the phase boundary, indicates that membrane packing plays an important biological role in cell function.[55] It can also explain why bacteria struggle to acquire resistance to LCAMPs, which exploit the close positioning of bacterial membranes to the lamellar to non-lamellar phase boundary to easily induce pore formation, compared to mammalian membranes which generally operate further from the boundary. The variation in lipid topography between different bacterial strains, combined with

the activity of LCAMPs reported in this thesis, suggests that the peptides will possess significantly different MICs within differing strains, and this is indeed the case.[62][68][148] This opens up the possibility of tailored antimicrobial peptides for individual bacterial strains, where the amino acid sequence of the peptide can be tailored to adjust the membrane penetration and lipid-peptide interactions, in order to achieve the highest σ_G and σ_L and lowest Υ possible within that strains membrane. It is likely that the selective LCAMPs like magainin represent compromise sequences, evolutionarily designed to exert broadband antimicrobial activity without being optimised for individual bacterial strains, leaving room for guided improvement.

6.22. Application to the literature

The model proposed in this work can be used to answer several contentious points within the literature, including the proposed intracellular targets reported for some LCAMPs and the biphasic nature of the leakage induced by the peptides. The differences between the graded and all-or-none responses contained within the literature can also be explained by the application of the new model.

6.22.1. Intracellular target mechanism

Several intracellular targets for LCAMPs have been reported, but can be explained by consideration of the effects of LCAMP binding on the target membrane, which induce changes to the membranes mechanical properties and lipid packing. Coupled to the bacterial cells membrane homeostatic responses, which attempt to maintain its preferred membrane packing state, these changes can initiate "false-flag" cellular responses, designed to combat similar changes occurring during normal cellular processes. For example, treatment of bacteria with the LCAMP melittin activates both phospholipases and autolysins.[63] Phospholipases cleave acyl chains from lipids, resulting in a dramatic change in the topography of the target lipid, and reducing its packing parameter and hydrophobic volume. Deep penetrating peptide helices like melittin which occupy significant hydrophobic volume and increases the lateral pressure in the membrane core, could easily induce phospholipase activation as part of a bacterial homeostasis response. Autolysins are enzymes which break down peptidoglycan in bacteria, in order for cellular growth or division to occur, processes that are accompanied by changes in the membranes mechanical properties.[149] Again the increase in lateral pressure and membrane thinning that occur during LCAMP binding could lead to accidental activation of a normal cellular process, in this case activation of the autolysin pathway. Disruption of membrane domains by binding LCAMPs and the modulation of membrane lateral pressure that follows, could also lead to the appearance of pseudo–intracellular targets by activating/deactivating membrane proteins, leading to downstream effects.

6.22.2. Biphasic leakage

The biphasic leakage reported for LCAMP-induced leakage, with both slow and fast components,[58][77] can be explained via two potential mechanisms. The two leakage rates could be the result of different leakage modes of the pore-mediated leakage induced by the peptides, or more likely, due to the carpet mechanism producing the fast phase and the pore-mediated leakage events producing the slow phase of the leakage. This scenario is considered more likely due to the work of Degrado and colleagues, which linked the fast phase of the leakage from human erythrocytes, to a rapid decrease in cell numbers.[77] This associates the fast leakage phase with the carpet mechanism, which invariably ends with the destruction of the vesicle within the *in-vivo* experiments contained within this thesis.

6.22.3. Graded versus all-or-none leakage

A conflicting picture of the pore-mediated leakage mechanism induced by LCMAPs from lipid vesicles emerges, with reports of graded[95] all-or-none leakage[96][97] behaviour, even from papers produced by the same laboratories under different experimental conditions.[98][99] The difference between graded leakage, where the entire population of vesicles display steady dye efflux, and all-or-none leakage, where the population will be split into those vesicles which have completely lost their contents and those which retain membrane integrity, can be explained by taking into consideration the new model and the microfluidic based experimental protocols. Within conventional dye-leakage experiments, an amount of peptide is introduced into a sample containing SUV or LUV vesicles, to achieve the desired bulk LCAMP concentration and leakage measured as the averaged leakage from a large vesicle population. Uncertainties in both the exact amount of lamellar lipids within the sample, and the amount of peptide bound to each vesicle, introduce sample treatment issues into the experimental analysis. Coupled to the large variation in initiation times for pore-mediated leakage, this could easily result in the interpretation of experimental data as an all-or-none mechanism, when in fact the different leakage kinetics result from the heterogeneous population of lipid-LCAMP systems present. With the added complicating factor of differing leakage kinetics induced by the same peptide within identical membrane systems, it is easy to imagine how a confusing picture of the leakage behaviour of AMPs has emerged. The work of Wheaten and colleagues, which seeks to determine the answer to the graded and all-or-none question, seems to confirm this assessment.[150] Using acute exposure of GUVs to AMPs, they find both the large variation in initiation times for leaks (> 10 min) and significant differences in the kinetics for both the graded and all-or-none leakage mechanisms. The tighter control exerted over peptide exposure within the microfluidic device reduces uncertainty in the experimental conditions, and coupled to the high-throughput nature of the data collection, allows increased confidence in the results compared to traditional dye-leakage experiments.

7. References

[1] Cohen ML. *Changing patterns of infectious disease.* Nature (2000) **406**, pages 762 – 767.

[2] CDC Threat report: Antibiotic resistance threats in the United States, 2013.

[3] Davies J and Davies D. *Origins and evolution of antibiotic resistance.* Microbiology and Molecular Biology Reviews, (2010), **74**, (3), pages 417 – 433.

[4] Davies J. *Bacteria on the rampage,* Nature, (1996), **383**, pages 219 – 220.

[5] Walsh C. *Molecular mechanisms that confer antibacterial drug resistance.* Nature (2000) **406**, pages 775 – 781.

[6] Andersson DI and Hughes D. *Antibiotic resistance and its cost: is it possible to reverse resistance?* Nature Reviews: Microbiology (2010) **8**, pages 260 – 271.

[7] Blower S, Koelle and Lietman T. *Antibiotic resistance – to treat…or not to treat.* Nature Medicine (1999) **5**, (4), page 358.

[8] Palumbi SR. *Humans as the worlds greatest evolutionary force.* Science (2001) **293**, pages 1786 – 1790.

[9] Aalipour F, Mirlohi M and Jalali M. *Determination of antibiotic consumption index for animal originated foods produced in animal husbandry in Iran, 2010.* Journal of Enivironmental Health, Science and Engineering (2014) **12**, pages 42 – 49.

[10] Khachatryan AR, Hancock DD, Besser T and Cal DR. *Role of calf-adapted Escherichia coli in maintenance of antimicrobial drug resistance in dairy calves.* Applied and Environmental Microbiology (2004) **70**, (2), pages 752 – 757.

[11] Bugg TDH, Braddick D, Dowson CG and Roper DI. *Bacterial cell wall assembly: still an attractive antibacterial target.* Trends in Biotechniology (2011) **29**, (4), pages 167 – 173.

[12] Mingeot-LeClercq MP, Glupczynski Y and Tulkens PM. *Aminoglycosides: activity and resistance.* Antimicrobial Agents and Chemotherapy (1999) **99**, pages 727 – 737.

[13] Silhavy TJ, Kahne D and Walker S. *The bacterial cell envelope.* Cold Spring Harbour Perspective on Biology (2010).

[14] Black, Jacquelyn (2012). *Microbiology: Principles and exploration 8th edition*. John Wiley & Sons. p. 68. ISBN 978-0-470-54109-8.

[15] Kohanski MA, Dwyer DJ, Collins JJ. *How antibiotics kill bacteria: from targets to networks.* National Reviews in Microbiology (2010) **8**, (6), pages 423 – 435.

[16] Williams DH. *The glycopeptide story – how to kill the deadly "superbugs".* Natural Product Reports (1996) **13**, pages 469 – 477.

[17] Roberts MC. *Tetracycline resistance determinants: mechanisms of action, regulation of expression, genetic mobility and distribution.* FEMS Microbiology Reviews, (1996), **19**, pages 1 – 24.

[18] Peschel A and Sahl HG. *The co-evolution of host cationic antimicrobial peptides and microbial resistance.* Nature Reviews: Microbiology (2006) **4**, pages 529 – 536.

[19] Bush J and Jacoby GA. *Updated functional classification of ß-lactamases.* Antimicrobial Agents and Chemotherapy (2010) **54**, pages 969 – 976.

[20] Tripathi R and Nair NN. *Mechanism of acyl enzyme complex formation from the Henry Michaelis complex of class C ß-lactamases with ß-lactam antibiotics.* American Chemical Society (2013) **135**, pages 14679 – 14690.

[21] Kumarasamy KK, Toleman MA, Walsh TR, Bagaria J, Butt F, Balakrishnan R, Chaudhary U, Doumith M, Giske CG, Irfan S, Krishnan P, Kumar AV, Maharjan S, Mushtaq S, Noorie T, Paterson DL, Pearson A, Perry C, Pike R, Rao B, Ray U, Sarma JB, Sharma M, Sheridan E, Thirunarayan MA, Turton J, Upadhay S, Warner M, Welfare W, Livermore DM and Woodford N. *Emergence of a new antibiotic resistance mechanism in India, Pakistan and the UK: a molecular biological and epidemiological study.* The Lancet Infectious Diseases (2010) **10**, (9), pages 597 – 602.

[22] Piddock LJV. *Mulitdrug-resistance efflux pumps – not just for resistance.* (2006) Nature Revies: Microbiology (2006) **4**, pages 629 – 636.

[23] Stavri M, Piddock LJV and Gibbons S. *Bacterial efflux pump inhibitors from natural sources.* Journal of Antimicrobial Chemotherapy (2007) **59**, pages 1247 – 1260.

[24] Piton J, Petrella S, Delarue M, Leroux GA, Jarlier V, Aubry A and Mayer C. *Structural insights into the quinolone resistance mechanism of Mycobacterium tuberculosis DNA gyrase.* PLoS ONE (2010) **5**, (8), pages 1 – 14.

[25] Heddle J and Maxwell A. *Quinolone-binding pocket of DNA gyrase: role of GyrB.* Antimicrobial Agents and Chemotherapy (2002) **46**, (6), pages 1805 – 1815.

[26] Furuya EY and Lowy FD. *Antimicrobial-resistant bacteria in the community setting.* Nature Reviews: Microbiology (2006) **4**, pages 36 – 45.

[27] Barlow M. *What antimicrobial resistance has taught us about horizontal gene transfer.* Methods in Molecular Biology, (2009), **532**, pages 397 – 411.

[28] Velayati AA, Masjedi MR, Farnia P, Tabarsi P, Ghanavi J, ZiaZarifi AH and Hoffner SE. *Emergence of new forms of totally drug-resistant tuberculosis bacilli: super extensively drug-resistant tuberculosis or totally drug-resistant strains in Iran.* Chest (2009) **136**, pages 420 – 425.

[29] Centres for Disease Control and Prvention. National nosocomial infections surveillance (NNIS) report, data summary from January 1990 – May 1999, issued June 1999. American Journal of Infection Control (1999) **27**, pages 520 – 532.

[30] van Meer G, Voelker DR and Feigenson GW. *Membrane lipids: where they are and how they behave.* Nature Reviews: Molecular Cell Biology (2008) **9**, (2), pages 112 – 124.

[31] Anderson OS and Koeppe RE. *Bilayer thickness and membrane protein function: an energetic perspective.* Annual Review of Biophysics and Biomolecular Structure (2007) **36**, pages 107 – 130.

[32] Brown DA and London E. *Functions of lipid rafts in biological membranes.* Annual Reviews in Cell Developmental Biology (1998) **14**, pages 111 – 136.

[33] Sprong H, van der Sluijs P and van Meer G. *How proteins move lipids and lipids move proteins.* Nature Reviews: Molecular Cell Biology (2001) **2**, pages 604 – 613.

[34] Simons K and Toomre D. *Lipid rafts and signal transduction.* Nature Reviews: Molecular Cell Biology (2000) **1**, pages 31 – 41.

[35] Rohrbough J and Broadie K. *Lipid regulation of the synaptic vesicle cycle.* Nature Reviews: Neuroscience (2005) **6**, pages 139 – 160.

[36] Binder H. *The molecular architecture of lipid membranes – new insights from hydration-tuning infrared linear dichroism spectroscopy.* Applied Spectroscopy Reviews (2003) **38**, (1), pages 15 – 69.

[37] Israelachvili J, Mitchel J and Ninham B. *Theory of self-assembly of hydrocarbon amphiphiles into micelles and bilayers.* Journal of the Chemical Society, Farady Transactions 2: Molecular and Chemical Physics (1976).

[38] Deuling HJ and Helfrich W. *The curvature elasticity of fluid membranes: a catalogue of vesicle shapes.* Journal Physique (1976) **37**, pages 1335 – 1345.

[39] Letter to the editor. *On the analysis of elastic deformations in hexagonal phases.* Biophysical Journal (2004) **86**, pages 3324 – 3328.

[40] Kumar VV. *Complementary molecular shapes and addivity of the packing parameter of lipids.* Proceeds of the National Academy of Science USA (1991) **88**, pages 444 – 448.

[41] Chernomordik L. *Non-bilayer lipids and biological fusion intermediates.* Chemistry and Physics of Lipids (1996) **81**, (2), pages 203 – 213.

[42] Burger KNJ. *Greasing membrane fusion and fission machineries.* Traffic (2000) **1**, pages 605 – 613.

[43] Chernomordik LV and Koslov MM. *Protein-lipid interplay in fusion and fission of biological membranes.* Annual Reviews in Biochemistry (2003) **72**, pages 175 – 207.

[44] Rietveld AG, Koorengevel MC and de Kruijff B. *Non-bilayer lipids are required for efficient protein transport across the plasma membrane of Escherichia coli.* EMBO Journal (1995) **14**, (22), pages 5506 – 5513.

[45] Veach RA, Liu D, Yao S, Chen Y, Liu XY, Downs S and Hawiger J. *Receptor/transporter independent targeting of functional peptides across the plasma membrane.* The Journal of Biological Chemistry (2004) **279**, pages 11425 – 11431.

[46] Almeida PFF, Pokorny A and Hinderliter A. *Thermodynamics of membrane domains.* Biochimica et Biophysica Acta 1720 (2005) pages 1 – 13.

[47] Nagle JF and Tristram S. *Structure of lipid bilayers.* Biochimica et Biophysica Acta (2000) **1469**, (3), pages 159 – 195.

[48] Epand RM. *Cholesterol and the interaction of proteins with membrane domains.* Progress in Lipid Research (2006) **45**, pages 279 – 294.

[49] Leventis PA and Grinstein S. *The distribution and function of Phosphatidylserine in cellular membranes.* Annual Reviews in Biophysics (2010) **39**, pages 407 – 427.

[50] Devaux PF and Morris R. *Transmembrane asymmetry and lateral domains in biological membranes.* Trafiic (2004) **5**, pages 241 – 246.

[51] Kollmitzer B, Heftberger P, Rappolt M and Pabst G. *Monolayer spontaneous curvature of raft-forming membrane lipids.* Soft Matter (2013) **9**, pages 10877 – 10884.

[52] van de Vossenberg JLCM, Driessen AJM, da Costa MS and Konigs WN. *Homeostasis of the membrane protein permeability in Bacillus subtilis grown at different temperatures.* Biochimica et Biophysica Acta 1419 (1999) pages 97 – 104.

[53] Morein S, Andersson AS, Rilfors L and Lindblom G. *Wild-type Escherichia coli cells regulate the membrane lipid composition in a window between gel and non-lamellar structures.* The Journal of Biological Chemistry (1996) **271**, pages 6801 – 6809.

[54] Osterberg F, Rilfors L, Wieslander A, Lindblom G and Gruner SM. *Lipid extracts from membranes of Acholeplasma laidlawii A grown with different fatty acids have a nearly constant spontaneous curvature.* Biochimica et Biophysica Acta, (1995), **1257**, pages 18 – 24.

[54] Siegel DP and Epand RM. *The mechanism of lamellar-to-inverted hexagonal phase transitions in phosphatidyethanolamine: implications for membrane fusion mechanisms.* Biophysical Journal (1997) **73**, pages 3089 – 3111.

[55] Gruner SM, *Stability of lyotropic phases with curved interfaces.* The Journal of Physical Chemistry (1989) **93**, (22), pages 7562 – 7570.

[56] Ge Y, MacDonald DL, Holroyd KJ, Thornsberry C, Wexler H and Zasloff M. *In-vitro antibacterial properties of pexiganan, an analogue of magainin.* Antimicrobial Agents and Chemotherapy (1999) pages 782 – 788.

[57] Shai Y. *Mechanism of the binding, insertion and destabilization of phospholipid bilayer membranes by K-helical antimicrobial and cell non-selective membrane-lytic peptides.* Biochimica et Biophysica Acta 1462 (1999) pages 55 – 70.

[58] Raghuraman H and Chattopadhyay A. *Melittin: a membrane-active peptide with diverse functions.* Bioscience Reports (2007) **27**, pages 189 – 223.

[59] Matsuzaki K, Sugishita K, Harada M, Fujii N and Miyajima K. *Interactions of an antimicrobial peptide, magainin 2, with outer and inner membranes of gram-negative bacteria.* Biochimica et Biophysica Acta 1327 (1997) pages 119 – 130.

[60] Matsuzaki K, Sugishita K, Ishibe N, Ueha M, Nakata S, Miyajima K and Epand RM. *Relationship of membrane curvature to the formation of pores by magainin 2.* Biochemistry (1998) **37**, pages 11856 – 11863.

[61] Seil M, Nagant C, Dehave JP, Vandenbranden M and Lensink MF. *Spotlight on human LL-37, an immunomodulatory peptide with promising cell-penetrating properties.* Pharmaceuticals (2010) **3**, pages 3435 – 3460.

[62] Bechinger B and Lohner K. *Detergent-like actions of linear amphipathic cationic antimicrobial peptides.* Biochimica et Biophysica Acta 1758 (2006) pages 1529 – 1539.

[63] Brogden KA. *Antimicrobial peptides: pore formers or metabolic inhibitors in bacteria?* Nature Reviews: Microbiology (2005) **3**, pages 238 – 250.

[64] Zasloff M. *Antimicrobial peptides of multicellular organisms.* Nature (2002) **41**, pages 389 – 395.

[65] Dathe M and Wieprecht T. *Structural features of helical antimicrobial peptides: their potential to modulate activity on model membranes and biological cells.* Biochimica et Biophysica Acta 1462 (1999) pages 71 – 87.

[66] Andes D and Craig WA. *In-vivo activities of amoxicillin and amoxicillin-clavulanate against Streptococcus pneumonia: application to breakpoint determination.* Antimcrobial Agents and Chemotherapy (1998) pages 2375 – 2379.

[67] Zhane GG, DeCorby M, Noreddin A, Mendoza C, Cumming A, Nichol K, Wierzbowski A and Hoban DJ. *Pharmacodynamic activity of azithromycin against macrolide-susceptible and –resistant Streptococcus pneumonia, simulating clinically achievable free serum, epithelial lining fluid and middle ear fluid concentrations.* Journal of Antimicrobial Chemotherapy (2003) **52**, pages 83 – 88.

[68] Gad SC (editior). Development of therapeutic agents handbook (2012) ISBN: 978-0-471-21385-7.

[69] Ladokhin AS, Selsted ME and White SH. *Sizing membrane pores in lipid vesicles by leakage of coencapsulated markers.* Biophysical Journal (1997) **72**, pages 1762 – 1766.

[70] Ladokhin AS and White SH. *Folding of amphipathic alpha helices on membranes: energetics of helix formation by melittin.* Journal of Molecular Biology (1999) **285**, pages 1363 – 1369.

[71] Wimley WC and Hristova K. *Antimicrobial peptides: successes, challenges and unanswered questions.* Journal of Membrane Biology (2011) **239**, (1-2), pages 27 – 34.

[72] Mecke A, Lee DK, Ramamoorthy A, Orr BG and Banaszak MM. *Membrane thinning due to antimicrobial peptide binding: an atomic force microscopy study of MSI-78 in lipid bilayers.* Biophysical Journal (2005) **89**, pages 4043 – 4050.

[73] Yang L, Harroun TA, Weiss TM, Ding L and Huang HW. *Barrel-stave model or toroidal model? A case study on melittin pores.* Biophysical Journal (2001) **81**, pages 1475 – 1485.

[74] Schumann M, Dathe M, Wieprecht T, Beyermann M and Bienart M. *The tendency of magainin to associate upon binding to phospholipid bilayers.* Biochemistry (1997) **36**, pages 4345 – 4351.

[75] Matsuzaki K, Murase O, Fujii N and Miyajima K. *An antimicrobial peptide, magainin 2, induced rapid flip-flop of phospholipids coupled with pore formation and peptide translocation.* Biochemistry (1996) **35**, pages 11361 – 11368.

[76] Matsuzaki K, Yoneyama S and Miyajima K. *Pore formation and translocation of melittin.* Biophysical Journal (1997) **73**, pages 831 – 838.

[77] Degrado WF, Musso GF, Lieber M, Kaiser ET and Kizdy FJ. *Kinetics and mechanism of hemolysis induced by melittin and by a synthetic melittin analogue.* Biophysical Journal (1982) **37**, pages 329 – 338.

[78] Qian S, Wang W, Yang L and Huang HW. *Structure of transmembrane pore induced by Bax-derived peptide: evidence for lipidic pores.* PNAS (2008) **105**, pages 17379 – 17383.

[79] Cruciani RA, Barker JL, Durell SR, Raghunathan G, Guy HR, Zasloff M and Stanley EF. *Magainin 2, a natural antibiotic from frog skin, forms ion channels in lipid bilayer membranes.* European Journal of Pharmacology (1992) **226**, pages 287 – 296.

[80] Sengupta D, Leontiadou H, Mark E and Marrink SJ. *Toroidal pores formed by antimicrobial peptides show significant disorder.* Biochimica et Biophysica Acta 1778 (2008) pages 2308 – 2317.

[81] Kragh-Hansen U, le Maire M and Moller JV. *The mechanism of detergent solubilisation of liposomes and protein-containing membranes.* Biophysical Journal (1998) **75**, pages 2932 – 2946.

[82] Kang JH, Shin SY, Jang SY, Lee MK and Hahm KS. *Release of aqueous contents from phospholipid vesicles induced by cecropin A (1-8), magainin 2 (1-12) hybrid and its analogues.* Journal of Peptide Research (1998) **52**, pages 45 – 50.

[83] Sieprawska-Lupa M. *Degradation of human antimicrobial peptide LL-37 by Staphylococcus aureus-derived proteinases.* Antimicrobial Agents and Chemotherapy (2004) **48**, pages 4673 – 4679.

[84] Koller D and Lohner K. *The role of spontaneous lipid curvature in the interaction of interfacially active peptides with membranes.* Biochimica et Biophysica Acta (BBA) (2014) **1838**, (9), pages 2250 – 2259.

[85] Blondelle SE, Simpkins LR, Perez-Paya E and Houghten RA. *Influence of tryptophan residues on melittins haemolytic activity.* Biochimica et Biophysica Acta (1993) **1202,** pages 331 – 336.

[86] Yau WM, Wimley WC and Gawrisch K. *The preference of tryptophan for membrane interfaces.* Biochemistry (1998) **37**, pages 14713 – 14718.

[87] Dempsey CE. *The actions of melittin on membranes.* Biochimica et Biophysica Acta 1031 (1990) **143**, pages 143 – 161.

[88] Jacobs RE and White SH. *The nature of the hydrophobic binding of small peptides at the bilayer interface: implications for the insertion of transbilayer helices.* Biochemistry (1989) **28**, pages 3421 – 3437.

[89] Blondelle SE and Houghton RA. *Hemolytic and antimicrobial activities of the twenty-four individual omission analogues of melittin.* Biochemistry (1991) **30**, pages 4671 – 4678.

[90] Takei J, Remenyi A and Dempsey CE. *Generalised bilayer perturbation from peptide helix dimerization at membrane surfaces: vesicle lysis induced by disulphide-dimerised melittin analogues.* FEBS Letters (1999) **442**, (1), pages 11 – 14.

[91] Matsuzaki K, Sugishita K, Fujii N and Miyajima K. *Molecular basis for membrane selectivity of an antimicrobial peptide, magainin 2.* Biochemistry (1995) **34**, pages 3423 – 3429.

[92] McHenry AJ, Sciacca MFM, Brender JR and Ramamoorthy A. *Does cholesterol suppress the antimicrobial peptide induced disruption of lipid raft containing membranes?* Biochimica et Biophysica Acta (2012) **1818**, (12), pages 3019 – 3024.

[93] Katsu TC, Ninomiya M, Kuroko H, Kobayashi H, Hirota T and Fujita Y. *Action mechanism of amphipathic peptides gramicidin S and melittin on erythrocyte membrane.* Biochimica et Biophysica Acta (1988) **939**, pages 57 – 63.

[94] Benachir T and Lafleur M. *Osmotic and pH transmembrane gradients control the lytic power of melittin.* Biophysical Journal (1996) **70**, pages 831 – 840.

[95] Matsuzaki K, Murase O and Miyajima K. *Kinetics of pore formation by an antimicrobial peptide, magainin 2, in phospholipid bilayers.* Biochemistry (1995) **34**, pages 12553 – 12559.

[96] Grant E, Beeler TJ, Taylor KMP, Gable K and Roseman MA. *Mechanism of magainin 2a induced permeabilization of phospholipid vesicles.* Biochemistry (1992) **31**, pages 9912 – 9918.

[97] Gregory SM, Pokorny A and Almeida PFF. *Magainin 2 revisited: a test of the quantitative model for the all-or-none permeabilization of phospholipid vesicles.* Biophysical Journal (2009) **96**, pages 116 – 131.

[98] Schwarz G, Zong R and Popescu T. *Kinetics of melittin induced pore formation in the membrane of lipid vesicles.* Biochimica et Biophysica Acta (BBA) (1992) **1110**, (1), pages 97 – 104.

[99] Rex S and Schwarz G. *Quantitative studies on the melittin-induced leakage mechanism of lipid vesicles.* Biochemistry (1998) **37**, pages 2336 – 2345.

[100] Garcia-Saez AJ, Chiantia S, Salgado J and Schwille P. *Pore formation by a Bax-derived peptide: effect on the line tension of the membrane probed by AFM.* Biophysical Journal (2007) **93**, pages 103 – 112.

[101] Last NB and Miranker AD. *Common mechanism unites membrane poration by amyloid and antimicrobial peptides.* PNAS USA (2013) **110**, (16), pages 6382 – 6382.

[102] Barnham KJ, Monks SA, Hinds MG, Azad AA and Norton RS. *Solution structure of a polypeptide from the N terminus of the HIV protein Nef.* Biochemistry (1997) **36**, pages 5970 – 5980.

[103] Dunton TA, Goose JE, Gavaghan DJ, Sansom MSP and Osborne JM. *The free energy landscape of dimerization of a membrane protein, NanC.* PloS ONE (2014) **10**, (1), e1003417.

[104] Jacobson K, Mouritsen OG and Anderson RG. *Lipid rafts: at a crossroad between cell biology and physics.* Nature Cell Biology (2007) **9**, (1), pages 7 – 14.

[105] Brown DA. *Lipid rafts, detergent-resistant membranes and raft targeting signals.* Physiology (2006) **21**, pages 430 – 439.

[106] Boesze-Battaglia K and Schimmel RJ. *Cell membrane lipid composition and distribution: implications for cell function and lessons learned from photoreceptors and platelets.* The Journal of Experimental Biology (1997) **200**, pages 2927 – 2936.

[107] Lee AG. *How lipids affect the activities of integral membrane proteins.*Biochimica et Biophysica Acta (2004) **1666**, pages 62 – 87.

[108] Lazaridis T. *Effective energy function for proteins in lipid membranes.* PROTEINS: Structure, function and genetics (2003) **52**, pages 176 – 192.

[109] Dibble AR and Feigenson GW. *Detection of coexisting fluid phospholipid phases by equilibrium Ca^{2+} binding: peptide-poor L_α and peptide-rich HII phase coexsitance in gramicidin A/phospholipid dispersions.* Biochemistry (1994) **33**, pages 12945 – 12953.

[110] Sorre B, Callan-Jones A, Manneville JB, Nassoya P, Joannya JF, Prosta J, Goud B and Bassereaua P. *Curvature-driven lipid sorting needs proximity to a demixing point and is aided by proteins.* PNAS (2009) **106**, (14), pages 5622 – 5626.

[111] Ludtke S, He K, Huang H. *Membrane thinning caused by magainin 2.* Biochemistry (1995) **34**, pages 16764 – 16769.

[112] Chen FY, Lee MT and Huang HW. *Evidence for the membrane thinning effect as the mechanism for peptide-induced pore formation.* Biophysical Journal (2003) **84**, pages 3751 – 3758.

[113] Epand RF, Maloy WL, Ramamoorthy A and Epand RM. *Probing the "charge cluster mechanism" in amphipathic cationic antimicrobial peptides.* Biochemistry (2010) **49**, (19), pages 4076 – 4084.

[114] Doux JPF, Hall BA and Killian JA. *How lipid headgroups sense the membrane environment: an application of 14N NMR.* Biophysical Journal (2012) **103**, pages 1245 – 1253.

[115] Raghuraman H and Chattopadhyay A. *Influence of lipid chain unsaturation on membrane-bound melittin: a fluorescence approach.* Biochimica et Biophysica Acta (2004) **1665**, pages 29 – 39.

[116] Batenberg AM, Demel RA Verkleij AJ and de Kruijff B. *Penetration of the signal sequence of Escherichia coli PhoE protein into phospholipid model membranes leads to lipid-specific changes in signal peptide structure and alterations of lipid organization.* Biochemistry (1988) **27**, pages 5678 – 5685.

[117] Strandberg E, Zerweck J, Wadhwani P and Ulrich AS. *Synergistic insertion of antimicrobial magainin-family peptides in membranes depends on the lipid spontaneous curvature.* Biophysical Journal (2013) **104**, (6), Pages 9 – 11.

[118] Wieprecht T, Beyermann M and Seelig J. *Binding of antimicrobial magainin peptides to electrically neutral membranes: thermodynamics and structure.* Biochemistry (1999) **38**, pages 10377 – 10387.

[119] Raghuraman H and Chattopadhyay A. *Interaction of melittin with membrane cholesterol: a fluorescence approach.* Biophysical Journal (2004) **87**, (4), pages 2419 – 2432.

[120] Lohner K and Blondelle SE. *Molecular mechanisms of membrane perturbation by antimicrobial peptides and the use of biophysical studies in the design of novel peptide antibiotics.* Combinatorial Chemistry and High Throughput Screening (2005) **8**, pages 241 – 256.

[121] Sakuma Y, Taniguchi T and Imai M. *Pore formation in a binary giant vesicle induced by cone shaped lipids.* Biophysical Journal (2010) **99**, pages 472 – 479.

[122] Paterson DJ, Reboud J, Wilson R, Tassieri M and Cooper JM. *Integrating microfluidic generation, handling and analysis of biomimetic giant unilamellar vesicles.* Lab on a Chip (2014) **14**, (11), pages 1806 – 1810.

[123] Cantor RS. *The influence of membrane lateral pressures on simple geometrical models of protein conformation equilibria.* Chemistry and Physics of Lipids (1999) **101**, pages 45 – 56.

[124] White SH and Wimley WC. *Hydrophobic interactions of peptides with membrane interfaces.* Biochimica et Biophysica Acta (1998) **1376**, pages 339 – 352.

[125] Mahalka AK and Kinnunen PKJ. *Binding of amphipathic α-helical antimicrobial peptides to lipid membranes: Lessons from temporins B and L.* Biochimica et Biophysica Acta (2009) **1788**, (8), pages 1600 – 1609.

[126] Popot JL and Engelman DM. *Membrane protein folding and oligomerization: the two stage model.* Biochemistry (1990) **29**, (19), pages 4031 – 4037.

[127] Henzler-Wildman K and Kern D. *Dynamic personalities of proteins.* Nature (2007) **450**, pages 664 – 672.

[128] Ben-Shaul A, Ben-Tal N and Honig B. *Statistical thermodynamic analysis of peptide and protein insertion into lipid membranes.* Biophysical Journal (1996) **71**, pages 130 – 137.

[129] Yeagle PL. *The structure of biological membranes.* Second edition, (2004), ISBN 0-8493-1403-8, page 287.

[130] Wenk MR and Seelig J. *Magainin 2 amide interaction with lipid membranes: calorimetric detection of peptide binding and pore formation.* Biochemistry (1998) **37**, pages 3909 – 3916.

[131] Almeida PF, Ladokhin AS and White SH. *Hydrogen-bond energetics drive helix formation in membrane interfaces.* Biochimica et Biophysica Act (2012) **1818**, pages 178 – 182.

[132] Ben-Tal N, Honig B, Peitzsch RM, Denisov G and McLaughlin S. *Binding of small basic peptides to membranes containing acidic lipids: theoretical models and experimental results.* Biophysical Journal (1996) **71**, pages 561 – 575.

[133] Trauble H, Teubner M, Woolley P and Eible H. *Electrostatic interactions at charged lipid interfaces: effects of pH and univalent cations on membrane structure.* Biophysical Chemistry (1976), **4**, pages 319 – 342.

[134] Seelig J. *Thermodynamics of lipid-peptide interactions.* Biochimica et Biophysica Acta (2004) **1666**, pages 40 – 50.

[135] Marsh D. *Handbook of lipid bilayers.* Second edition, (2013), ISBN 9-7814-2008-8328, page 476.

[136] Ma G and Allen HC. *DPPC Langmuir monolayer at the air-water interface: probing the tail and head groups by vibrational sum frequency generation spectroscopy.* Langmuir (2006) **22**, pages 5341 – 5349.

[137] Sachs JN, Nanda H, Petrache HI and Woolf TB. *Changes in phosphatidylcholine headgroup tilt and water order induced by monovalent salts: molecular dynamics simulations.* Biophysical Journal (2004) **86**, pages 3772 – 3782.

[138] Glukhov E, Stark M, Burrows LL and Deber CM. *Basis for selectivity of cationic antimicrobial peptides for bacterial versus mammalian membranes.* The Journal of Biological Chemistry (2005) **280**, (40), pages 33960 – 33967.

[139] Planque MRR de and Killian JA. *Protein-lipid interactions studied with designed transmembrane peptides: role of hydrophobic matching and interfacial anchoring (Review).* Molecular Membrane Biology (2003) **20**, pages 271 – 284.

[140] Jesus A.J. de and Allen TW. *The role of tryptophan side chains in membrane protein anchoring and hydrophobic mismatch.* Biochimica et Biophysica Acta (BBA) – Biomembranes (2013) **1828**, (2), pages 864 – 876.

[141] Leikin S, Kozlov MM, Fuller NL and Rand RP. *Measured effects of diacylglycerol on structural and elastic properties of phospholipid membranes.* Biophysical Journal (1996) 71, pages 2623 – 2632.

[142] Letter to the editor. *Nonlamellar packing parameters for diacylglycerols.* Biophysical Journal (1997) 72, pages 2834 – 2836.

[143] Hristova K, Dempset CE and White SH. *Structure, location and lipid perturbations of melittin at the membrane interface.* Biophysical Journal (2001) **80**, (2), pages 801 – 811.

[144] Zhu WL, Song YM, Park Y, Park KH, Yang S-T, Kim J, Park I-L, Hahm K-S and Shin SY. *Substitution of the leucine zipper sequence in melittin with peptoid residues affects self-association, cell selectivity and mode of action.* Biochimica et Biophysica Acta (2007) **1768**, pages 1506 – 1517.

[145] Asthana N, Yadav SP and Ghosh JK. *Dissection of antibacterial and toxic activity of melittin.* The Journal of Biological Chemistry (2004) **279**, (53), pages 55042 – 55060.

[146] Cullis PR, Hope MJ, Bally MB, Madden TD, Mayer LD and Fenske DB. *Influence of pH gradients on the transbilyer transport of drugs, lipids, peptides and metal ions into large unilamellar vesicles.* Biochimica et Biophysica Acta (1997) **1331**, pages 187 – 211.

[147] Huang HW, Chen F-Y, Lee M-T. *Molecular mechanism of peptide-induced pores in membranes.* Physical Review Letters (2004) **92**, (9) pages 198301 – 198304.

[148] Ge Y, MacDonald DL, Holroyd KJ, Thornsberry C, Wexler H and Zasloff M. *Invitro antibacterial properties of pexihanan, and analogue of magainin.* Antimicrobial Agents and Chemotherapy (1999) **43**, (4), pages 782 – 788.

[149] Dow CE, Rodger A, Roper DI and van den Berg HA. *A model of membrane contraction predicting initiation and completion of cell division.* Integrated Biology (2013) **5**, pages 778 – 795.

[150] Wheaten SA, Lakshmanan A and Almeida PF. *Statistical analysis of peptide-induced graded and all-or-none fluxes in giant vesicles.* Biophysical Journal (2013) **105**, pages 432 – 443.